NASA-CR-195730

NAGI-343 -
p. 193
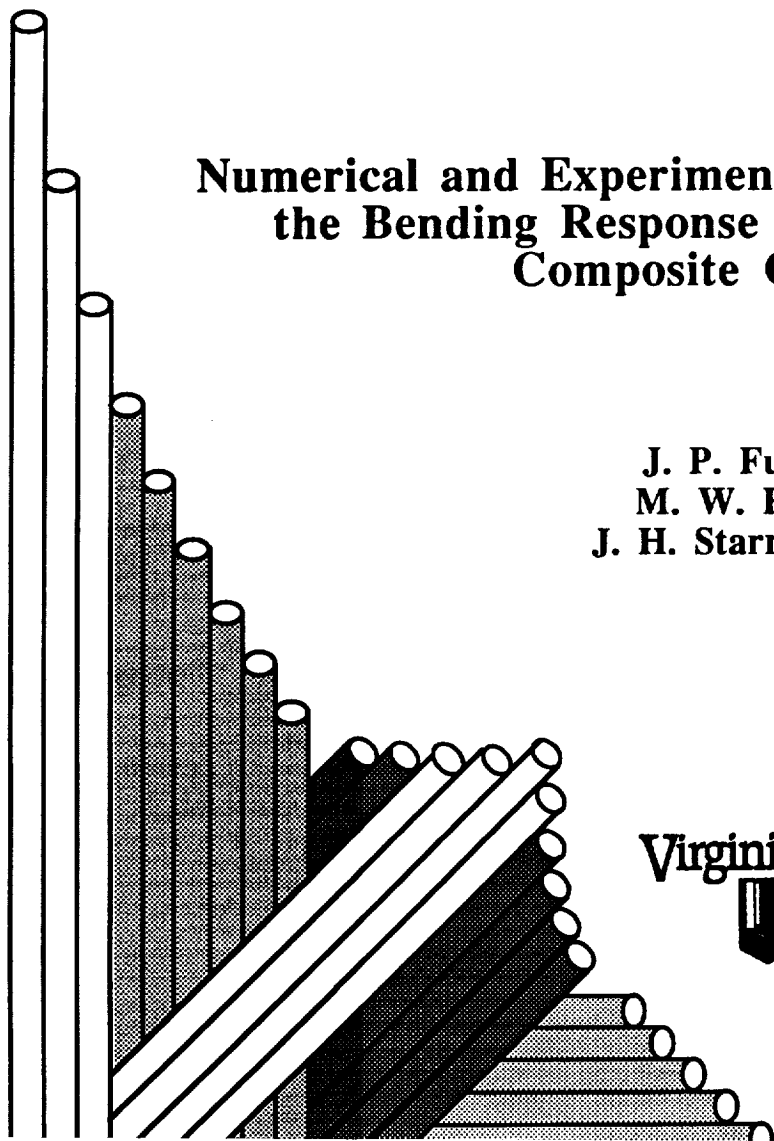
CENTER FOR COMPOSITE MATERIALS AND STRUCTURES

Numerical and Experimental Investigation of the Bending Response of Thin-Walled Composite Cylinders

J. P. Fuchs
M. W. Hyer
J. H. Starnes, Jr.

Virginia Tech
VIRGINIA POLYTECHNIC INSTITUTE
AND STATE UNIVERSITY

BLACKSBURG , VIRGINIA
24061

(NASA-CR-195730) NUMERICAL AND
EXPERIMENTAL INVESTIGATION OF THE
BENDING RESPONSE OF THIN-WALLED
COMPOSITE CYLINDERS Interim Report
No. 95, Aug. 1988 - Sep. 1993
(Virginia Polytechnic Inst. and
State Univ.) 193 p

N94-28801

Unclas

G3/39 0002615

September 1993

College of Engineering
Virginia Polytechnic Institute and State University
Blacksburg, Virginia 24061

September, 1993

VPI-E-93-11
CCMS-93-19

Numerical and Experimental Investigation of the Bending Response of Thin-Walled Composite Cylinders

J. P. Fuchs[1]

M. W. Hyer[2]

J. H. Starnes, Jr.[3]

Prepared for: Aircraft Structures Branch
                      National Aeronautics and Space Administration
                      Langley Research Center
                      Hampton, Virginia 23681-0001

---

[1] Research Associate, Department of Engineering Science and Mechanics, Virginia Polytechnic Institute and State University

[2] Professor, Department of Engineering Science and Mechanics, Virginia Polytechnic Institute and State University

[3] Head, Aircraft Structures Branch, NASA Langley Research Center, Hampton, Virginia

Abstract

A numerical and experimental investigation of the bending behavior of six eight-ply graphite-epoxy circular cylinders is presented. Bending is induced by applying a known end-rotation to each end of the cylinder, analogous to a beam in bending. The cylinders have a nominal radius of 6 inches, a length-to-radius ratio of 2 and 5, and a radius-to-thickness ratio of approximately 160. A $[\mp 45/0/90]_S$ quasi-isotropic layup and two orthotropic layups, $[\mp 45/0_2]_S$ and $[\mp 45/90_2]_S$, are studied. A geometrically nonlinear special-purpose analysis, based on Donnell's nonlinear shell equations, is developed to study the prebuckling responses and gain insight into the effects of non-ideal boundary conditions and initial geometric imperfections. A geometrically nonlinear finite element analysis is utilized to compare with the prebuckling solutions of the special-purpose analysis and to study the buckling and postbuckling responses of both geometrically perfect and imperfect cylinders. The imperfect cylinder geometries are represented by an analytical approximation of the measured shape imperfections. Extensive experimental data are obtained from quasi-static tests of the cylinders using a test fixture specifically designed for the present investigation. A description of the test fixture is included. The experimental data are compared to predictions for both perfect and imperfect cylinder geometries. Prebuckling results are presented in the form of displacement and strain profiles. Buckling end-rotations, moments, and strains are reported, and predicted mode shapes are presented. Observed and predicted moment vs. end-rotation relations, deflection patterns, and strain profiles are illustrated for the postbuckling responses. It is found that a geometrically nonlinear boundary layer behavior characterizes the prebuckling responses. The boundary layer behavior is sensitive to laminate orthotropy, cylinder geometry, initial geometric imperfections, applied end-rotation, and non-ideal boundary conditions. Buckling end-rotations, strains,

and moments are influenced by laminate orthotropy and initial geometric imperfections. Measured buckling results correlate well with predictions for the geometrically imperfect specimens. The postbuckling analyses predict equilibrium paths with a number of scallop-shaped branches that correspond to unique deflection patterns. The observed postbuckling deflection patterns and measured strain profiles show striking similarities to the predictions in some cases. Ultimate failure of the cylinders is attributed to an interlaminar shear failure mode along the nodal lines of the postbuckling deflection patterns.

Acknowledgments

Nomenclature

Laminate Properties and Geometry

A_{ij} laminate extensional stiffnesses, see Eq. (B.4)

A^* extensional stiffness combination, $\dfrac{A_{11}A_{22} - A_{12}^2}{A_{11}}$

B_{ij} laminate coupling stiffnesses, see Eq. (B.4)

D_{ij} laminate bending stiffnesses, see Eq. (B.4)

D_1^* bending stiffness combination, $\dfrac{D_{11}D_{22} - D_{12}^2}{D_{11}}$

D_2^* bending stiffness combination, $\dfrac{D_{11}D_{26} - D_{12}D_{16}}{D_{11}}$

D_3^* bending stiffness combination, $\dfrac{D_{11}D_{66} - D_{16}^2}{D_{11}}$

E_1, E_2 inplane Young's moduli

E_x effective axial inplane Young's modulus, $\dfrac{A_{11}A_{22} - A_{12}^2}{HA_{22}}$

E_θ effective circumferential inplane Young's modulus, $\dfrac{A_{11}A_{22} - A_{12}^2}{HA_{11}}$

G_{12} inplane shear modulus

$G_{x\theta}$ effective inplane shear modulus, $\dfrac{A_{66}}{H}$

h lamina thickness

H cylinder wall thickness

Nomenclature

I	cylinder cross-section moment of inertia, $\pi R^3 H$
L	cylinder length
$Q_{ij}, \overline{Q}_{ij}$	reduced ply stiffnesses, transformed reduced ply stiffnesses
R	cylinder midsurface radius
x, θ, z	axial, circumferential, and radial coordinates, respectively, of reference surface
X, Y, Z	global cartesian coordinate directions
α	lamina orientation angle
ν_{12}, ν_{21}	lamina Poisson's ratios
$\nu_{x\theta}$	effective laminate Poisson's ratio, $\dfrac{A_{12}}{A_{22}}$

Displacements, Strains, Stresses, and Resultants

$N_x, N_\theta, N_{x\theta}$	force resultants, see Eqs. (B.2) and (B.3)
$M_x, M_\theta, M_{x\theta}$	moment resultants, see Eqs. (B.2) and (B.3)
$N_x^P, N_\theta^P, N_{x\theta}^P$	force resultants due to initial pre-straining, see Eq. (B.6)
$M_x^P, M_\theta^P, M_{x\theta}^P$	moment resultants due to initial pre-straining, see Eq. (B.6)
Q_x	shear resultant, $\dfrac{\partial M_x}{\partial x} + 2\dfrac{\partial M_{x\theta}}{R\partial\theta} - \left[N_x \cdot \beta_x^o + N_{x\theta} \cdot \beta_\theta^o \right]$
u^o, v^o, w^o	axial, circumferential, and radial displacements, respectively, of cylinder midsurface
$\beta_x^o, \beta_\theta^o$	midsurface rotations, see Eq. (2.2)
$\varepsilon_x, \varepsilon_\theta, \gamma_{x\theta}$	total inplane strains, see Eq. (2.3)
$\varepsilon_x^o, \varepsilon_\theta^o, \gamma_{x\theta}^o$	inplane midsurface strains, see Eq. (2.4)

κ_x^o, κ_θ^o, $\kappa_{x\theta}^o$	midsurface curvatures, see Eq. (2.5)
σ_x, σ_θ, $\tau_{x\theta}$	inplane stresses, see Eq. (B.1)

Analysis

$\vec{F}(x, \vec{y}(x))$	$(16N + 8) \times 1$ array of right-hand sides of first order nonlinear ordinary differential equations, see Eq. (2.29)
$\vec{g}(\vec{y}(\pm\frac{L}{2}))$	$(16N + 8) \times 1$ array of boundary conditions, see Eq. (2.30)
K_M	rotational spring stiffness of elastic support, see Eq. (2.17)
K_Q	radial spring stiffness of elastic support, see Eq. (2.17)
M	applied bending moment
N	number of circumferential harmonics considered in expansion of the primary response variables
$\overline{w}$	known radial shape imperfection, see Eqs. (2.35) and (B.7)
w_R	applied radial deformation boundary condition, see Eq. (2.16)
$\vec{y}(x)$	$\left[y_1(x), y_2(x), ..., y_{16N+8}(x) \right]^T$, $(16N + 8) \times 1$ array of axial components of primary response variables, see definition of $\mathbf{Y}(x)$ below
$\mathbf{Y}(x)$	$\begin{bmatrix} y_1(x) & y_2(x) & \cdots & y_{2N+1}(x) \\ y_{2N+2}(x) & \cdots & \cdots & y_{4N+2}(x) \\ \cdots & \cdots & \cdots & \cdots \\ y_{14N+8}(x) & y_{14N+9}(x) & \cdots & y_{16N+8}(x) \end{bmatrix}$, $8 \times (2N+1)$ matrix, see Eq. (2.27)
ξ	amplitude of axisymmetric shape imperfection normalized by H, see Eq. (2.35)

Nomenclature

$\vec{\Upsilon}(x, \theta)$
  $\left[u^{\circ}, \ v^{\circ}, \ w^{\circ}, \ \beta_x^{\circ}, \ N_x, \ N_{x\theta}, \ Q_x, \ M_x \right]^T$, 8×1 array of primary response variables, see Eq. (2.27)

$\vec{\Phi}(x, \theta, \vec{\Upsilon}(x, \theta))$
  8×1 array of right-hand sides of first order nonlinear partial differential equations, see Eq. (2.18) and Eqs. (2.19) through (2.26)

$\vec{\Psi}(\theta)$
  $\left[1, \ cos\theta, \ cos2\theta, \ ..., \ cosN\theta, \ ..., \ sin\theta, \ sin2\theta, \ ..., \ sinN\theta \right]^T$, $(2N + 1) \times 1$ array of circumferential components of primary response variables, see Eq. (2.27)

Ω
  applied end-rotation, see Eq. (2.16)

Response Parameters

m
  number of axial half-waves corresponding to classical axisymmetric buckling of axially compressed cylinder, see Eq. (1.2)

δ
  measure of cross-section ovalization, see Eq. (2.33)

λ
  characteristic half-wavelength of boundary layer responses, see Eq. (2.34)

Buckling Parameters

M_{cr}
  classical buckling moment for short cylinders, see Eqs. (1.4) and (2.40)

M_{cr}^B
  classical Brazier cross-section collapse moment for long cylinders, see Eqs. (1.5) and (2.39)

M_{cr}^{exp}
  experimental buckling moment

M_{cr}^{fe}
  buckling moment predicted by finite element analysis

N_{cr}
  classical axial compression buckling force resultant, see Eq. (1.1)

$N_{cr}^{isotropic}$
  classical axial compression buckling force resultant for isotropic cylinders, see Eq. (1.3)

Nomenclature

u_{cr}	classical axial compression buckling end-shortening, see Eq. (2.43)
ε_{cr}	classical buckling midsurface compressive strain, see Eq. (2.42)
ε_{cr}^{exp}	experimental buckling midsurface compressive strain
ε_{cr}^{fe}	buckling midsurface compressive strain predicted by finite element analysis
Λ	nondimensional length, $\sqrt{L^2 H / R^3}$, see Fig. 1-3
Ω_{cr}	classical buckling end-rotation, see Eq. (2.41)
Ω_{cr}^{exp}	experimental buckling end-rotation
Ω_{cr}^{fe}	buckling end-rotation predicted by finite element analysis

Failure Strains

$\varepsilon_1^c, \varepsilon_1^t$	maximum longitudinal compressive strain, tensile strain
$\varepsilon_2^c, \varepsilon_2^t$	maximum transverse compressive strain, tensile strain
γ_{12}^s	maximum shear strain

Table of Contents

Table of Contents

Table of Contents

List of Figures

List of Figures

List of Figures

List of Figures

List of Tables

1. Introduction

The thin-walled circular cylinder is an important configuration found in a host of structural applications. Due to its structurally efficient shape, cylinders are commonly utilized to resist various combinations of axial, torsional, bending, and pressure loads. Structural and shell wall stiffness parameters can be tailored to meet the loading requirements frequently encountered in aerospace, transportation, and other commercial and military applications. Advanced composite materials offer high strength, low weight, good corrosion resistance, and the excellent fatigue properties often desired in these applications. It would seem to be natural to combine the efficiency of a cylindrical structure with the superior characteristics of composite materials. However, typical structural composites, such as thermosets, are brittle by nature. Material failure can occur suddenly and without prior indication. Since the load carrying capacity of a shell structure is determined by either a stable loading condition in which local deformations can induce material failure, or by an unstable loading condition which can trigger large deformations and subsequent material failure, it is apparent that sudden material failure could be a detriment. To take advantage of the properties of advanced composite materials and to achieve maximum structural performance and efficiency despite this sudden material failure characteristic, it will be necessary to predict and verify the behavior and failure characteristics of composite shell structures more accurately than previously necessary with metallic shell structures.

It is with this goal in mind that the problem of bending of thin-walled composite cylinders was investigated in depth. In the present investigation bending refers to the loading state where one side of the cylinder is in compression in the axial direction and the other side is in tension. This type of bending load is analogous to a beam in bending and is intended to simulate a primary loading condition prevalent in a number of structural configurations typically found in transport aircraft fuselage sections, launch vehicles, and transportation and storage containers.

1

To follow in this chapter is a survey of some of the literature felt to be relevant to this topic, followed by an overview of the approach used in this study. The survey will begin with a brief description of the axial compression problem and then will review the literature pertinent to the stable and unstable bending of isotropic and anisotropic thin-walled cylinders.

1.1 Literature Survey

Stability issues often arise in problems involving compression-loaded shell structures. For example, it is well known that axially compressed cylinders buckle in an unstable fashion. Since a cylinder in bending experiences compression as well as tension, it is not surprising to find that buckling is also a key feature of this problem. Therefore, it seems that a brief discussion on the axial compression of circular cylinders is appropriate. Insight into the bending problem and useful analogies can result from discussing the axial compression problem.

1.1.1 Axial Compression

Axial compression is often a primary loading state in many thin-walled, circular cylinder applications. As a result, the axial compression problem has been the focus of many investigations in the literature. Numerous studies of the compression response have been conducted for both isotropic and anisotropic material wall constructions. Most often, these studies are concerned with the determination of the bifurcation buckling load. Excluding the case of column buckling, this is the load at which a cylinder in axial compression will suddenly buckle into either an axisymmetric or doubly periodic* mode shape. These two types of mode shapes are shown in Fig. 1-1. The critical axial force resultant associated with the axisymmetric buckling of an imperfection-free anisotropic cylinder, shown in Fig. 1-1 (a), can be computed from a relation given in [1][†]. This relation can be reduced to the simple equation

$$N_{cr} = \frac{2}{R} \sqrt{E_{\theta} H D_{11}}$$ (1.1)

---

* Often referred to as the 'diamond-shaped' or 'checkerboard' deflection pattern.
[†] Numbers in square brackets designate references.

2

for the practical case of balanced symmetric laminates. The corresponding number of axial half-waves of the buckling mode, m, is given by the equation

$$\frac{m\pi}{L} = \left[\frac{E_\theta H}{D_{11}R^2}\right]^{\frac{1}{4}}.$$ (1.2)

It can be shown that Eq. (1.1) reduces to the well known isotropic buckling relation

$$N_{cr}^{isotropic} = 0.605EH^2/R$$ (1.3)

assuming a Poisson's ratio of 0.3.

The buckling phenomenon is a complex process that typically results in large out-of-plane, or radial, deformations which are accompanied by significant reductions in the shell stiffness and the load carrying capacity. Material damage, either inplane or interlaminar, may occur during this buckling deformation process if damage has not already occurred during the prebuckling process. It is possible, however, for a cylinder to buckle elastically without material damage if the buckling strains remain sufficiently small.

Buckling test data for cylinders in axial compression are widely reported in the literature for isotropic cylinders, and to a lesser extent, for anisotropic cylinders. Generally, it has been found that large discrepancies exist between experimental buckling data and analytical predictions. Since the 1940's, it has become known that cylindrical shells are extremely imperfection sensitive so that many of the observed discrepancies could be

(a) Axisymmetric Mode　　　　　(b) Doubly Periodic Mode
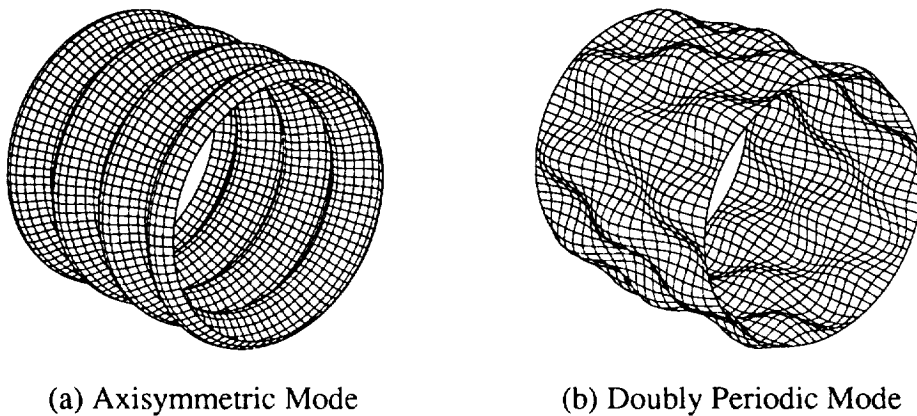
Fig. 1-1 Axial Compression Buckling Patterns

3

attributed to imperfections such as shape variations, thickness variations, and nonuniform loading conditions. Other important factors that have been found to contribute to these differences are the consideration of geometrically nonlinear prebuckling conditions and the effect of boundary conditions. The full explanation of these discrepancies is still an active topic of investigation. See references [2] and [3] for a comprehensive review of the subject until the mid 1980's.

Based on some of the observations made from the axial compression problem, one might expect that imperfections, boundary conditions, and geometric nonlinearities play an important role in the bending problem as well. A survey of the bending problem is presented next.

1.1.2 Bending

The treatment in the literature of cylinders subjected to bending is not nearly as extensive as that of cylinders in compression. As in the case of axial compression, it appears that most of the literature is concerned with the determination of the point of instability for cylindrical shells in bending. This is indeed a very important problem since buckling instability determines the range of stable bending for many practical shell structures. However, it is also very important to understand the prebuckling behavior as well as the parameters that influence it. An understanding of the prebuckling problem will allow greater insight into the buckling behavior.

Prebuckling

The stable bending problem has been considered at various levels of complexity. The simplest analyses consider the cylinder in bending as a beam with a circular cross-section in flexure. This approach is characterized by a geometrically linear axial membrane stress state in which end effects and cross-sectional deformations are neglected. Solutions to this problem can be obtained through mechanics of materials approaches, three-dimensional elasticity approaches, or two-dimensional shell theory approaches. These solutions are well known for isotropic materials but are not as readily available for anisotropic materials. See for example references [4-9].

More refined solutions can be obtained for the bending of finite length anisotropic cylinders using a two-dimensional shell theory approach. Fuchs and Hyer [10] used a Kantorovich procedure and obtained closed form solutions for the geometrically linear

4

displacement, inplane stress, and interlaminar stress responses for symmetric laminates. It was found that end supports significantly affect the displacement, force resultant, intralaminar and interlaminar stress responses in a boundary layer region near the supported ends. It was also shown that the shell wall stiffnesses and cylinder geometry affect the character of this boundary layer region. The geometrically nonlinear prebuckling response of finite length anisotropic cylinders was also solved by Fuchs and Hyer [11] using a similar approach to the one used in [10]. It was found that the geometrically nonlinear behavior of balanced symmetric laminates significantly affects the prebuckling boundary layer. Unlike in the geometrically linear problem, it was found that the character of the geometrically nonlinear boundary layer responses is a function of the load level in addition to the shell wall stiffness and geometric parameters.

Buckling

Studies of the buckling of cylinders in bending have been conducted in a manner analogous to the studies conducted of buckling due to axial compression. However, in bending, unlike in axial compression loading, there are two classical structural collapse modes that may result in large deformations. In the case of relatively short cylinders, sudden bifurcation buckling can occur on the compression side of the cylinder, much like the case of axial compression, triggering short wavelength buckling deformations. For very long cylinders, there is the additional possibility of cross-section instability, where the cross-section flattens, or ovalizes. This ovalization effect reduces the cross-sectional moment of inertia until the cylinder can no longer sustain the applied bending moment, resulting in a large 'kink' in the center of the cylinder. For this case, collapse is defined by the maximum moment or limit point. With intermediate-length cylinders, both classical modes interact to cause the formation of local buckles on the compression side. These collapse modes are depicted schematically in Fig. 1-2.

The bifurcation buckling problem depicted in Fig. 1-2 (a) was first considered by Flügge in 1932 [12]. Flügge used a Rayleigh-Ritz approach to solving the bending buckling equations for isotropic cylinders assuming a membrane prebuckling solution. Unfortunately, Flügge was unable to conduct an extensive numerical study due to the inadequate computational capabilities of the day. It was not until 1961 that more complete results were obtained for isotropic cylinders by Seide and Weingarten [13]. They computed the critical bending buckling stresses using the Galerkin procedure assuming a membrane prebuckling state. They found that the critical buckling stress was essentially equal to the buckling

stress corresponding to the case of uniform axial compression. Both edge effects and ovalization effects are neglected in their solution. The critical moment can therefore be computed from Eq. (1.3) as

$$M_{cr} = \pi R^2 N_{cr}^{isotropic} = 0.605\pi ERH^2.$$ (1.4)

Dramatic improvements in computer technology since the 1960's has generated considerable attention to this buckling problem. A number of investigators considered the buckling of isotropic cylinders in [14-16], anisotropic cylinders [11,17-24], and sandwich cylinders [25-28]. Membrane prebuckling conditions are assumed in nearly all instances with the exception of [11] and [24].

The problem of cross-section instability of isotropic cylinders, illustrated in Fig. 1-2 (b), was first addressed by Brazier in 1926 [29]. Brazier found that infinitely long cylinders collapsed when the radially inward deflection reached a value of 2/9 of the cylinder radius, regardless of the shell wall thickness and stiffness properties. The corresponding bending moment was found to be

$$M_{cr}^B = 0.329\pi ERH^2$$ (1.5)

for the case of a Poisson's ratio equal to 0.3, a value somewhat greater than half the value found by Seide and Weingarten. Many investigators have since studied the ovalization of isotropic cylinders [30-38], in many cases refining Brazier's original solution. Anisotropic cylinders are considered in the analyses of [11,39-40].

(a) Compression Buckling
Mode of Short Cylinder

(b) Cross-section Collapse
Mode of Long Cylinder

(c) Interaction for Cylinder
of Intermediate Length
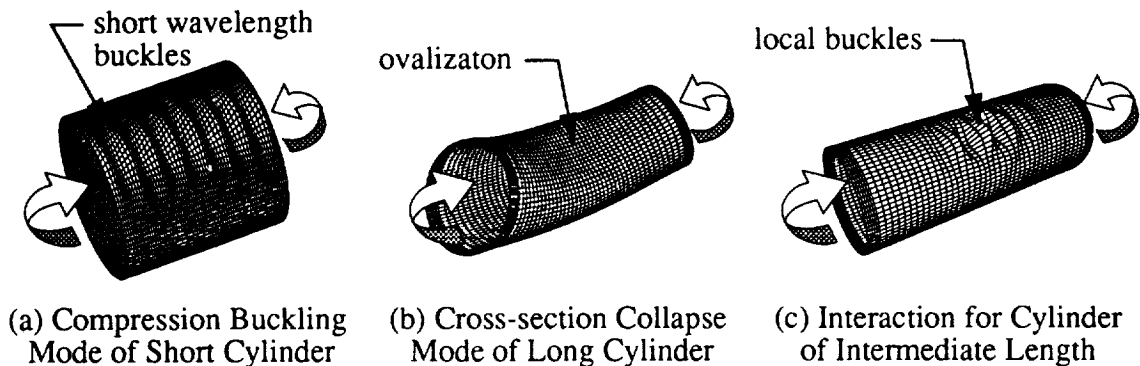
Fig. 1-2 Cylinder Bending Collapse Modes

6

Introduction

The bending collapse of finite length cylinders was first investigated by Axelrad[*] in 1965 [41]. Axelrad considered the effect of localized buckling on the cross-section ovalization of isotropic cylinders. It was shown that buckling occurred for short cylinders according to Eq. (1.4), while buckling with ovalization occurred at a bending moment approximately 10% to 15% lower than predicted by Eq. (1.5) for very long cylinders. The buckling moment of intermediate length cylinders was found as a function the nondimensional length, Λ, which is proportional to the quantity $\sqrt{L^2 H/R^3}$. A simplified treatment of Axelrad's ideas is presented by Calladine [42]. Other investigations can be found in [43-50].

The bending collapse response characteristics discussed in the preceding are summarized schematically in Fig. 1-3, where the moment values are normalized with respect to Eq. (1.4). It is seen in Fig. 1-3 (a) that short cylinders, i.e., small values of Λ, collapse in a compression buckling mode. As Λ increases from small to large values, there is a region of interaction between the compression buckling and cross-section collapse modes. Very long cylinders, i.e., large values of Λ, buckle predominantly due to cross-section ovalization. The corresponding moment-rotation characteristics for these various situations are shown in Fig. 1-3 (b). It is observed from this figure that the moment-rotation relation is essentially linear until buckling for small values of Λ. Cylinders with large values of Λ, in contrast, are characterized by the limit point behavior. Intermediate length cylinders exhibit a combination of both the linear behavior and the limit point behavior.

Postbuckling

The postbuckling analysis of cylindrical shells is an extremely complex and computationally intense task, even with state-of-the-art analysis tools. This fact is reflected by the extremely limited number of postbuckling investigations in the literature, particularly in the area of bending [51]. It is well known, however, that the initial postbuckling path of cylindrical shells is extremely unstable and that a high degree of imperfection sensitivity can be expected. Suffice it to say, there is much to be considered in the area of postbuckling of cylinders in bending.

---

[*] also written as Akselrad or Aksel'rad.

Experimental Investigations

Nearly all experimental investigations regarding cylinders center on the buckling of relatively short unstiffened [52-61] and stiffened [62-74] isotropic cylinders. Experimental data for anisotropic wall constructions are extremely limited and are primarily confined to relatively long and thick-walled constructions [75-81]. One notable exception, however, is the investigation by Holston et al. [77], which provides detailed information on the buckling of filament wound fiberglass-epoxy cylinders subjected to bending, compression, torsion, and combined loading. One source was located for a thin-walled, stiffened, corrugated cylinder subjected to bending [82].

In the experimental investigations, measures of the global bending responses, such as bending moments and strains, are typically reported. Strain data are usually limited to the circumferential variation of the axial strains far removed from the cylinder ends.

1.2 Objective of Current Study

It is evident from the literature cited in the section 1.1.2 that very few investigations consider both an in-depth analytical study and an experimental investigation of the bending of

(a) Collapse Moment vs.
Dimensionless Length, Λ
(after Calladine [42])

(b) Moment vs. Rotation
(after Axelrad [41])
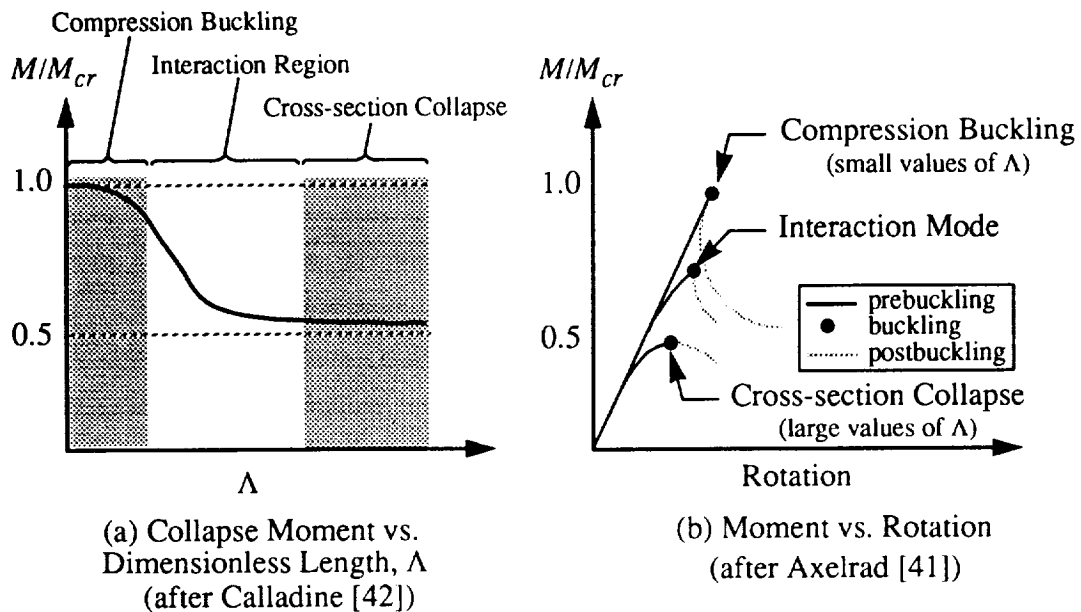
Fig. 1-3 Cylinder Bending Collapse Response Characteristics

composite cylinders. Previous analytical investigations generally lacked detailed prebuckling analyses, and experimental data were found to be scarce and limited in scope. The objective of the present work is to provide a detailed investigation of this problem, considering the geometrically nonlinear prebuckling responses, the buckling responses, and the postbuckling responses. Additionally, essential experimental data are provided for composite cylinders. Although practical cylindrical shell structures are often stiffened and can be subjected to combined loading conditions in service, it is important to gain fundamental insight into the basic problem of unstiffened composite cylinders. Understanding of the influence of laminate stiffness and structural parameters on the prebuckling, buckling, and postbuckling response characteristics can then be used to gain insight into the bending behavior of more complex shell structures.

1.3 Approach

The approach used in the present study involves both a numerical and an experimental investigation of six composite cylinders with three layups and two lengths. The cylinders were tested in a bending test fixture constructed specifically for the present investigation and were analyzed in consideration of geometric nonlinearities and initial geometric shape imperfections.

Chapter 2 describes the analyses used to study the prebuckling, buckling, and postbuckling responses. The theory for a computationally efficient special-purpose program is developed for the purpose of gaining insight into the prebuckling responses. This program is employed to study the effects of non-ideal boundary conditions and axisymmetric geometric imperfections in addition to determining the onset of buckling. A finite element program is utilized to compare prebuckling results with the special-purpose program and to study the buckling and postbuckling responses. Selected responses, computed with the various computational approaches, are presented to illustrate the general character and features of the bending behavior of six idealized cylinders. Supporting information for the prebuckling analysis is provided in Appendices A, B, and C.

The experimental program is discussed in Chapter 3. The bending test apparatus, specimens, instrumentation, and experimental procedures are described in detail. Specifics of the specimen fabrication and preparation procedures are provided in Appendix D. Infor-

mation regarding the specimen properties and surface shape measurements are presented in Appendix E and Appendix F, respectively.

The measured and observed bending responses are reported and compared to the numerical predictions for the individual test specimens in Chapter 4. Numerical predictions for both perfect and imperfect cylinder geometries are presented. The moment vs. end-rotation characteristics, prebuckling displacements and strain distributions, buckling end-rotations and corresponding moments, and postbuckling deflection shapes and strain profiles are presented and discussed. Observed material damage is also addressed.

As might be expected, the observed and predicted responses do not always exhibit perfect correlation. Non-ideal boundary conditions and slight irregularities in the fixture and specimens can in some cases have a measurable effect on the responses. A number of potential sources of discrepancies are described and it is illustrated that they can influence the predicted responses. These issues are addressed in Chapter 5.

Finally, in Chapter 6, conclusions are drawn based on the various aspects of the prebuckling, buckling, and postbuckling responses and the observed material failure. Also, recommendations are made for the further research of some important issues not addressed in the current study.

2. Analysis

The analysis of the cylinder bending responses is divided into three major response categories. The first section considers the prebuckling responses and is based on a semi-analytical approach. The governing equations, boundary conditions, and solution methodology for this approach are developed. Non-ideal boundary conditions, initial shape imperfections, and the possibility of prebuckling material failure are also considered. Solutions for the prebuckling problem are computed with a special-purpose program. The second section is concerned with the prediction of the buckling responses. Buckling end-rotations and moments are computed from a classical analysis, a special use of the prebuckling analysis, and a finite element analysis. The final section considers the postbuckling responses which are studied using a finite element analysis. The analyses of the buckling and postbuckling responses are based on the STAGS [83]* finite element program. Selected prebuckling, buckling, and postbuckling responses are illustrated through numerical examples.

2.1 Prebuckling

The governing equations for the thin-walled cylinder of Fig. 2-1 are based on Donnell's nonlinear kinematics [54]. These kinematics are used throughout the prebuckling analysis for the reason that geometrically nonlinearities are included and that the resulting equations are amenable to solution by the methods to be discussed in this section. It is the most fundamental shell theory available and as such is occasionally the subject of controversy (see Appendix A).

---

* The QSTAGS implementation of the STAGS program was used throughout this work. Documentation was under development at the time of this writing. The STAGSC-1 implementation is documented in this reference.

11
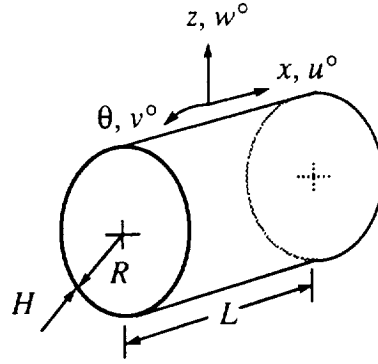
Fig. 2-1 Cylinder Geometry

2.1.1 Equations and Solution Procedure

Kinematics

It is assumed that the strains are small compared to unity and that the cylinder wall is thin compared to the cylinder radius so that z/R-terms can neglected in comparison to unity. Further, it is assumed that the Kirchhoff-Love hypothesis is applicable so that the displacements at any point in the shell wall can be approximated by the relations

$$u(x, \theta, z) = u^\circ(x, \theta) + z \cdot \beta_x^\circ(x, \theta)$$
$$v(x, \theta, z) = v^\circ(x, \theta) + z \cdot \beta_\theta^\circ(x, \theta) \tag{2.1}$$
$$w(x, \theta, z) = w^\circ(x, \theta).$$

The midsurface rotations are defined as

$$\beta_x^\circ \equiv -\frac{\partial w^\circ}{\partial x} \qquad \text{and} \qquad \beta_\theta^\circ \equiv -\frac{\partial w^\circ}{R\partial \theta}. \tag{2.2}$$

The axial, circumferential, and radial displacements of the midsurface of the shell wall are defined as u°, v°, and w°, respectively. These midsurface quantities are shown in Fig. 2-2.

The intralaminar strains at any point in the shell wall are given as

$$\varepsilon_x(x, \theta, z) = \varepsilon_x^\circ(x, \theta) + z \cdot \kappa_x^\circ(x, \theta)$$
$$\varepsilon_\theta(x, \theta, z) = \varepsilon_\theta^\circ(x, \theta) + z \cdot \kappa_\theta^\circ(x, \theta) \tag{2.3}$$
$$\gamma_{x\theta}(x, \theta, z) = \gamma_{x\theta}^\circ(x, \theta) + z \cdot \kappa_{x\theta}^\circ(x, \theta).$$

12

The geometrically nonlinear midsurface strains are related to the displacement quantities by the relations

$$\varepsilon_x^o = \frac{\partial u^o}{\partial x} + \frac{1}{2}(\beta_x^o)^2$$

$$\varepsilon_\theta^o = \frac{\partial v^o}{R\partial\theta} + \frac{w^o}{R} + \frac{1}{2}(\beta_\theta^o)^2 \qquad (2.4)$$

$$\gamma_{x\theta}^o = \frac{\partial u^o}{R\partial\theta} + \frac{\partial v^o}{\partial x} + \beta_x^o \cdot \beta_\theta^o \ ,$$

and the changes in curvature are

$$\kappa_x^o = \frac{\partial\beta_x^o}{\partial x} = -\frac{\partial^2 w^o}{\partial x^2}$$

$$\kappa_\theta^o = \frac{\partial\beta_\theta^o}{R\partial\theta} = -\frac{\partial^2 w^o}{R^2\partial\theta^2} \qquad (2.5)$$

$$\kappa_{x\theta}^o = \frac{\partial\beta_\theta^o}{\partial x} + \frac{\partial\beta_x^o}{R\partial\theta} = -2\frac{\partial^2 w^o}{R\partial x\partial\theta}.$$

Equilibrium Equations

The governing equations for the right circular cylinder shown in Fig. 2-1 are derived from the principle of virtual work,

$$\delta V = \delta U + \delta W = 0. \qquad (2.6)$$

The first variation of the internal energy, δU, is represented by the volume integral

$$\delta U = \int_{x=-\frac{L}{2}}^{+\frac{L}{2}} \int_{\theta=0}^{2\pi} \int_{z=-\frac{H}{2}}^{+\frac{H}{2}} (\sigma_x\delta\varepsilon_x + \sigma_\theta\delta\varepsilon_\theta + \tau_{x\theta}\delta\gamma_{x\theta})\, dzR\,(1+z/R)\, d\theta dx. \qquad (2.7)$$

The δW term in Eq. (2.6) represents the first variation of the so-called potential energy of external traction forces. Examples of external traction forces are lateral pressure, axial tension or compression, and torsion. The effects of flexible end supports can also be included in this manner. In this study, only flexible end supports are assumed to contribute to the potential energy of external forces.

13
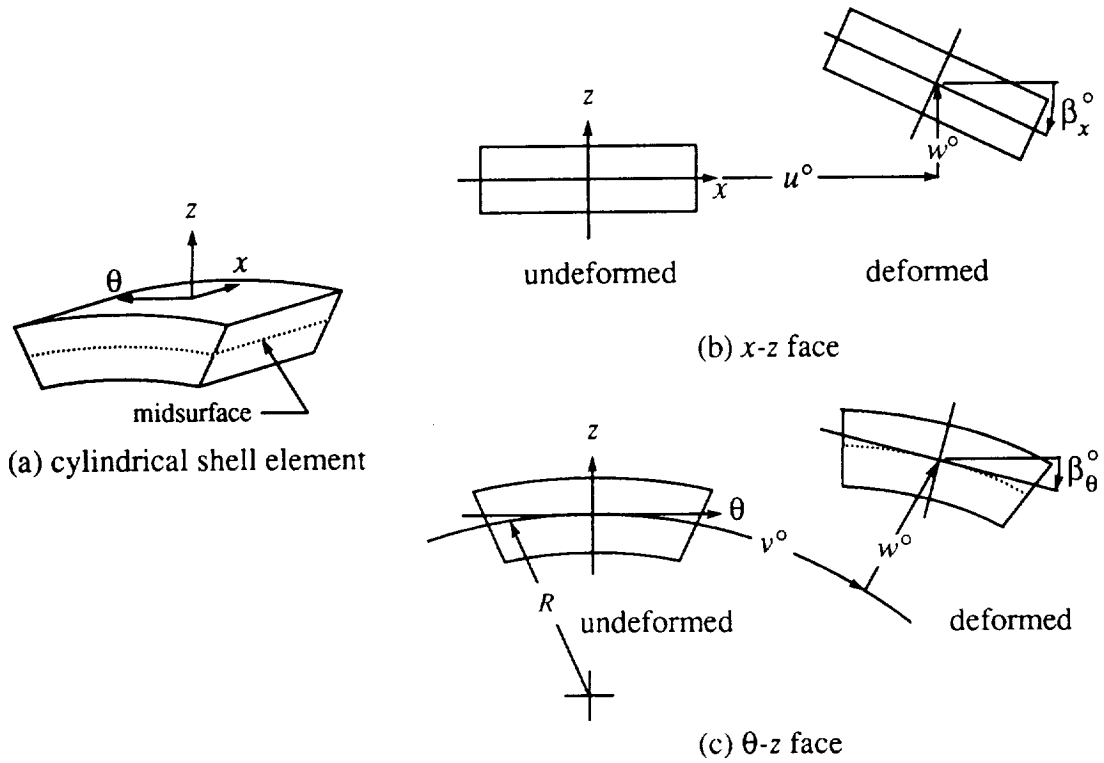
Fig. 2-2 Kinematics of a Cylindrical Shell Element

The flexible end supports are modeled as radial and rotational springs, as shown in Fig. 2-3 (a). The contribution to the virtual work is

$$\delta W = \int_{\theta=0}^{2\pi} \left[F_Q^+ \cdot \delta w^\circ \, (+\frac{L}{2}, \theta) + F_Q^- \cdot \delta w^\circ \, (-\frac{L}{2}, \theta) \right.$$
$$\left. + F_M^+ \cdot \delta\beta_x^\circ \, (+\frac{L}{2}, \theta) + F_M^- \cdot \delta\beta_x^\circ \, (-\frac{L}{2}, \theta) \right] R d\theta,$$

(2.8)

where F_Q^+ and F_Q^- are the radial spring forces, and F_M^+ and F_M^- are the rotational spring moments associated with each end of the cylinder. The linear-elastic spring constants for the radial and rotation springs are K_Q and K_M, respectively.

Due to the thinness assumption, z/R is neglected in comparison to unity in the volume integral in Eq. (2.7). Further, it is assumed that loading is quasi-static so that inertial body forces may be neglected. The nonlinear equilibrium equations and corresponding boundary conditions are derived by substituting Eq. (2.3) through Eq. (2.5), along with Eq. (2.2),

into Eq. (2.7). The resulting equation is integrated through the thickness and the definitions of the force and moment resultants, as defined in Appendix B, are applied. Integration by parts results in the three equilibrium equations

$$\frac{\partial N_x}{\partial x} + \frac{\partial N_{x\theta}}{R\partial\theta} = 0 \tag{2.9}$$

$$\frac{\partial N_{x\theta}}{\partial x} + \frac{\partial N_\theta}{R\partial\theta} = 0 \tag{2.10}$$

$$\frac{\partial Q_x}{\partial x} + \frac{\partial^2 M_\theta}{R^2\partial\theta^2} - \frac{\partial}{R\partial\theta}\left[N_{x\theta}\cdot\beta_x^\circ + N_\theta\cdot\beta_\theta^\circ\right] - \frac{N_\theta}{R} = 0. \tag{2.11}$$

The accompanying variationally consistent boundary conditions at the ends of the cylinder, $x = \pm L/2$, are

$$N_x = \text{specified} \qquad \text{or} \qquad u^\circ = \text{specified} \tag{2.12}$$

$$N_{x\theta} = \text{specified} \qquad \text{or} \qquad v^\circ = \text{specified} \tag{2.13}$$

$$Q_x = \text{specified} \qquad \text{or} \qquad w^\circ = \text{specified} \tag{2.14}$$

$$M_x = \text{specified} \qquad \text{or} \qquad \beta_x^\circ = \text{specified}. \tag{2.15}$$

The bending test fixture, to be discussed in Chapter 3, was designed to enforce support conditions best described as 'clamped'. In practice, however, it is difficult to achieve ideally clamped supports. Since flexibility of the end supports may affect the bending responses, the supports are modeled as the radial and rotational springs mentioned previously. These flexible spring supports may also be used to simulate ring stiffeners.

Bending of the cylinder is accomplished by the application of the appropriate boundary conditions, Eqs. (2.12) through (2.15). An equal rotation, Ω, is applied to each end of the cylinder by specifying the kinematic quantities u° and β_x°, as illustrated in Figs. 2-3 (b) and (c). The associated bending moment is given by the quantity M. Non-ideal boundary conditions are modeled by including the flexibility of the end supports, K_Q and K_M, and an applied radial deformation of the cylinder ends, w_R, as shown in Fig. 2-3 (c). The quantity w_R, as will be explained later, is due to thermal stresses that arise during the preparation of the test specimens. The resulting kinematic boundary conditions are given by

$$u^\circ (\pm\frac{L}{2}, \theta) = \mp R\Omega\cos\theta$$

$$v^\circ (\pm\frac{L}{2}, \theta) = 0$$

$$w^\circ (\pm\frac{L}{2}, \theta) \pm \frac{Q_x(\pm\frac{L}{2}, \theta)}{K_Q} = w_R \tag{2.16}$$

$$\beta_x^\circ (\pm\frac{L}{2}, \theta) \pm \frac{M_x(\pm\frac{L}{2}, \theta)}{K_M} = \mp\Omega\cos\theta.$$

In the above, the displacements and rotations in the radial and rotational springs, and hence, the displacements and rotations at the cylinder ends, are related to the forces and moments in the springs by the expressions

$$w^\circ (+L/2, \theta) = \frac{F_Q^+}{K_Q} = -\frac{Q_x(+\frac{L}{2}, \theta)}{K_Q} + w_R,$$

$$w^\circ (-L/2, \theta) = \frac{F_Q^-}{K_Q} = +\frac{Q_x(-\frac{L}{2}, \theta)}{K_Q} + w_R,$$

$$\beta_x^\circ (+L/2, \theta) = \frac{F_M^+}{K_M} = -\frac{M_x(+\frac{L}{2}, \theta)}{K_M} - \Omega\cos\theta, \tag{2.17}$$

$$\beta_x^\circ (-L/2, \theta) = \frac{F_M^-}{K_M} = -\frac{M_x(-\frac{L}{2}, \theta)}{K_M} + \Omega\cos\theta.$$

Solution of Equations

It proves convenient to choose the eight variables that naturally arise in the derivation of the variationally consistent boundary conditions, Eqs. (2.12) through (2.15), as the primary response variables. The equilibrium equations, Eqs. (2.9) through (2.11), can be reduced to a set of eight coupled first-order nonlinear partial differential equations of the form

$$\frac{\partial \vec{\Upsilon}(x, \theta)}{\partial x} = \vec{\Phi}\left(x, \theta, \vec{\Upsilon}(x, \theta), \frac{\partial \vec{\Upsilon}(x, \theta)}{R\partial\theta}\right). \tag{2.18}$$

16

(a) Elastic Support Model   (b) Applied Rotation   (c) Boundary Conditions
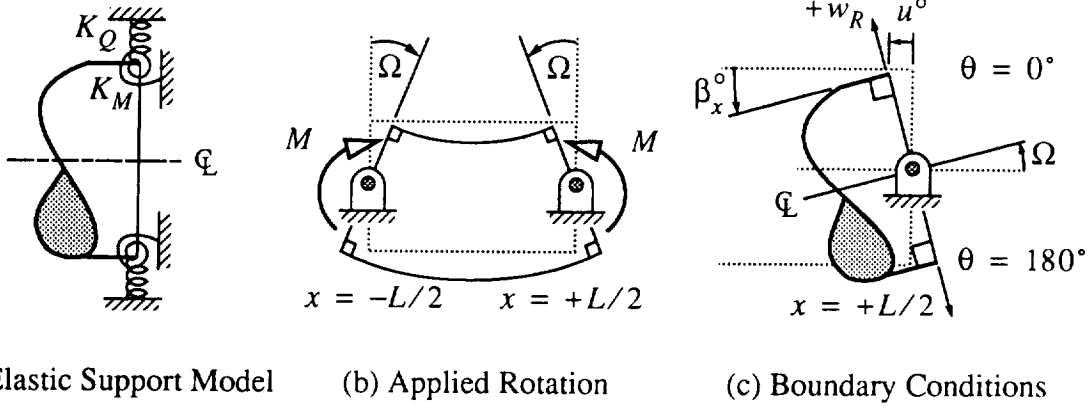
Fig. 2-3 Loading and Boundary Conditions

The arrays $\vec{\Upsilon}$ and $\vec{\Phi}$ represent the eight primary problem variables and the right-hand sides of the governing partial differential equations, respectively. The steps involved in obtaining this form are described in the section "Two-Dimensional Partial Differential Equations" in Appendix C. The eight governing partial differential equations are

$$\frac{\partial u^\circ}{\partial x} = \frac{N_x}{A_{11}} - \frac{1}{2}\beta_x^{\circ 2} - \frac{A_{12}}{A_{11}}\left\{ \frac{\partial v^\circ}{R\partial\theta} + \frac{w^\circ}{R} + \frac{1}{2}(\frac{\partial w^\circ}{R\partial\theta})^2 \right\} + \left[\frac{N_x^P}{A_{11}}\right] \tag{2.19}$$

$$\frac{\partial v^\circ}{\partial x} = \frac{N_{x\theta}}{A_{66}} - \frac{\partial u^\circ}{R\partial\theta} + \beta_x^\circ \cdot \frac{\partial w^\circ}{R\partial\theta} + \left[\frac{N_{x\theta}^P}{A_{66}}\right] \tag{2.20}$$

$$\frac{\partial w^\circ}{\partial x} = -\beta_x^\circ \tag{2.21}$$

$$\frac{\partial \beta_x^\circ}{\partial x} = \frac{M_x}{D_{11}} + \frac{D_{12}}{D_{11}}\frac{\partial^2 w^\circ}{R^2\partial\theta^2} - 2\frac{D_{16}}{D_{11}}\frac{\partial\beta_x^\circ}{R\partial\theta} + \left[\frac{M_x^P}{D_{11}}\right] \tag{2.22}$$

$$\frac{\partial N_x}{\partial x} = -\frac{\partial N_{x\theta}}{R\partial\theta} \tag{2.23}$$

$$\frac{\partial N_{x\theta}}{\partial x} = -\frac{A_{12}}{A_{11}}\frac{\partial N_x}{R\partial\theta} - A^*\left(\frac{\partial^2 v^\circ}{R^2\partial\theta^2} + \frac{\partial w^\circ}{R^2\partial\theta}\left(1 + \frac{\partial^2 w^\circ}{R\partial\theta^2}\right)\right) + \left[\frac{\partial N_\theta^P}{R\partial\theta} - \frac{A_{12}}{A_{11}}\frac{\partial N_x^P}{R\partial\theta}\right] \tag{2.24}$$

17

$$\frac{\partial Q_x}{\partial x} = \frac{1}{R}\left(1 - \frac{\partial^2 w^o}{R\partial\theta^2}\right)\left(\frac{A_{12}}{A_{11}}N_x + A^*\left(\frac{\partial v^o}{R\partial\theta} + \frac{w^o}{R} + \frac{1}{2}(\frac{\partial w^o}{R\partial\theta})^2\right)\right)$$

$$-\frac{D_{12}}{D_{11}}\frac{\partial^2 M_x}{R^2\partial\theta^2} + D_1^*\frac{\partial^4 w^o}{R^4\partial\theta^4} - 2D_2^*\frac{\partial^3\beta_x^o}{R^3\partial\theta^3}$$

$$+\frac{\partial N_{x\theta}}{R\partial\theta}\cdot\beta_x^o + N_{x\theta}\cdot\frac{\partial\beta_x^o}{R\partial\theta} - \frac{A_{12}}{A_{11}}\frac{\partial N_x}{R\partial\theta}\cdot\frac{\partial w^o}{R\partial\theta}$$

$$-A^*\left(\frac{\partial^2 v^o}{R^2\partial\theta^2}\cdot\frac{\partial w^o}{R\partial\theta} + \frac{1}{R}(\frac{\partial w^o}{R\partial\theta})^2\left(1 + \frac{\partial^2 w^o}{R\partial\theta^2}\right)\right)$$

$$+\frac{1}{R}\left(1 - \frac{\partial^2 w^o}{R\partial\theta^2}\right)\left(\frac{A_{12}}{A_{11}}N_x^P - N_\theta^P\right)$$

$$-\frac{D_{12}}{D_{11}}\frac{\partial^2 M_x^P}{R^2\partial\theta^2} + \frac{\partial^2 M_\theta^P}{R^2\partial\theta^2} - \frac{\partial w^o}{R\partial\theta}\left(\frac{A_{12}}{A_{11}}\frac{\partial N_x^P}{R\partial\theta} - \frac{\partial N_\theta^P}{R\partial\theta}\right)$$

$$\text{(2.25)}$$

$$\frac{\partial M_x}{\partial x} = Q_x - 2\frac{D_{16}}{D_{11}}\frac{\partial M_x}{R\partial\theta} + 2D_2^*\frac{\partial^3 w^o}{R^3\partial\theta^3} - 4D_3^*\frac{\partial^2\beta_x^o}{R^2\partial\theta^2} + N_x\cdot\beta_x^o - N_{x\theta}\cdot\frac{\partial w^o}{R\partial\theta}$$

$$+2\left[\frac{\partial M_{x\theta}^P}{R\partial\theta} - \frac{D_{16}}{D_{11}}\frac{\partial M_x^P}{R\partial\theta}\right].$$

$$\text{(2.26)}$$

The superscript 'P' in the above equations indicates known pre-straining quantities that are discussed in Appendix B. These pre-straining quantities may include initial geometric imperfections, thermal effects, mechanical pre-loading, etc. The essential features of the governing equations are that they are first-order equations in the axial coordinate, x, and only the primary variables themselves, the θ-derivatives of these primary variables, and known pre-straining quantities appear on the right-hand sides. These features make it possible to transform the two-dimensional problem into a one-dimensional problem by substituting a separable solution of the form

$$\vec{\Upsilon}(x,\theta) = \mathbf{Y}(x)\cdot\vec{\Psi}(\theta) \qquad\qquad \text{(2.27)}$$

into the eight partial differential equations and using the Kantorovich technique. The matrix $\mathbf{Y}(x)$ and the array $\vec{\Psi}(\theta)$ represent the unknown axial components and the known circumferential components, respectively, of the primary problem variables. The

dimension of both $\mathbf{Y}(x)$ and $\vec{\Psi}(\theta)$ depend on the number of circumferential harmonics, N, retained in the analysis. The resulting one-dimensional problem requires the solution of $16N + 8$ nonlinear first-order coupled ordinary differential equations for the unknown elements of the $\mathbf{Y}(x)$ matrix. It will be demonstrated in section 2.1.5 that retaining three θ-harmonics is sufficient to accurately predict the prebuckling responses. When $N = 3$, each response variable consists of $2N + 1$, or seven, components. For example, the axial displacement of the midsurface is represented by the relation

$$u^\circ(x, \theta) = y_1(x) + y_2(x) \cdot cos\theta + y_3(x) \cdot cos2\theta + y_4(x) \cdot cos3\theta$$
$$+ y_5(x) \cdot sin\theta + y_6(x) \cdot sin2\theta + y_7(x) \cdot sin3\theta. \tag{2.28}$$

In principle, there is no limit to the range of end-rotation, Ω, for which the present solution technique can be applied. It is possible to compute the postbuckling response using this method. However, many more harmonic terms and a more complex solution algorithm would be required to compute the postbuckling responses. It is more efficient to compute the postbuckling responses using existing programs in order to take full advantage of state-of-the-art solution techniques.

The present investigation assumes $N = 3$, requiring the solution of 56 first-order equations. The 56 first-order equations were derived with the aid of the symbolic manipulator MACSYMA [84]. The procedure followed to derive the equations is outlined in the section "One-Dimensional Ordinary Differential Equations" in Appendix C. The result of this procedure is a nonlinear two point boundary value problem of the form

$$\frac{d\vec{y}(x)}{dx} = \vec{F}(x, \vec{y}(x)), \qquad -\frac{L}{2} \le x \le +\frac{L}{2}, \tag{2.29}$$

with boundary conditions of the form

$$\vec{g}(\vec{y}(\pm\frac{L}{2})) = 0. \tag{2.30}$$

The vector $\vec{y}$ represents the 56 unknown axial components of $\mathbf{Y}(x)$ and the vector $\vec{F}$ is shorthand notation for the right-hand sides of the first-order equations. The vector $\vec{g}$ represents the 56 boundary conditions that are associated with the elements of $\vec{y}$. For example, the first boundary condition of Eq. (2.16) is expressed in terms of Eq. (2.28) as

$$u^\circ \, (\pm\frac{L}{2}, \theta) \; = \mp R\Omega \cdot cos\theta$$

$$= y_1 \, (\pm\frac{L}{2}) + y_2 \, (\pm\frac{L}{2}) \cdot cos\theta + y_3 \, (\pm\frac{L}{2}) \cdot cos2\theta + y_4 \, (\pm\frac{L}{2}) \cdot cos3\theta \quad (2.31)$$

$$+ \; y_5 \, (\pm\frac{L}{2}) \cdot sin\theta + y_6 \, (\pm\frac{L}{2}) \cdot sin2\theta + y_7 \, (\pm\frac{L}{2}) \cdot sin3\theta.$$

Equating coefficients of the constant and harmonic terms in Eq. (2.31) leads to 14 boundary conditions for u°. These are

$$y_2 \, (\pm\frac{L}{2}) \; = \mp R\Omega,$$

$$y_i \, (\pm\frac{L}{2}) \; = \; 0 \qquad i = 1, \, 3 \le i \le 7. \tag{2.32}$$

The remaining 42 boundary conditions for v°, w°, and β_x° are obtained in a similar fashion.

Equations (2.29) and (2.30) are amenable to numerical solution by commercially available computer library routines such as the IMSL subroutine DBVPFD [85]. This subroutine is based on a variable order, variable step, finite difference algorithm using Newton's method. The theory is documented in references [86-87]. A FORTRAN computer program was developed using this subroutine to compute the prebuckling bending responses. The responses due to axial tension or compression, torsion, lateral pressure, or any combination of these can also be studied with this program by applying the appropriate displacement boundary conditions and pressure values. In addition to the non-ideal boundary conditions mentioned previously, various initial geometric imperfections can be studied by specifying the appropriate pre-straining quantities.

The prebuckling problem was also solved with the STAGS finite element program as a check on the analysis just described. This approach will be compared to the present analysis in the context of the buckling analysis to be described in section 2.2.3.

Numerical examples of the characteristic bending responses are presented next. The effects of non-ideal boundary conditions, axisymmetric shape imperfections, a higher-order harmonic representation, and prebuckling material failure are also discussed.

2.1.2 Prebuckling Responses of Idealized Cylinders

The prebuckling responses are presented for six idealized laminated graphite-epoxy cylinders for the purpose of understanding the experimentally observed responses to be discussed in Chapter 4. In the present chapter, the term "idealized" refers to the uniformity of geometric parameters and material properties among the six cylinders. In Chapter 4, slight variations in the geometric parameters and material properties will be taken into account. The cylinders have a quasi-isotropic $[\mp45/0/90]_S$ layup, an axially-stiff $[\mp45/0_2]_S$ layup, and a hoop-stiff $[\mp45/90_2]_S$ layup. The idealized cylinder geometries are described by $R/H = 160$, $L/R = 2$ and 5, and $R = 6$ inches. The mechanical properties summarized in Table 2-1 are assumed to be representative of the idealized cylinders. The mechanical properties of the actual test specimens will be discussed in connection with Chapter 3.

Table 2-1 Mechanical Properties for Idealized Graphite-Epoxy Cylinders

E_1, Msi	E_2, Msi	G_{12}, Msi	v_{12}
23.4	1.75	1.03	0.285

Bending responses were computed using the nonlinear prebuckling analysis described in section 2.1.1. Displacement and axial strain responses are compared at two values of end-rotation. The end-rotations and axial strains are normalized by the corresponding classical buckling end-rotations and compressive axial buckling strains, Ω_{cr} and ε_{cr}, respectively, as a matter of convenience. These classical buckling parameters and the corresponding classical buckling moment, M_{cr}, will be discussed in further detail in section 2.2.1. The values of the buckling parameters are summarized in Table 2-2.

Table 2-2 Classical Buckling Parameters for Idealized Cylinders

Wall Construction	M_{cr}, in.-lbs	$\Omega_{cr} \cdot \frac{R}{L}$, degrees	ε_{cr}, $\mu\varepsilon$
$[\mp45/0/90]_S$	141,445	0.102	3,615
$[\mp45/0_2]_S$	95,966	0.048	1,661
$[\mp45/90_2]_S$	148,114	0.244	8,525

Displacement Response

Displacement responses are compared at the circumferential locations $\theta = 0°$, $90°$, and $180°$ in Fig. 2-4 for $L/R = 2$ and in Fig. 2-5 for $L/R = 5$. The value of end-rotation in these figures is $\Omega/\Omega_{cr} = 0.5$ and 1.0. Radial displacements at $\theta = 0°$ and $180°$ are denoted by w_0 and w_{180}, respectively, and tangential displacements at $\theta = 90°$ are denoted by v_{90}. All displacements are normalized with respect to the cylinder wall thickness, H, and are plotted as a function of the normalized axial location, x/L. Please note, positive values of w_0 correspond to radially outward deflections at the top of the cylinder and positive values of w_{180} correspond to radially inward deflections at the bottom of the cylinder. Positive values of v_{90} correspond to downward deflections in the direction of bending at the side of the cylinder, as indicated in the inset in Fig. 2-4 (c). In this way, the 'shape' of the w_0, w_{180}, and v_{90} profiles correspond physically to the familiar parabolic deflection shape of a beam in bending.

The w_0, v_{90}, and w_{180} displacement responses of the three laminates are similar to one another. The displacements exhibit the overall parabolic deflection shape encountered in classical beam bending. However, unlike in classical beam bending theory, cross-section deformations are predicted to occur. The cross-section deformations for these relatively short cylinders are primarily due to the development of a boundary layer region near the cylinder ends. Cross-section ovalization, defined as

$$\delta = \left. \frac{|w_0| - |w_{180}|}{2} \right|_{\frac{x}{L} = 0}, \tag{2.33}$$

is negligibly small compared to R for all six cylinders. For example, for the cylinders with $L/R = 5$, the values of δ do not exceed 0.2% of the radius for $\Omega/\Omega_{cr} = 1.0$. These values of δ are significantly smaller than the inward radial deflections of 2/9, or 22%, of the cylinder radius required to initiate cross-section collapse in the Brazier problem.

The boundary layer region is most pronounced on the compression side of the cylinders, $\theta = 0°$, but is also evident to a lesser extent on the tension side, $\theta = 180°$. The deflection at the side of the cylinders, $\theta = 90°$, is identical to the parabolic deflection shape predicted by beam bending theory and exhibits no boundary layer.

Comparing parts (a) and (b) of Figs. 2-4 and 2-5 demonstrates that the peak amplitudes, attenuation length, and overall shape characteristics of the w_0 displacements in the bound-

(a) $\Omega/\Omega_{cr} = 0.5$, $\theta = 0°$

(b) $\Omega/\Omega_{cr} = 1.0$, $\theta = 0°$

(c) $\Omega/\Omega_{cr} = 0.5$, $\theta = 90°$

(d) $\Omega/\Omega_{cr} = 1.0$, $\theta = 90°$

(e) $\Omega/\Omega_{cr} = 0.5$, $\theta = 180°$

(f) $\Omega/\Omega_{cr} = 1.0$, $\theta = 180°$
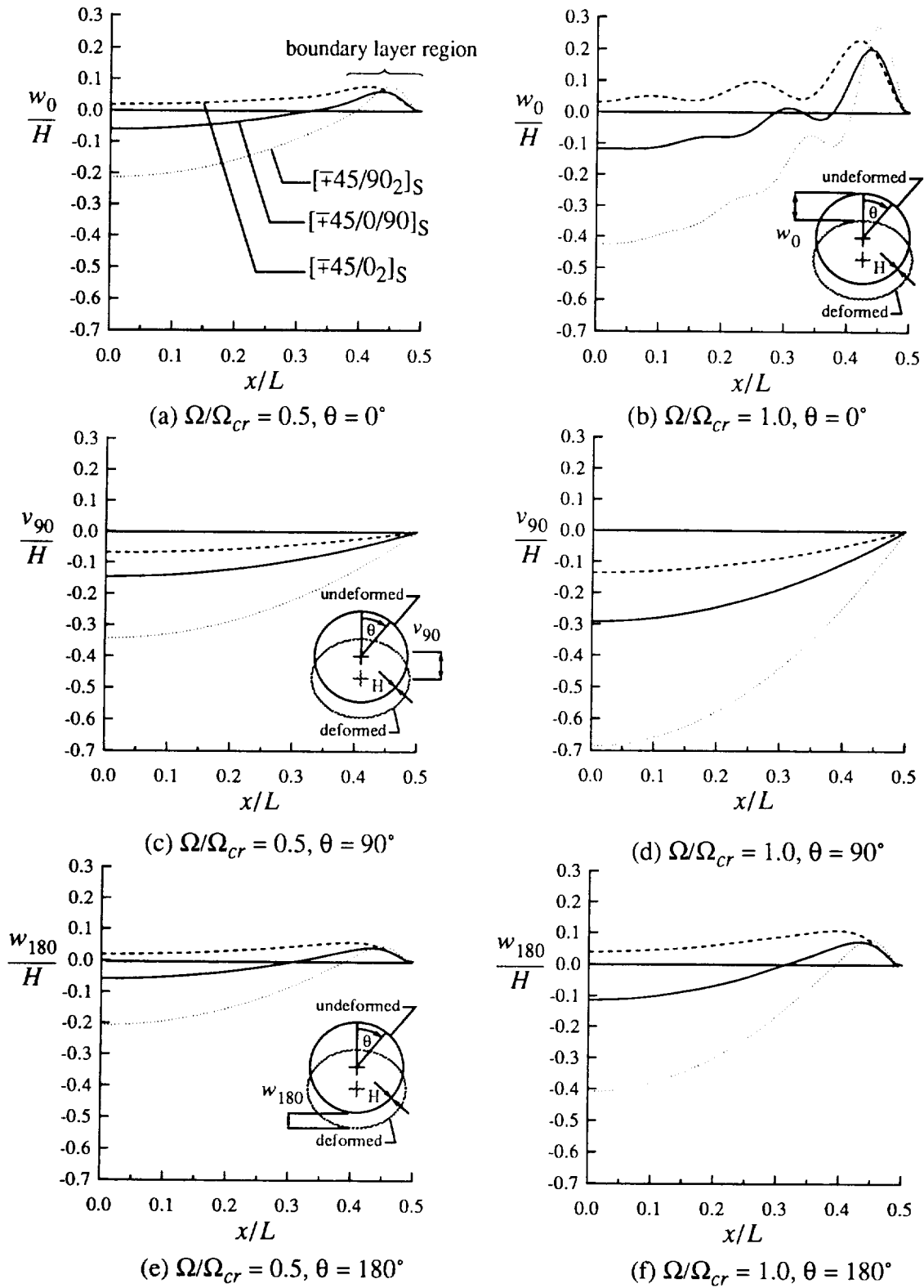
Fig. 2-4 Displacement Response Comparison, $L/R = 2$
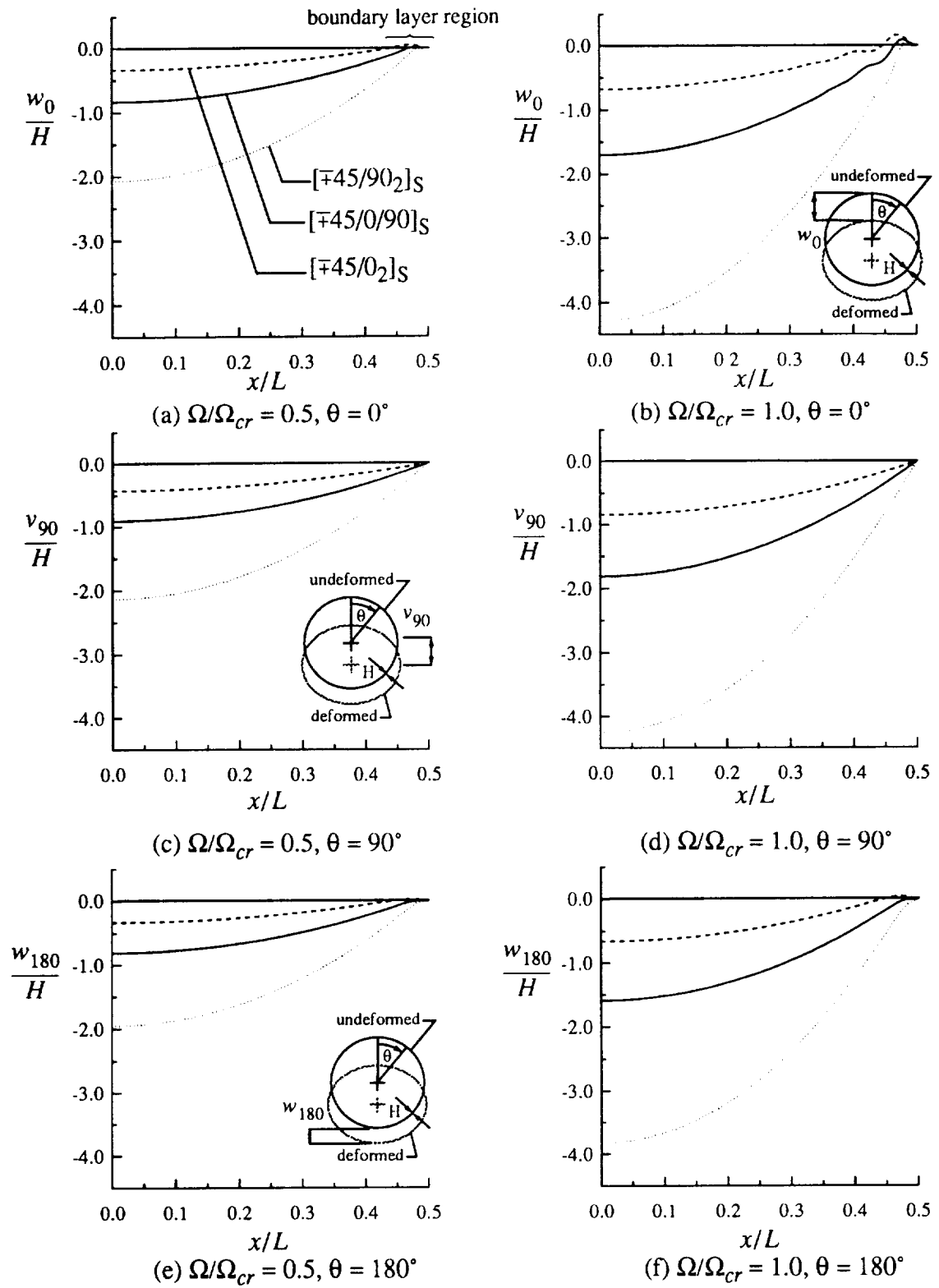
Fig. 2-5 Displacement Response Comparison, $L/R = 5$

ary layer region have a nonlinear relation to the applied end-rotation. As the end-rotation is increased from $\Omega/\Omega_{cr} = 0.5$ to 1.0, the w_0 displacements take on an oscillatory character that becomes attenuated away from the ends. Fig. 2-4 (b) indicates that the attenuation length for $\Omega/\Omega_{cr} = 1.0$ is of the order of the half-length of the cylinders with $L/R = 2$, or approximately six inches. For the cylinders with $L/R = 5$, shown in Fig. 2-5 (b), the attenuation length is also approximately six inches, or 40% of the half-length of these cylinders. It is concluded from these figures that the peak amplitudes, attenuation length, and half-wavelength of the oscillations associated with the boundary layer region are layup dependent. The characteristic half-wavelength of the oscillations, termed λ, appears to be largest for the $[\mp45/0_2]_S$ cylinders, followed by the $[\mp45/0/90]_S$ and $[\mp45/90_2]_S$ cylinders.

Comparing the w_{180} deflections in parts (e) and (f) of Figs. 2-4 and 2-5 indicates that the boundary layer region attenuation length and the shape characteristics on the tension side of the cylinder are relatively insensitive to the value of applied end-rotation. Only the magnitude of the deflections appear to be affected by the applied end-rotations.

A comparison between Figs. 2-4 and 2-5 demonstrates the relative effect of the cylinder length on the deflection shapes. It is observed that the boundary layer deformations on the compression and tension sides of the $L/R = 2$ cylinders, Figs. 2-4 (a)-(b) and (e)-(f), have a significant influence on the overall parabolic bending shape. In comparison to the cylinders with $L/R = 2$, the influence of the boundary layer is substantially diminished for $L/R = 5$, as seen in Figs. 2-5 (a)-(b) and (e)-(f). The parabolic shape of v_{90}, Figs. 2-4 and 2-5 (c)-(d), is seen to be unaffected by length.

It is interesting to note that the radial deflections at $\theta = 0°$ are directed radially outward for the $[\mp45/0_2]_S$ cylinder with $L/R = 2$ whereas they are directed radially inward for the $[\mp45/0/90]_S$ and $[\mp45/90_2]_S$ cylinders (see Figs. 2-4 (a)-(b)). This difference in radial deflections can be attributed, in part, to a Poisson effect. The radial expansion due to Poisson's ratio can overcome the radial inward deflections due to bending, resulting in a net outward deflection. This is the case with the $[\mp45/0_2]_S$ cylinder which has a relatively large effective laminate Poisson's ratio of 0.65, compared to 0.30 and 0.19 for the $[\mp45/0/90]_S$ and $[\mp45/90_2]_S$ cylinders, respectively. The opposite effect is evident at $\theta = 180°$ (see Figs. 2-4 (e)-(f)). For the cylinders with $L/R = 5$, the corresponding radial deflections are all directed either radially inward at $\theta = 0°$ or radially outward at $\theta = 180°$ due to the relatively large bending deflections.

Three-dimensional views of the deformed quasi-isotropic [∓45/0/90]$_S$ cylinders, illustrated in Fig. 2-6 for L/R = 2 and 5, show the circumferential variation of the boundary layer deformations. The deflections in this figure are exaggerated for emphasis. It is observed that the boundary layer region at θ = 0° has an attenuation length that extends to 90° in the circumferential direction.

boundary layer region

boundary layer region

Ω/Ω_{cr} = 1.0,
[∓45/0/90]$_S$,
R/H = 160

(a) L/R = 2   (b) L/R = 5
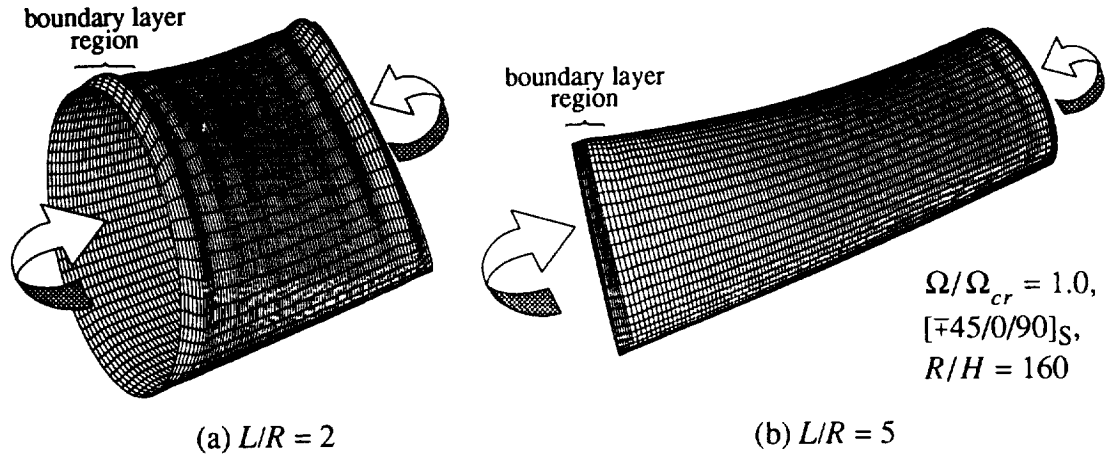
Fig. 2-6 Prebuckling Deformations, L/R = 2 and 5

Strain Response

Axial strains are illustrated for the cylinders with L/R = 2 and 5 in Figs. 2-7 and 2-8, respectively. The strains are plotted as a function of the axial position at the wall thickness locations z/H = +0.5, 0.0, and −0.5 and at the circumferential locations θ = 0° and 180°. The end-rotations in these figures are Ω/Ω_{cr} = 0.5 and 1.0 and the classical buckling strain, ε_{cr}, is the normalization factor.

The axial strain response characteristics shown in these figures are similar for all three laminates. Figures (a), (c), and (e) clearly indicate a progressive development of the boundary layer on the compression side of the cylinders as the end-rotation is increased from Ω/Ω_{cr} = 0.5 to 1.0. The boundary layer region on the tension side, shown in figures (b), (d), and (f), remains relatively insensitive to the value of end-rotation.

Although the displacement responses for the cylinders with L/R = 2 and 5 are substantially different from one another, the overall character of the corresponding axial strain responses are quite similar to one another. A comparison of the axial strain responses as a

function of the absolute axial position demonstrates that the boundary layer strain responses are identical for both cylinder lengths. Furthermore, it is evident from Figs. 2-7 (a) and (e) that the axial surface strains are sensitive indicators of the boundary layer responses and are therefore well suited for comparative studies.

It is observed in the axial strain comparisons in (a), (c), and (e) of Figs. 2-7 and 2-8 that the characteristic half-wavelength of the boundary layer responses is laminate dependent. The characteristics of the boundary layer are discussed next.

Boundary Layer Characteristics

A comparison of the boundary layer attenuation length of the geometrically linear bending responses, discussed in [10], and the axisymmetric buckling response, discussed in the section 1.1.1, indicates that the characteristic half-wavelength can be computed from Eq. (1.2) as the ratio $\lambda = L/m$. Re-writing Eq. (1.2), which is valid for the case of balanced symmetric laminates, results in the relation

$$\lambda = \frac{L}{m} = \pi \left[\frac{D_{11} R^2}{E_\theta H} \right]^{\frac{1}{4}}. \tag{2.34}$$

The characteristic half-wavelength parameters computed from Eq. (2.34) are presented in Table 2-3 for the three laminates under consideration. The second column in Table 2-3 represents the characteristic length compared to H. The remaining two columns indicate the number of half-waves, m, associated with the two values of L/R. The table indicates that, compared to the quasi-isotropic $[\mp 45/0/90]_S$ cylinder, the attenuation length of the boundary effects is predicted to be approximately 23% longer for the $[\mp 45/0_2]_S$ cylinder and 16% shorter for the $[\mp 45/90_2]_S$ cylinder.

Table 2-3 Characteristic Half-Wavelength Parameters for Idealized Cylinders

Wall Construction	$\dfrac{\lambda}{H}$	$m, L/R = 2$	$m, L/R = 5$
$[\mp 45/0/90]_S$	21.4	15.0	37.5
$[\mp 45/0_2]_S$	26.4 (+23%[a])	12.1	30.3
$[\mp 45/90_2]_S$	18.0 (-16%[a])	17.8	44.5

a. Percent difference relative to $[\mp 45/0/90]_S$ cylinder.
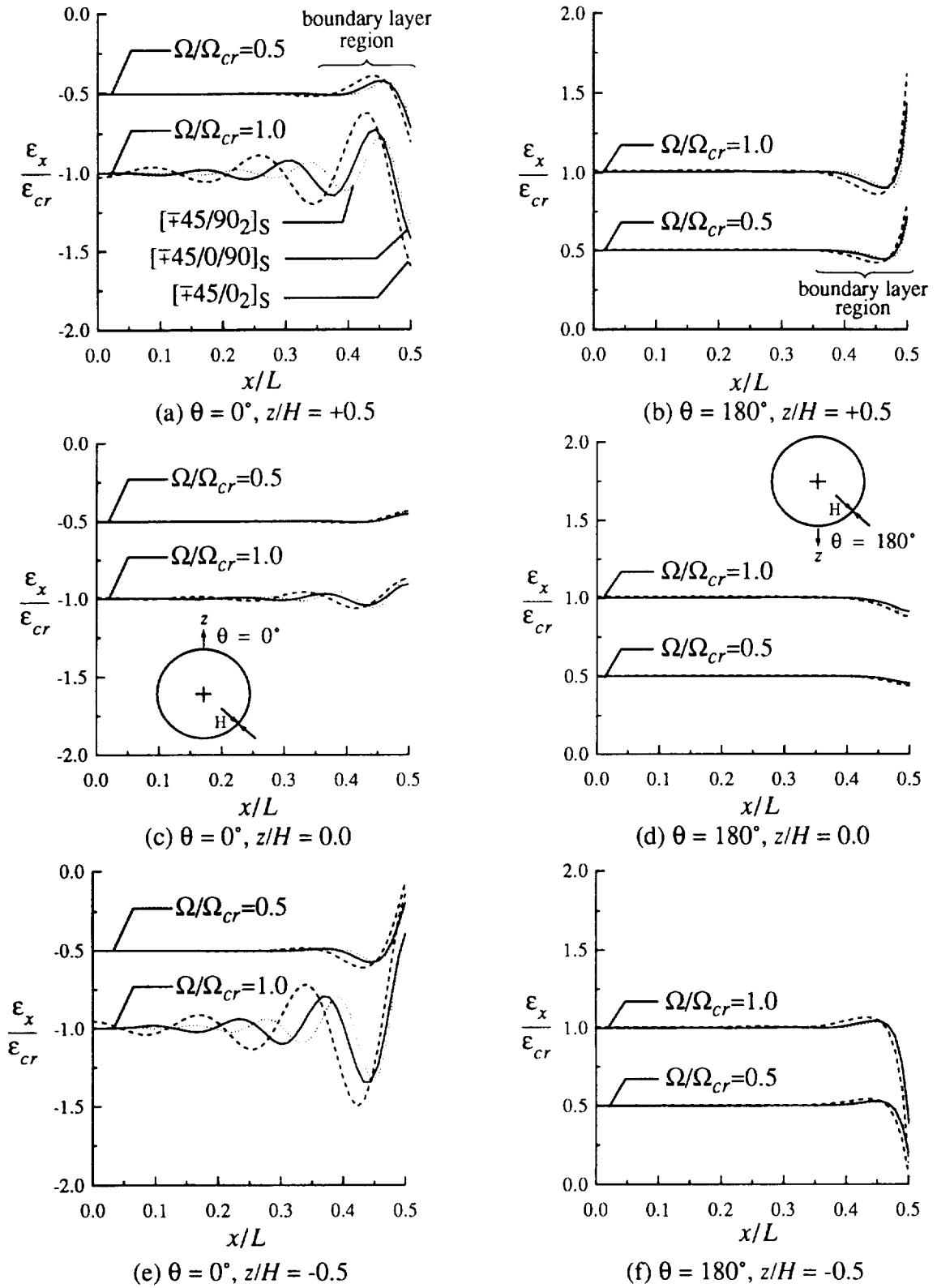
Fig. 2-7 Axial Strain Response Comparison, $L/R = 2$
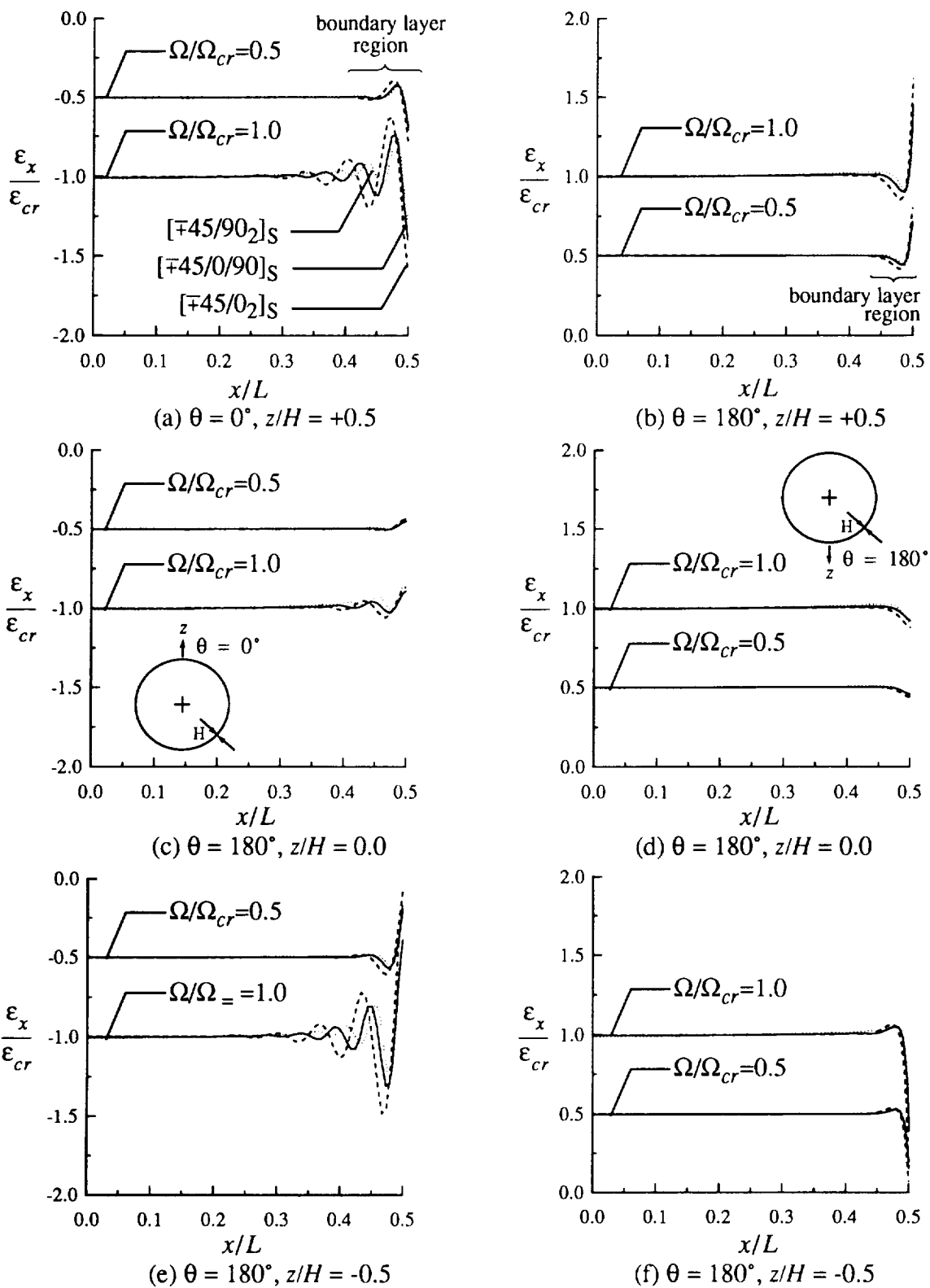
Fig. 2-8 Axial Strain Response Comparison, $L/R = 5$

The characteristic half-wave length of the axial surface strain response, λ, is illustrated in Fig. 2-9 for the $[\mp45/0_2]_S$ cylinder with $L/R = 2$. The end-rotation in this figure is $\Omega/\Omega_{cr} = 1.0$. The intersections between the induced axial surface strains and the nominal applied midsurface strain in this figure define the characteristic half-wave length of the boundary layer.

This section discussed the character of the bending responses of ideal cylinders. It is well known that deviations from the ideal can influence the responses. The effect of several non-ideal conditions on the cylinder bending responses is discussed next.

$\Omega/\Omega_{cr} = 1.0$,
$[\mp45/0_2]_S$,
$L/R = 2$, $R/H = 160$,
$z/H = +0.5$
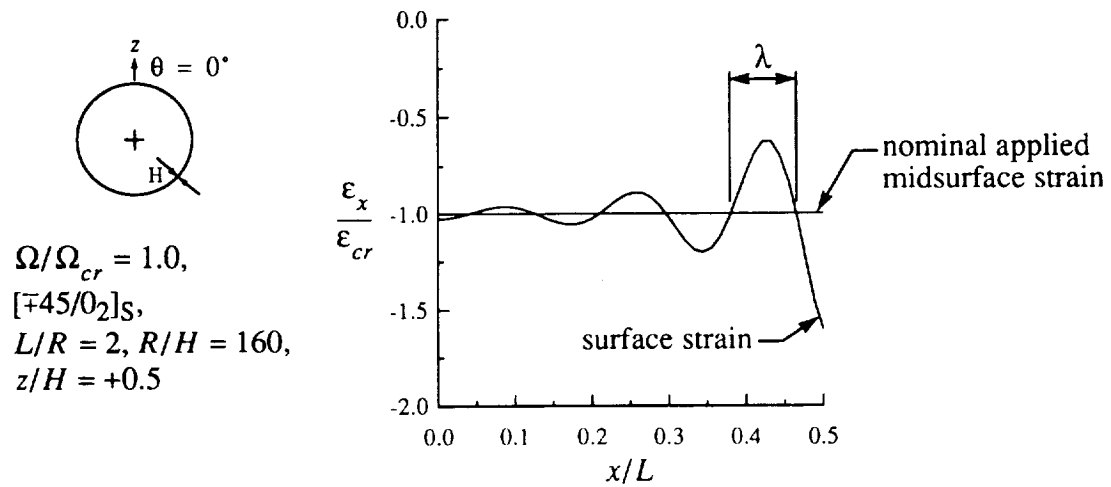
Fig. 2-9 Characteristic Boundary Layer Response

2.1.3 Effect of Non-Ideal Boundary Conditions

As mentioned at the outset of this study, the boundaries of the cylinder are assumed to be rigidly clamped. However, to aid in the interpretation of the experimental results, it is instructive to study the effects of elastic boundary conditions. As discussed previously, elasticity of the supports is modeled by the radial and rotational springs depicted in Fig. 2-3 (a). Here, radial displacement and axial strain responses are compared for clamped supports, simple supports, and elastic supports for the $[\mp45/0_2]_S$ cylinder with $L/R = 2$ and $R/H = 160$. The effect of localized initial radial deformations on the cylinder ends, shown as w_R in Fig. 2-3 (c), is also examined.

30

Elastic Supports

The elastic support boundary conditions were presented in Eqs. (2.16). A parameter study was conducted to determine the range of rotational and radial spring stiffness values that correspond to different support conditions. Based on the insight gained from the parameter study, three values of the rotational spring stiffness, K_M, were chosen to simulate a 'simple support', an 'elastic support', and a 'clamped' support. Also, the radial spring stiffness, K_Q, was varied to simulate a rigid radial support and an elastic radial support. These six support conditions are summarized in Table 2-4.

The radial displacements, w_0 and w_{180}, are presented in Fig. 2-10 and the corresponding axial strains are presented in Fig. 2-11. Responses with rigid radial supports are shown in figures (a) and (b) and responses with elastic radial supports are shown in figures (c) and (d). The end-rotation in these figures is $\Omega/\Omega_{cr} = 1.0$.

Table 2-4 Elastic Support Example Cases

Support Condition	$K_Q = 1 \times 10^6$, psi	$K_Q = 1 \times 10^3$, psi	Support Model
'simple support', $K_M = 1 \times 10^{-3}$, lbs 'elastic support', $K_M = 1 \times 10^2$, lbs 'clamped support', $K_M = 1 \times 10^4$, lbs	'rigid' radial support[a]	'elastic' radial support[b]	

a. Radial expansion inhibited so that ends remain circular.

b. Radial deformations allowed.

It is observed in Fig. 2-10 that w_0 is sensitive to the rotational support stiffness while w_{180} is relatively insensitive by comparison. Figure (a) indicates that the peak deflections are larger for both the simple supports and the elastic supports in comparison to the clamped supports. The effect of elastic radial support conditions on w_0 is shown in figure (c). The peak amplitudes are again larger for the simple support condition and the elastic support condition in comparison to the clamped support condition. However, unlike the case of the rigid radial support shown in figure (a), the maximum value of w_0 for the sim-

ple support condition occurs at the cylinder ends. On the tension side, it is observed that the elastic radial support allows the ends of the cylinder to deform radially inward.

The corresponding axial surface strains, shown in Fig. 2-11, are similar in character to the radial displacements. It is observed in figure (a) that the peak strains at the end of the cylinder, $x/L = \pm 0.5$, are lowered as the rotational spring stiffness, K_M, is relaxed. However, peak values are increased away from the ends as a result. Figure (c) demonstrates that relaxing the radial spring stiffness, K_Q, results in significant changes in the peak strain val-

(a) Rigid Radial Support, $\theta = 0°$

(b) Rigid Radial Support, $\theta = 180°$

(c) Elastic Radial Support, $\theta = 0°$

(d) Elastic Radial Support, $\theta = 180°$
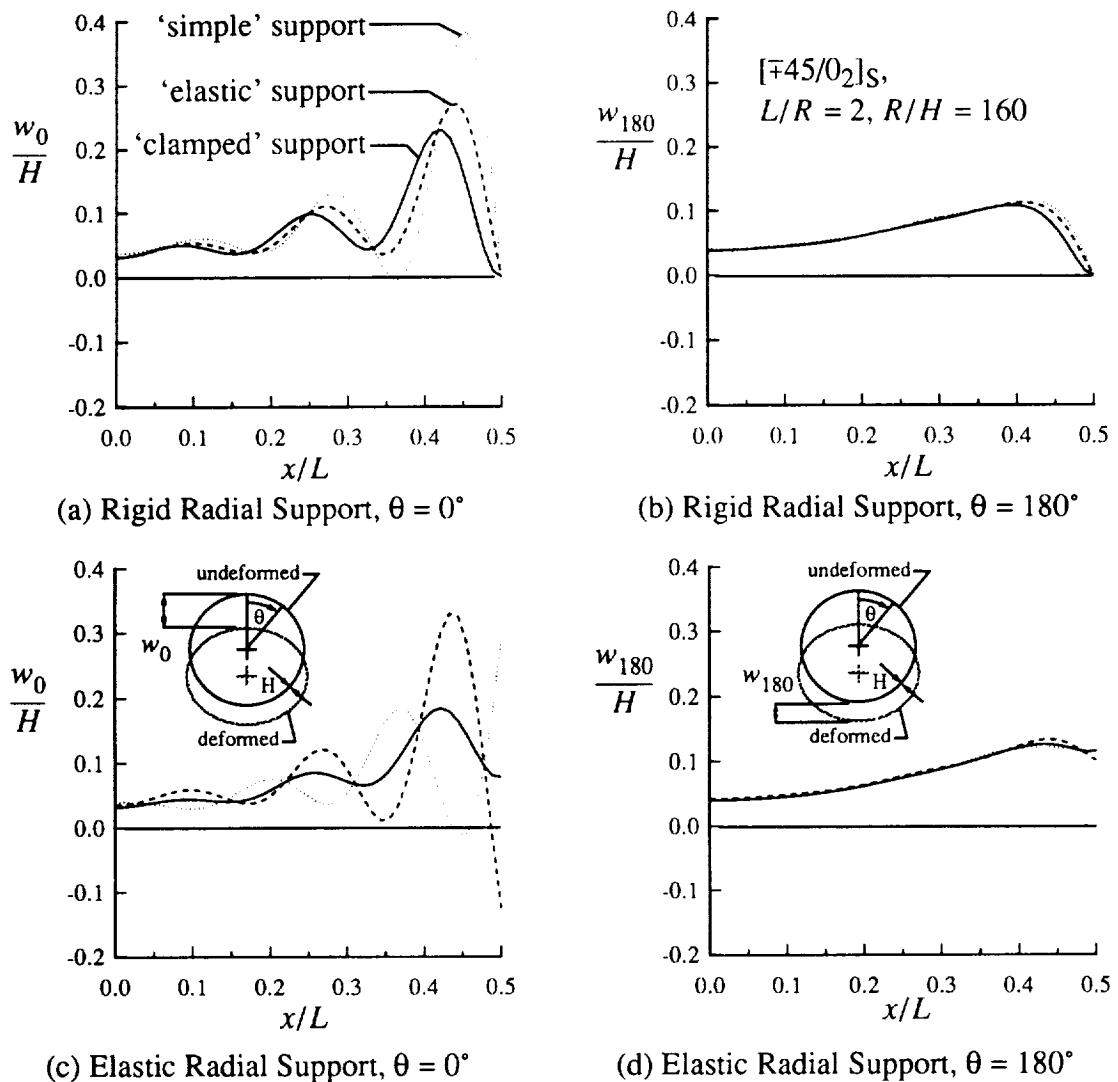
Fig. 2-10 Effect of Elastic Support Conditions, Radial Displacements

32

ues compared to figure (a). In fact, the entire character of the strain profile changes as the rotational spring stiffness is relaxed. The peak strain values are alleviated on the tension side of the cylinder, shown in figures (b) and (d), as a result of relaxing either K_M or K_Q.

Radial End-Deformations

The study of the radial end-deformation type of boundary condition, depicted in Fig. 2-3 (c), is motivated by the fact that radial deformations were observed to occur during the
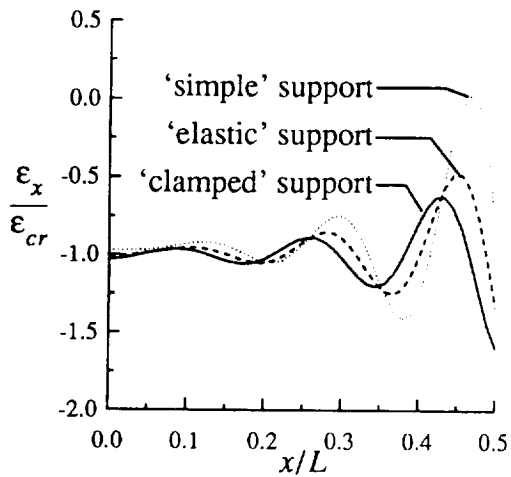
(a) Rigid Radial Support, $\theta = 0°$
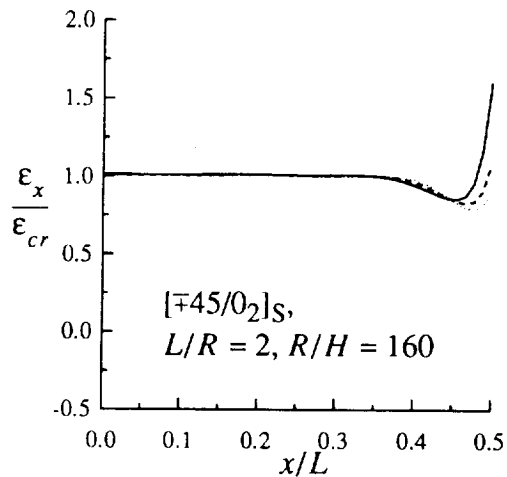
(b) Rigid Radial Support, $\theta = 180°$
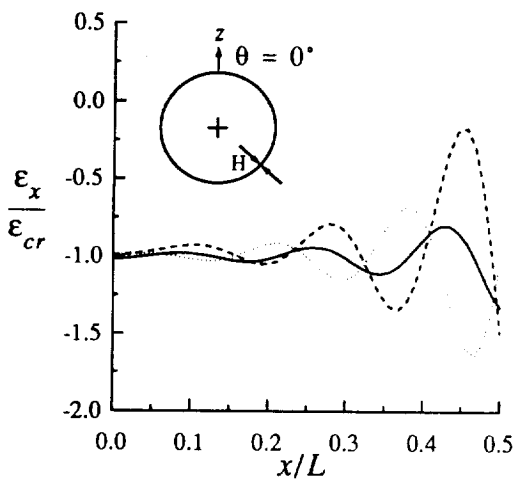
(c) Elastic Radial Support, $\theta = 0°$
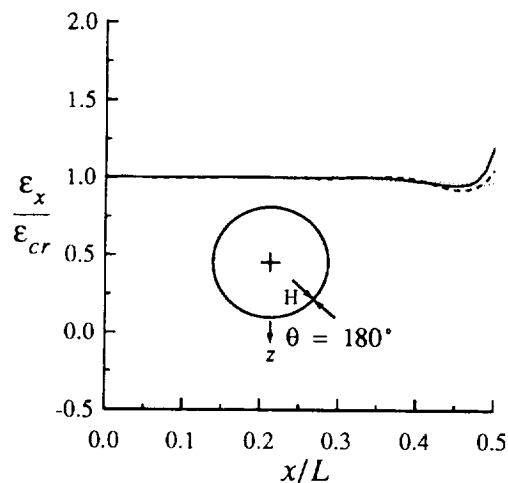
(d) Elastic Radial Support, $\theta = 180°$

Fig. 2-11 Effect of Elastic Support Conditions, Axial Strains at $z/H = +0.5$

specimen preparation process. Details of the specimen preparation will be described in connection with Chapter 3.

For simplicity, it is assumed that constant radial displacements, w_R, are applied at the cylinder ends, $x/L = \pm 0.5$, to simulate either an initial uniform radial 'pinching' or 'expansion'. The effect of w_R on the radial displacement and axial strain responses is illustrated in Fig. 2-12 for the $[\mp 45/0_2]_S$ cylinder with $L/R = 2$. The values of radial end-deformations considered in this figure are $w_R/H = -0.2, -0.1, 0.0, +0.1,$ and $+0.2$. The end-rotation is $\Omega/\Omega_{cr} = 1.0$ and the cylinder ends are clamped.

Fig. 2-12 indicates that radial deformations of only 10% and 20% of the wall thickness significantly affect the responses on both the compression and tension sides of the cylinder. It is seen in figures (a) and (c), that negative values of w_R (pinching) tend to increase the peak boundary layer amplitudes on the compression side. Positive values of w_R (expansion) tend to decrease the severity of the peak boundary layer amplitudes. The opposite effect is observed on the tension side of the cylinder, shown in figures (b) and (d).

2.1.4 Effect of Axisymmetric Imperfections

It is well known that geometric shape imperfections can significantly reduce the buckling resistance of cylinders subjected to axial compression. An axisymmetric radial imperfection of the form

$$\bar{w}(x) = -\xi H \cos \frac{m\pi x}{L} \tag{2.35}$$

was introduced in the nonlinear prebuckling analysis in the form of a pre-strain to study its effect on the bending responses. The implementation of this type of pre-strain is outlined in the section "Initial Geometric Imperfections" in Appendix B. The axial half-wave number of the imperfection is given by the integer m and the amplitude is given as a fraction of the wall thickness, ξ. This imperfection corresponds the axisymmetric buckling mode of a axially-loaded cylinder when m is computed from Eq. (2.34).

The radial displacement and axial strain responses were computed for the $[\mp 45/0_2]_S$ cylinder with $L/R = 2$. Although Table 2-3 indicates a value of $m = 12$ for this cylinder, an odd value of $m = 11$ was chosen for the imperfection to be symmetric about $x/L = 0$. The responses are compared in Fig. 2-13 for the imperfection amplitudes of $\xi = 0.01$ and 0.02. The value of end-rotation is $\Omega/\Omega_{cr} = 1.0$ in this figure.

It is seen in Fig. 2-13 (a) and (c) that relatively mild imperfection amplitudes of only 1% and 2% of the wall thickness appreciably affect the displacement and strain responses on the compression side of the cylinder. The displacement and strain responses on the tension side of the cylinder, shown in figures (b) and (d), respectively, are relatively unaffected.

2.1.5 Effect of Higher-Order Harmonic Representation

It was stated in section 2.1.1 that representing the response variables by three harmonics, or $N = 3$, is sufficient to accurately predict the prebuckling responses. An analysis including five harmonics, or $N = 5$, was developed to compare with the $N = 3$ analysis. The anal-

(a) Radial Displacements, $\theta = 0°$ (b) Radial Displacements, $\theta = 180°$

(c) Axial Strains, $z/H = +0.5, \theta = 0°$ (d) Axial Strains, $z/H = +0.5, \theta = 180°$
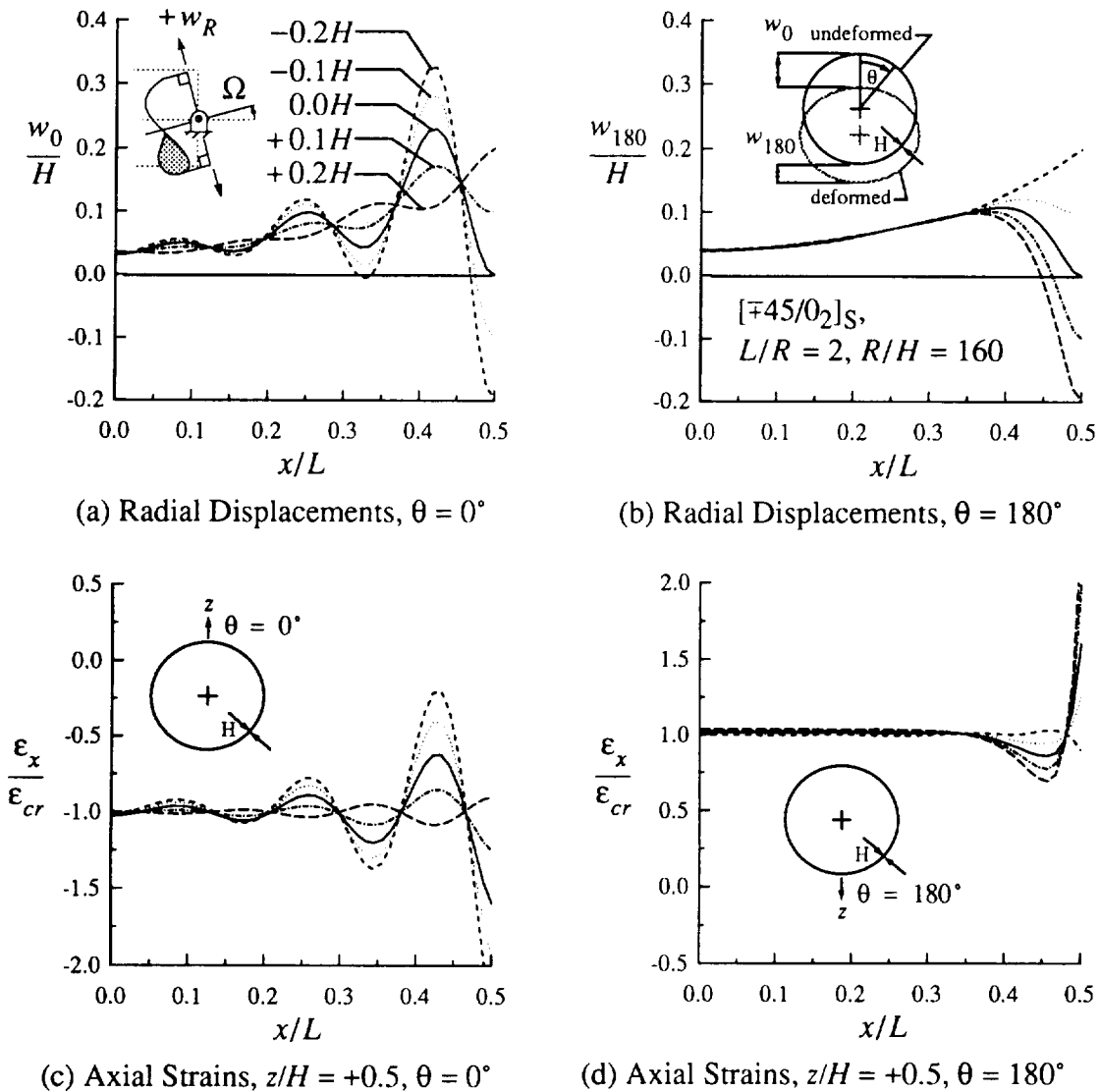
Fig. 2-12 Effect of Radial End-Deformations

35

ysis with five harmonics assumes an eleven-term series for the response variables. The axial midsurface displacement of Eq. (2.28), for example, is represented by the relation

$$u^\circ(x, \theta) = y_1(x) + y_2(x) \cdot \cos\theta + y_3(x) \cdot \cos 2\theta + y_4(x) \cdot \cos 3\theta$$
$$+ y_5(x) \cdot \cos 4\theta + y_6(x) \cdot \cos 5\theta$$
$$+ y_7(x) \cdot \sin\theta + y_8(x) \cdot \sin 2\theta + y_9(x) \cdot \sin 3\theta \tag{2.36}$$
$$+ y_{10}(x) \cdot \sin 4\theta + y_{11}(x) \cdot \sin 5\theta.$$

$$\bar{w}(x, \theta) = -\xi H \cos\frac{11\pi x}{12}$$

(a) Radial Displacements, $\theta = 0°$

(b) Radial Displacements, $\theta = 180°$

(c) Axial Strains, $z/H = +0.5, \theta = 0°$

(d) Axial Strains, $z/H = +0.5, \theta = 180°$
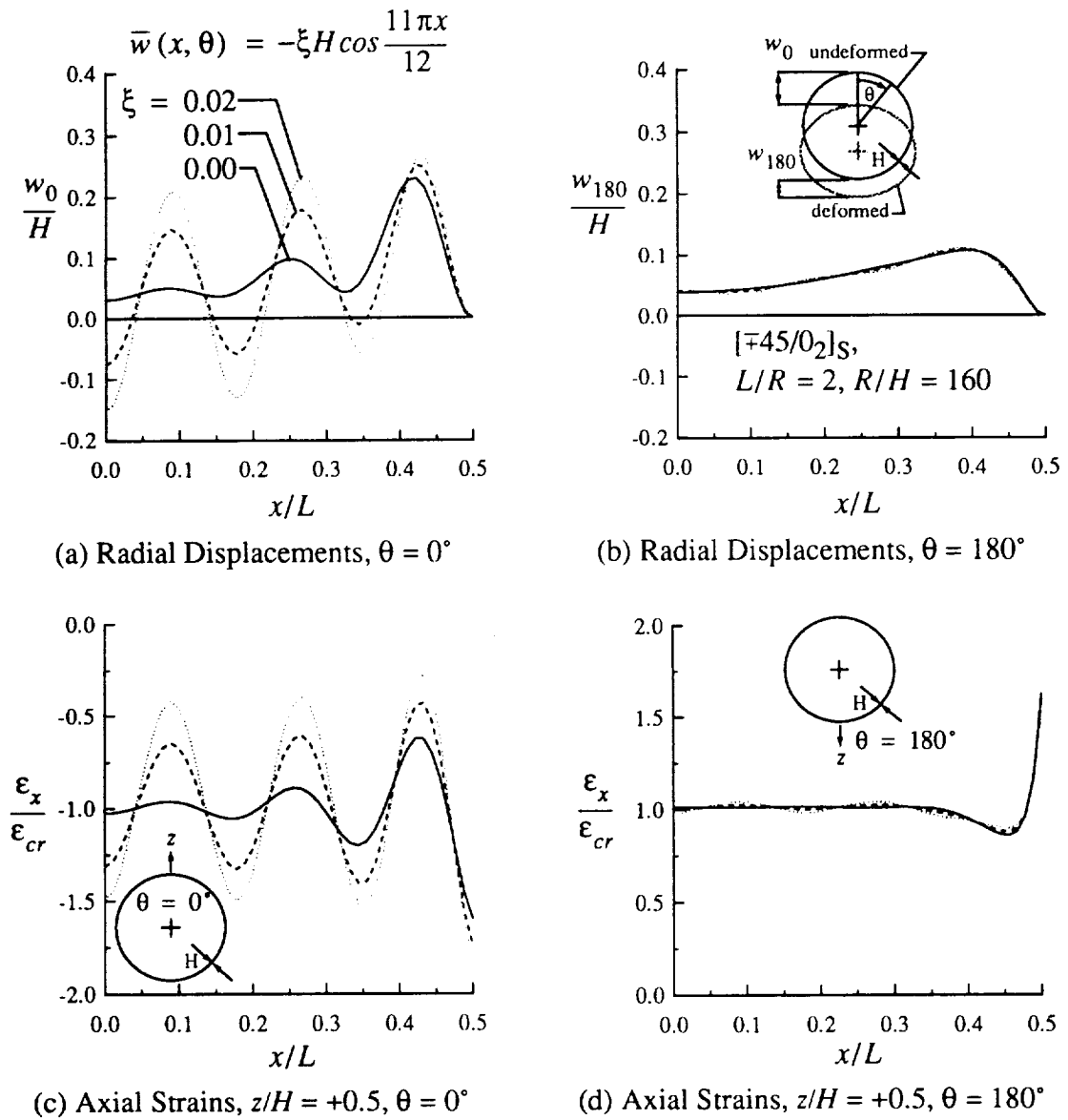
Fig. 2-13 Effect of Axisymmetric Radial Imperfection

36

The $N = 5$ harmonic analysis requires the solution of 88 first-order equations and requires substantially longer computer run times than the $N = 3$ analysis. As an example, results from the analysis with five harmonics are compared to results from the analysis with three harmonics in Fig. 2-14 for the $[\mp45/0_2]_S$ cylinder with $L/R = 2$ and $R/H = 160$. The end-rotation values in this figure are $\Omega/\Omega_{cr} = 0.5$ and 1.0 and the radial displacement and axial strain responses are shown on the compression and tension sides of the cylinder, $\theta = 0°$ and $\theta = 180°$, respectively. For this example, the analysis with five harmonics required approximately 340% more computer run time than the corresponding analysis with three harmonics. A compuitional mesh of 91 grid points was used.

Fig. 2-14 demonstrates that both analyses predict the same bending responses for $\Omega/\Omega_{cr} = 0.5$. Some deviations in the peak amplitudes of the displacement and strain responses are evident on the compression side of the cylinder at $\Omega/\Omega_{cr} = 1.0$. These deviations occur only when the end-rotation is in the vicinity of the buckling end-rotation. Therefore, it is concluded that the prebuckling responses can be predicted by the $N = 3$ analysis with sufficient accuracy for all prebuckling end-rotations up to the end-rotation at buckling.

2.1.6 First-Ply Failure

Predicting the initiation of first-ply material failure in composite laminates is a complex problem and an entire subject in itself. There are a number of failure theories available to predict the initiation of both intralaminar and interlaminar failure. Since there does not appear to be a universally applicable failure criterion, the maximum strain criterion is applied here to gain some insight in the first-ply failure of the three laminates under consideration.

It is evident from the discussion in sections 2.1.2 through 2.1.4 that large prebuckling deformations near the ends of the cylinder lead to significant strain levels. The maximum strain failure criterion was implemented in the nonlinear prebuckling analysis to determine the propensity for first-ply failure. The inplane strain components were computed on a point-wise basis through the wall thickness at every grid point of the computational mesh used in solving Eqs. (2.29) and (2.30). First-ply failure is defined by the end-rotation and associated bending moment which causes a component of strain in the fiber oriented coordinate system to exceed its corresponding failure strain. The propensity for a compressive, tensile, or shear failure mode at a given location in the cylinder wall is determined by the magnitude of the three ratios F_1, F_2, and F_3. These ratios are defined as

$$F_1 = \frac{\varepsilon_1^{max}}{\varepsilon_1^c}, \quad \varepsilon_1^{max} < 0 \qquad \text{or} \qquad F_1 = \frac{\varepsilon_1^{max}}{\varepsilon_1^t}, \quad \varepsilon_1^{max} > 0$$

$$F_2 = \frac{\varepsilon_2^{max}}{\varepsilon_2^c}, \quad \varepsilon_2^{max} < 0 \qquad \text{or} \qquad F_2 = \frac{\varepsilon_2^{max}}{\varepsilon_2^t}, \quad \varepsilon_2^{max} > 0 \qquad (2.37)$$
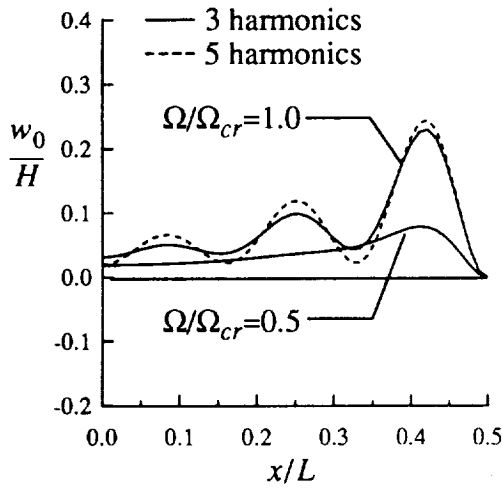
$$F_3 = \frac{|\gamma_{12}^{max}|}{\gamma_{12}^s}.$$

(a) Radial Displacements, $\theta = 0°$
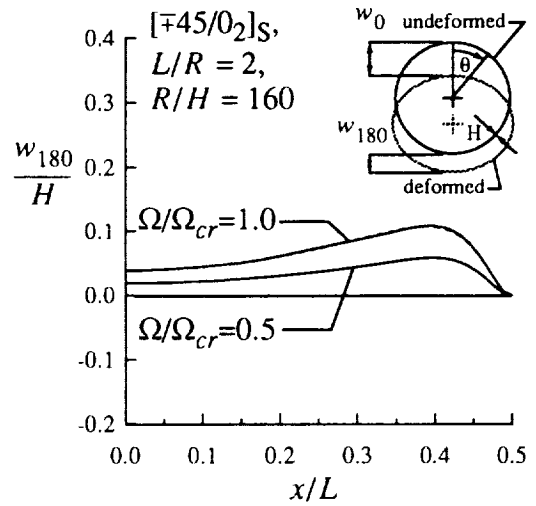
(b) Radial Displacements, $\theta = 180°$
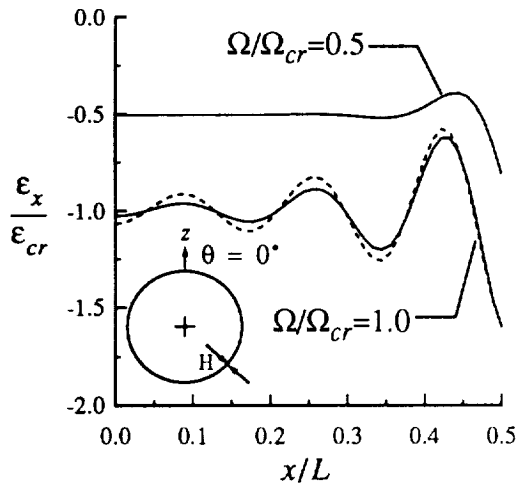
(c) Axial Strains, $z/H = +0.5$, $\theta = 0°$
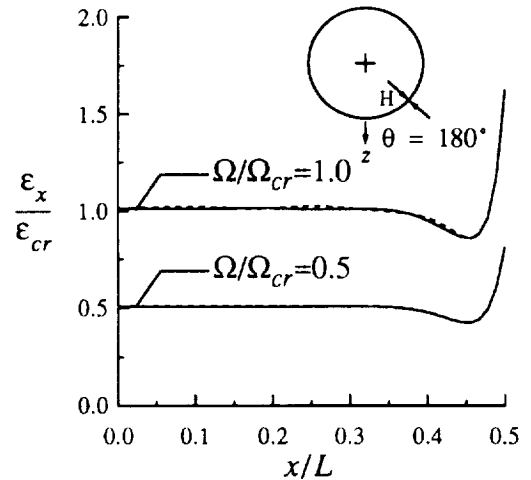
(d) Axial Strains, $z/H = +0.5$, $\theta = 180°$

Fig. 2-14 Comparison between 3-θ and 5-θ Harmonic Representation

38

The tensile, compressive, and shear failure strains in Eq. (2.37) are denoted by the superscripts 't', 'c', and 's', respectively, and the maximum strain values at a point are denoted by the superscript 'max'. The five failure modes corresponding to Eq. (2.37) are (1) fiber compression failure in the 1-direction, (2) fiber tension failure in the 1-direction, (3) compressive transverse failure in the 2-direction, (4) tensile transverse failure in the 2-direction, and (5) shear failure in the 1-2 plane. First-ply failure is assumed to occur when either F_1, F_2, or F_3 exceed unity. Since the character of the strain responses varies with the applied end-rotation, Ω, the failure ratios must be computed at increasing values of Ω to determine the magnitude of Ω that induces the first-ply failure.

The failure ratios were computed for the three cylinders with $L/R = 2$ discussed in section 2.1.2 and are illustrated in Fig. 2-15. The ratios are compared at the classical buckling end-rotation $\Omega/\Omega_{cr} = 1.0$. The failure ratios are not shown for the cylinders with $L/R = 5$ since the strains in the boundary layer region were found to be identical to the strains in the boundary layer region of the cylinders with $L/R = 2$. The values of F_1, F_2, and F_3 are represented by the horizontal bars in the figure and were computed at the indicated locations. The corresponding fiber orientation angle, α, is also indicated in the figure. The failure strains were assumed to be

$$\varepsilon_1^c = 6,700 \ \mu\varepsilon, \qquad \varepsilon_1^t = 6,530 \ \mu\varepsilon,$$

$$\varepsilon_2^c = 10,000 \ \mu\varepsilon, \qquad \varepsilon_2^t = 5,000 \ \mu\varepsilon, \qquad (2.38)$$

$$\gamma_{12}^s = 13,300 \ \mu\varepsilon.$$

The failure ratios in Fig. 2-15 indicate that the $[\mp45/0/90]_S$ and $[\mp45/0_2]_S$ cylinders are likely to buckle before material failure occurs, while the $[\mp45/90_2]_S$ cylinder is likely to exhibit matrix failure due to transverse tensile strains before buckling occurs. For the $[\mp45/0/90]_S$ and $[\mp45/0_2]_S$ cylinders, the maximum value of F_1 occurs in a $0°$ ply at the axial positions $x/L = \pm0.43$ and ±0.42, respectively. These positions correspond to the location of the peak value of w_0 in the boundary layer region near the cylinder ends shown in Fig. 2-4 (b). For the $[\mp45/90_2]_S$ cylinder, the maximum value of F_1 occurs on the tensile side in a $-45°$ ply at the axial positions $x/L = \pm0.50$. For all cylinders, the propensity for transverse failure, indicated by the value of F_2, is greatest on the tensile side at axial positions $x/L = \pm0.50$. As indicated in Fig. 2-15, the value of F_2 is greatest in either a $90°$ or a $-45°$ degree ply since these have the least transverse strength. The maximum value of F_3

occurs on the compressive side in a $-45°$ ply for all three cylinders, at the axial location where the value of w_0 is maximum in the boundary layer region (see Fig. 2-4 (b)).
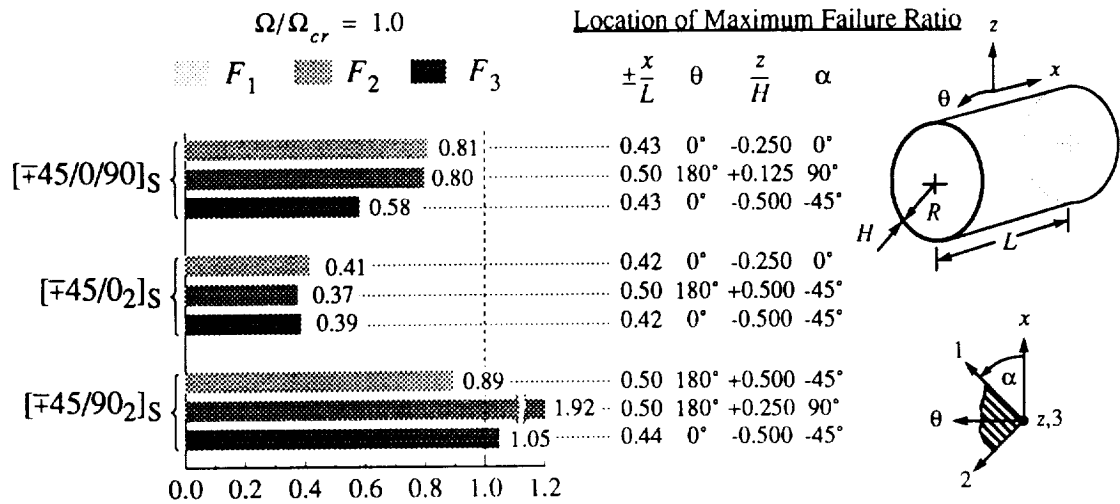
Fig. 2-15 First-Ply Failure Ratio Comparison

If it is assumed that only fiber failure controls material failure in the cylinders during the prebuckling phase of response, then the range of validity of the prebuckling solution, and hence all the results just discussed, is determined by the stability of the solution. It is assumed that matrix failure, as exhibited by the $[\mp45/90_2]_S$ cylinder, does not significantly affect the structural integrity, and therefore the buckling resistance, of the cylinders. Stability is the topic of the next section.

2.2 Buckling

The prebuckling solution discussed in section 2.1 is stable until buckling occurs. The onset of buckling is usually indicated by a rapid increase in the peak amplitudes of the prebuckling responses. Here, the buckling phenomenon is studied at increasing levels of sophistication. The most elementary buckling estimates are given by classical theory. Further detail is obtained by studying certain aspects of the prebuckling solution discussed in section 2.1. A more sophisticated solution is obtained by a finite element analysis. These various approaches are discussed in the following sections.

40

2.2.1 Classical Estimates

It was seen from the literature survey, section 1.1.2, that classical collapse moments can be computed for two different length extremes when boundary effects are neglected. It was seen that the Brazier effect, shown in Fig. 1-2 (b), determines the collapse moment for very long cylinders according to Eq. (1.5). Specialization of Brazier's analysis to the case of balanced symmetric laminates leads to the more general expression for the critical moment [11, 39]

$$M_{cr}^B = 2\pi R \sqrt{\frac{8}{27} E_x H D_{22}}. \tag{2.39}$$

It was also seen that short cylinders tend to buckle in the short-wavelength mode depicted in Fig. 1-2 (a). If it is assumed that the observations made by Seide and Weingarten [13] are applicable to anisotropic cylinders, then the critical bending moment can be estimated for the case of balanced symmetric laminates from the theoretical axial compression buckling load, Eq. (1.1), as

$$M_{cr} = \pi R^2 N_{cr} = 2\pi R \sqrt{E_\theta H D_{11}}. \tag{2.40}$$

It was shown in the discussion on the prebuckling displacements in section 2.1.2 that cross-section ovalization, i.e. the Brazier effect, is negligible for the cylinders studied in this investigation. As a result, Eq. (2.39) will significantly underestimate the buckling moment for the relatively short cylinders studied here. Hence, the appropriate classical buckling estimate, referred to in the present work as the classical buckling moment, is given by Eq. (2.40).

With an estimate for the classical buckling moment, given by Eq. (2.40), the beam bending relationship may be used to compute the corresponding classical end-rotation angle as

$$\Omega_{cr} = \frac{M_{cr}L}{2E_x J} = \frac{L}{R^2} \sqrt{\frac{A_{22}}{A_{11}} \frac{D_{11}}{E_x H}}. \tag{2.41}$$

The nominal maximum compressive strain of the cylinder midsurface at buckling can be computed from the end-rotation and the kinematic relation

$$\varepsilon_{cr} = 2\Omega_{cr} \cdot \frac{R}{L} = \frac{2}{R} \sqrt{\frac{A_{22}}{A_{11}} \frac{D_{11}}{E_x H}}. \tag{2.42}$$

Eqs. (2.40) through (2.42) represent a reasonable first approximation to the buckling values. A more detailed analysis is generally required for determining the end-rotation and corresponding moment at buckling for cases in which boundary effects, geometric shape imperfections, or more complex buckling modes are important.

To that end, it will be demonstrated that the nonlinear prebuckling analysis discussed in section 2.1 can be used as a means to predict the onset of buckling. These predictions are comparable to the classical buckling result of Eqs. (2.40) through (2.42). However, the influence of boundary effects, geometric shape imperfections, and the like can be included with this use of nonlinear prebuckling analysis. It is not possible to study these influences with the classical estimate.

2.2.2 Estimate from Prebuckling Solution

It is instructive to compare the behavior of the nonlinear prebuckling solution for a cylinder subjected to axial compression to the solution of a cylinder subjected to bending. The force resultant corresponding to the axisymmetric buckling of an axially-compressed cylinder is given by Eq. (1.1). The end-shortening at buckling can be computed from the column compression formula,

$$u_{cr} = \frac{N_{cr}L}{E_x H}. \tag{2.43}$$

Axial surface strains induced by axial compression are compared to the strains induced by bending for a $[\mp 45/0_2]_S$ cylinder in Fig. 2-16 (a). The geometry of this cylinder is described by $L/R = 2$ and $R/H = 160$. The axial surface strain distributions are compared at three values of axial strain corresponding to 50%, 100%, and 110% of u_{cr}. The equivalent bending end-rotation applied at each cylinder end is computed from Eq. (2.41). The responses in Fig. 2-16 (a) represent the axial surface strains at $\theta = 0°$ for the cylinder in bending and the strains at any θ-location for the cylinder in compression. The responses for both the bending and the compression problems were computed using the nonlinear prebuckling analysis discussed in section 2.1.

It is seen in Fig. 2-16 (a) that the axial strains are essentially the same for both loading cases at 50% of u_{cr}. At 100% of u_{cr}, however, it is observed that the peak amplitude in the boundary layer due to axial compression is more pronounced than the peak amplitude in the boundary layer due to bending. The difference between the two responses is further

pronounced at 110% of u_{cr}. The peak amplitude of the axial compression response has grown such that the peak value near the center of the cylinder, $x/L = 0$, exceeds the peak value near the ends, $x/L = 0.5$. The difference between the two boundary layer responses suggests that a cylinder in bending will buckle at a higher axial strain level than a cylinder in compression.

(a) Axial surface strain comparison

(b) Load vs. deformation comparison
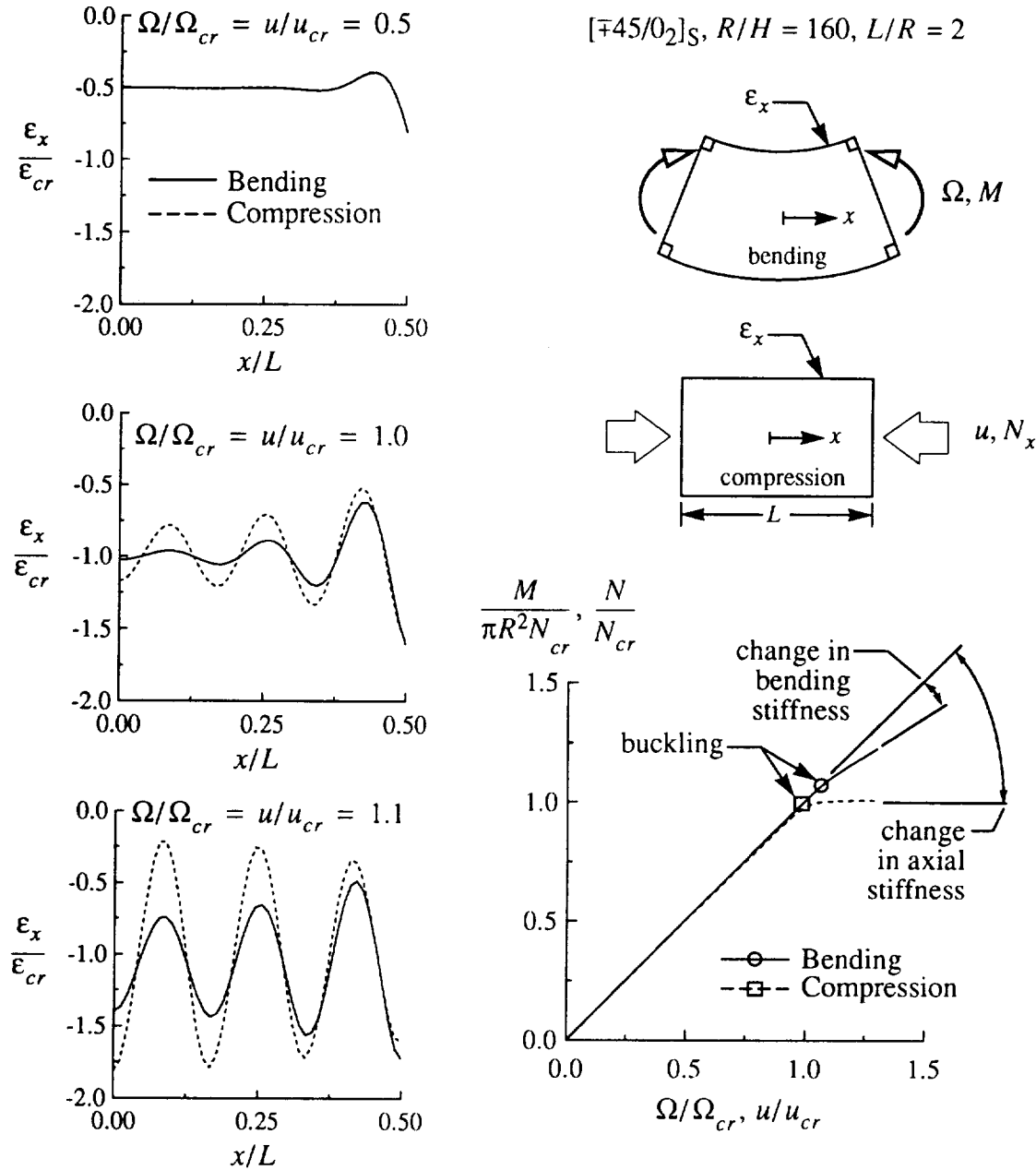
Fig. 2-16 Buckling Prediction by Means of Nonlinear Prebuckling Analysis

The load vs. axial deformation responses corresponding to the axial compression and the bending moment vs. end-rotation responses illustrated in Fig. 2-16 (a) are shown in Fig. 2-16 (b). It is observed in this figure that both the axial and bending stiffnesses of the cylinder are significantly reduced in the vicinity of $\Omega/\Omega_{cr} = u/u_{cr} = 1.0$. The reduction in stiffness reflects the rapid growth of the radial displacements in the boundary layer regions, shown in Fig. 2-16 (a), and is an indicator of the onset of buckling. Therefore, buckling can be predicted by the change in prebuckling stiffness from the load vs. end-shortening response curve. It is seen from Fig. 2-16 (b) that axisymmetric buckling is predicted to occur for the axially-compressed cylinder when the axial force resultant reaches the classical buckling force resultant, N_{cr}. The bending moment at buckling is predicted to occur at a moment value which is slightly higher than $\pi R^2 N_{cr}$. The difference between the buckling values for axial compression and bending is expected to depend on the cylinder stiffness and geometry parameters.

It is concluded that the nonlinear prebuckling analysis can be used as an effective tool to estimate the buckling moment and end-rotation values for cylinders that buckle in a short wavelength mode. As mentioned earlier, the way in which the boundary conditions and geometric imperfections, discussed in sections 2.1.3 and 2.1.4, affect the buckling end-rotation and moment may be evaluated using this approach.

A more sophisticated buckling analysis is necessary if asymmetrical buckling modes are prevalent, or if general geometric shape imperfections require consideration. A finite element approach to the buckling problem is the subject of the following section.

2.2.3 Finite Element Analysis

The STAGS finite element program was selected to predict the buckling end-rotations and moments due to its extensive nonlinear solution and bifurcation buckling capabilities, and its ability to include general geometric shape imperfections.

Model and Boundary Conditions

The cylinders were modeled with a mesh consisting of four-noded STAGS 410 quadrilateral shell elements. The axial mesh density was uniform for all models except for the $[\mp45/90_2]_S$ cylinders, for which the axial mesh density was increased slightly near the ends to capture the boundary layer responses. The theory behind the 410 element is documented in [88]. Specifics of the finite element model and the element topology are illustrated in

Fig. 2-17. The 410 element is a flat facet-type element that is based on the Kirchhoff-Love shell hypothesis and the nonlinear Lagrangian strain tensor. The element nodes include a so-called 'drilling' rotational degree of freedom, β_z^o, in addition to the rotations, β_x^o and β_θ^o, and the three translational degrees of freedom (see Fig. 2-17 (b)). Large rotations are accounted for by the use of a corotational algorithm.

L/R = 2 model:
41 axial nodes
97 circumferential nodes

3977 nodes
3840 elements

L/R = 5 model:
103 axial nodes
97 circumferential nodes

9991 nodes
9792 elements
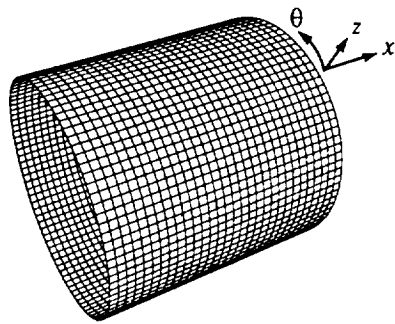
(a) Finite Element Model
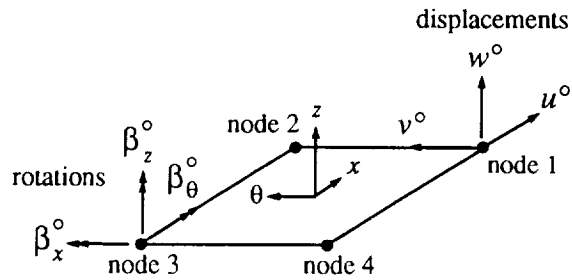
(b) 410 Element Topology

Fig. 2-17 Finite Element Model and Element Topology

The bending end-rotation, Ω, is applied to the model in the form of displacements in a manner analogous to Eq. (2.16). A minor difference lies in the fact that six conditions must be specified at each grid point on the boundary compared to the four conditions of Eq. (2.16). The boundary conditions for the finite element analysis, which do not include the elasticity of the supports or an applied radial deformation, are

$$u^o\left(\pm\frac{L}{2}, \theta\right) = \mp R\Omega\cos\theta, \qquad \beta_x^o\left(\pm\frac{L}{2}, \theta\right) = \mp\Omega\cos\theta,$$

$$v^o\left(\pm\frac{L}{2}, \theta\right) = 0, \qquad \beta_\theta^o\left(\pm\frac{L}{2}, \theta\right) = 0, \qquad (2.44)$$

$$w^o\left(\pm\frac{L}{2}, \theta\right) = 0, \qquad \beta_z^o\left(\pm\frac{L}{2}, \theta\right) = \mp\Omega\sin\theta.$$

It was demonstrated in section 2.1.4 that geometric shape imperfections can affect the prebuckling responses. Imperfections with arbitrary axial variation can be modeled using the approach discussed in section 2.1, but it is not possible to model shape imperfections with arbitrary circumferential variation due to the finite number of harmonics, i.e. $N = 3$ or 5, accounted for in the expansion of the response variables. Many more harmonic terms would be required to accurately represent general shape imperfections. It is possible, however, to model general shape imperfections in the finite element analysis. Fourier series representations were used to accurately model the measured test specimen shape imperfections. The imperfections were introduced into the analysis in the form of an initial strain imperfection. Details of the measured test specimen shape imperfections will be discussed in the context of the test specimens in Chapter 3.

Analysis Procedure

The STAGS program has the capability to compute the buckling end-rotations and moments in consideration of either a geometrically linear or a geometrically nonlinear state of prebuckling. Nonlinear prebuckling will be considered here for the buckling calculations for the test specimens. The prebuckling solutions were obtained assuming both perfect and imperfect geometries using the nonlinear solution option which is based on Newton's method. The end-rotations were increased incrementally until a bifurcation point was reached. The bifurcation point was indicated by the appearance of one or more negative roots in the tangent stiffness matrix. A linear bifurcation buckling analysis was then conducted relative to the nonlinear prebuckling state in the vicinity of the bifurcation point to compute the lowest eigenvalue and the associated eigenvector, or mode shape. The applied bending moment was computed for each converged prebuckling solution by summing the moment contribution of each nodal reaction force on the end of the cylinder.

Comparison to Donnell Theory Prebuckling Solutions

As a matter of interest, and to provide comparisons between the analysis methods being used, the prebuckling responses computed with the STAGS program are compared to the responses computed with the three-harmonic and the five-harmonic nonlinear Donnell analyses. Prebuckling displacements and strains are compared at the circumferential location $\theta = 0°$ in Fig. 2-18 for the applied end-rotation $\Omega/\Omega_{cr} = 1.0$. The responses shown in this figure are for the $[\mp 45/0_2]_S$ cylinder with $L/R = 2$ and $R/H = 160$ that was discussed previously.

(a) Radial Displacements

(b) Axial Strains, $z/H = +0.5$
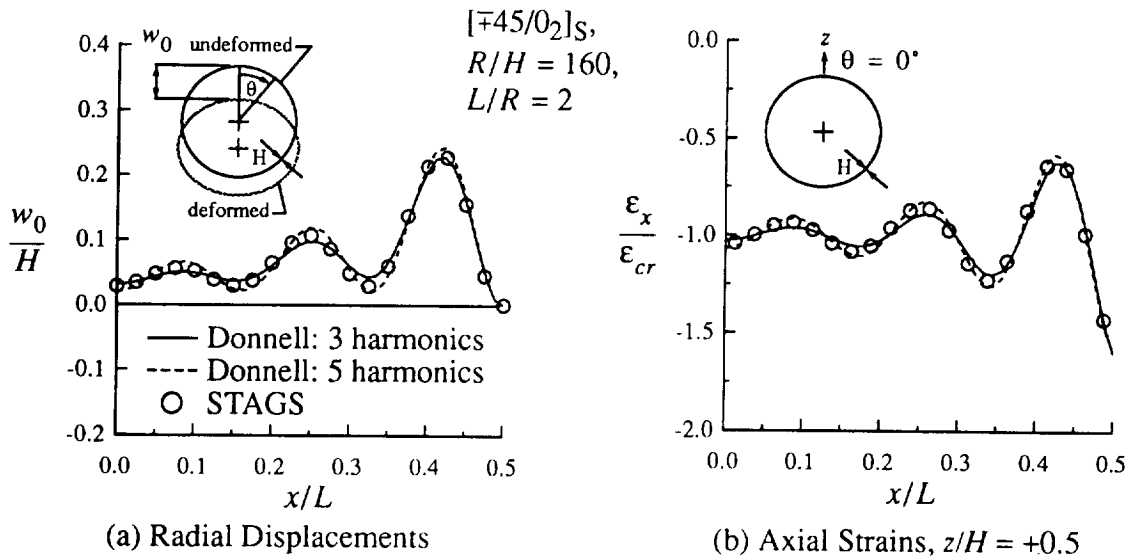
Fig. 2-18 Prebuckling Response Comparison, Donnell vs. STAGS

Only minor differences are observed between the radial displacement and axial strain responses predicted by the three analyses. The finite element data points fall in between the predictions from the three-harmonic and five-harmonic Donnell analyses, indicating excellent correlation with the Donnell shell theory results. The differences between the Donnell theory and the STAGS analyses are virtually indistinguishable at other circumferential locations and at smaller values of end-rotation. The differences observed in this comparison are typical of the other cylinders discussed in section 2.1.2.

Comments on STAGS Analysis

Other elements are available in the STAGS element library, notably the 411 and the 480[*] element. The 411 element is similar to the 410 element except that it includes midside nodes. It was found to give nearly identical results to the 410 element and therefore did not warrant the additional computational expense associated with an increase in the number of degrees of freedom. The 480 element is a curved nine-noded isoparametric element which includes transverse shearing. It was found to be more flexible than the 410 element, yielding slightly larger deflections for values of end-rotation in the vicinity of the bifurcation point. Overall, it was found that the benefits of the 480 element did not outweigh the additional computational costs.

---

[*] The normal rotations are suppressed for the 480 element so that the last of Eqs. (2.44) is identically zero.

47

A comparison between different shell finite element formulations is presented in [48] for various elastic shell collapse problems. It is shown that for some problems, higher order elements, such as the STAGS 480 element, can predict collapse loads up to 10% lower than for the STAGS 410 element. Similar results were found for the present problem.

2.2.4 Buckling Predictions for Idealized Cylinders

The three approaches to predicting the onset of buckling, discussed in sections 2.2.1 through 2.2.3, are compared here. The buckling predictions based on the Donnell theory prebuckling analysis and the STAGS finite element analysis are compared to the classical buckling end-rotations (see Table 2-2) in Fig. 2-19 for the six idealized cylinders. The associated buckling moments, strains, and end-rotation values can be computed from Eq. (2.40), Eq. (2.42), and Table 2-2. For comparison, the finite element results in Fig. 2-19 were computed relative to a geometrically linear prebuckling state in addition to the geometrically nonlinear state.

It is observed in Fig. 2-19 that, overall, the Donnell theory prebuckling analysis and the STAGS analyses predict buckling to occur within approximately ±15% of the classical predictions. The Donnell prebuckling analysis predicts the largest buckling values in nearly every instance. The STAGS analysis with linear prebuckling predicts similar results to the STAGS analysis with nonlinear prebuckling. It is also observed that the cylinders with $L/R = 5$ tend to buckle at a slightly lower value of Ω than the cylinders with $L/R = 2$. Further examination of Fig. 2-19 indicates that the buckling end-rotations predicted by STAGS for the [∓45/0/90]$_S$ and the [∓45/0$_2$]$_S$ cylinders are greater than Ω_{cr} while they are lower for the [∓45/90$_2$]$_S$ cylinders. This fact can be explained by considering the mode shapes computed from the finite element analyses.

The mode shapes associated with the buckling end-rotations predicted by the STAGS analysis with nonlinear prebuckling are illustrated in Figs. 2-20 and 2-21 for $L/R = 2$ and 5, respectively. Both a three-dimensional view of the deformed shapes and a two-dimensional contour plot of the radial buckling displacements are shown in these figures. The mode shapes were computed from a linear bifurcation analysis which was conducted relative to the nonlinear prebuckling solution at the end-rotation value indicated in the figures.

It is observed that the [∓45/0/90]$_S$ and the [∓45/0$_2$]$_S$ cylinders, shown in (a) and (b) of Figs. 2-20 and 2-21, respectively, buckle in a manner similar to the short wavelength mode predicted by the classical analysis and the Donnell theory prebuckling analysis. The [∓45/

$90_2]_S$ cylinders, however, do not buckle in the short wavelength mode but buckle in the modes shown in (c) of Figs. 2-20 and 2-21. These modes, unlike the short wavelength modes seen in figures (a) and (b) of Figs. 2-20 and 2-21, exhibit one axial half-wave and a number of circumferential waves and, as is evident from Fig. 2-19, result in lower buckling end-rotations than those predicted by the classical analysis.

Furthermore, it can be seen in Figs. 2-20 and 2-21 that material anisotropy has an effect on the mode shapes. This anisotropic effect is manifested in the skewing of the mode shapes and is attributed to the presence of the anisotropic bending terms D_{16} and D_{26}. The skewing of the mode shapes is known to be a factor in the buckling of anisotropic cylinders in axial compression [89-90] and has been observed to occur in the buckling of anisotropic cylinders in bending [19]. The skewing phenomenon is the least pronounced in the $[\mp45/0_2]_S$ cylinders and is the most pronounced in the $[\mp45/90_2]_S$ cylinders.

The modes computed in consideration of linear prebuckling conditions were found to be similar to the modes computed in consideration of nonlinear prebuckling conditions for these idealized cylinders. The consideration of geometric imperfections, however, can result in significant differences between the buckling predictions using linear prebuckling conditions and nonlinear prebuckling conditions. It is for this reason that the nonlinear prebuckling conditions will be used when analyzing the test specimens.
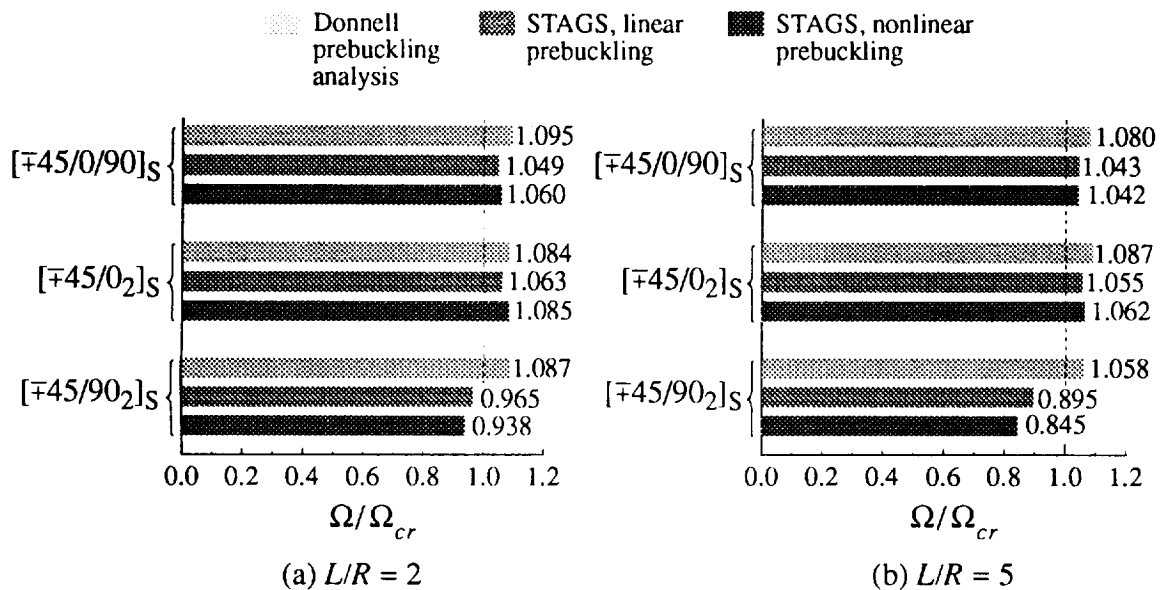
Fig. 2-19 Buckling Predictions for Idealized Cylinders
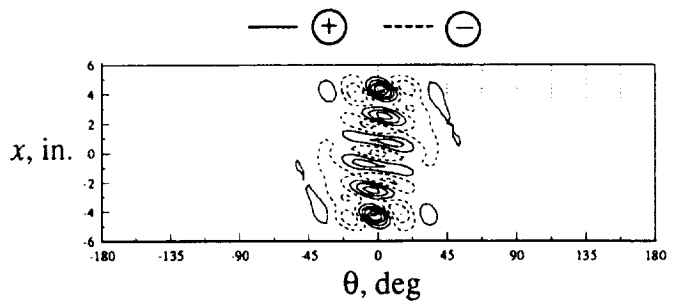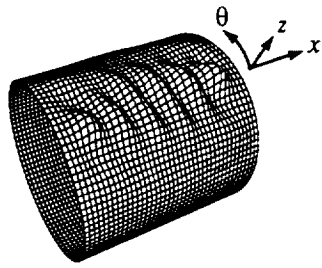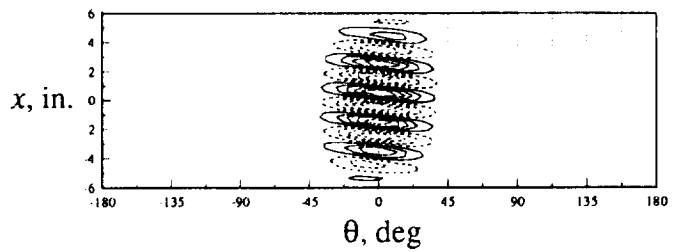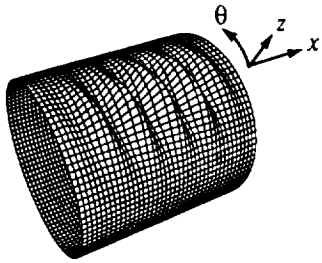
(a) $[\mp 45/0/90]_S$, $\Omega/\Omega_{cr} = 1.025$

(b) $[\mp 45/0_2]_S$, $\Omega/\Omega_{cr} = 1.02$
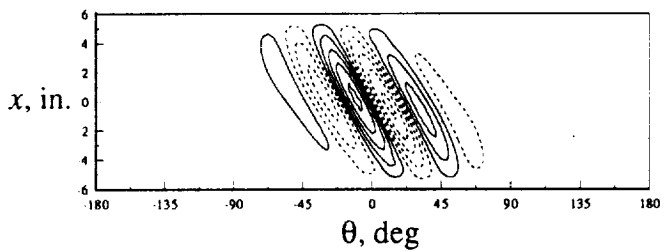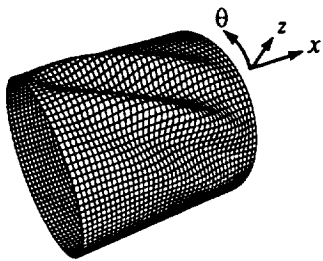
(c) $[\mp 45/90_2]_S$, $\Omega/\Omega_{cr} = 0.90$

Fig. 2-20 Buckling Shapes, $L/R = 2$
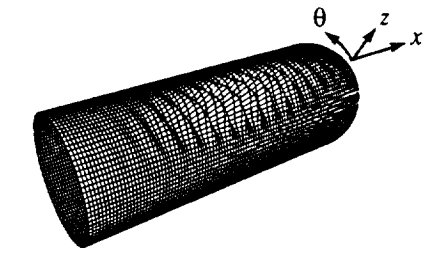
(a) $[\mp 45/0/90]_S$, $\Omega/\Omega_{cr} = 1.00$
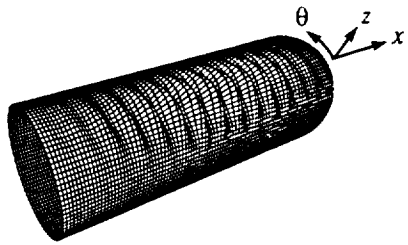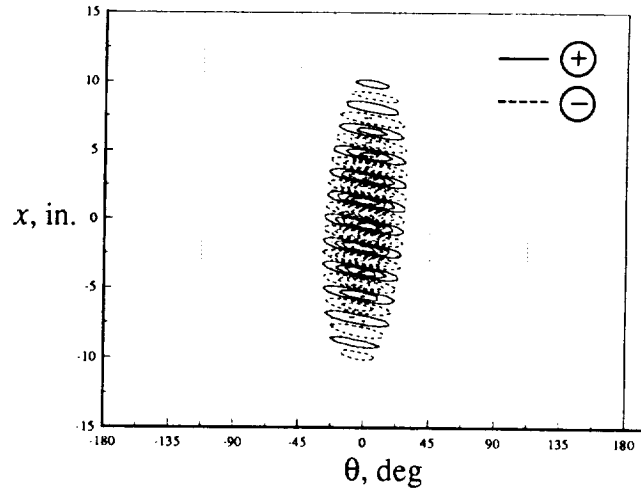
(b) $[\mp 45/0_2]_S$, $\Omega/\Omega_{cr} = 1.00$
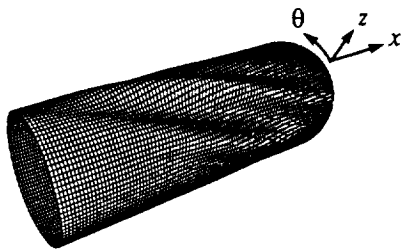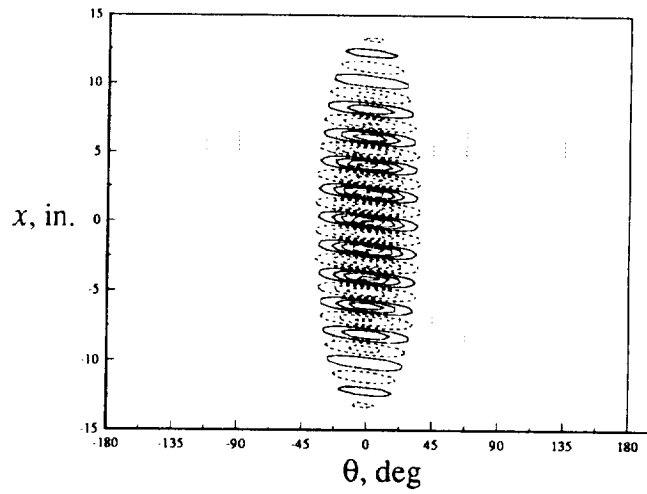
(c) $[\mp 45/90_2]_S$, $\Omega/\Omega_{cr} = 0.78$
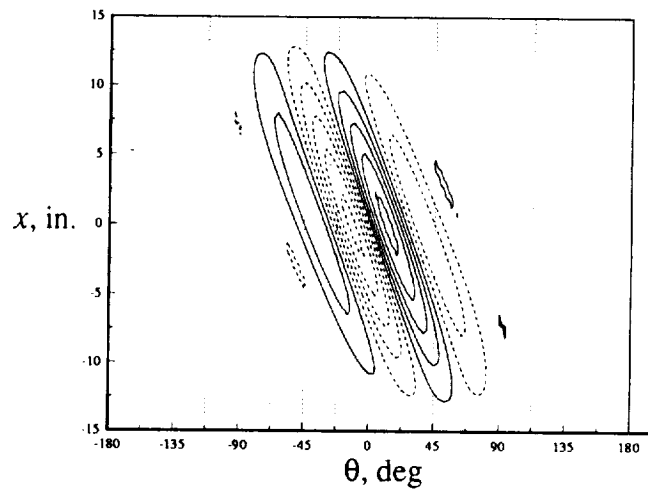
Fig. 2-21 Buckling Shapes, $L/R = 5$

51

2.3 Postbuckling

The postbuckling behavior of cylinders in bending or axial compression is extremely complex and is a difficult problem to solve. Postbuckling solution paths are often numerous and closely spaced and are therefore highly dependent on the presence and character of assumed initial imperfection shapes. The problem is further complicated by the fact that the initial postbuckling solution paths are extremely unstable.

The postbuckling responses were computed with the STAGS finite element program using a so-called path-parameter strategy to compute solutions beyond the bifurcation point. Since displacement control breaks down in the vicinity of the bifurcation point, the incremental applied displacement loading parameter is replaced with an increment of arc-length along the solution path as the independent loading parameter. The arc-length increments are then automatically adjusted as a function of the solution behavior. Considerable computational effort was required due to the small step-size increments required to overcome local extrema.

2.3.1 Postbuckling Response of Idealized Cylinders

The idealized cylinders with $L/R = 2$ (see sections 2.1.2 and 2.2.4) were analyzed to gain insight into the bending postbuckling behavior. Geometric shape imperfections in the form of the first buckling mode, shown in Fig. 2-20, were introduced as an idealized imperfection to facilitate the calculations. The imperfection amplitudes were assumed to be 20% of the cylinder wall thickness.

Relatively successful postbuckling analyses were conducted for the $[\mp45/0/90]_S$ and the $[\mp45/0_2]_S$ cylinders. Solution difficulties were encountered in the analysis of the $[\mp45/90_2]_S$ cylinder. The postbuckling behavior is presented for the $[\mp45/0/90]_S$ and the $[\mp45/90_2]_S$ cylinders to illustrate some features of the postbuckling behavior and the difficulties encountered in obtaining the numerical solutions.

The computed moment vs. end-rotation relations are depicted for the $[\mp45/0/90]_S$ and the $[\mp45/90_2]_S$ cylinders in Figs. 2-22 (a) and (b), respectively. The insets in these figures provide details of the postbuckling response near the bifurcation point. The prebuckling moment vs. end-rotation relations are linear up to the bifurcation buckling point and have slope s_A. The bifurcation point is labeled as point A in the figures. Comparing the bifurcation buckling end-rotation in these figures, denoted as Ω_{cr}^{fe} in the figures, to those reported
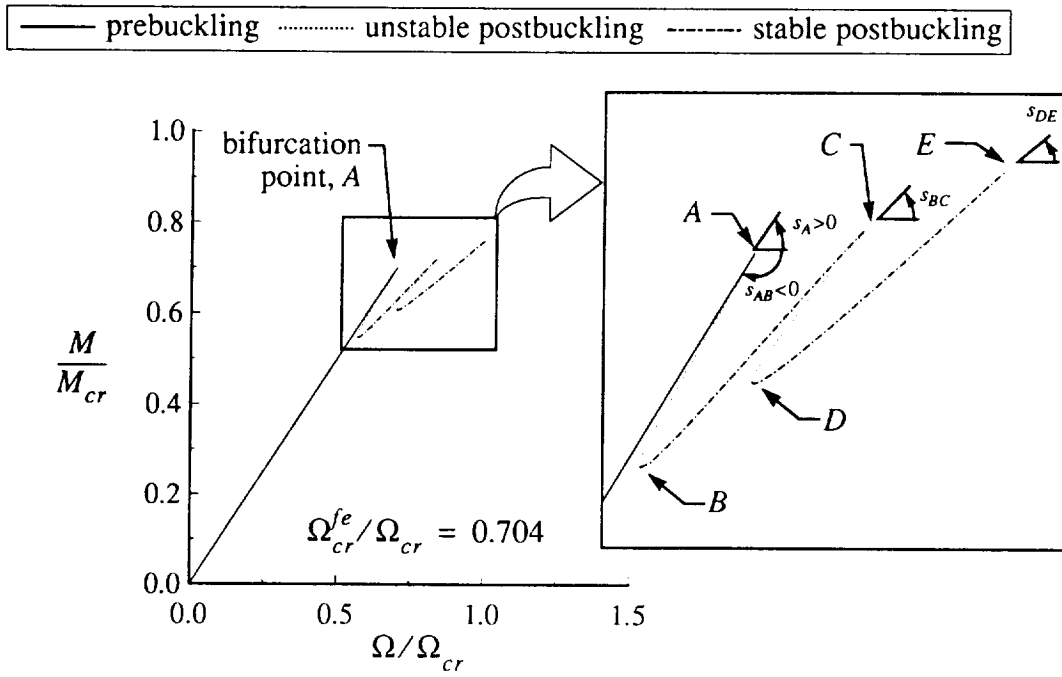
(a) $[\mp45/0/90]_S$ cylinder with $R/H = 160$, $L/R = 2$, and shape imperfection in form of the 1st buckling mode, amplitude equal to 20% of wall thickness
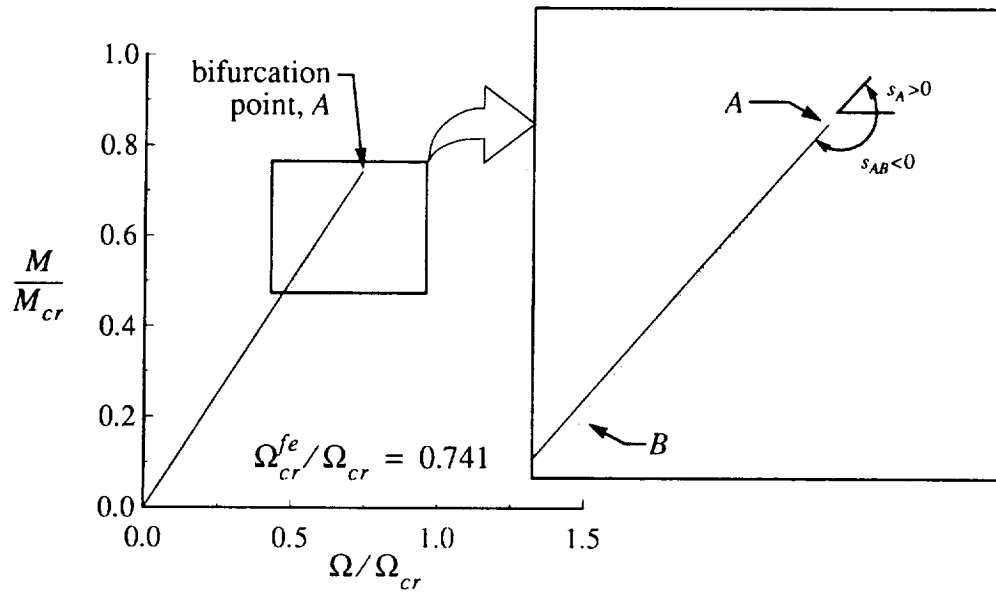
(b) $[\mp45/90_2]_S$ cylinder with $R/H = 160$, $L/R = 2$, and shape imperfection in form of the 1st buckling mode, amplitude equal to 20% of wall thickness

Fig. 2-22 Predicted Postbuckling Moment vs. End-Rotation Characteristics

in Fig. 2-19 (a) indicates that the buckling resistance of the idealized $[\mp45/0/90]_S$ and $[\mp45/90_2]_S$ cylinders with $L/R = 2$ is reduced by 34% and 21%, respectively.

The initial slope of the postbuckling moment vs. end-rotation relation, s_{AB}, is an indicator of whether buckling will occur gradually or suddenly [89]. A positive slope indicates a gradual buckling process and a negative slopes indicates a sudden, and possibly catastrophic, buckling process. The insets of Fig. 2-22 indicate a slope with a high negative value, suggesting that buckling will occur suddenly for these cylinders. The postbuckling solution along path A-B represents an unstable unloading path. The instability of this path is indicated in the STAGS analysis by the appearance of a single negative root in the tangent stiffness matrix. The point labeled B represents a minimum along path A-B.

For the $[\mp45/0/90]_S$ cylinder shown in Fig. 2-22 (a), further application of end-rotation results in the stable loading path B-C. The stability of this path is characterized by zero negative roots in the tangent stiffness matrix. Comparing the slope s_{BC} of path B-C to the prebuckling slope s_A in the inset figure, indicates that a change in the cylinder bending stiffness has taken place. Point C represents a second bifurcation point. The solution is again unstable along path C-D until the minimum point D is reached. The end-rotation is further increased along the stable path D-E until the third bifurcation point E is reached. The slope of path D-E, s_{DE}, indicates a further change in the cylinder bending stiffness. Solutions difficulties are encountered beyond point E and the analysis is halted.

For the $[\mp45/90_2]_S$ cylinder shown in Fig. 2-22 (b), numerous attempts to increment the end-rotation beyond point B leads to the appearance of a number of negative roots in the tangent stiffness matrix, signaling the presence of alternate postbuckling solution paths. The solution is no longer clearly defined and the analysis is halted.

The deflection patterns corresponding to the segments of the scallop-shaped postbuckling paths, labeled B-C and D-E in Figs. 2-22 (a), are illustrated in Fig. 2-23. The three-dimensional deformed shapes and two-dimensional contour plots shown in this figure indicate that large inward buckles have developed on the compression side of the cylinder. The buckles become deeper and more pronounced from path B-C to path D-E. It is clear that the presence of the buckles alters the cylinder cross-section moment of inertia, accounting for the different postbuckling slopes s_{BC} and s_{DE}.

(a) Deformed shape, path B-C
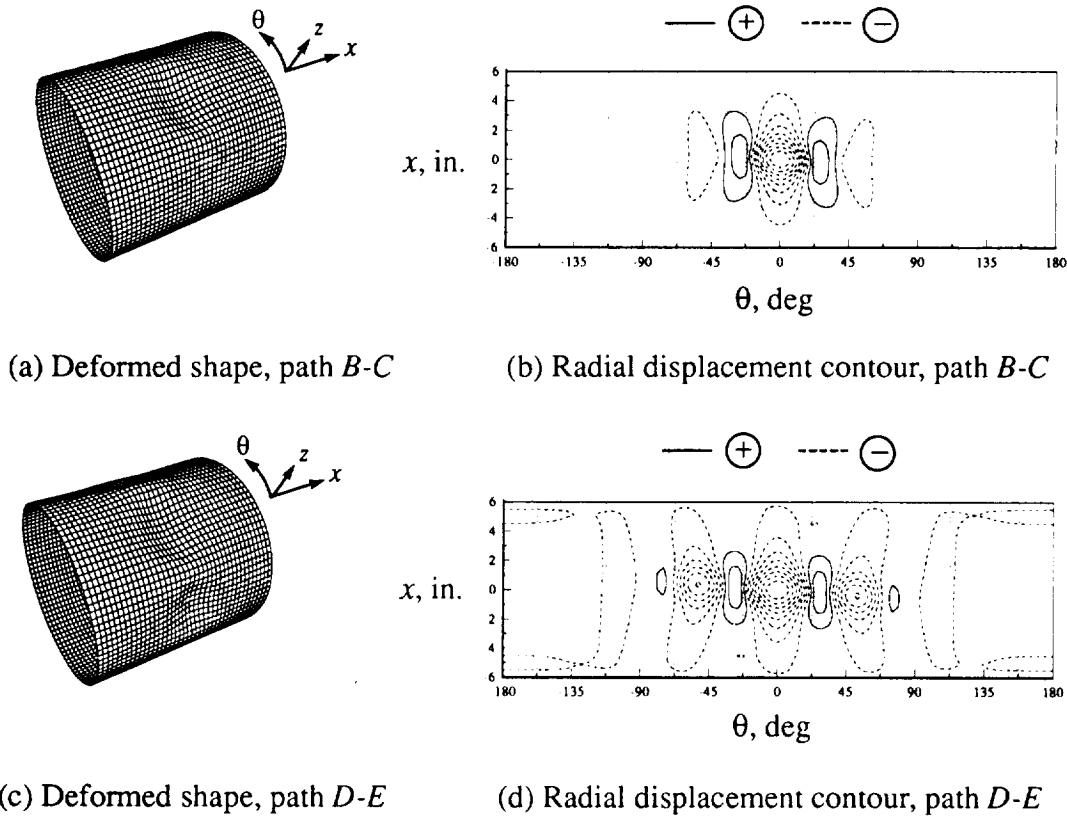
(b) Radial displacement contour, path B-C

(c) Deformed shape, path D-E

(d) Radial displacement contour, path D-E

$[\mp45/0/90]_S$ cylinder with $R/H = 160$, $L/R = 2$, and shape imperfection in form of the 1st buckling mode, amplitude equal to 20% of wall thickness

Fig. 2-23 Predicted Postbuckling Deflection Patterns

2.3.2 Comments on Postbuckling Analysis

It must be stressed that the bifurcation buckling values and the postbuckling behavior are highly sensitive to assumed imperfections shapes and amplitudes. The above examples are intended to highlight some of the features of the postbuckling behavior that can be expected in the experiments. The results may differ substantially for other assumed imperfection shapes and amplitudes. Further, the relative success of a postbuckling analysis may be affected by various finite element modeling issues such as mesh density and element aspect ratio.

As mentioned previously, the finite element analysis was conducted using arc-length control when the displacement control approach failed at the bifurcation point. Experimentally, buckling could take place in a perfectly rigid test fixture along either the load

control path or the displacement control path shown in Fig. 2-24. With either load or displacement control, buckling would cause a sudden jump to a postbuckling equilibrium position on path B-C or D-E as shown. A flexible test fixture, however, would cause buckling to occur along the diagonal path due to the sudden change in stiffness of the cylinder relative to the test fixture [91]. The arrows in the figure indicate a number of potential postbuckling equilibrium positions. The actual equilibrium position depends on the initial conditions, relative stiffness of the fixture, and the dynamic characteristics of the specimen and fixture.
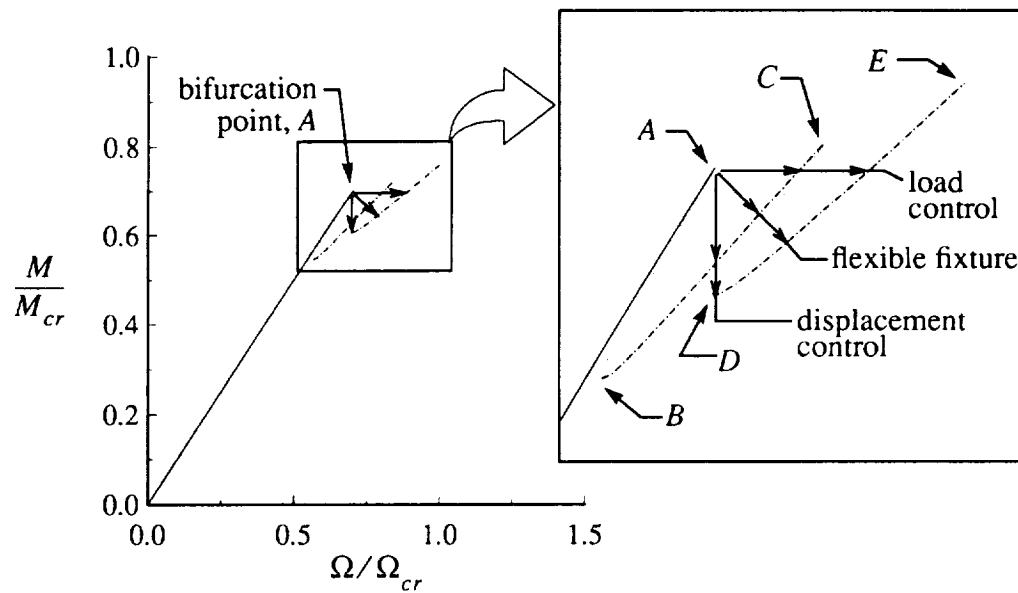
Fig. 2-24 Potential Buckling Paths

The postbuckling behavior of the test specimens will be discussed in Chapter 4. Although analytical representations of the actual measured surface shape imperfections were used in the analyses of the specimens, it will be seen that postbuckling solutions for the test specimens could only be computed with a mixed rate of success due to persistent numerical difficulties such as those described in Fig. 2-22 (b).

This chapter has provided an indication of what might be expected from the bending response of thin-walled composite cylinders. The prebuckling responses have been studied for three laminates and two cylinder geometries. The influence of non-ideal boundary conditions and geometric imperfections on the prebuckling responses has been investigated.

Analysis

Buckling has been discussed and the ramifications of the complex postbuckling response character has been presented. Attention now turns to the description of the test apparatus and the test cylinders. Later, attention is focused on comparing the responses just discussed with the experimental measurements and observations.

3. Description of Experiment

Several major tasks were undertaken in preparation for the experimental component of the present investigation. The first task was to develop the specifications for the graphite-epoxy test specimens and test apparatus. Size considerations resulted in a nominal specimen diameter of 12 inches and an eight-ply wall construction. The size specifications determined a minimum test fixture bending capacity of 135,000 in.-lbs. The second task was to develop a functional and economical design concept for the test apparatus and specimens. Key fabrication techniques and design concepts were evaluated and proven before the final design was given to a machine shop for fabrication. After fabrication, minor fixture adjustments were made based on the test loading of a comparatively thick-walled aluminum 'dummy' cylinder up to the fixture maximum capacity of 315,000 in.-lbs.

The preparatory tasks resulted in a 4-ft.-long aluminum mandrel used for the tape layup and curing of the cylinders, six 12-in.-diameter graphite-epoxy test specimens, a cylinder bending fixture, and other associated hardware and procedures.

Details of the test apparatus, specimens, and testing procedures will be described in the following sections.

3.1 Apparatus*

The load introduction concept posed a challenging test fixture design problem. The question arose on how to introduce a bending moment into the test specimen while precisely locating and gripping the specimen ends. The solution to this problem was to locate the

---

* The use of trademarks or names of manufacturers in this study is for accurate reporting and does not constitute an official endorsement, either expressed or implied, of such products or manufacturers by the author, Virginia Tech, or the National Aeronautics and Space Administration.

test specimen in the annular region between a set of inner and outer loading rings, using a low-temperature melting point alloy* as a potting compound. Also, stepped fiberglass tabs on the specimen provided the means with which to react tensile loads. A schematic of the loading concept is shown in Fig. 3-1, with the details shown in Fig. 3-2. A bending moment, M, is applied to the test specimen and loading rings as shown. Tensile loads are transferred from the inner and outer loading rings to the fiberglass tabs and cylinder wall through shearing of the potting compound. Compressive loads are transferred into the cylinder ends through direct contact with the test fixture, in addition to the shearing of the cylinder wall.

The schematic of Fig. 3-2 illustrates details of the inner and outer loading rings, the stepped fiberglass tabs, and the low-temperature melting point alloy potting compound. The potting compound mechanically locks the stepped fiberglass tabs on the cylinder in between the loading rings. The circumferential grooves in the loading rings prevent the
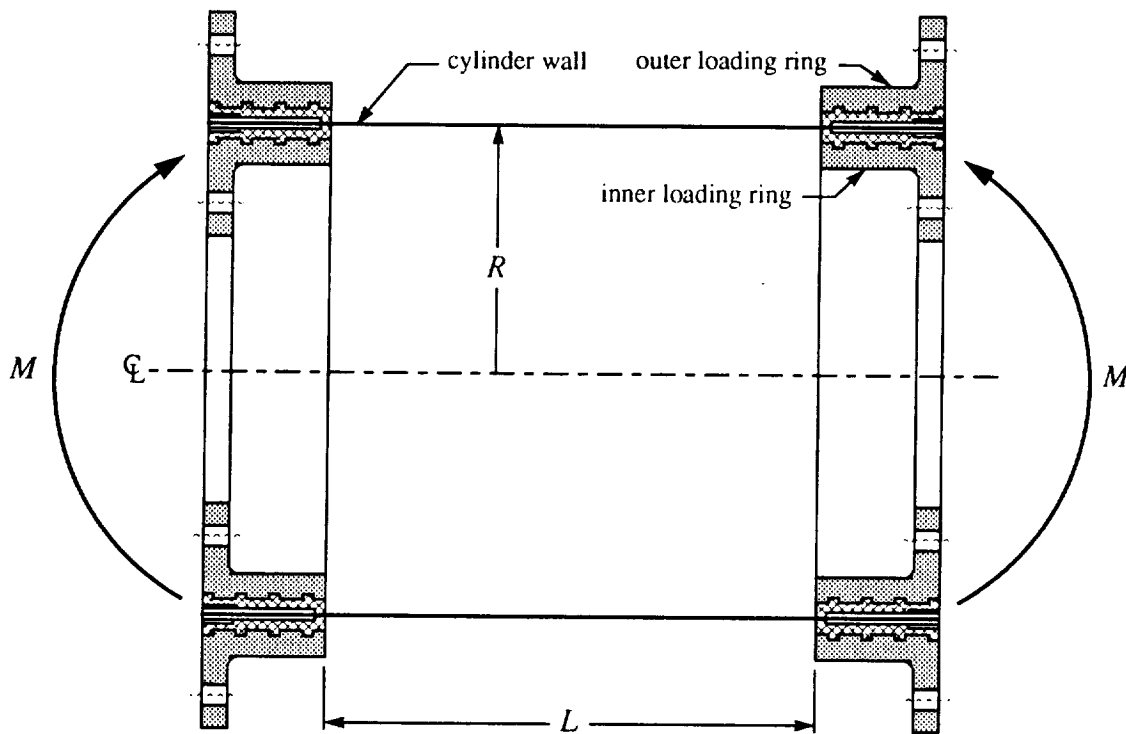
Fig. 3-1 Schematic of Test Specimen with Loading Rings

---

* Cerrobend® and Belmont Alloy 2505 were used and have a melting point of 158 °F. Tension and compression tests of three 0.45 in. x 2.0 in. x 7.0 in. bars yielded average values of approximately 1.55 Msi for Young's modulus, 0.36 Msi for the shear modulus, and 0.42 for Poisson's ratio.

cylinder from being pulled out in tension by providing a surface for potting compound to react against. This method has several advantages over direct mechanical attachment methods. Some of these are that (i) the gripping of the specimen is relatively uniform, (ii) additional precision machining of the specimen is not required, (iii) re-use of potting compound is possible, and (iv) ease of removal of the failed specimen by reheating the potting compound.

Schematic top and side views of the cylinder bending fixture are shown in Fig. 3-3 (a) and (b), respectively. The fixture is a symmetric design that applies bending equally at each end of the test specimen by a set of hydraulic jacks. The entire fixture is mounted to a slotted surface table to accommodate a wide range of specimen lengths. The loading rings are bolted to the back plates with the test specimen ends aligned with the pivot axis as shown in Fig. 3-3 (a). Load is transferred from the hydraulic jacks through the loading pins and loading grips into the moment arm and back plate assembly. The back plate assembly rotates about the pivot pins, inducing a state of pure bending in the test specimen. The top of the cylinder is in compression and the bottom is in tension as shown in Fig. 3-3 (b). The horizontal braces located between the supports are intended to inhibit relative axial motion

Fig. 3-2 Details of Loading Ring

(a) Top View

$$\Omega_1 \cong \frac{D_1 - D_2}{S}$$

$$\Omega_2 \cong \frac{D_3 - D_4}{S}$$

(b) Side View

Fig. 3-3 Cylinder Bending Fixture Schematic

61

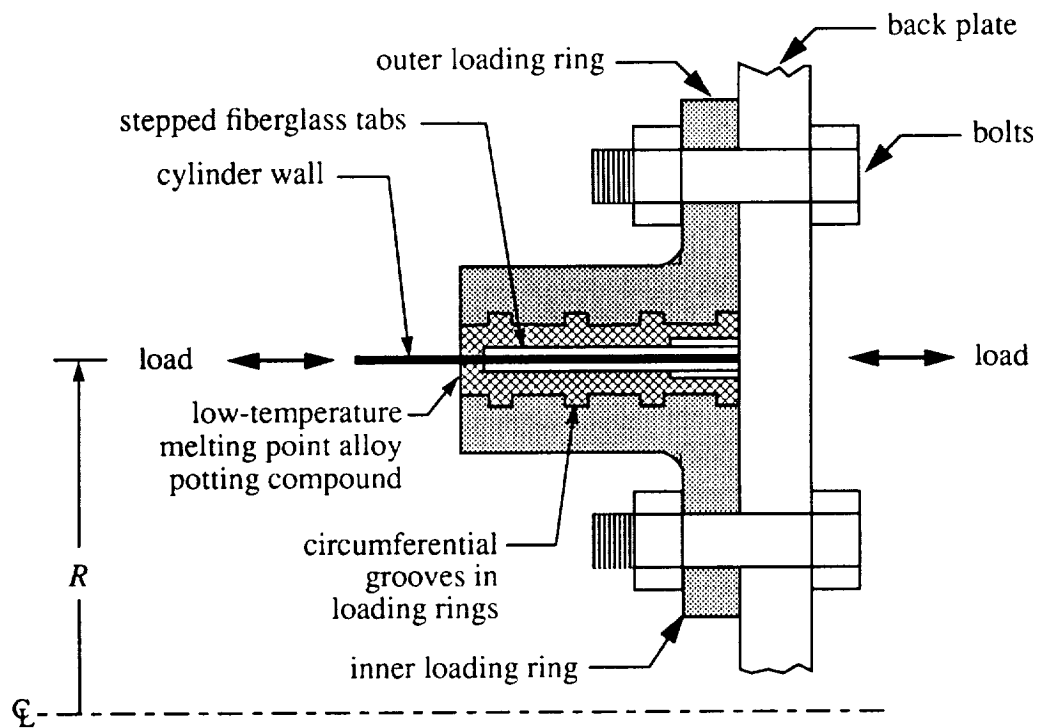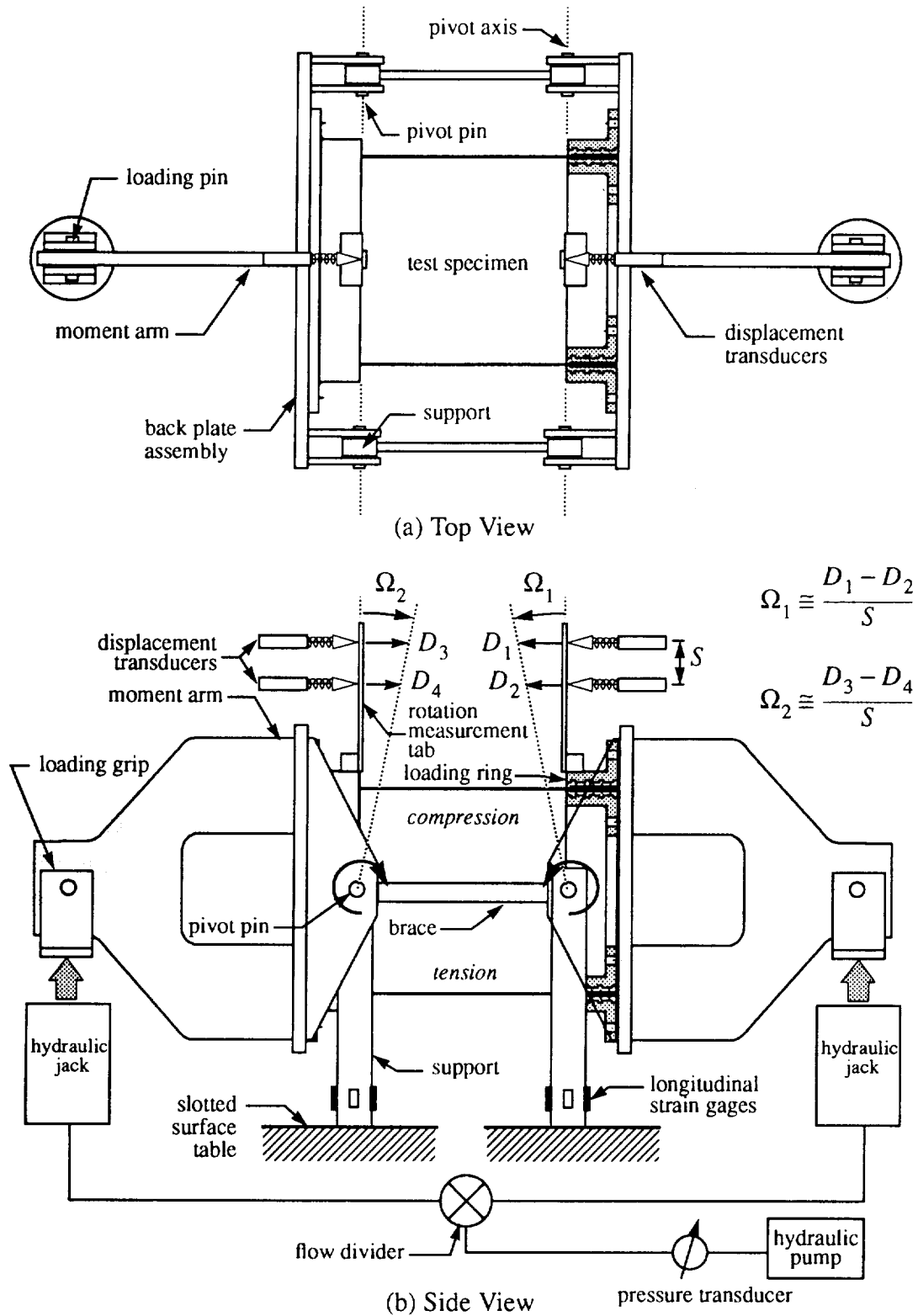between the ends of the cylinder. Pressure is supplied to the two hydraulic jacks by means of a hydraulic pump, and is monitored by a digital pressure transducer. Equal pressure is achieved in both jacks through the use of a flow divider[*]. The end-rotations, Ω_1 and Ω_2, are measured independently at each end of the specimen by tracking the motion of the cantilevered rotation measurement tabs with the displacement transducers D_1 through D_4, as shown in Fig. 3-3 (b). Tension and bending of the four fixture supports is monitored by the longitudinal strain gages mounted back-to-back near the base of each support as shown.

The primary fixture components were fabricated from A514-70 steel plate. Secondary components were fabricated from 1018 steel bar stock, C1144 steel, and A-36 steel plate. The loading rings were machined from 6061-T6 aluminum. The bending fixture and loading rings were fabricated under contract to LaRC by Advex Corp. of Hampton, Virginia.

3.2 Specimens

Six eight-ply graphite-epoxy specimens were fabricated and tested. A quasi-isotropic [∓45/0/90]$_S$ layup and two orthotropic layups, [∓45/0$_2$]$_S$ and [∓45/90$_2$]$_S$, were studied. The two orthotropic layups can be regarded as axially-stiff and hoop-stiff, respectively. The nominal radius of each specimen was 6 inches. Five specimens had a length-to-radius ratios of 2 and one specimen had a length-to-radius ratio of 5. The specifics of the specimen fabrication, properties, and surface shape measurements are provided in Appendix D, Appendix E, and Appendix F, respectively. The specimen identification codes, layups, and geometric parameters are summarized in Table 3-1.

All test specimens were fabricated from 12 in.-wide Hercules AS4/3502 graphite-epoxy prepreg tape, as described in Appendix D. The prepreg tape was layed-up on an aluminum mandrel by hand with the aid of a belt-winder. Curing took place in an autoclave using the manufacturer's recommended temperature, pressure, and vacuum cycles. The specimens were cut from four 48 in.-long cylinders (CYL-1, CYL-2, CYL-3, and CYL-4 in Table 3-1) that were fabricated by the Materials Processing and Development Section at LaRC. The specimen identification code numbers in Table 3-1 identify the 48 in.-long cylinder

---

[*] Fluid Controls, Inc., flow divider model 2V13-4-3-10-S.

Table 3-1 Summary of Test Specimen Dimensions

Specimen Identification Code	Wall Construction	L, in.	Average[a] R, in.	Average[b] H, in.	L/R	R/H
CYL-1A	$[\mp 45/0/90]_S$	12.0	5.993	0.0374	2.0	160.2
CYL-1B		12.0	5.996	0.0375	2.0	160.0
CYL-2		30.0	5.994	0.0368	5.0	162.9
CYL-3A	$[\mp 45/0_2]_S$	12.0	5.961	0.0381	2.0	157.5
CYL-4A	$[\mp 45/90_2]_S$	12.0	5.997	0.0369	2.0	162.5
CYL-4B		12.0	5.995	0.0358	2.0	167.5

a. Computed from surface shape measurements, see Appendix F.

b. Average of 48 measurements, see the section "Wall Thickness Measurement" in Appendix E.

and the axial location ('A' or 'B') from which each specimen was cut. The details of the wall thickness measurements, mechanical properties, and laminate stiffnesses of the test specimens are summarized in Appendix E.

A C-Scan of each of the four 48 in.-long cylinders was conducted to insure an initial defect-free condition. The number of originally proposed test specimens was reduced to a total of six specimens after a manufacturing defect was discovered in CYL-3 (see the section "Nondestructive Evaluation" in Appendix D). Fiberglass cloth tape was used to form the tabs on the specimen ends. The tabs were hand layed-up directly on the graphite-epoxy cylinders and cured at room temperature after cutting each cylinder to the approximate specimen length. The cylinder ends were then machined flat and parallel.

The specimens were instrumented after the fabrication procedure was completed. The interior of each specimen was gaged prior to mounting the loading rings as a matter of convenience. The details of the potting procedure are provided in the section "Specimen Potting" in Appendix D. After potting the specimens, the outer surface shape was accurately measured and analyzed according to the procedures discussed in Appendix F. With the loading rings mounted and the outer surface measured, the exterior surface was gaged.

Each specimen was carefully lifted into position in the bending fixture with the aid of an overhead crane. Forty-eight loading ring bolts on each end of the cylinder were incrementally tightened in a star-pattern to a final torque of 80 ft-lbs. The fixture was then bolted to

the slotted surface table in preparation for testing. The specimen was ready to be tested once the instrumentation and data acquisition setups were completed.

The tabbing and machining of the specimens, and mounting of the loading rings was performed under contract to LaRC by Advex Corp. of Hampton, Virginia. Surface measurements were preformed by the Quality Assurance and Inspection Office laboratory at LaRC. The strain gages were mounted by Modern Machine and Tool Co., Inc. of Newport News, Virginia, also under contract to LaRC.

3.3 Instrumentation and Data Acquisition

A typical test setup is illustrated in Fig. 3-4. An average of 167 channels of data were acquired electronically during each bending test. The data were acquired at the rate of approximately one reading of all channels per second. Surface strains were measured with pairs of back-to-back strain gages distributed over the surface of each specimen. Applied forces were measured with a calibrated load cell and displacements were measured with direct current differential transformers (DCDT's). All tests were video recorded and still photos were taken before and after loading. Acoustic emissions were recorded during the testing of the CYL-2, CYL-4A, and CYL-4B specimens. A shadow moiré interferometry setup was used during the testing of the CYL-1A specimen but was not used in subsequent tests. The surface of some specimens was painted white and marked with a grid pattern to improve visualization of the postbuckling deformation patterns. The instrumentation setup for each specimen is summarized in Table 3-2.

Selected radial displacement measurements were made during the testing of specimens CYL-1A and CYL-2. The displacements were measured at the locations specified in Table 3-3 and are shown schematically in Fig. 3-5. It should be noted that the displacement measurements are relative to the surface table and therefore include net vertical deflections of the test fixture.

Back-to-back surface strains were measured at over 60 locations in each cylinder. A typical strain gage pattern is shown in Fig. 3-6. Similar gage patterns were used for all specimens with the exception of CYL-1A. The gage pattern for CYL-1A was symmetric about
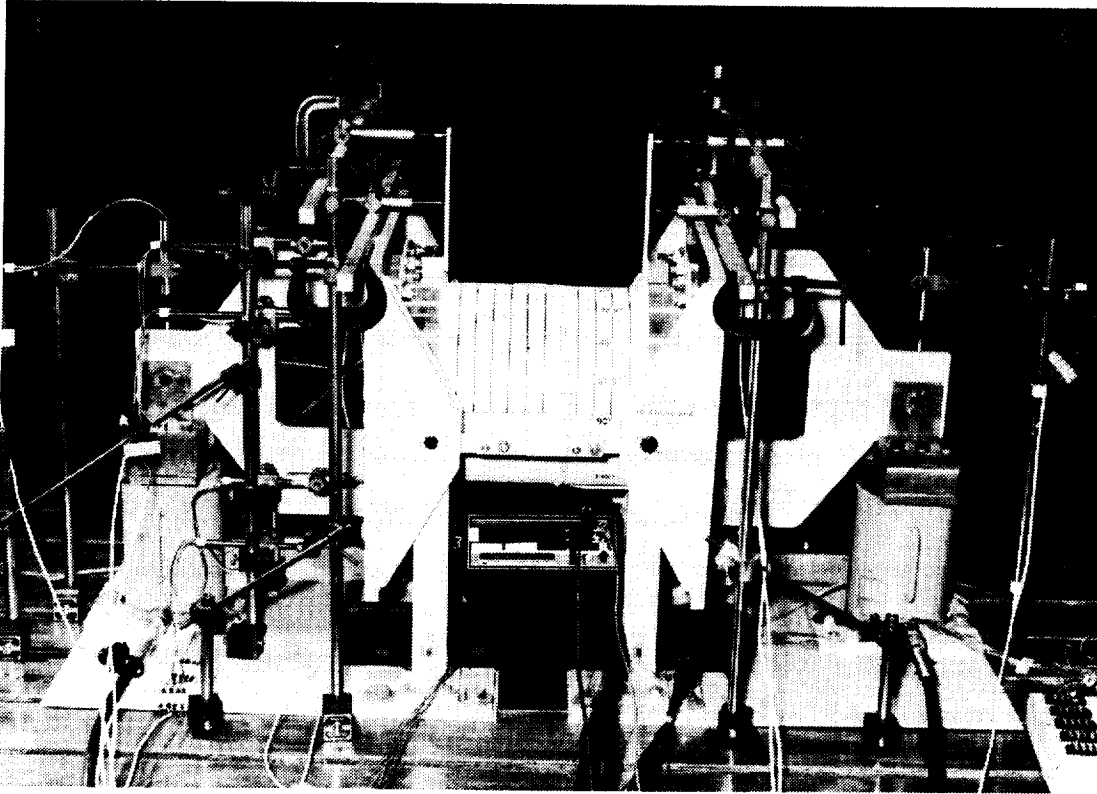
Fig. 3-4 Typical Test Setup

Table 3-2 Instrumentation Summary

Specimen Identification Code	Total No. of Data Channels	No. of Strain Gage Channels	DCDT's[a]	Acoustic Emissions	Shadow Moiré	Specimen Surface
CYL-1A	172	136	6	no	yes	partially[b] white
CYL-1B	155	124	0	no	no	white
CYL-2	169	136	2	yes	no	white w/grid
CYL-3A	159	128	0	no	no	white
CYL-4A	167	136	0	yes	no	white w/grid
CYL-4B	167	136	0	yes	no	white w/grid

a. For measurement of selected radial displacements.

b. Only region under moiré grating was painted white.

Table 3-3 Radial Displacement Measurement Locations

DCDT	d_1	d_2	d_3	d_4	d_5	d_6
Location, x/L, θ	-0.4, 0°	-0.3, 0°	-0.167, 0°	0.0, 0°	0.0, 180°	-0.3, 180°
CYL-1A	yes	yes	yes	yes	yes	yes
CYL-2	no	no	no	yes	yes	no

x/L = 0.0 but had approximately the same number of gages as the pattern shown in Fig. 3-6. It can be seen from strain gage pattern that a majority of the gages were oriented axially with the circumferential locations of 0° and 180° being instrumented most heavily.

The applied bending moment was computed from the average load in the hydraulic jacks, which was measured with the digital pressure transducer, multiplied by the length of the moment arm. The average end-rotation was computed from the rotation measurement tabs shown in Fig. 3-3 (b) from the simple relation

$$\Omega = \frac{\Omega_1 + \Omega_2}{2} .$$

(3.1)
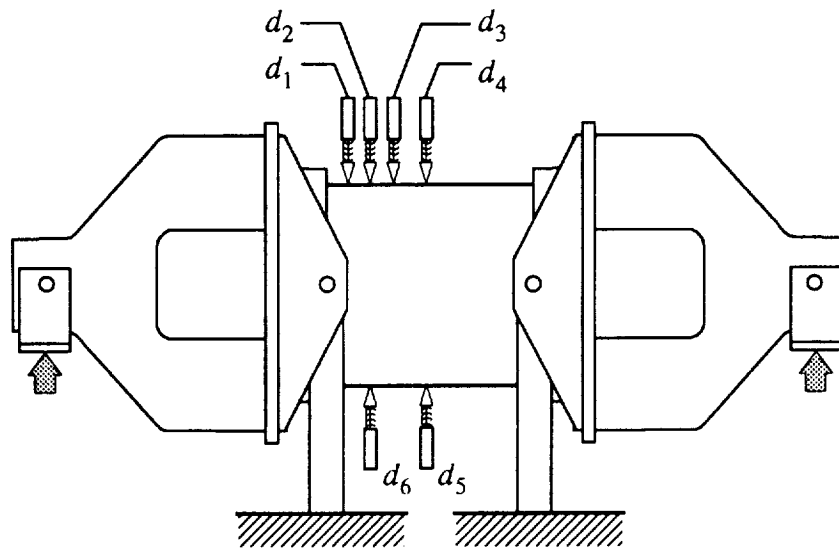
Fig. 3-5 Radial Displacement Measurement

It was found, however, that this measure of end-rotation was sensitive to minor distortions of the loading rings and test fixture and was therefore not always accurate.

Improved end-rotation measurement accuracy was achieved by measuring the end-rotation directly from the strain gages on the specimen. Average end-rotations were computed from a least-squares analysis of the normalized axial midsurface prebuckling strains, $\varepsilon_x^o / \varepsilon_{cr}$, plotted as a function of the normalized distance to the cylinder neutral axis, Z/R. The form of this relation is

$$Z/R = s \cdot \varepsilon_x^o / \varepsilon_{cr},$$ (3.2)

where s is the slope of the best-fit line computed from the least-squares analysis, computed at a given applied bending moment, M. A typical plot of this relation is shown in Fig. 3-7. This figure indicates the maximum axial midsurface compressive strain, given by the expression $\varepsilon_{max}^o = \varepsilon_{cr}/s$, occurs at the location $Z/R = 1$. The end-rotation applied to the specimen was then computed from ε_{max}^o and Eq. (2.42) as

$$\Omega = \frac{1}{2}\frac{L}{R} \cdot \varepsilon_{max}^o .$$ (3.3)

The least-squares analyses were carried out at a number of axial locations and averaged to obtain the overall applied end-rotation. Traces of the entire moment vs. end-rotation
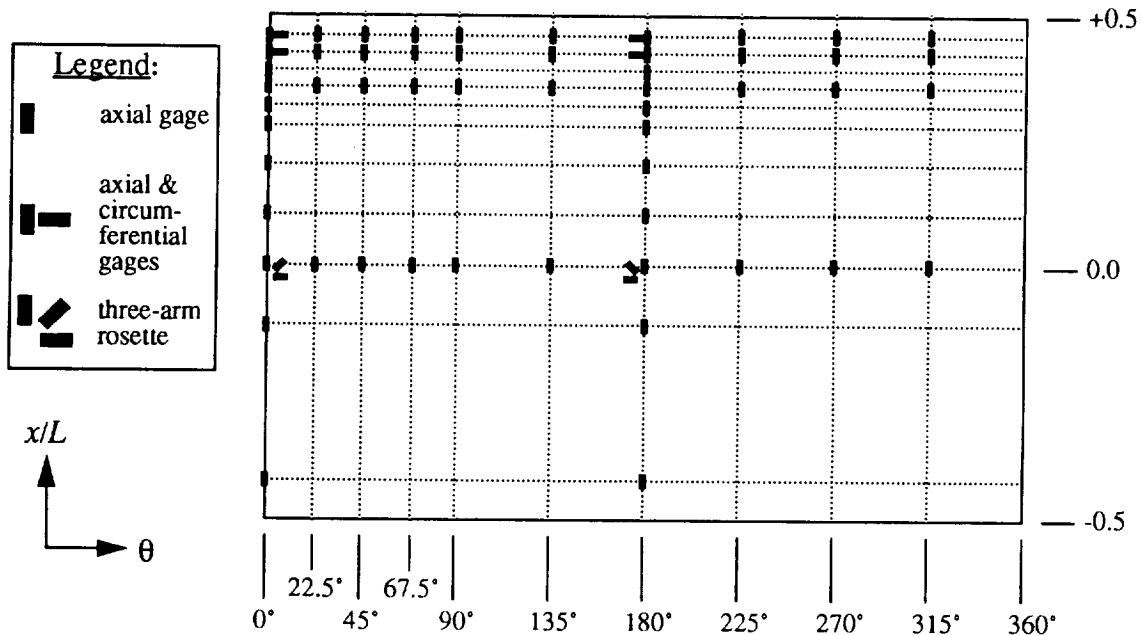
Fig. 3-6 Typical Strain Gage Pattern

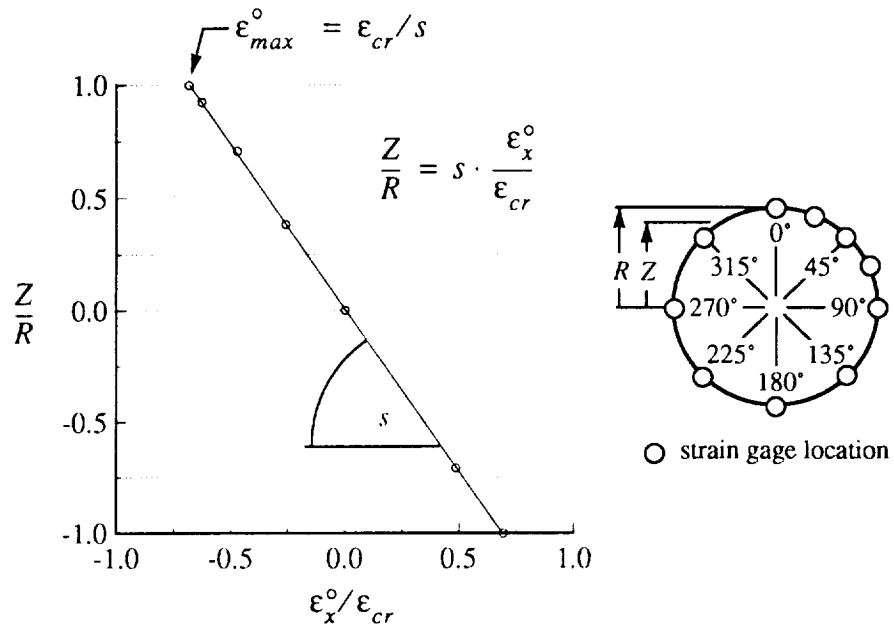relation were obtained by repeating the above calculations for each increment in applied moment. This method was found to provide an excellent measure of the applied end-rotation.

Fig. 3-7 Prebuckling Rotation Measurement

It should be noted that Eq. (3.3) could only be used to compute the prebuckling end-rotations since the strain relation shown in Fig. 3-7 was no longer linear after buckling. To obtain the moment vs. end-rotation relation beyond buckling, the end-rotation given by Eq. (3.1) was modified to compensate for any slight deformations of the loading rings encountered during prebuckling. The modification was achieved by scaling Eq. (3.1) to coincide with the prebuckling end-rotation computed from Eq. (3.3). An appropriate scale factor, sf, was computed from the ratio of the slope of the measured moment vs. end-rotation relation, using Eq. (3.3), to the slope of the measured moment vs. end-rotation relation, using Eq. (3.1). The slopes of these moment vs. end-rotation relations were determined by a separate least-squares procedure. The resulting end-rotation, which was used to compute the end-rotation over the entire range of loading, is given by the relation

$$\Omega = sf \cdot \frac{\Omega_1 + \Omega_2}{2}.$$ (3.4)

68

3.4 Procedure

The cylinder bending tests were conducted in the Aircraft Structures laboratory at LaRC. Quasi-static loading was achieved by manual adjustment of the flow rate of the hydraulic pump. Loading was increased until buckling of the specimen occurred. The load was held constant after buckling to observe the condition of the test specimen and to mark the deformation pattern. Seemingly undamaged specimens were unloaded, re-buckled, and loaded until failure. Specimens with prebuckling matrix cracking were buckled and loaded until ultimate failure occurred. The deformation patterns were marked on all cylinders with the exception of the first cylinder tested, specimen CYL-1A.

4. Results

The measured, observed, and predicted results of the individual specimens are presented according to the three major response categories of prebuckling, buckling, and postbuckling. The measured specimen moment vs. end-rotation relations are presented first as a guide to the overall observed bending behavior.

The prebuckling results are presented in the form of displacement and axial strain responses. Analytical prebuckling solutions were computed using the nonlinear Donnell analysis for the perfect cylinder geometries and using the STAGS analysis for the imperfect cylinder geometries, as described in sections 2.1 and 2.2.3, respectively. Experimental displacements and strains were measured using the methods described in section 3.3.

The measured buckling moments, end-rotations, and strains are compared to the predicted values. The predicted buckling values and buckling shapes were computed with the STAGS finite element program for perfect and imperfect cylinder geometries, as discussed in section 2.2.3. The measured shape imperfections, described in Appendix F, were included in the analysis of the imperfect cylinder geometries.

The observed postbuckling deflection patterns and strain profiles are presented and compared to predictions. The predicted postbuckling responses were computed using the STAGS program and the measured shape imperfections.

The classical buckling parameters are used to normalize the bending moment, end-rotation, and strain results. These parameters were computed for each specimen from Eqs. (2.40), (2.41), and (2.42) using the geometry and stiffness parameters presented in Table 3-1 and Appendix E. The individual buckling parameters are summarized in Table 4-1.

70

Table 4-1 Classical Buckling Parameters for Test Specimens

Specimen Identification Code	Wall Construction	L/R	M_{cr}, in.-lbs	Ω_{cr}, radians (deg)	ε_{cr}, $\mu\varepsilon$
CYL-1A	$[\mp 45/0/90]_S$	2	139,550	0.0036 (0.207)	3,610
CYL-1B		2	139,998	0.0036 (0.207)	3,617
CYL-2		5	139,550	0.0090 (0.518)	3,610
CYL-3A	$[\mp 45/0_2]_S$	2	95,809	0.0017 (0.098)	1,697
CYL-4A	$[\mp 45/90_2]_S$	2	144,378	0.0084 (0.484)	8,383
CYL-4B		2	140,298	0.0081 (0.465)	8,114

4.1 Measured Specimen Moment vs. End-Rotation Relations

As a view of the overall behavior, the measured moment vs. end-rotation responses are compared for four representative specimens in Fig. 4-1. The bending moments and end-rotations in this figure have been normalized by the classical buckling moment and end-rotation of the quasi-isotropic specimen CYL-1A (see Table 4-1). The moment and rotation normalization factors are denoted as M_{cr}^{quasi} and Ω_{cr}^{quasi}, respectively. The segments of the moment vs. end-rotation relation corresponding to the prebuckling, buckling, and postbuckling responses are identified in the figure.

The prebuckling moment vs. end-rotation relations shown in Fig. 4-1 are linear up to the buckling point for each specimen. The prebuckling slopes of each specimen, and hence, the bending stiffnesses, vary according to the individual laminate inplane stiffnesses, E_x (see Appendix E). The ratio of the bending stiffness of the $[\mp 45/0_2]_S$ specimen and the $[\mp 45/90_2]_S$ specimens to the bending stiffness of the quasi-isotropic specimen is 1.45 and 0.45, respectively.

The value of end-rotation at the bifurcation points are denoted as Ω_{cr}^{exp} in Fig. 4-1. The corresponding buckling moment and compressive buckling strain values are M_{cr}^{exp} and ε_{cr}^{exp}, respectively. These values were measured at an instant prior to buckling by the methods described in section 3.3 and are reported in Table 4-2 for all specimens.

The buckling events were indicated by a distinct 'popping' sound and the appearance of large diamond-shaped buckles on the compression side of the cylinder. The moment vs.
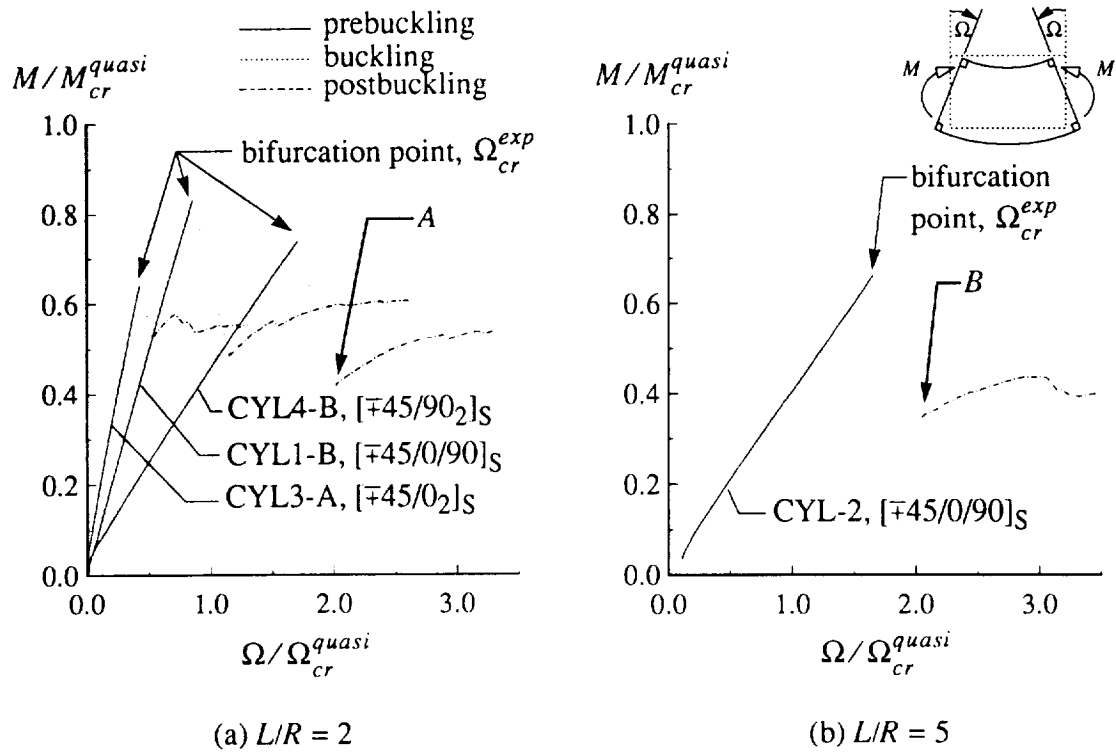
71

Fig. 4-1 Normalized Measured Moment vs. End-Rotation Comparison

end-rotation relation corresponding to the buckling events exhibits a substantial decrease in the bending moment and an increase in the end-rotation. This sudden increase in end-rotation is attributed, in part, to the flexibility of the test fixture (see section 2.3.2). However, the sudden increase in end-rotation is also due to the inability to maintain complete control of the hydraulic jacks when the cylinder suddenly changes configurations at buckling.

The postbuckling loading paths reflect a significant reduction in bending stiffness due to the effect of the large diamond-shaped buckles on the cylinder cross-section moment of inertia. Further loading in the postbuckling range was accompanied by pronounced definition of the buckles and subsequent visible and audible material damage. Changes in the postbuckling deflection shapes, referred to here as secondary postbuckling shapes, were visible in some instances and were accompanied by an additional 'popping' sound. A secondary postbuckling shape was observed before the ultimate failure of the $[\mp 45/0_2]_S$ specimen. The deflection patterns corresponding to the points labeled A and B on the postbuckling equilibrium paths in Fig. 4-1 will be described in section 4.4.1.

Table 4-2 Measured Buckling Parameters for Test Specimens

| Specimen Identification Code	Wall Construction	L/R	M_{cr}^{exp}, in.-lbs	Ω_{cr}^{exp}, radians (deg)	ε_{cr}^{exp}, $\mu\varepsilon$
CYL-1A	[∓45/0/90]$_S$	2	110,660	0.0030 (0.172)	3,000
CYL-1B		2	119,280	0.0032 (0.183)	3,170
Average for [∓45/0/90]$_S$, L/R = 2			114,970	0.0031 (0.178)	3,085
CYL-2	[∓45/0/90]$_S$	5	100,620	0.0065 (0.372)	2,610
CYL-3A	[∓45/0$_2$]$_S$	2	89,390	0.0016 (0.092)	1,550
CYL-4A	[∓45/90$_2$]$_S$	2	99,040	0.0060 (0.344)	6,040
CYL-4B		2	102,980	0.0063 (0.361)	6,290
Average for [∓45/90$_2$]$_S$, L/R = 2			101,010	0.0062 (0.353)	6,165

The individual measured specimen moment vs. end-rotation relations are summarized in Figs. 4-2 (a) through (f). The moment and end-rotation values in these figures are normalized with respect to the appropriate classical buckling moment and end-rotation values given in Table 4-1. The number of times each cylinder was loaded to buckling and beyond is indicated in the appropriate figure. Figs. 4-2 (a) through (c) show that the [∓45/0/90]$_S$ specimens CYL-1A, CYL-1B, and CYL-2 were loaded until buckling occurred, unloaded, and then re-loaded until failure. Specimen CYL-1B was buckled three times. Fig. 4-2 (d) indicates that the [∓45/0$_2$]$_S$ specimen CYL-3A was buckled, loaded until visible material damage occurred, unloaded, and finally re-loaded to assess the bucking resistance in the presence of material damage. Figs. 4-2 (e) through (f) indicate that the [∓45/90$_2$]$_S$ specimens CYL-4A and CYL-4B were buckled once and loaded to failure.

Specimens that were unloaded just after buckling the first time, snapped back into their initial circular shape without visual evidence of material damage. The postbuckling deflection patterns were repeated upon re-buckling, the buckling moment being somewhat lower than with the first buckling test. All cylinders fully recovered their initial circular shape, regardless of any material damage, upon unloading after ultimate failure occurred.

The predicted moment vs. end-rotation relations will be discussed in section 4.4.
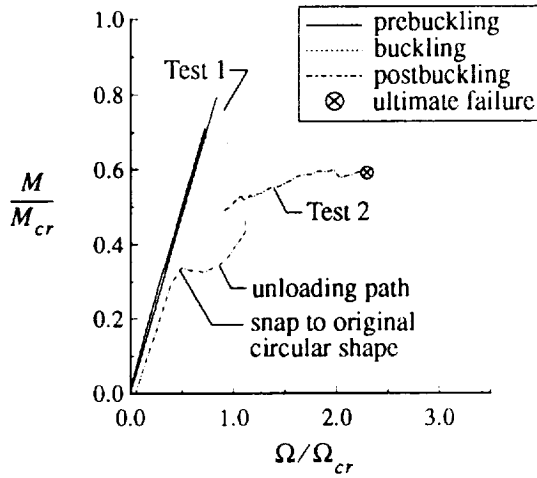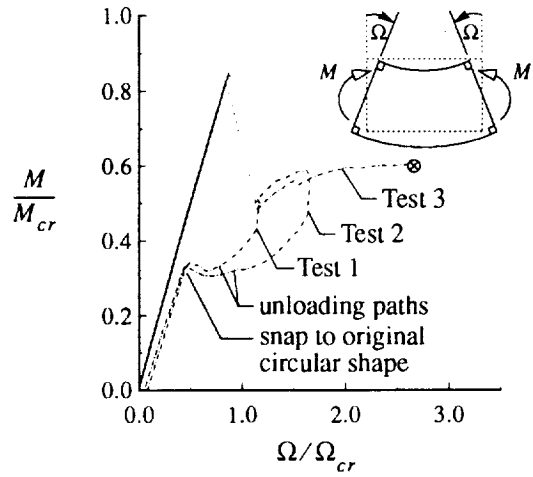
(a) CYL1-A, [∓45/0/90]$_S$, L/R = 2

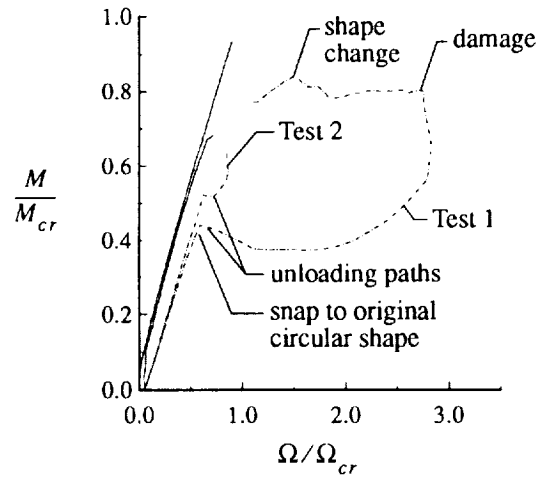(b) CYL1-B, [∓45/0/90]$_S$, L/R = 2
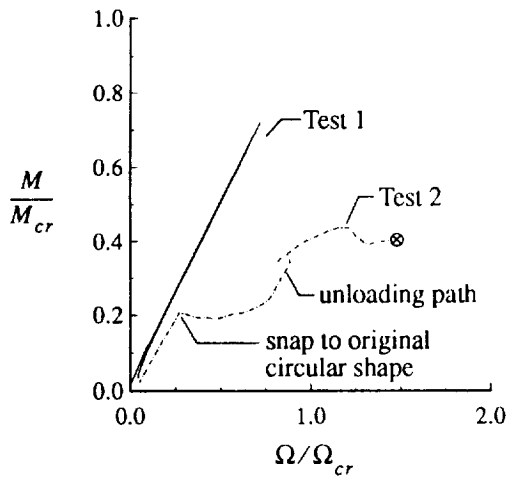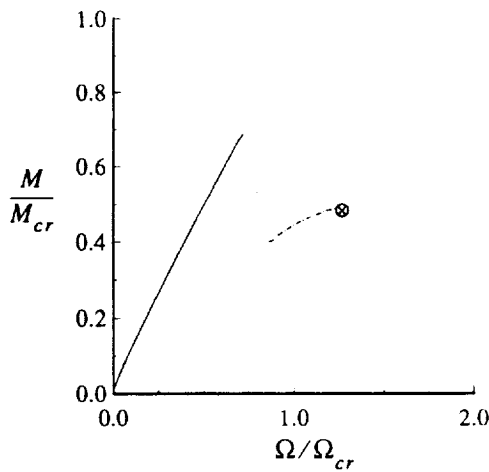
(c) CYL-2, [∓45/0/90]$_S$, L/R = 5

(d) CYL3-A, [∓45/0$_2$]$_S$, L/R = 2

(e) CYL4-A, [∓45/90$_2$]$_S$, L/R = 2
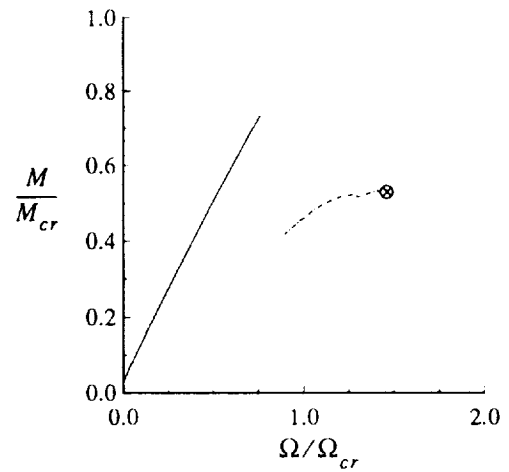
(f) CYL4-B, [∓45/90$_2$]$_S$, L/R = 2

Fig. 4-2 Summary of Experimental Moment vs. End-Rotation Relations

74

4.2 Prebuckling Responses

The prebuckling results are presented for two values of end-rotation corresponding to 45% and 90% of the experimental buckling end-rotation reported in Table 4-2, i.e. Ω/Ω_{cr}^{exp} = 0.45 and 0.90. Measured values, where available, are compared to analytical predictions based on the perfect and the imperfect cylinder geometries.

4.2.1 Displacement Responses

Prebuckling displacement profiles are illustrated in Fig. 4-3 for the $[\mp45/0/90]_S$ specimen CYL-1A. The radial displacements at $\theta = 0°$ and $180°$ are shown in Figs. 4-3 (a) and (b), and the tangential displacements at $\theta = 90°$ are shown in Fig. 4-3 (c). The displacements are denoted as w_0, w_{180}, and v_{90}, respectively, and are normalized with respect to the cylinder wall thickness, H, as in previous discussions in section 2.1.2.

A comparison between the displacement responses of the perfect and imperfect cylinders in Fig. 4-3 indicates that of the displacements shown, the measured shape imperfections have the largest influence on w_0. The presence of imperfections tends to perturb the responses of the perfect cylinder at several axial locations, particularly at the higher value of end-rotation, Ω/Ω_{cr}^{exp} = 0.90. The w_{180} displacements are only slightly influenced by the imperfections and the v_{90} displacements remain unaffected.

The measured radial displacements are compared to the predicted profiles for w_0 and w_{180} in Figs. 4-3 (a) and (b). The measured displacements were adjusted to compensate for vertical deflections of the test fixture. The adjustments were achieved by adding an appropriate constant to each of the measured displacement profiles. Each constant was computed from the difference between the measured and predicted displacement value at the center of the perfect cylinder, at the given value of end-rotation.

Overall, the measured displacements in Figs. 4-3 (a) and (b) are in good agreement with the predicted displacement profiles, particularly at the lower value of end-rotation, Ω/Ω_{cr}^{exp} = 0.45. The measured w_0 displacements tend to agree more closely with the predicted displacements for the imperfect cylinder, especially near the end of the cylinder. The largest discrepancies between the measured and predicted profiles occur at the axial location $x/L = -0.3$ on the compression side of the specimen, at the value of end-rotation of Ω/Ω_{cr}^{exp} = 0.90.

The predicted displacement responses for the remaining five specimens are presented in Figs. 4-4 through 4-8. The displacement profiles were not measured for these specimens. The predicted deflection shapes for the perfect specimens are similar to those of the idealized cylinders discussed in section 2.1.2. As with specimen CYL-1A, the w_0 displacements are most sensitive to the measured shape imperfections. The degree to which the w_0 displacements are affected by the imperfections depends on the shape characteristics of the particular measured shape imperfection. This is demonstrated by comparing the w_0 dis-
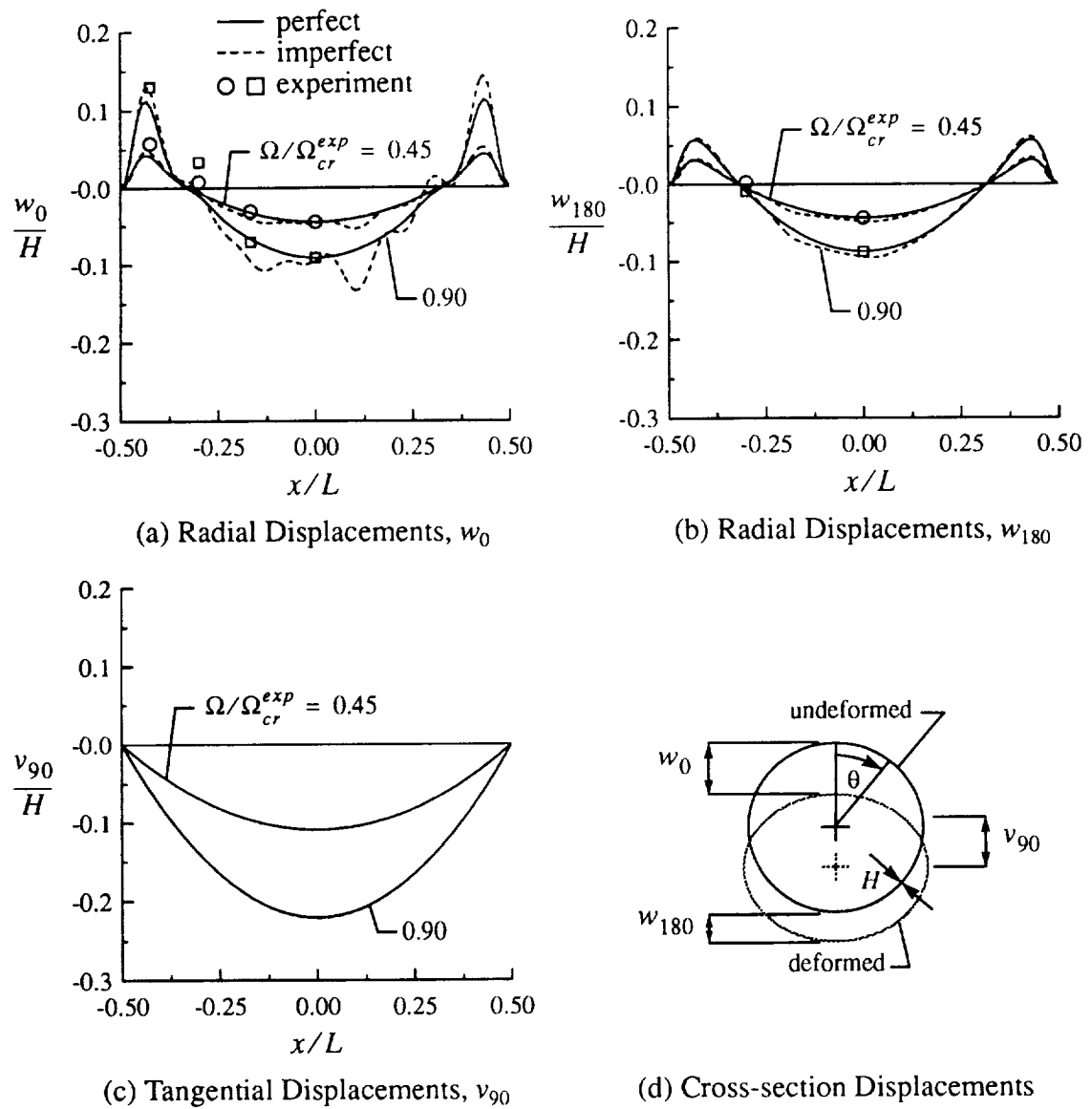

(a) Radial Displacements, w_0

(b) Radial Displacements, w_{180}

(c) Tangential Displacements, v_{90}

(d) Cross-section Displacements

Fig. 4-3 Displacement Response, CYL-1A, $[\mp 45/0/90]_S$, $L/R = 2$

76

placements for the $[\mp45/90_2]_S$ specimens CYL-4A and CYL-4B. Fig. 4-7 (a) indicates that the w_0 displacements for specimen CYL-4A are moderately affected by the imperfection. Fig. 4-8 (a) demonstrates that specimen CYL-4B is considerably affected by the shape imperfection, in comparison to specimen CYL-4A, particularly at the higher value of end-rotation. Similar behavior is observed with the $[\mp45/0/90]_S$ specimens CYL-1A and CYL-1B. As before, the w_{180} displacements are slightly influenced by the presence of the shape imperfections and the v_{90} displacements are unaffected.
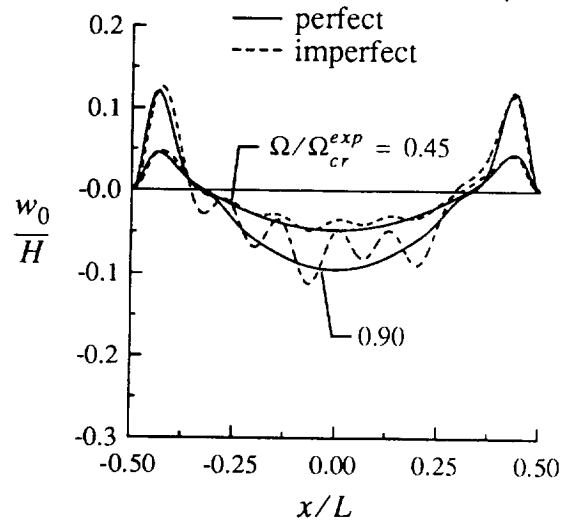
(a) Radial Displacements, w_0
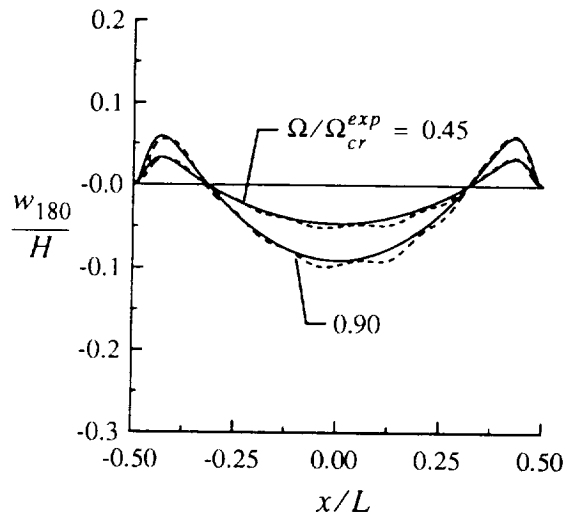
(b) Radial Displacements, w_{180}
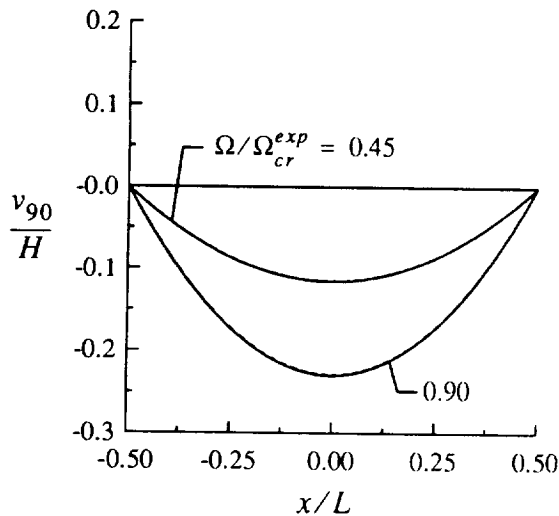
(c) Tangential Displacements, v_{90}
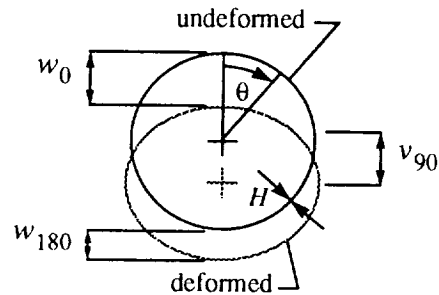
(d) Cross-section Displacements

Fig. 4-4 Displacement Response, CYL-1B, $[\mp45/0/90]_S$, $L/R = 2$

(a) Radial Displacements, w_0

(b) Radial Displacements, w_{180}

(c) Tangential Displacements, v_{90}

(d) Cross-section Displacements
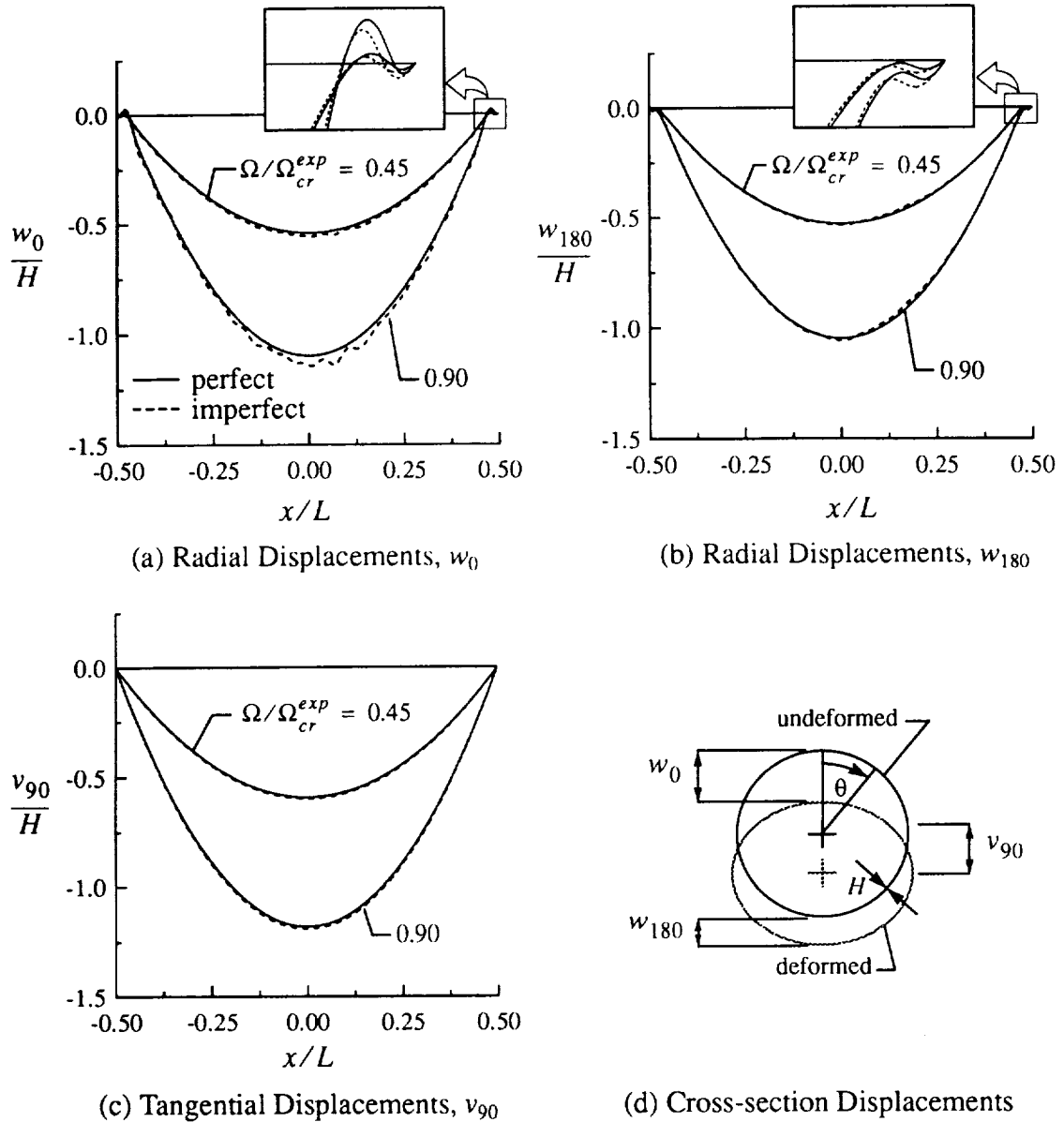
Fig. 4-5 Displacement Response, CYL-2, $[\mp 45/0/90]_S$, $L/R = 5$

4.2.2 Strain Responses

Measured and predicted axial surface strain profiles are illustrated for each test specimen in Figs. 4-9 through 4-14. The strains are normalized with respect to the appropriate classical axial buckling strain, ε_{cr} in Table 4-1, and are plotted as a function of the normalized axial coordinate, x/L, for one half of each cylinder. The strains are presented for the cir-

78

C1-2

cumferential locations $\theta = 0°$, $45°$, $67.5°$, $90°$, $135°$, and $180°$[*]. The thickness locations in these figures correspond to the outer surface, midsurface, and inner surface of the cylinder wall, i.e. $z/H = +0.5$, 0.0, and -0.5. The midsurface strains are the average of the outer and inner surface strains.


(a) Radial Displacements, w_0
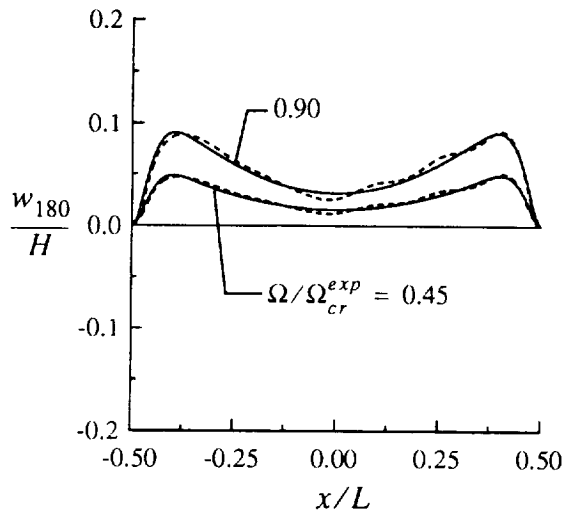
(b) Radial Displacements, w_{180}
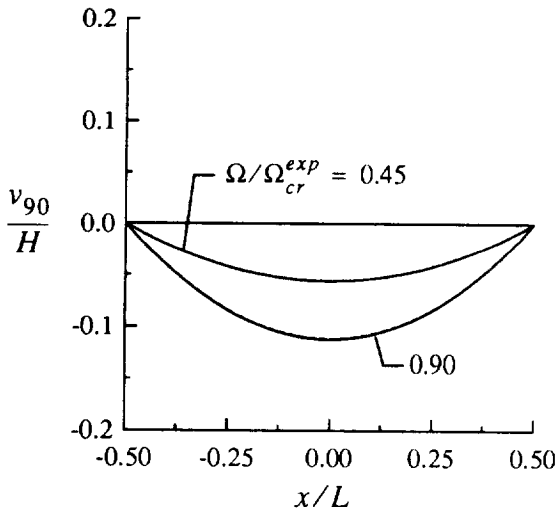
(c) Tangential Displacements, v_{90}
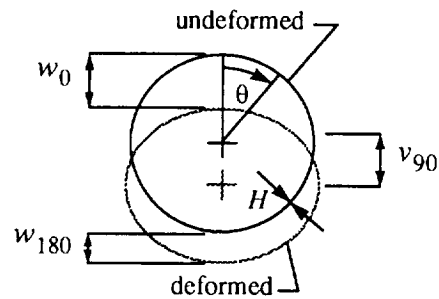
(d) Cross-section Displacements

Fig. 4-6 Displacement Response, CYL-3A, $[\mp45/0_2]_S$, $L/R = 2$

---

[*] The strains computed from the finite element analysis were obtained at the element centroids. The element centroids were located $1.875°$ from the circumferential locations of the measured data and the Donnell analysis, resulting in a slight shift in the results at some circumferential locations.

The boundary layer behavior discussed previously in section 2.1.2 is clearly evident in these figures. The shape and strength of the strain profile in the boundary layer region is determined by the magnitude of the applied end-rotation and the circumferential location. 'The boundary layer region is most pronounced at the locations of maximum compressive and tensile strains, $\theta = 0°$ and $180°$, respectively.

As with the displacement responses, comparing the perfect cylinder responses to the imperfect cylinder responses demonstrates that the measured shape imperfections exert the

(a) Radial Displacements, w_0

(b) Radial Displacements, w_{180}

(c) Tangential Displacements, v_{90}

(d) Cross-section Displacements

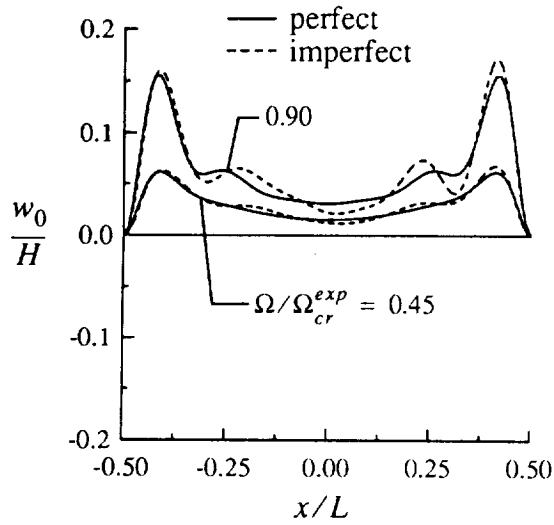Fig. 4-7 Displacement Response, CYL-4A, $[\mp 45/90_2]_S$, $L/R = 2$

greatest influence on the strains on the compressive side of the cylinders at the larger of the two values of end-rotation. The influence of the imperfections is diminished as the tensile side of the cylinder is approached in the circumferential direction. For all cylinders, the strain data reflect the predicted geometrically nonlinear strain boundary layer behavior and show good overall agreement with the predicted responses. The measured strains compare more favorably to the imperfect cylinder predictions than the perfect cylinder predictions on the compressive side of the cylinders. The measured and predicted responses are in excellent agreement when $\Omega/\Omega_{cr}^{exp} = 0.45$. Some discrepancies are evident when Ω/Ω_{cr}^{exp}


(a) Radial Displacements, w_0

(b) Radial Displacements, w_{180}

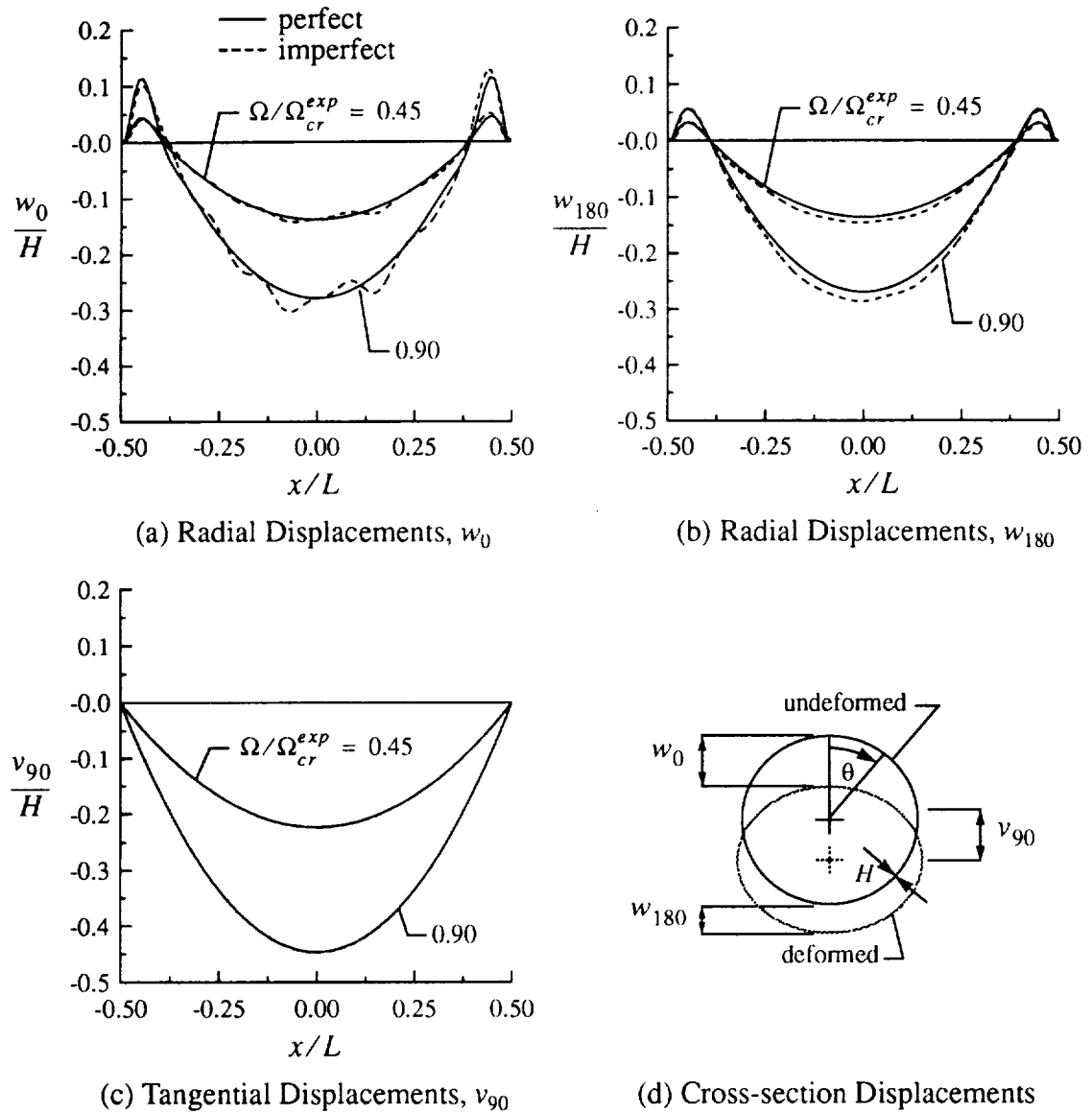(c) Tangential Displacements, v_{90}

(d) Cross-section Displacements
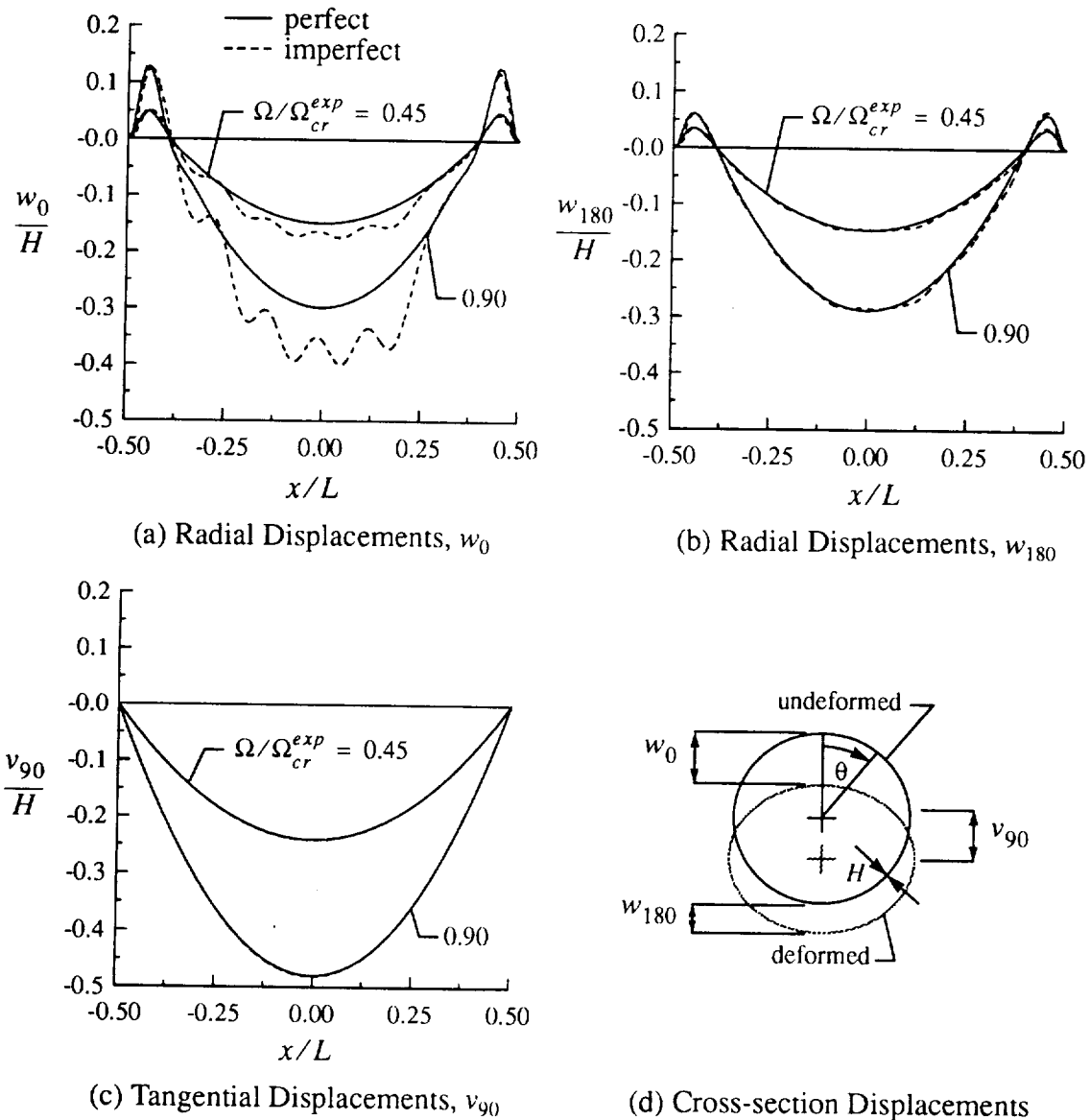
Fig. 4-8 Displacement Response, CYL-4B, $[\mp45/90_2]_S$, $L/R = 2$
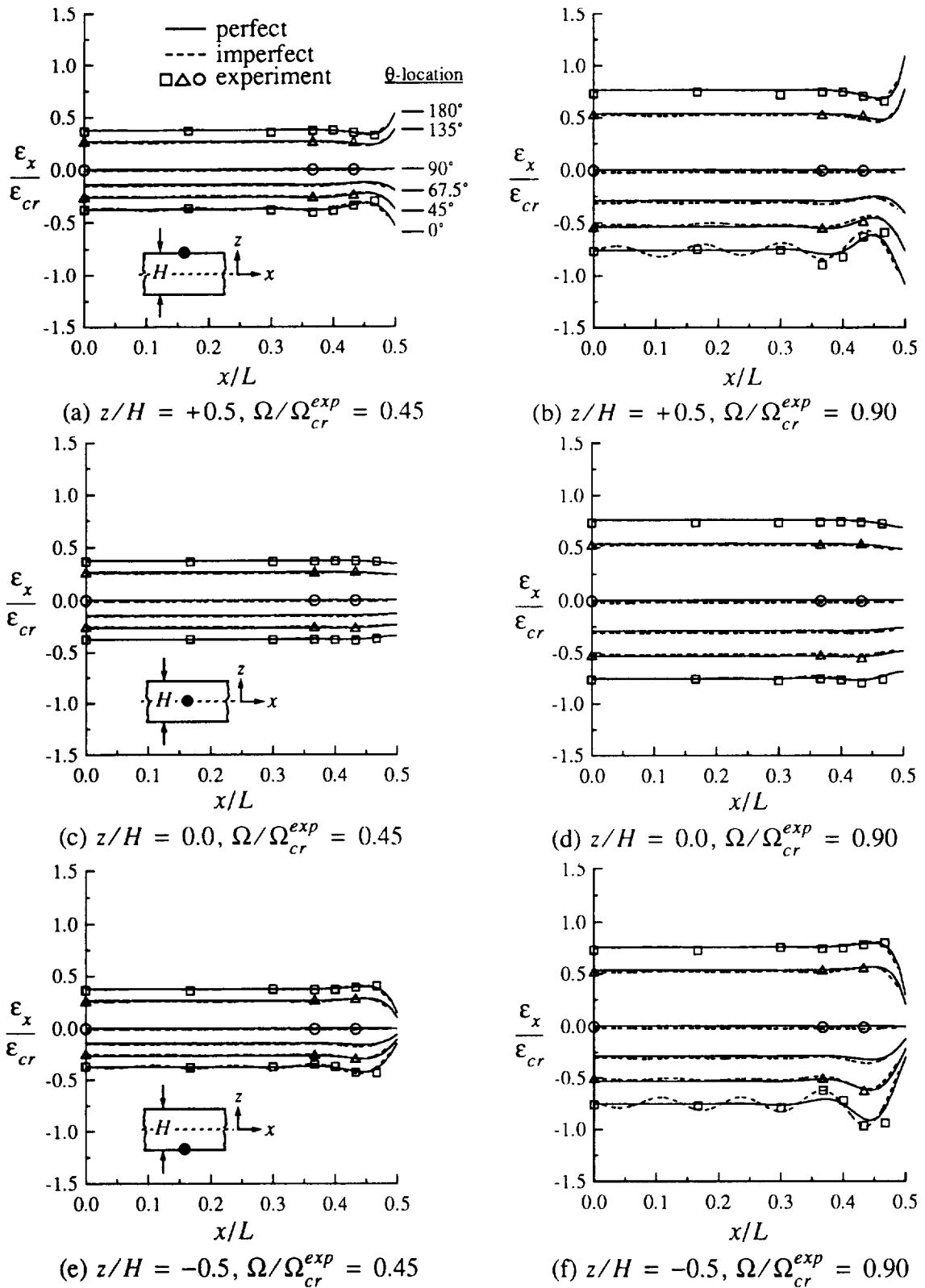
Fig. 4-9 Axial Strain Response CYL-1A, [∓45/0/90]$_S$, $L/R = 2$
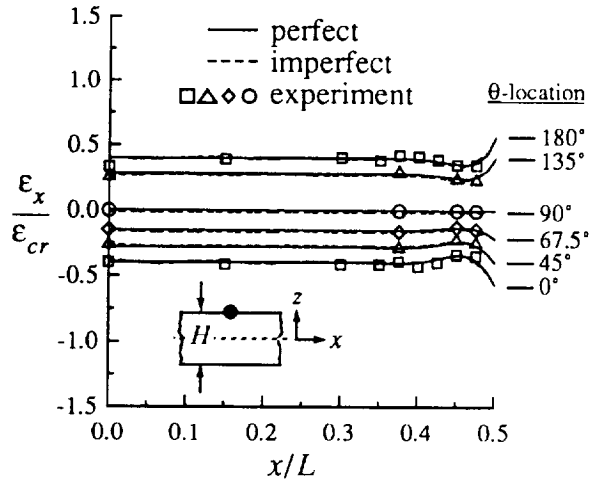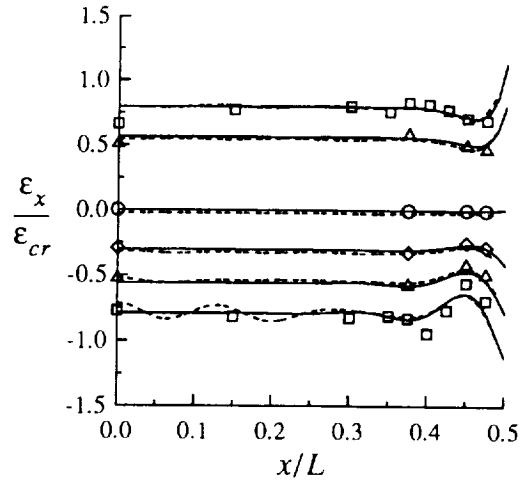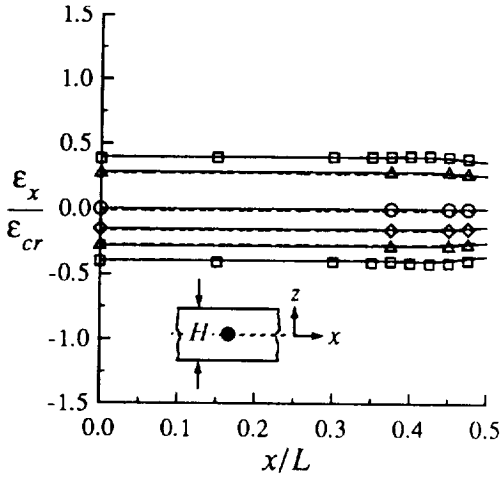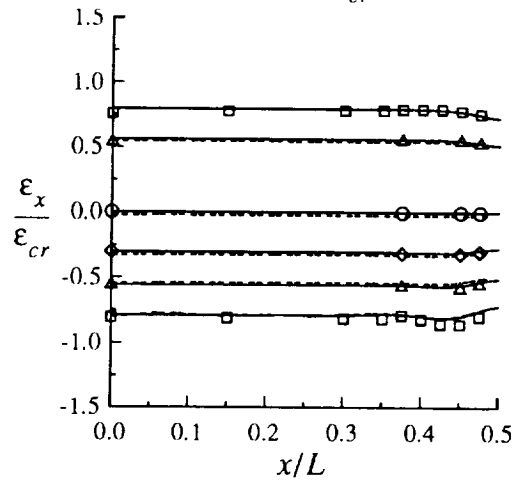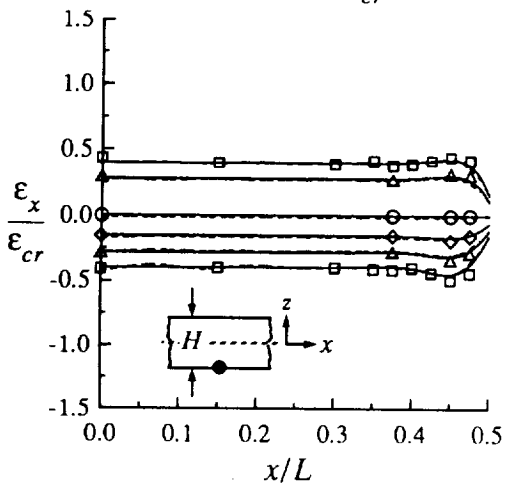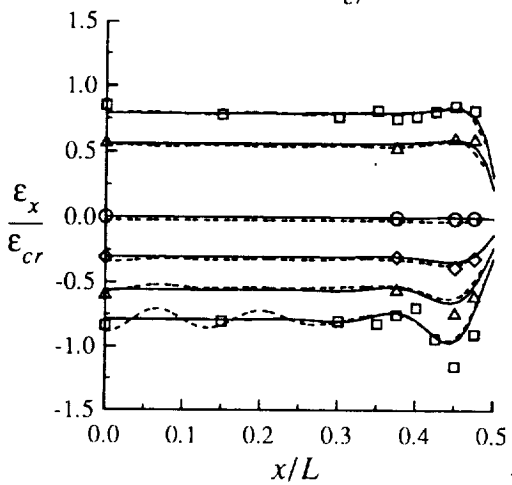
Fig. 4-10 Axial Strain Response, CYL-1B, [∓45/0/90]$_S$, $L/R = 2$

(a) $z/H = +0.5$, $\Omega/\Omega_{cr}^{exp} = 0.45$

(b) $z/H = +0.5$, $\Omega/\Omega_{cr}^{exp} = 0.90$

(c) $z/H = 0.0$, $\Omega/\Omega_{cr}^{exp} = 0.45$

(d) $z/H = 0.0$, $\Omega/\Omega_{cr}^{exp} = 0.90$

(e) $z/H = -0.5$, $\Omega/\Omega_{cr}^{exp} = 0.45$
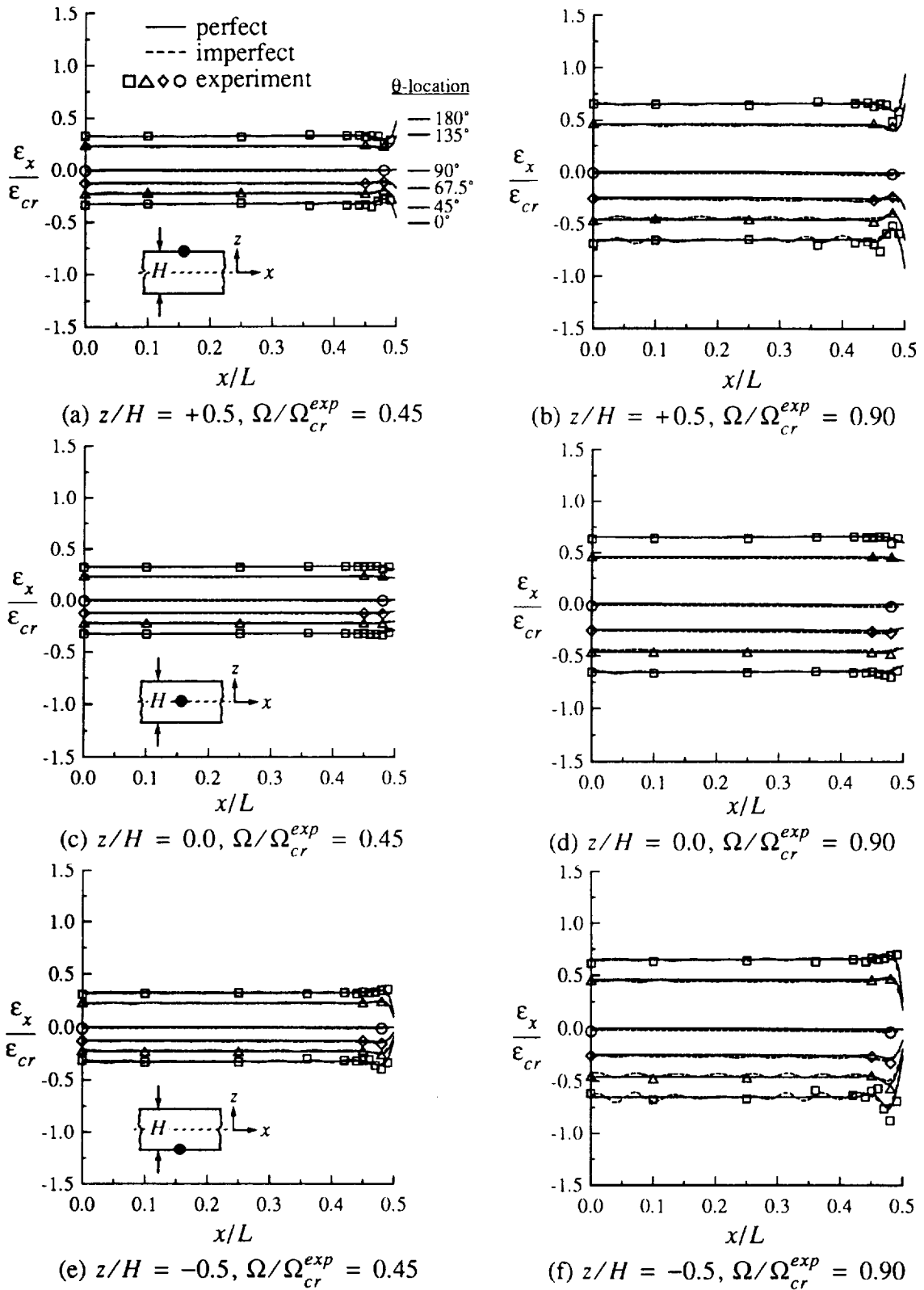
(f) $z/H = -0.5$, $\Omega/\Omega_{cr}^{exp} = 0.90$

Fig. 4-11 Axial Strain Response, CYL-2, $[\mp45/0/90]_S$, $L/R = 5$
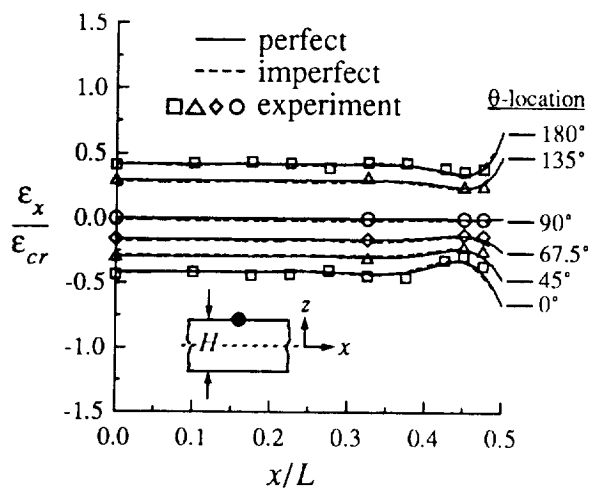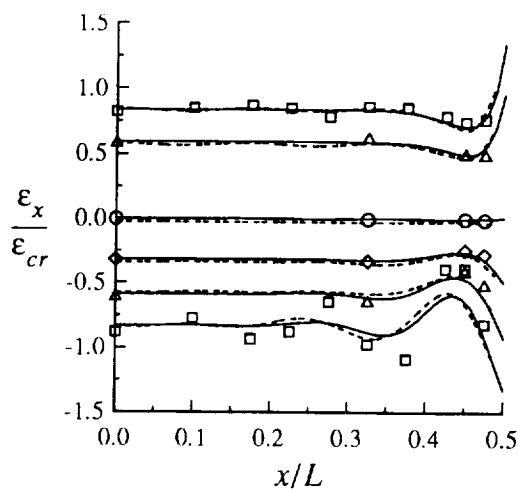
84
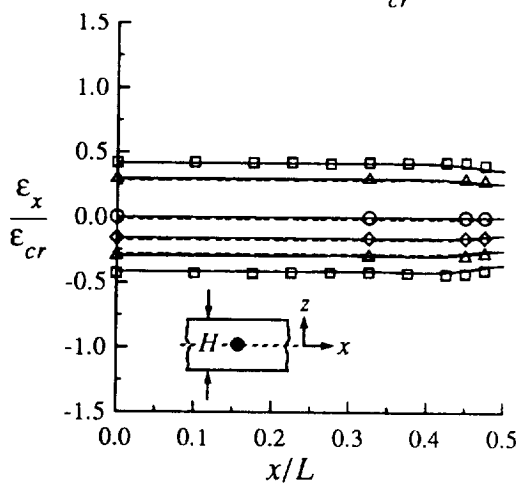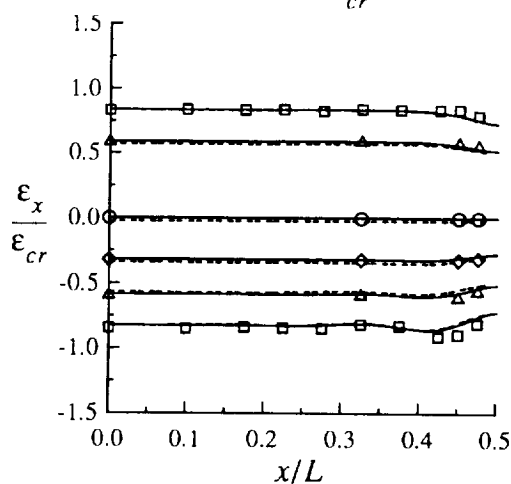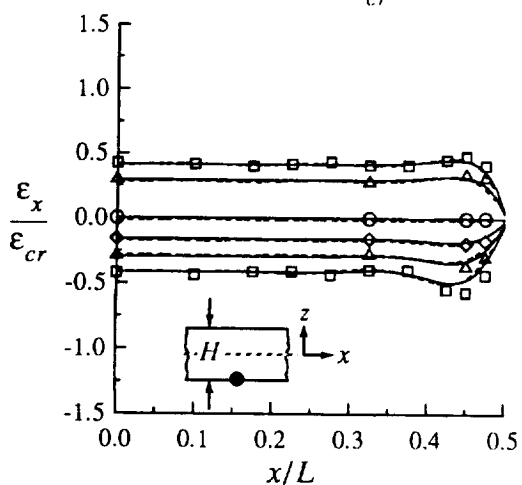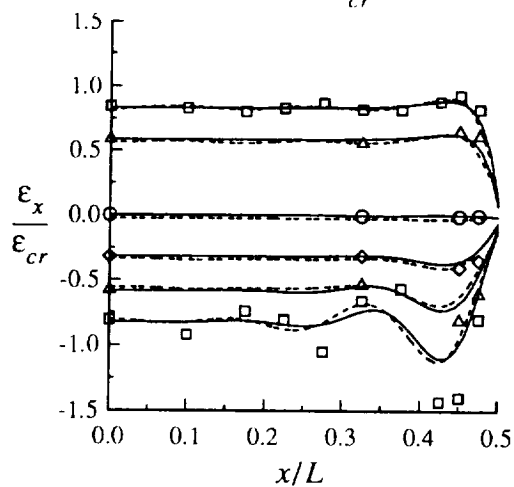
Fig. 4-12 Axial Strain Response, CYL-3A, [∓45/0₂]ₛ, L/R = 2

85
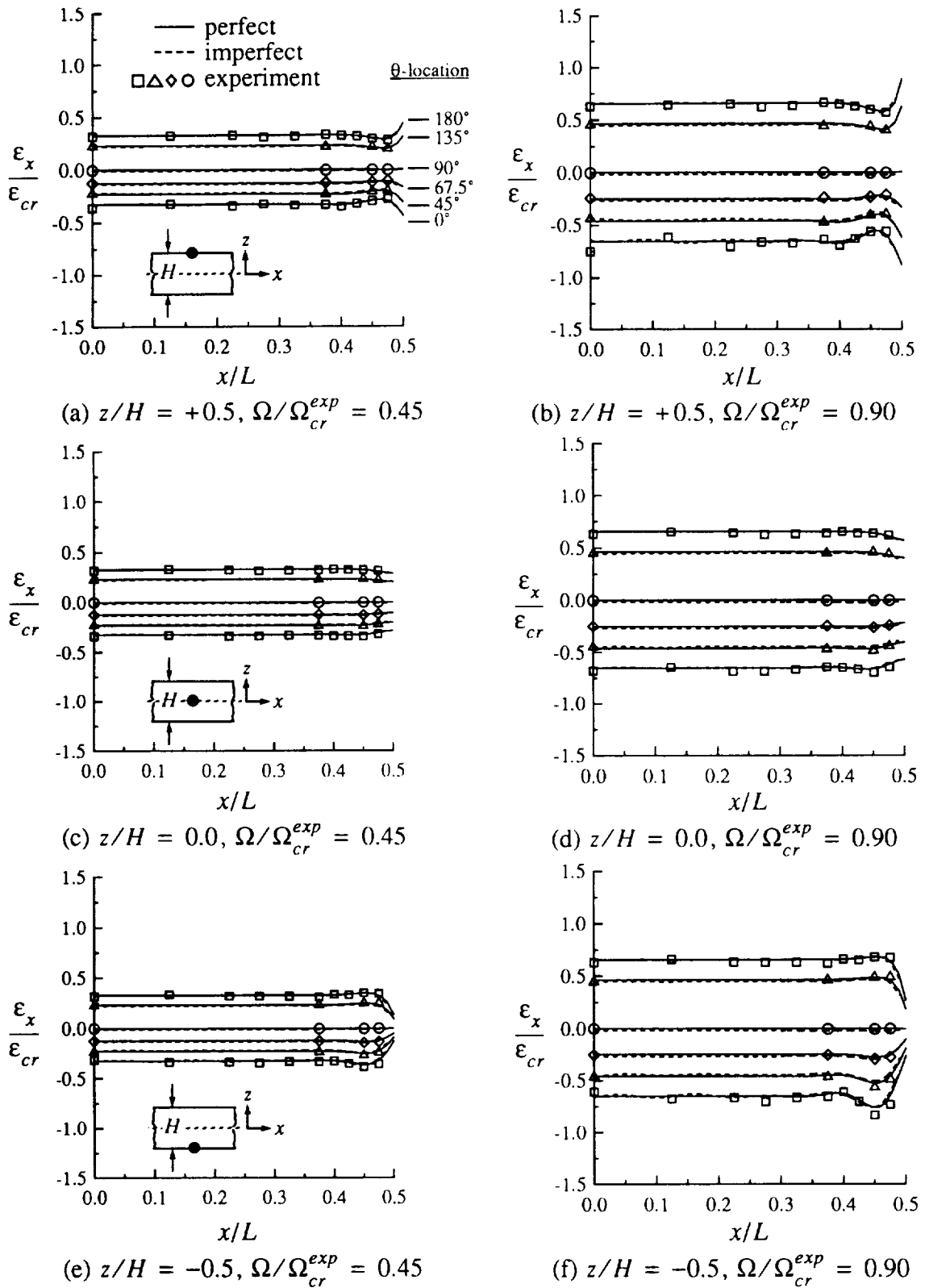
Fig. 4-13 Axial Strain Response, CYL-4A, [∓45/90₂]ₛ, L/R = 2
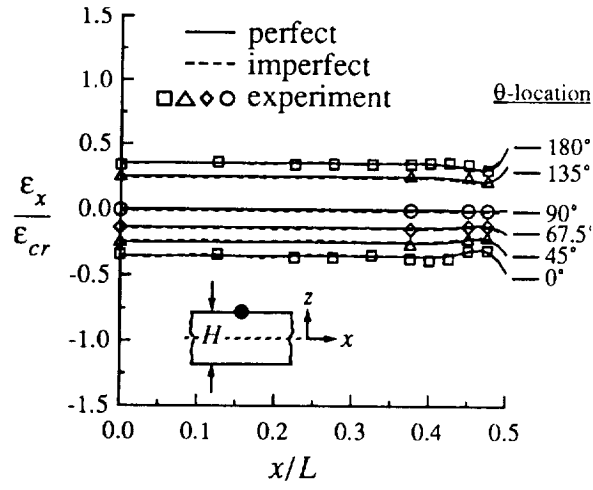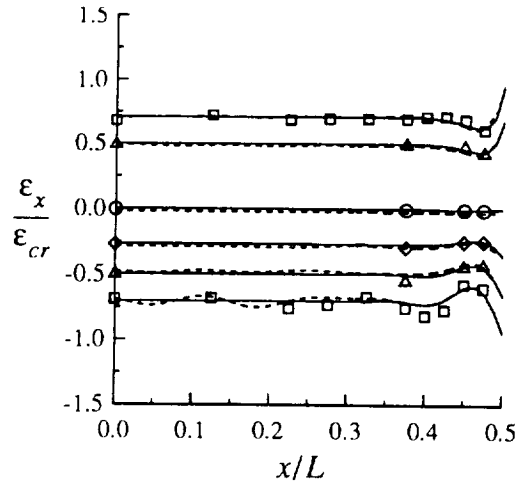
(a) $z/H = +0.5$, $\Omega/\Omega_{cr}^{exp} = 0.45$
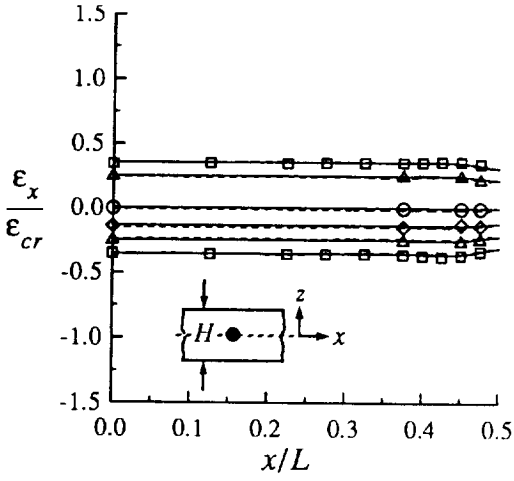
(b) $z/H = +0.5$, $\Omega/\Omega_{cr}^{exp} = 0.90$
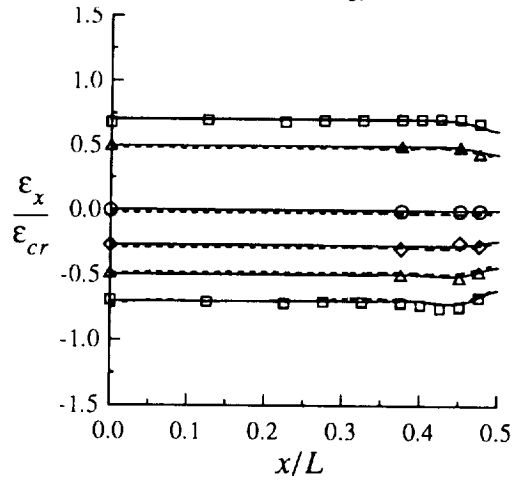
(c) $z/H = 0.0$, $\Omega/\Omega_{cr}^{exp} = 0.45$

(d) $z/H = 0.0$, $\Omega/\Omega_{cr}^{exp} = 0.90$
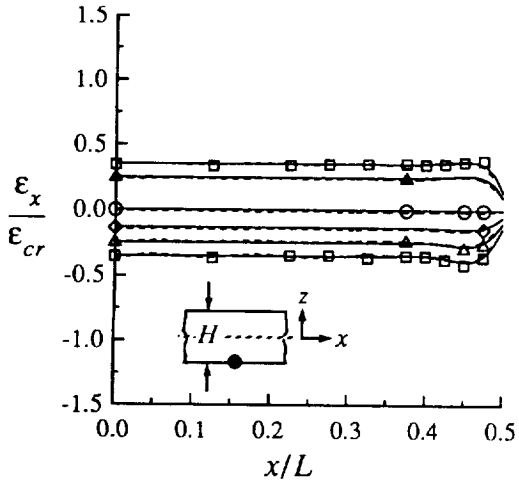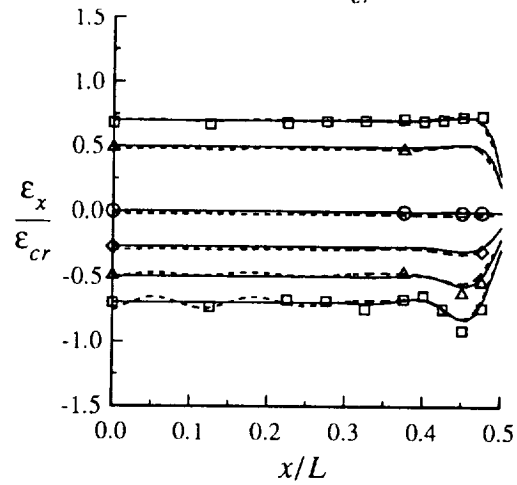
(e) $z/H = -0.5$, $\Omega/\Omega_{cr}^{exp} = 0.45$

(f) $z/H = -0.5$, $\Omega/\Omega_{cr}^{exp} = 0.90$

Fig. 4-14 Axial Strain Response, CYL-4B, [∓45/90₂]ₛ, *L/R* = 2

= 0.90. In most instances, these discrepancies are observed, to some extent, at the outer and inner surface of the cylinder wall, in the region of the peak boundary layer strains near the cylinder ends. The severity of these discrepancies is specimen dependent and appears to be most pronounced for the $[\mp45/0_2]_S$ specimen, as indicated by the square symbols in Fig. 4-12 (b) and (f). Although the oscillatory character of the compressive boundary layer region is correctly predicted for this specimen, the magnitude of the strains is significantly under-predicted. Several potential sources of discrepancies will be discussed in Chapter 5.

The circumferential variation of the boundary layer strains, evident in the strain profiles, reflects the variation of the boundary layer deformations depicted in Fig. 2-6. The axial oscillations of the compressive surface strains attenuate rapidly in the circumferential direction, with all evidence of the boundary layer vanishing at $\theta = \pm90°$. A boundary layer builds up again on the tensile side of the cylinder.

4.2.3 Prebuckling Material Failure

It was mentioned previously in section 2.1.6 that first-ply failure during prebuckling was unlikely to occur in the idealized $[\mp45/0/90]_S$ and the $[\mp45/0_2]_S$ cylinders. First-ply matrix failure in the $[\mp45/90_2]_S$ cylinders, however, was found to be highly probable. Matrix failure in a 90° ply, in the form of matrix cracking, was predicted to occur on the tension side at the end of these idealized cylinders.

A first-ply failure analysis was conducted for the $[\mp45/90_2]_S$ specimens, with no geometric imperfections included, to obtain an estimate of the value of the applied end-rotation at the onset of matrix cracking. The initial cracking and popping sounds were clearly audible at approximately 90% of the experimental buckling end-rotation, a value of end-rotation 20% higher than predicted. However, the matrix cracking did not appear to appreciably influence the measured bending responses.

4.3 Buckling Responses

The STAGS finite element buckling predictions are reported in Table 4-3 for the perfect geometry specimens and in Table 4-4 for the imperfect geometry specimens. The predicted buckling moment, end-rotation, and strain values in these tables are denoted as M^{fe}_{cr}, Ω^{fe}_{cr}, and ε^{fe}_{cr}, respectively. The values of M^{fe}_{cr} and Ω^{fe}_{cr} were computed using the methods

described in "Analysis Procedure" in section 2.2.3. The values of ε_{cr}^{fe} were computed from Ω_{cr}^{fe} and Eq. (2.42).

Table 4-3 Predicted Buckling Parameters for Perfect Test Specimens

Specimen Identification Code	Wall Construction	L/R	M_{cr}^{fe}, in.-lbs	Ω_{cr}^{fe}, radians (deg)	ε_{cr}^{fe}, $\mu\varepsilon$
CYL-1A	$[\mp45/0/90]_S$	2	143,310	0.0037 (0.212)	3,700
CYL-1B		2	142,900	0.0037 (0.212)	3,700
Average for $[\mp45/0/90]_S$, $L/R = 2$			143,105	0.0037 (0.212)	3,700
CYL-2		5	141,160	0.0090 (0.531)	3,710
CYL-3A	$[\mp45/0_2]_S$	2	103,870	0.0018 (0.105)	1,830
CYL-4A	$[\mp45/90_2]_S$	2	134,100	0.0076 (0.437)	7,620
CYL-4B		2	132,530	0.0075 (0.430)	7,510
Average for $[\mp45/90_2]_S$, $L/R = 2$			133,315	0.0076 (0.434)	7,565

Table 4-4 Predicted Buckling Parameters for Imperfect Test Specimens

Specimen Identification Code	Wall Construction	L/R	M_{cr}^{fe}, in.-lbs	Ω_{cr}^{fe}, radians (deg)	ε_{cr}^{fe}, $\mu\varepsilon$
CYL-1A	$[\mp45/0/90]_S$	2	132,570	0.0034 (0.197)	3,430
CYL-1B		2	130,130	0.0034 (0.193)	3,360
Average for $[\mp45/0/90]_S$, $L/R = 2$			131,350	0.0034 (0.195)	3,395
CYL-2		5	122,650	0.0081 (0.463)	3,230
CYL-3A	$[\mp45/0_2]_S$	2	104,590	0.0019 (0.107)	1,860
CYL-4A	$[\mp45/90_2]_S$	2	125,390	0.0073 (0.415)	7,250
CYL-4B		2	118,320	0.0068 (0.391)	6,820
Average for $[\mp45/90_2]_S$, $L/R = 2$			121,855	0.0071 (0.403)	7,035

The measured buckling end-rotations are graphically compared to the predicted values in Fig. 4-15. The end-rotation values in this figure are normalized with respect to the appropriate classical buckling end-rotations, Ω_{cr}, given in Table 4-1. It is seen from Fig. 4-15 that the classical and the finite element predictions over-estimate the measured buck-

ling values in all cases. The finite element buckling analyses of the perfect specimens over-estimate the measured values by 17% to 42%. As was evident with the prebuckling results, the measured shape imperfections can couple with the prebuckling displacement and strain responses and cause a reduction in the predicted buckling resistance of the specimens. Correlation between the predictions and the experiment is appreciably improved in most instances by incorporating the measured shape imperfections. The buckling predictions of the imperfect specimens over-estimate the measured buckling end-rotations by 6% to 20%. It is interesting to note that the buckling prediction for the $[\mp 45/0_2]_S$ specimen increases slightly when including the shape imperfections. This effect may be attributed to a stabilizing effect due to the radially outward prebuckling deflections on the compression side of the cylinder shown in Fig. 4-6 (a).
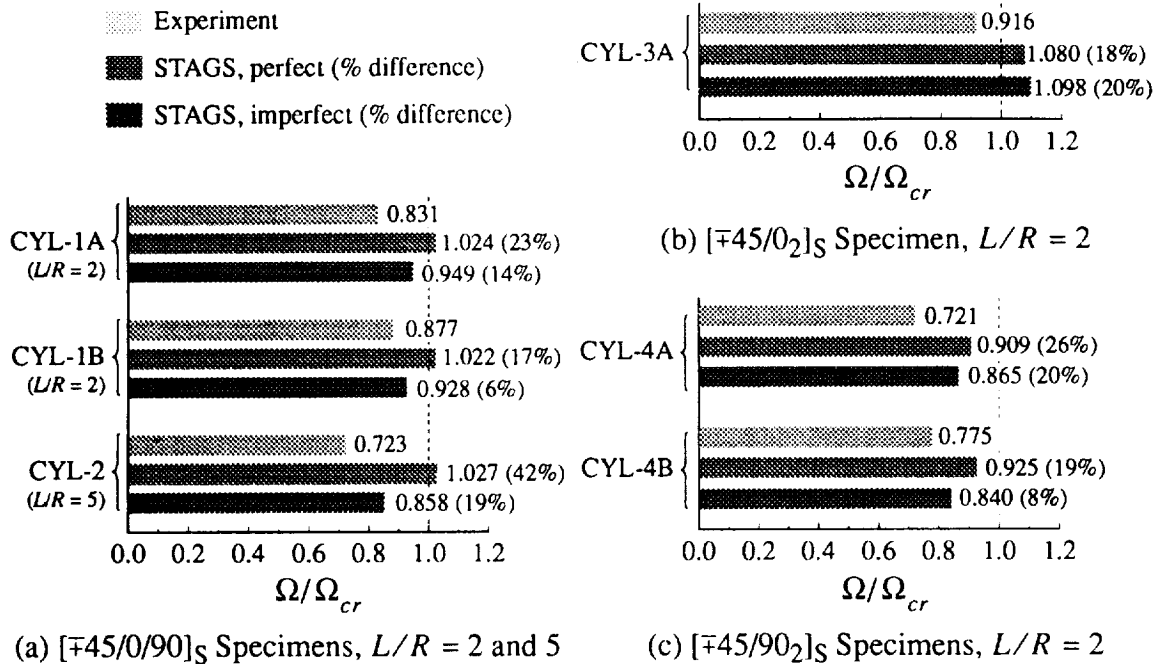
Fig. 4-15 Buckling End-Rotation Results

Although there is some discrepancy between the measured buckling end-rotations and the predictions, overall trends are still apparent. As seen previously in Fig. 2-19 with the idealized cylinders, Fig. 4-15 indicates for both the perfect and imperfect cylinders that the ratio of the buckling end-rotations predicted by STAGS to the classical buckling end-rotation, $\Omega_{cr}^{fe}/\Omega_{cr}$, varies as a function of the layup. The $[\mp 45/0_2]_S$ cylinder exhibits the larg-

est value of $\Omega_{cr}^{fe}/\Omega_{cr}$, followed by the [∓45/0/90]$_S$ cylinders, and the [∓45/90$_2$]$_S$ cylinders. The experimental data in Fig. 4-15 shows a similar trend for the cylinders with $L/R = 2$. The largest value of $\Omega_{cr}^{exp}/\Omega_{cr}$ is observed for the [∓45/0$_2$]$_S$ cylinder with $\Omega_{cr}^{exp}/\Omega_{cr} = 0.916$, followed by the [∓45/0/90]$_S$ cylinders with $\Omega_{cr}^{exp}/\Omega_{cr} = 0.831$ and 0.877, and the [∓45/90$_2$]$_S$ cylinders with $\Omega_{cr}^{exp}/\Omega_{cr} = 0.721$ and 0.775.

Comparing the measured buckling values in Table 4-2 and the buckling predictions for the cylinders with imperfect geometries in Table 4-4 further highlights the relative differences between the quasi-isotropic and orthotropic cylinders. The average measured buckling moment values reported in Table 4-2 for the orthotropic [∓45/90$_2$]$_S$ and [∓45/0$_2$]$_S$ cylinders are approximately 12% and 22%, respectively, lower the average buckling moment for the quasi-isotropic [∓45/0/90]$_S$ cylinders with $L/R = 2$. The buckling moment for the quasi-isotropic [∓45/0/90]$_S$ cylinder with $L/R = 5$ is 12% lower than the average buckling moment for the [∓45/0/90]$_S$ cylinders with $L/R = 2$. The predicted buckling moment values in Table 4-4 compare similarly, with the orthotropic [∓45/90$_2$]$_S$ and [∓45/0$_2$]$_S$ cylinders exhibiting buckling moments approximately 7% and 20%, respectively, lower than those predicted for the quasi-isotropic [∓45/0/90]$_S$ cylinders with $L/R = 2$. The predicted buckling moment for the quasi-isotropic [∓45/0/90]$_S$ cylinder with $L/R = 5$ is 7% lower than the predicted buckling moment for the [∓45/0/90]$_S$ cylinders with $L/R = 2$. The average measured buckling strain and end-rotation values reported in Table 4-2 for the orthotropic [∓45/0$_2$]$_S$ cylinder are approximately 50% of the buckling strain and end-rotation values for the [∓45/0/90]$_S$ cylinders with $L/R = 2$. The measured buckling strain and end-rotation values for the orthotropic [∓45/90$_2$]$_S$ are approximately 200% of the corresponding values for the [∓45/0/90]$_S$ cylinders with $L/R = 2$. The strain and end-rotation values for the [∓45/0/90]$_S$ cylinder with $L/R = 5$ are 85% and 210%, respectively, of the buckling strain and end-rotation values for the cylinder with $L/R = 2$. The predicted buckling strain and end-rotation values reported in Table 4-4 compare similarly.

The buckling shapes predicted for the imperfect cylinders are shown in the form of three-dimensional views and two-dimensional radial displacement contour plots in Figs. 4-16 through 4-21. The buckling shapes corresponding to the perfect cylinders are similar to those presented for the idealized cylinders in Figs. 2-20 and 2-21.

Figs. 4-16 through 4-21 demonstrate that inclusion of the measured shape imperfections can alter the predicted buckling shapes relative to the perfect specimens. The buckling

shapes of the imperfect [∓45/0/90]$_S$ cylinders, shown in Figs. 4-16 through 4-18, no longer exhibit the short wavelength modes shown in Figs. 2-20 (a) and 2-21 (a). Instead, buckling on the compression side is confined to a region near the center of the cylinder. The buckling shapes of the [∓45/0$_2$]$_S$ and [∓45/90$_2$]$_S$ cylinders, shown in Figs. 4-19 through 4-21, are relatively unaffected in comparison to the modes illustrated in Figs. 2-20 (b) and (c).

(a) Deformed shape   (b) Radial displacement contour
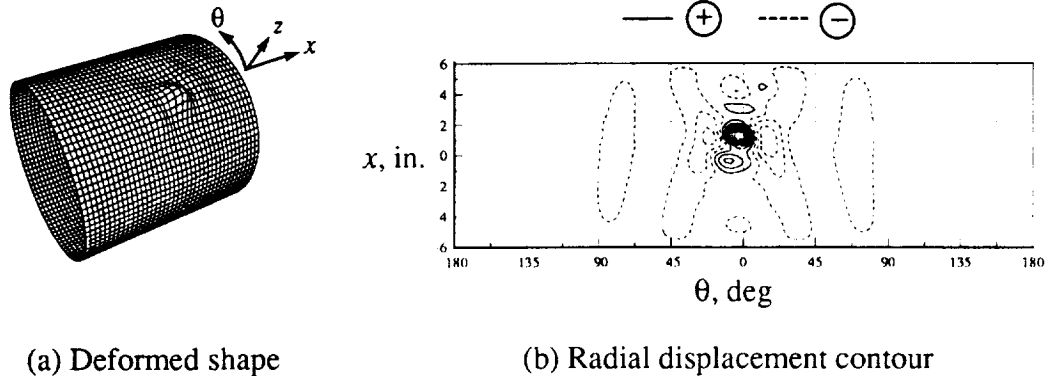
Fig. 4-16 Buckling Shape, CYL-1A, [∓45/0/90]$_S$, L/R = 2

(a) Deformed shape   (b) Radial displacement contour
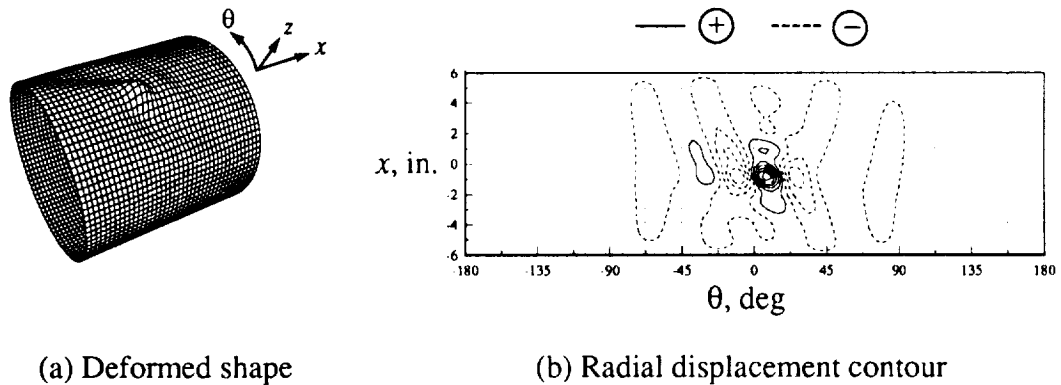
Fig. 4-17 Buckling Shape, CYL-1B, [∓45/0/90]$_S$, L/R = 2

4.4 Postbuckling Responses

As with the postbuckling analyses of the idealized cylinders discussed in section 2.3.1, the postbuckling analyses of the test specimens were marked by numerical difficulties. The extent of success of the postbuckling analyses was ascertained from the computed moment

vs. end-rotation relations. Analyses for which several scallop-shaped branches of the post-buckling moment vs. end-rotation relation could be computed, similar to relation depicted in Fig. 2-22 (a), were considered highly successful. Cases for which only the first scallop-shaped branch of the postbuckling moment vs. end-rotation relation could be computed were considered moderately successful, and the remaining cases, in which only the initial postbuckling solution was computed, as shown in Fig. 2-22 (b), were considered some-what successful.

Various types of numerical difficulties were encountered in the postbuckling analyses of the test specimens. Typically, difficulties occurred in the vicinity of extrema on the scal-
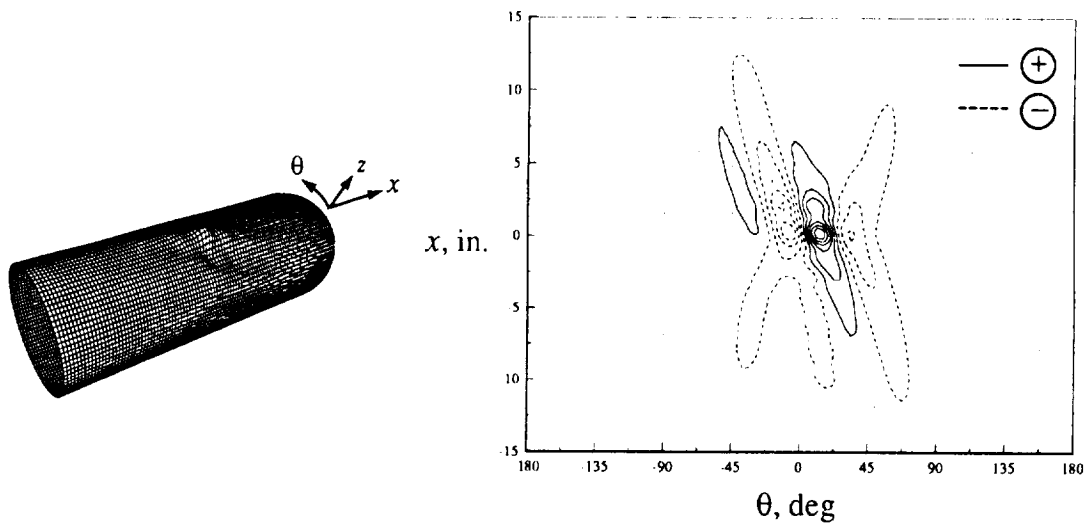
(a) Deformed shape   (b) Radial displacement contour

Fig. 4-18 Buckling Shape, CYL-2, $[\mp 45/0/90]_S$, $L/R = 5$
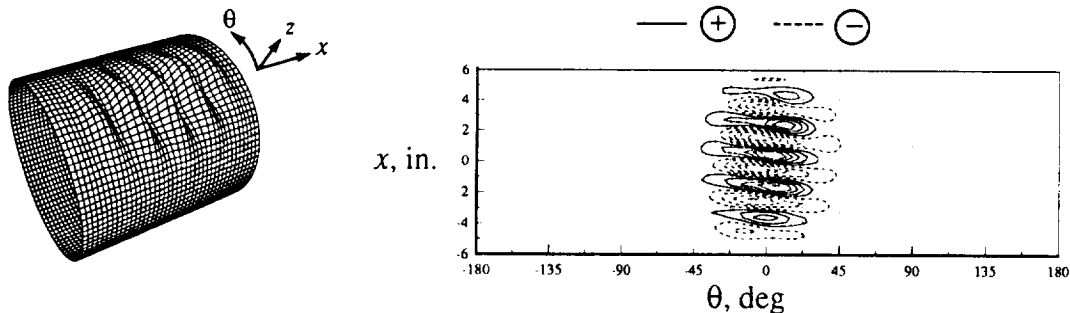
(a) Deformed shape   (b) Radial displacement contour

Fig. 4-19 Buckling Shape, CYL-3A, $[\mp 45/0_2]_S$, $L/R = 2$

93
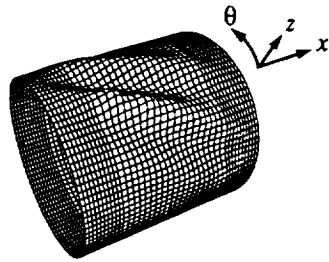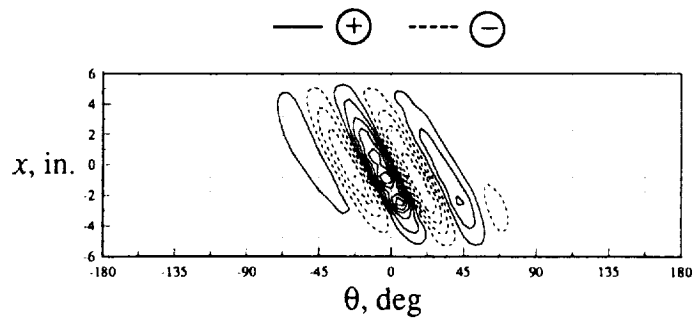
(a) Deformed shape   (b) Radial displacement contour

Fig. 4-20 Buckling Shape, CYL-4A, $[\mp 45/90_2]_S$, $L/R = 2$
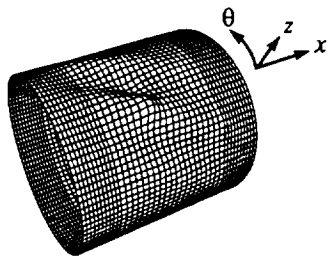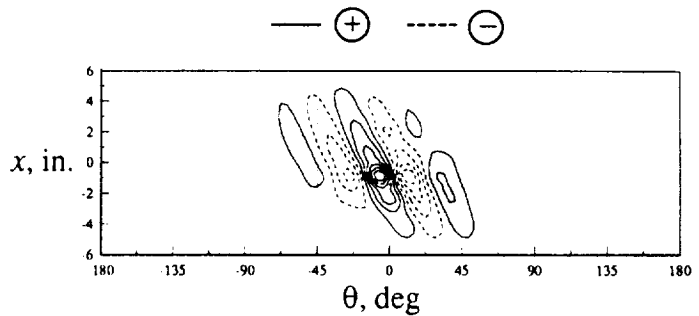
(a) Deformed shape   (b) Radial displacement contour

Fig. 4-21 Buckling Shape, CYL-4B, $[\mp 45/90_2]_S$, $L/R = 2$

lop-shaped postbuckling path. Attempts to overcome these extrema required a number of small arc-length increments. In many instances, the analysis failed to converge on a solution on the desired path, converging instead on a previously obtained solution, or on an undesirable adjacent path. The analysis was restarted with a smaller step size in an effort to proceed along the desired equilibrium path. The analysis was halted if a number of attempts failed to make any progress.

The predicted moment vs. end-rotation relations of the test specimens are summarized in Fig. 4-22 (a) through (f). The moment and end-rotation values in these figures are normalized with respect to the appropriate classical buckling moment and end-rotation values reported in Table 4-1. The extreme values of each stable and unstable segment of the moment vs. end-rotation relations are labeled as points *A* through *I*. The values of the end-rotation and moment corresponding to the extrema are listed in each figure. The various

94

degrees of success of the postbuckling analyses are evident in this figure. Rating the success of the individual postbuckling analyses according to the criteria outlined above suggests that the analyses of the $[\mp 45/0_2]_S$ specimen CYL-3A and the $[\mp 45/90_2]_S$ specimen CYL-4B were extremely successful. The analysis of the $[\mp 45/0/90]_S$ specimen CYL-1B was moderately successful and the analyses of all other specimens were considered somewhat successful.

The predicted moment vs. end-rotation relations are compared in Fig. 4-23 for three representative specimens with $L/R = 2$ (CYL-1B, CYL-3A, and CYL-4B) and the one specimen with $L/R = 5$ (CYL-2). The moment and end-rotation values in this figure are normalized with respect to the classical buckling moment and end-rotation of the quasi-isotropic specimen CYL-1A (see Table 4-1). The normalization factors are denoted as M_{cr}^{quasi} and Ω_{cr}^{quasi}, respectively. As with the measured moment vs. end-rotation relations shown in Fig. 4-1, the predicted prebuckling relations are linear up to the bifurcation point. The bifurcation points are labeled as points A_1 through D_1. The successful postbuckling analyses indicate numerous scallop-shaped branches beyond the bifurcation point. Each scalloped-shaped branch was previously shown to correspond to a unique postbuckling configuration.

The postbuckling analyses, although not always entirely successful, provide valuable insight into the postbuckling behavior. As mentioned previously, the bifurcation point occurs at a sharp maximum of the moment vs. end-rotation relation as shown in Fig. 4-23. Each specimen in the figure exhibits an initial postbuckling slope with a high negative value that is nearly coincident with the prebuckling slope, indicating that the buckling of these cylinders occurs suddenly.

Fig. 4-23 indicates that the difference between the moment value at the bifurcation points, A_1 through D_1, and the corresponding moment value at the first minima on the postbuckling path, denoted by points A_2 through D_2, is laminate, cylinder length, and imperfection dependent. The magnitude of this difference is taken as an indicator of the intensity of the buckling process. For the specimens with $L/R = 2$, the relative differences are 43%, 21%, and 53% for the $[\mp 45/0/90]_S$, $[\mp 45/0_2]_S$, and $[\mp 45/90_2]_S$ specimens, respectively. The difference for the $[\mp 45/0/90]_S$ specimen with $L/R = 5$ is 54%.

The minima observed in Fig. 4-23, points A_2 through D_2, provide a lower bound estimate for the buckling moment of a cylinder with a particular shape imperfection. Fig. 4-23
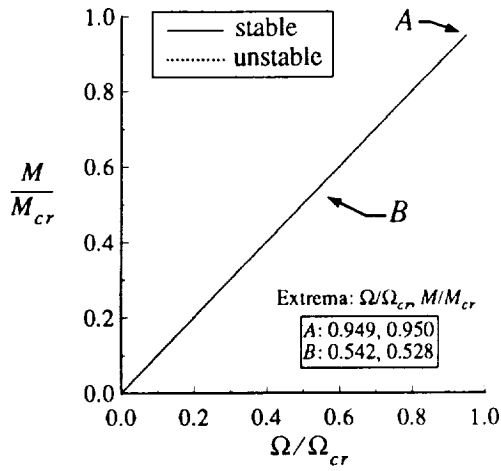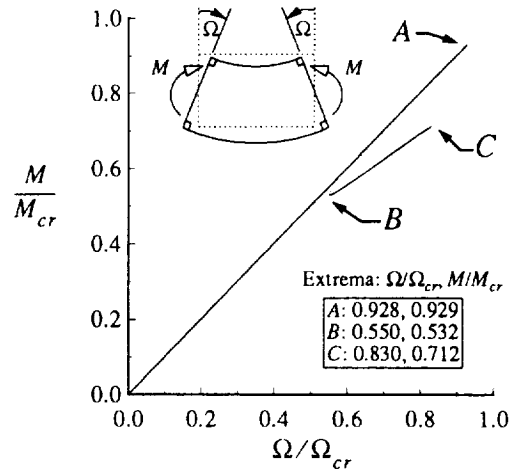
(a) CYL1-A, [∓45/0/90]$_S$, $L/R = 2$

(b) CYL1-B, [∓45/0/90]$_S$, $L/R = 2$
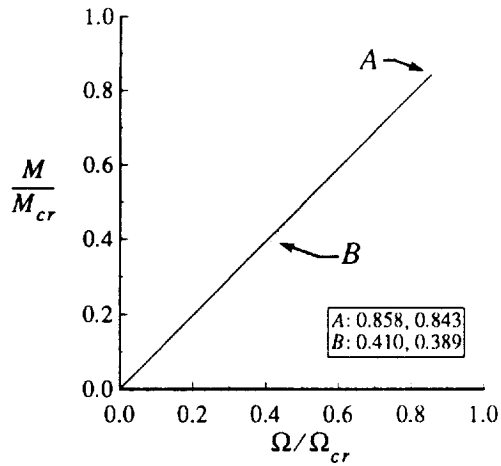
(c) CYL-2, [∓45/0/90]$_S$, $L/R = 5$
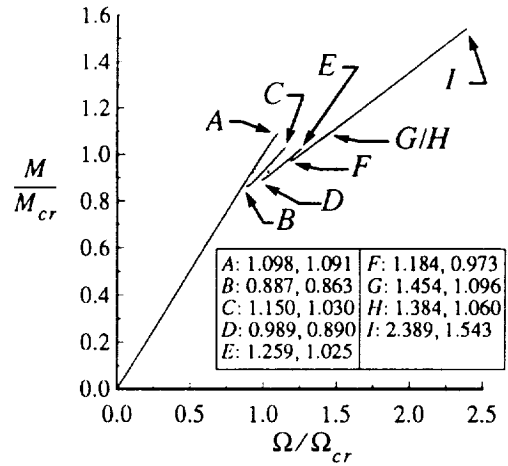
(d) CYL3-A, [∓45/0$_2$]$_S$, $L/R = 2$
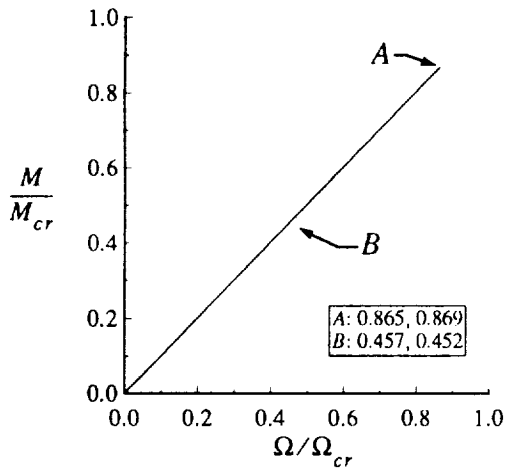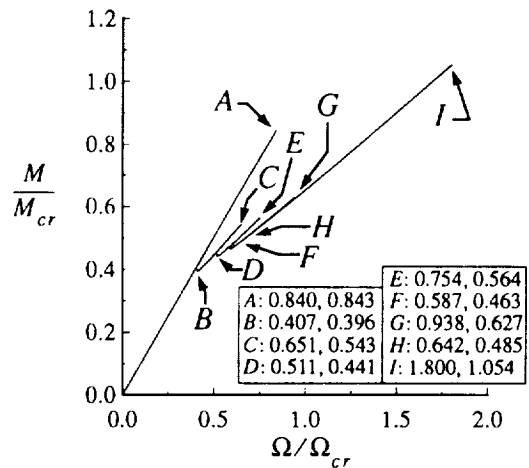
(e) CYL4-A, [∓45/90$_2$]$_S$, $L/R = 2$

(f) CYL4-B, [∓45/90$_2$]$_S$, $L/R = 2$

Fig. 4-22 Summary of Predicted Moment vs. End-Rotation Relations

(a) indicates that the $[\mp45/0/90]_S$ specimen has the greatest bifurcation buckling moment $(M_{cr}^{fe}/M_{cr}^{quasi} = 0.932)$ of the three cylinders with $L/R = 2$, followed by the $[\mp45/90_2]_S$ specimen $(M_{cr}^{fe}/M_{cr}^{quasi} = 0.848)$ and the $[\mp45/0_2]_S$ specimen $(M_{cr}^{fe}/M_{cr}^{quasi} = 0.749)$. Fig. 4-23 (b) indicates that the buckling moment for the $[\mp45/0/90]_S$ specimen with $L/R = 5$ is approximately 10% lower than the corresponding cylinder with $L/R = 2$. Assuming that points A_2 through D_2 define a lower bound for the buckling moments for these cylinders, it is seen that the $[\mp45/0_2]_S$ cylinder has the greatest buckling moment capacity $(M_{cr}^{fe}/M_{cr}^{quasi} = 0.592)$, followed by the $[\mp45/0/90]_S$ cylinder $(M_{cr}^{fe}/M_{cr}^{quasi} = 0.535)$ and the $[\mp45/90_2]_S$ cylinder $(M_{cr}^{fe}/M_{cr}^{quasi} = 0.398)$. The $[\mp45/0/90]_S$ specimen with $L/R = 5$ exhibits a buckling capacity 27% lower than the corresponding quasi-isotropic cylinder with $L/R = 2$. It is clear from this figure that the lower bound estimate for the buckling moment depends greatly on the cylinder layup and length. It is not clear, however, how this lower bound estimate is affected by geometric shape imperfections. Comparing the lower bound estimate for the buckling moment to the predicted buckling moment for cylinders with perfect geometries and $L/R = 2$ (see Table 4-3) indicates that the predicted buckling moments for the perfect cylinders are reduced by approximately 45%, 50%, and

(a) $L/R = 2$ (b) $L/R = 5$
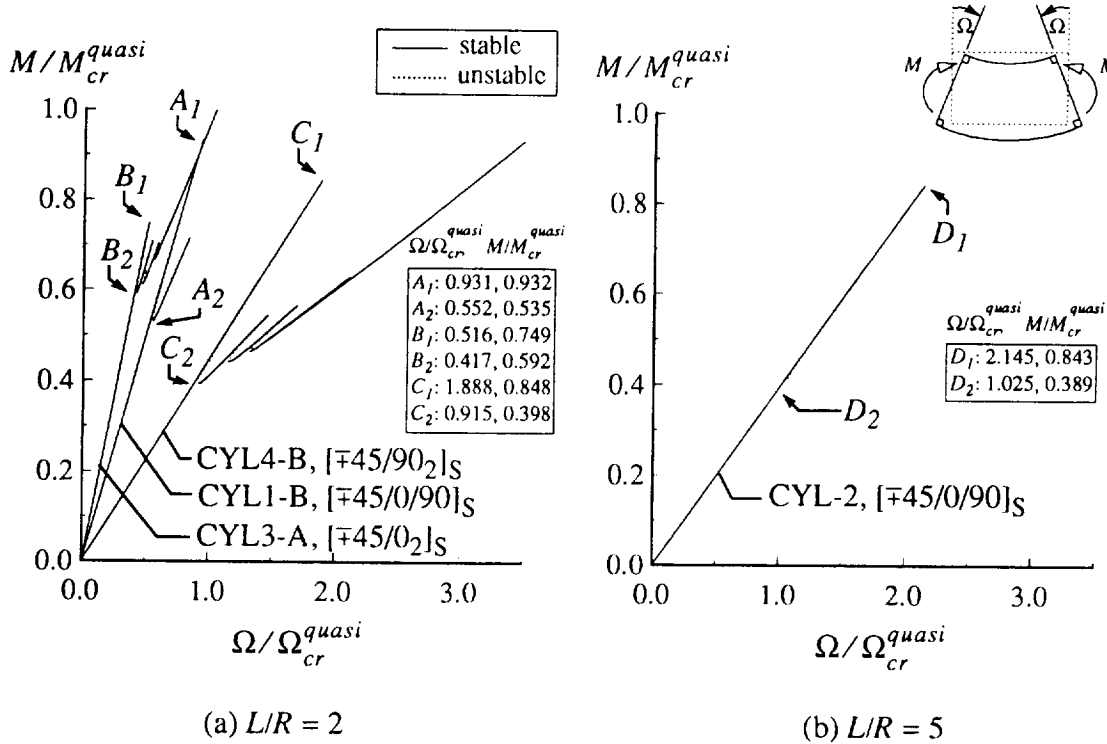
Fig. 4-23 Normalized Predicted Moment vs. End-Rotation Comparison

60% for the $[\mp45/0_2]_S$, $[\mp45/0/90]_S$, and $[\mp45/90_2]_S$ cylinders, respectively. For the perfect $[\mp45/0/90]_S$ cylinder with $L/R = 5$, the buckling moment is reduced by approximately 60%.

Correlation between the observed and predicted postbuckling responses is discussed in the remainder of this chapter. It should be noted that the conditions under which the transition from buckling to postbuckling occurred in the experiments may have differed appreciably from those assumed in the analytical postbuckling calculations. In the analysis, it was assumed that the cylinder ends rotated about fixed pivot pins (see Fig. 3-3 (b)). In the experiment, axial motion of the pivot pins may have occurred as a result of buckling of the specimen, effectively reducing the actual postbuckling stiffness of the specimens. Also, the analysis was conducted quasi-statically using arc-length control, resulting in gradual changes in the postbuckled shapes of the cylinder as the various branches of the postbuckling path were traversed. In the experiment, buckling occurred dynamically so that a number of branches of the theoretical postbuckling solution may not have been visible to the naked eye. As with other dynamic processes, the outcome depends on the initial conditions and dynamic characteristics of the system. Without prior knowledge of the initial conditions and characteristics, it is difficult to model the experiments and predict the resulting postbuckling equilibrium paths. Therefore, the reader should not be surprised to find that direct correlation is not possible in most cases and that comparisons are based on qualitative observations. To illustrate the differences between the measured and predicted postbuckling responses, the moment vs. end-rotation relations are shown in Fig. 4-24 for the $[\mp45/90_2]_S$ cylinder CYL-4B. This figure shows that the measured postbuckling path is quite different than the predicted path. The moment values are significantly lower than the predicted values. Also, the measured postbuckling stiffness changes as the end-rotation increases, indicating possible material damage in the specimen. Material damage was not taken into account in the analysis.

Finally, as was observed in Fig. 4-22, it was not possible to obtain numerical predictions far into the postbuckling range for all specimens. For specimen CYL-3A and CYL-4B (Figs. 4-22 (d) and (f)) it was possible. For the other cylinders, it was not possible. Thus, for some cylinders, even though there were measurements far into the postbuckling range, there are no predictions there. Hence, there is a lack of uniformity among the cylinders in comparing measured and predicted postbuckling responses.
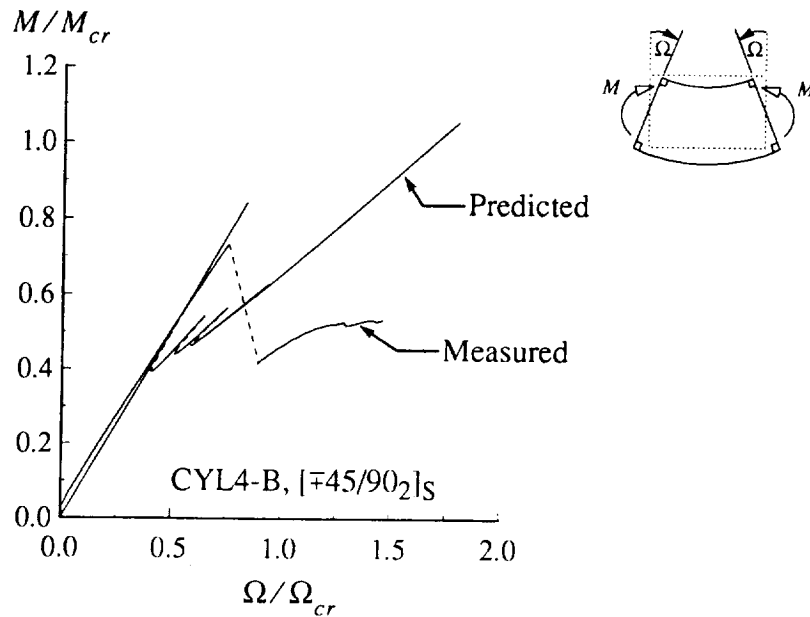
Fig. 4-24 Postbuckling Moment vs. End-Rotation Comparison

4.4.1 Deflection Patterns

Photographs of two representative postbuckling deflection patterns are illustrated in Figs. 4-25 and in 4-26. The deflection patterns shown in these figures correspond to the $[\mp45/90_2]_S$ specimen CYL-4B $(L/R = 2)$ and the $[\mp45/0/90]_S$ specimen CYL-2 $(L/R = 5)$. The values of applied moment and end-rotation corresponding to the photographs are indicated in Fig. 4-1 by the points labeled A and B. The most prominent feature in these figures are the large diamond-shaped buckles on the compression side of the specimens. The inward buckles were outlined on the specimens for visualization purposes. These figures are typical examples of the symmetric and asymmetric patterns, relative to $\theta = 0°$, observed during testing of the specimens.

The predicted and the observed postbuckling deflection patterns are compared in Figs. 4-27 and 4-28 for the $[\mp45/0_2]_S$ specimen CYL-3A and the $[\mp45/90_2]_S$ specimen CYL-4B, respectively. As was mentioned previously, extensive postbuckling predictions were possible for these two specimens. Predicted radial displacement contours on the compression side of the cylinders are compared to outlines of the observed inward buckles in these figures. Part (a) of each figure shows a radial displacement contour of the predicted deflection patterns. The contours were scaled to show only the inward radial deflections and were
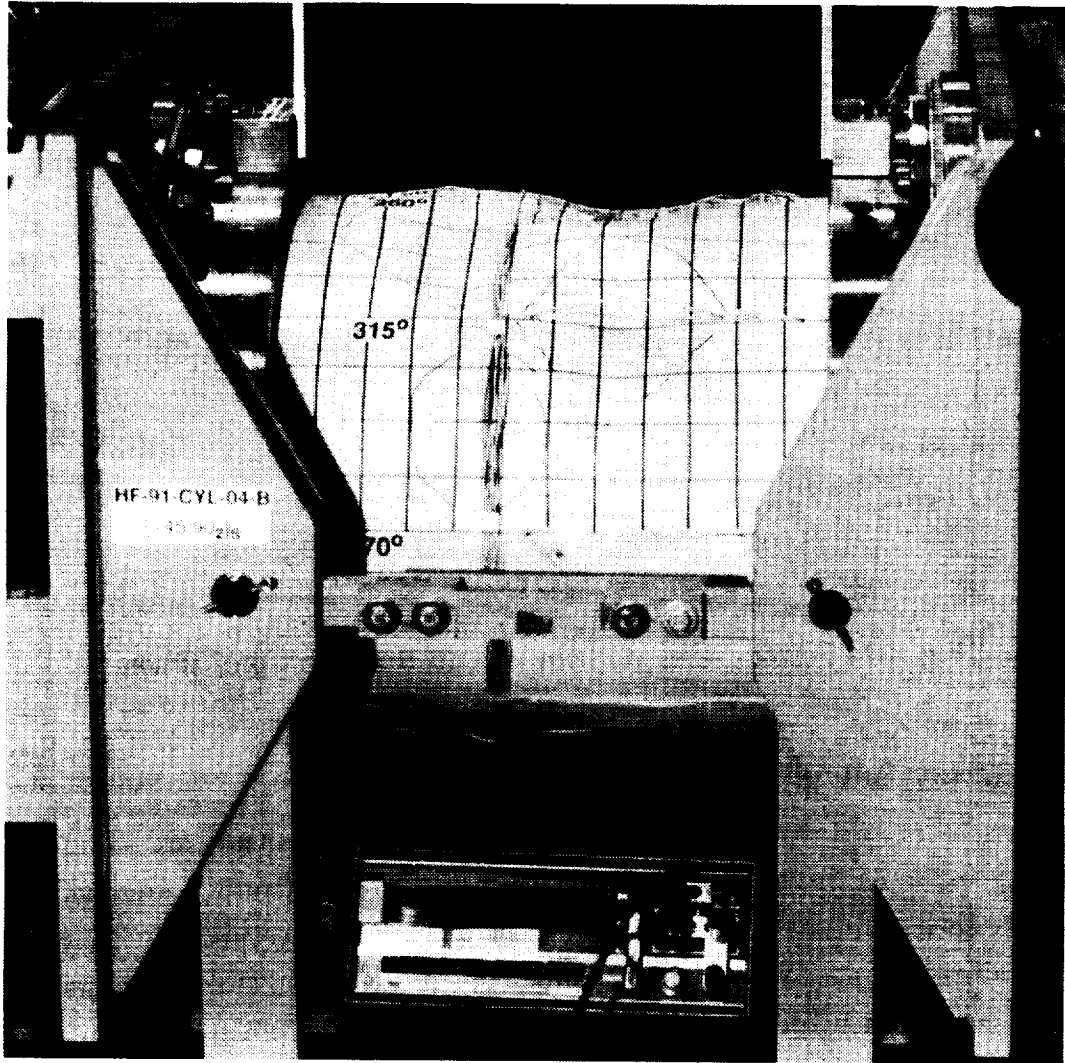
Fig. 4-25 Representative Postbuckling Deflection Pattern, $L/R = 2$

computed from solutions near the points labeled H in Fig. 4-22 (d), and I in Fig. 4-22 (f), respectively. Traced outlines of the inward buckles of the initial deflection patterns are illustrated in part (b) in Figs. 4-27 and 4-28. Outlines of observed material damage at final failure are also indicated in these figures. The locations of selected strain gages are shown in Fig. 4-27 (b) for the purpose of later discussion. The predicted and observed deflection patterns for the $[\mp45/0_2]_S$ specimen indicate a symmetric pattern about $\theta = 0°$. Correlation between the deflection patterns is considered to be good for this specimen. The secondary postbuckling shape shown in Fig. 4-27 (b) was not evident in the analysis, suggesting that
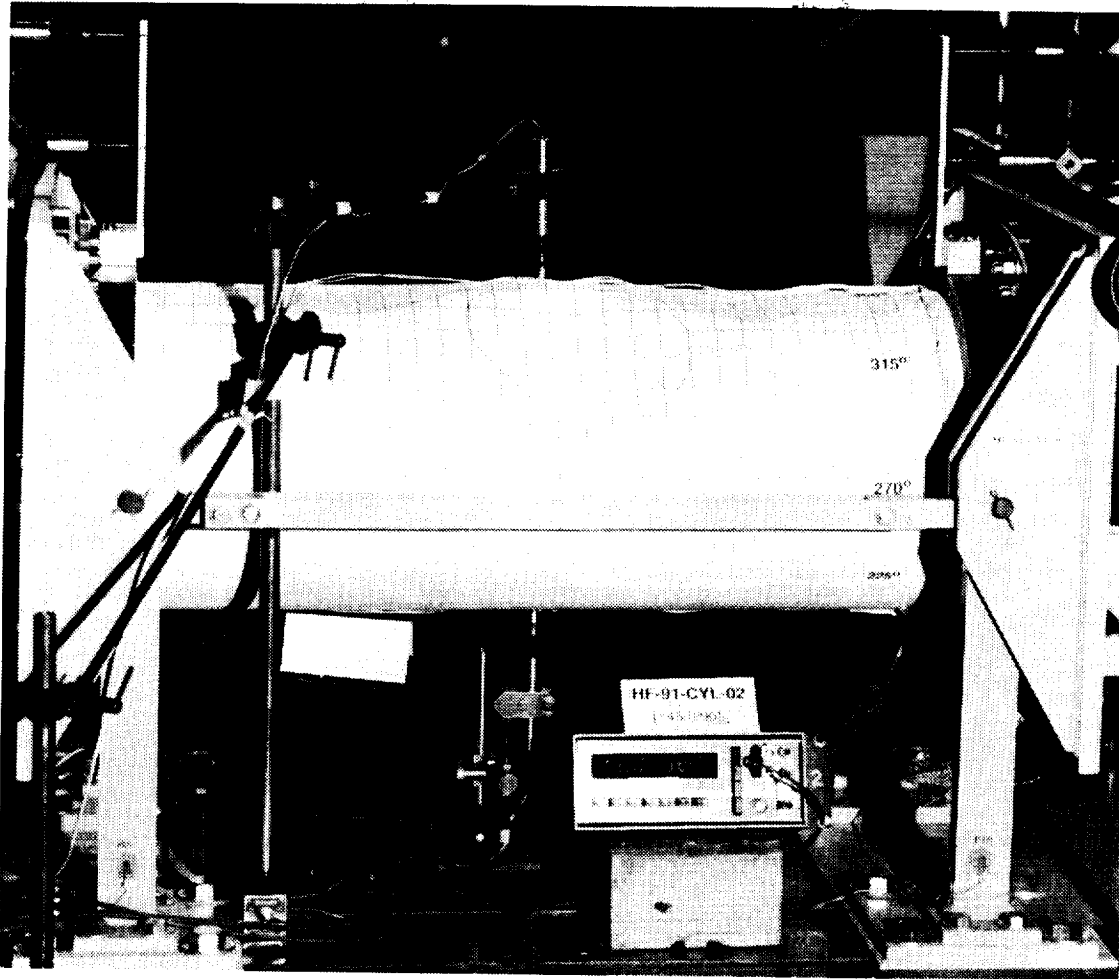
Fig. 4-26 Representative Postbuckling Deflection Pattern, $L/R = 5$

it may have been initiated by a local disturbance such as a material failure. The predicted deflection pattern for the $[\mp45/90_2]_S$ specimen indicates a symmetric pattern about $\theta = 0°$, similar to the predicted deflection pattern for the $[\mp45/0_2]_S$ specimen. The observed deflection pattern for this specimen, however, differs from the prediction, showing an asymmetric pattern relative to $\theta = 0°$. Correlation between the predicted and observed deflection patterns is considered to be relatively poor for this specimen. Qualitatively, Figs. 4-27 and 4-28 indicate that there are distinct similarities between the general characteristics of the buckles seen in the predicted and observed deflection patterns.

$x = +6.0$ in.

inward radial
displacement
contours

$x = 0.0$ in.

$x = -6.0$ in.

| 90° | 60° | 30° | θ=0° | 330° | 300° | 270° |

(a) Predicted deflection pattern

—— buckles
----- secondary
      buckles
▨▨▨ material
      damage

$x = +6.0$ in.

$x = 0.0$ in.

selected strain
gage locations

$x = -6.0$ in.

| 90° | 60° | 30° | θ=0° | 330° | 300° | 270° |
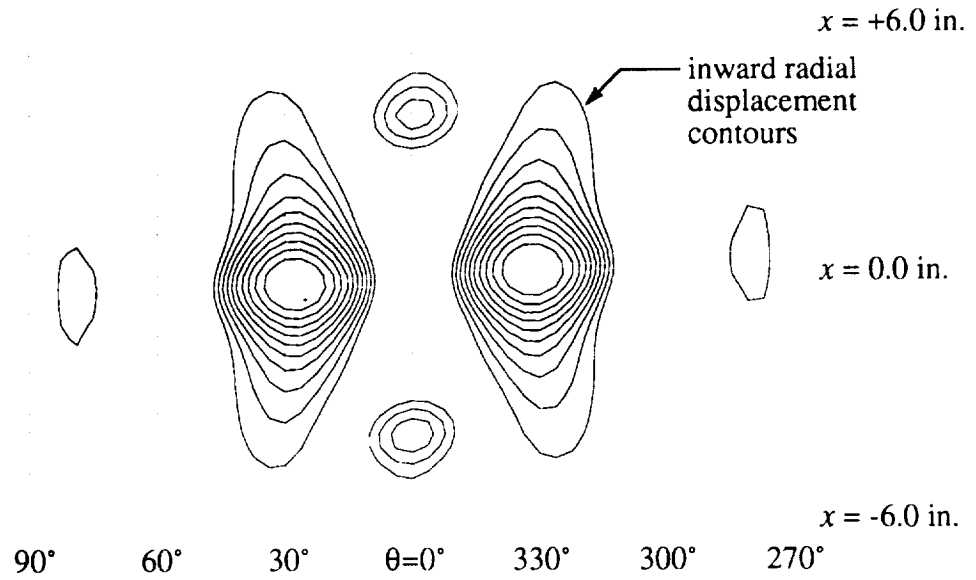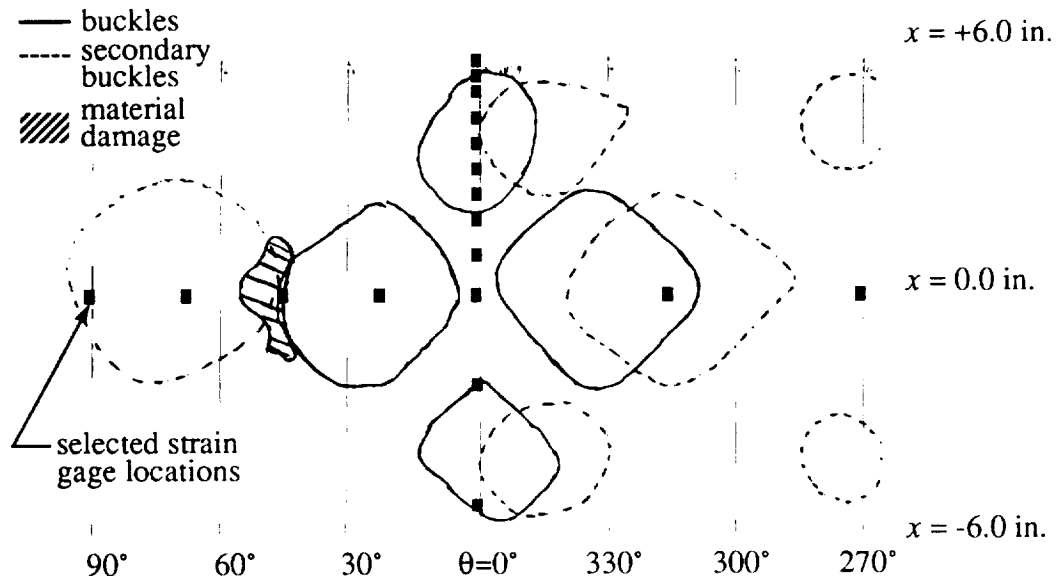
(b) Observed deflection pattern

Fig. 4-27 Postbuckling Deflection Patterns, CYL-3A, [∓45/0₂]ₛ, $L/R = 2$

$x = +6.0$ in.

inward radial
displacement
contours

$x = 0.0$ in.

$x = -6.0$ in.

90°   60°   30°   θ=0°   330°   300°   270°

(a) Predicted deflection pattern

—— buckles
▨▨ material
     damage

$x = +6.0$ in.

$x = 0.0$ in.
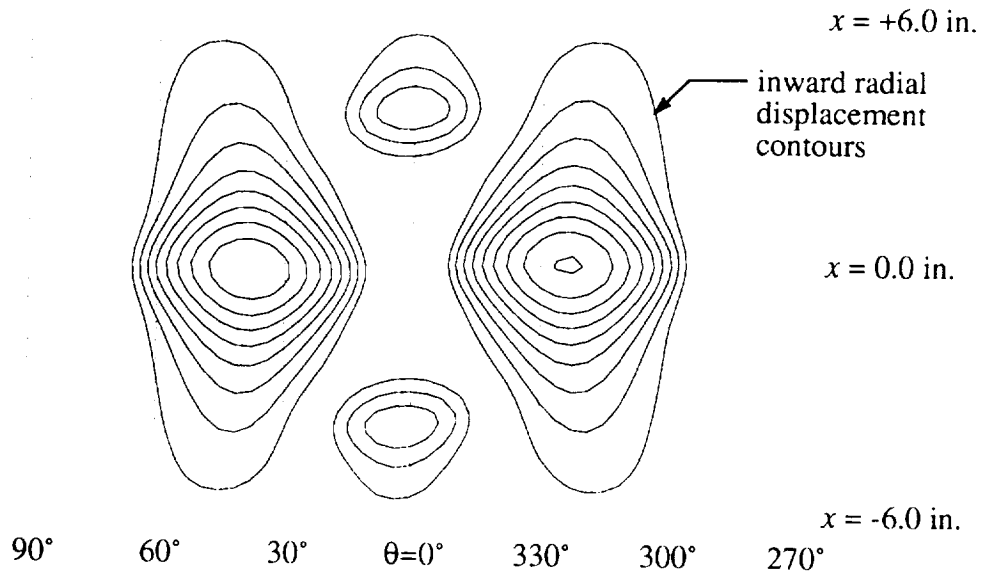
90°   60°   30°   θ=0°   330°   300°   270° $x = -6.0$ in.
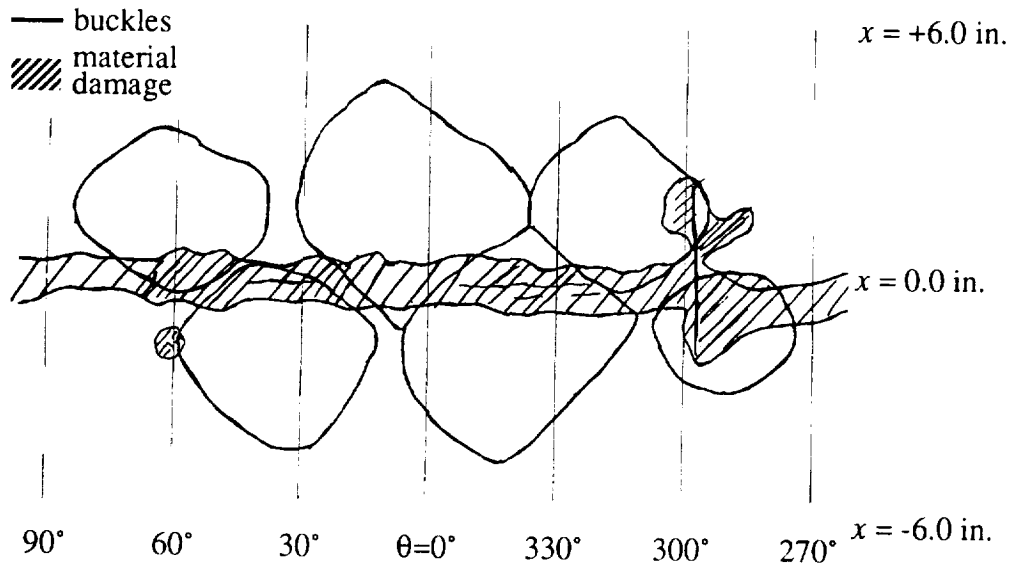
(b) Observed deflection pattern

Fig. 4-28 Postbuckling Deflection Patterns, CYL-4B, $[\mp 45/90_2]_S$, $L/R = 2$

Traces of the observed postbuckling deflection patterns for all other specimens are presented in Figs. 4-29 through 4-32. Although not traced during the test, examination of the video recording indicated that the postbuckling pattern of the $[\mp 45/0/90]_S$ specimen CYL-1A was very similar to the symmetric postbuckling pattern of the corresponding idealized cylinder shown in Fig. 2-23. A schematic of the observed deflection pattern, as determined indirectly from the video recording, is illustrated in Fig. 4-29. In contrast to specimen
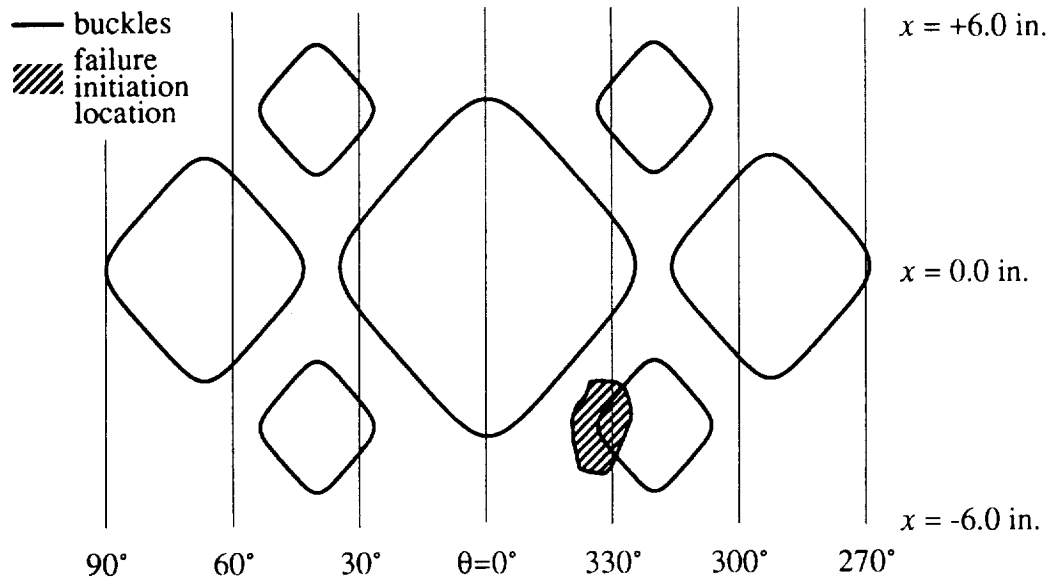
Fig. 4-29 Schematic Postbuckling Deflection Pattern, CYL-1A, $[\mp 45/0/90]_S$, $L/R = 2$
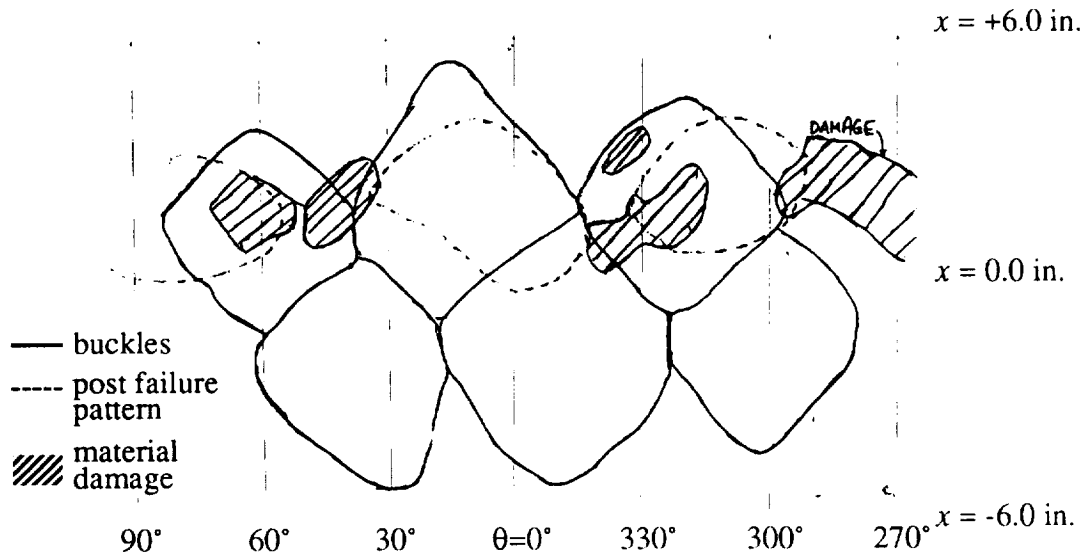
Fig. 4-30 Trace of Postbuckling Deflection Pattern, CYL-1B, $[\mp 45/0/90]_S$, $L/R = 2$

CYL-1A, specimen CYL-1B exhibited the asymmetric postbuckling pattern seen in Fig. 4-30. The deflection pattern for the $[\mp45/0/90]_S$ specimen CYL-2 (L/R = 5) shown in Fig. 4-31 is relatively symmetric about $\theta = 0°$ and similar to the pattern of the $[\mp45/0_2]_S$ specimen CYL-3A. A trace of the buckles exhibited by the $[\mp45/90_2]_S$ specimen CYL-4A is depicted in Fig. 4-32. The asymmetric deflection pattern for CYL-4A is similar to the deflection patterns for specimens CYL-1B and CYL-4B.

Three-dimensional views of the deformed shapes and two-dimensional contour plots of the predicted postbuckling deflection patterns are illustrated in Figs. 4-33 through 4-36 for the three representative specimens with L/R = 2 (CYL-1B, CYL-3A, CYL-4B) and the
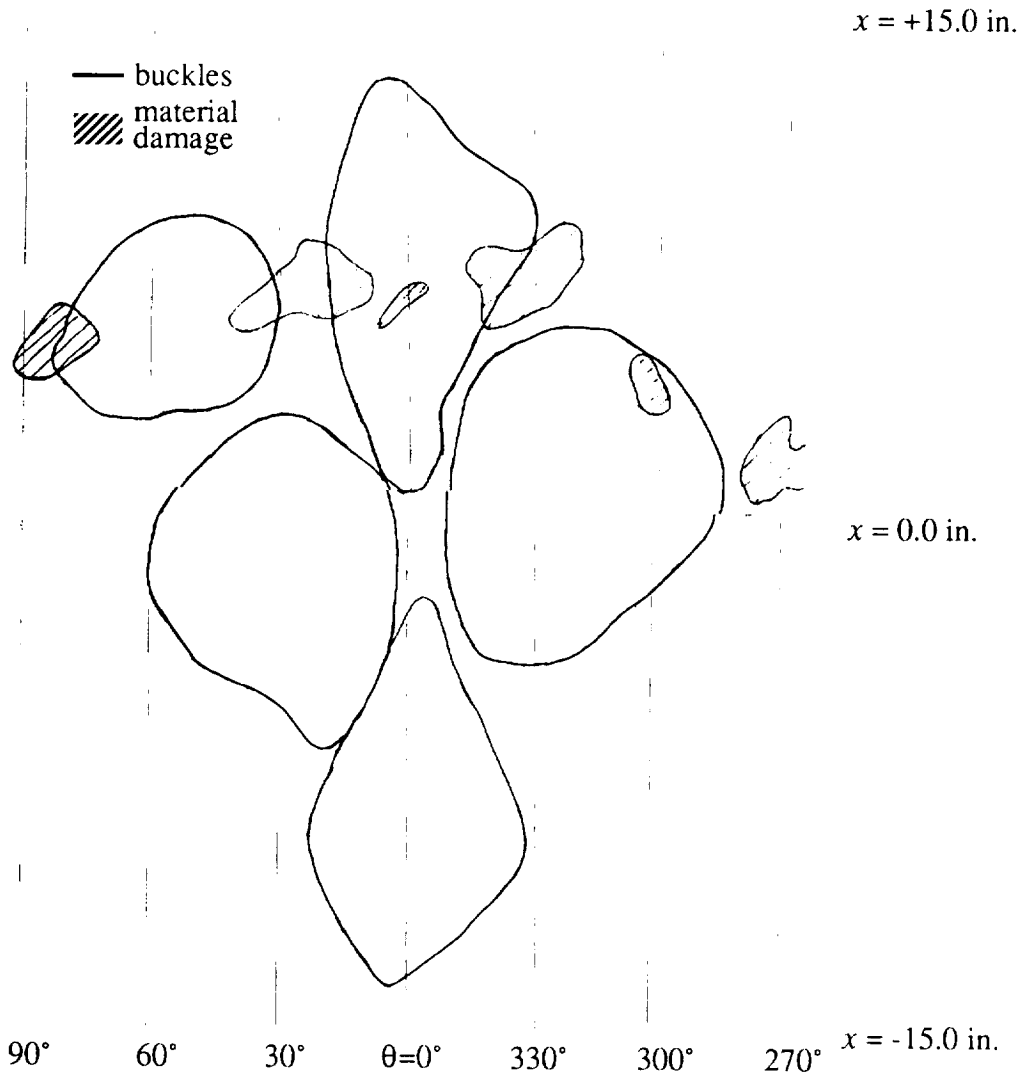
Fig. 4-31 Trace of Postbuckling Deflection Pattern, CYL-2, $[\mp45/0/90]_S$, L/R = 5
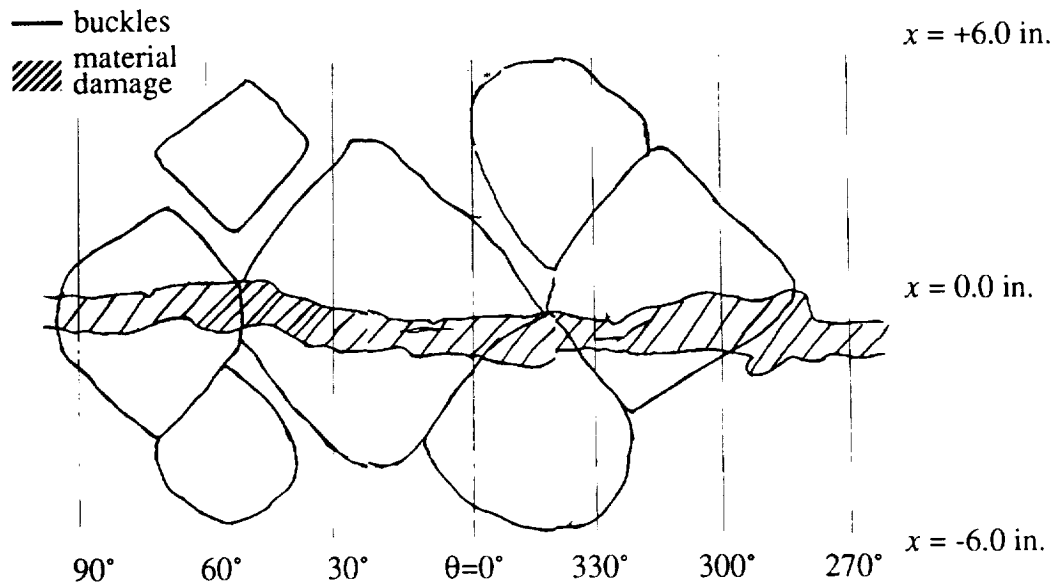
Fig. 4-32 Trace of Postbuckling Deflection Pattern, CYL-4A, $[\mp45/90_2]_S$, $L/R = 2$

specimen with $L/R = 5$ (CYL-2). The deflection patterns for the cylinders with $L/R = 2$ correspond to the maxima of the postbuckling moment vs. end-rotation relations shown in Fig. 4-22 (b), (d), and (f). The deflection patterns for the cylinder with $L/R = 5$ correspond to the minimum point of the postbuckling moment vs. end-rotation relations shown in Fig. 4-22 (c). Although these patterns did not necessarily correlate with the observations, they are presented to show how the deflection patterns progressively develop as the scallop-shaped segments of the postbuckling path are traversed. The development of the postbuckling deflection patterns is strikingly similar for the $[\mp45/0_2]_S$ and the $[\mp45/90_2]_S$ cylinders with $L/R = 2$. A comparison to the quasi-isotropic cylinders is not possible due to the limited success of those particular analyses.

4.4.2 Postbuckling Strain Responses

Measured postbuckling strain profiles are presented in Figs. 4-37 through 4-42. The prebuckling strains are shown in these figures for comparison. The prebuckling strain profiles correspond to the value of end-rotation at the instant before buckling and the postbuckling strain profiles correspond to the value of end-rotation an instant just after buckling. The axial strain profiles are shown at $\theta = 0°$ and are compared at $z/H = +0.5$ and 0.0. The circumferential strain profiles are shown at $x/L = 0$ and are compared at $z/H = +0.5$, 0.0, and -0.5.

106

Recall, good correlation was observed between the predicted and observed postbuckling deflection patterns for the [∓45/0₂]ₛ specimen CYL-3A. The predicted and measured axial strains are shown for this specimen in Fig. 4-37. The strain gage locations from which the data were obtained are superimposed on the deflection pattern of Fig. 4-27 (b). The predicted strain profiles in Fig. 4-37 (a) and (b) were obtained from the last stable prebuckling solution and from a postbuckling solution corresponding to point H on the last scallop-shaped branch of the moment vs. end-rotation relation shown in Fig. 4-22 (d).
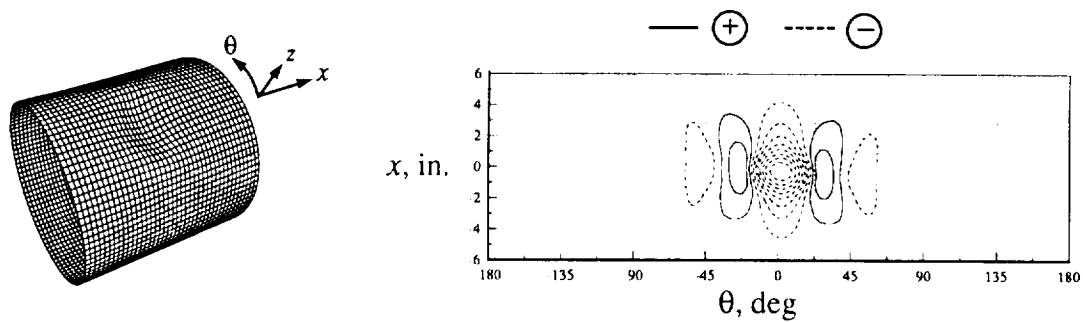
Deflection Pattern, point C in Fig. 4-22 (b), $\Omega/\Omega_{cr} = 0.830$, $M/M_{cr} = 0.712$

Fig. 4-33 Predicted Postbuckling Deflection Patterns, CYL-1B, [∓45/0/90]ₛ, $L/R = 2$
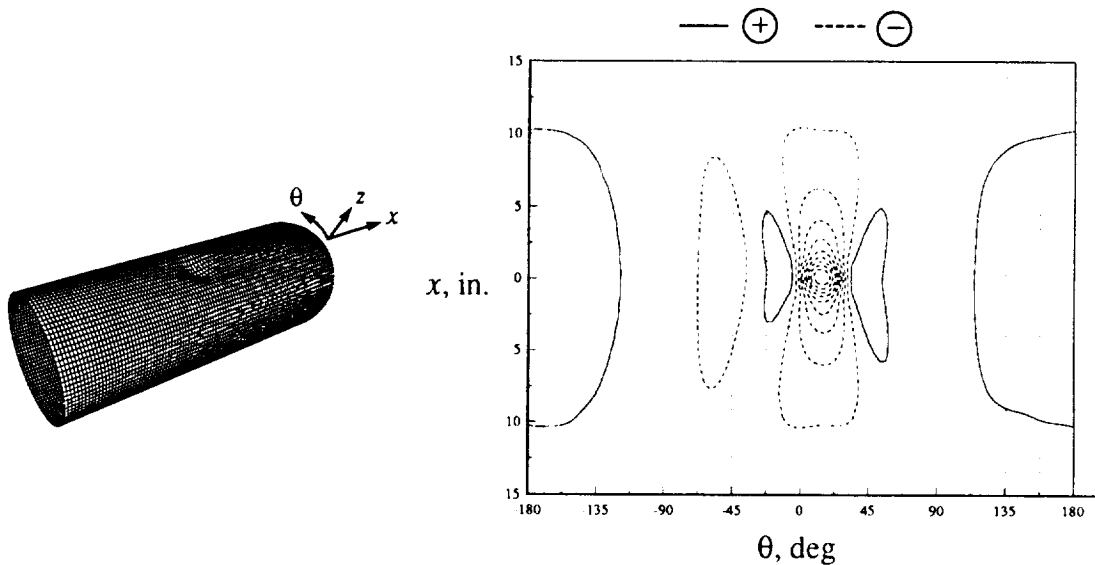
Deflection Pattern, point B in Fig. 4-22 (c), $\Omega/\Omega_{cr} = 0.410$, $M/M_{cr} = 0.389$

Fig. 4-34 Predicted Postbuckling Deflection Patterns, CYL-2, [∓45/0/90]ₛ, $L/R = 5$
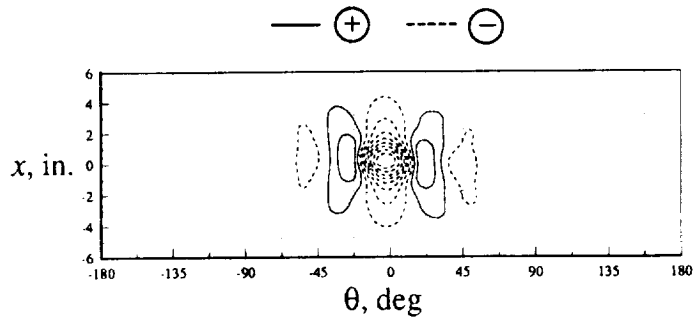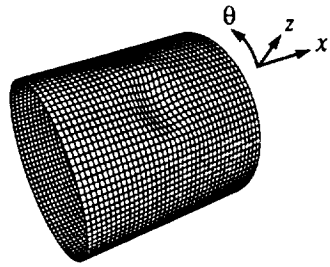
(a) Deflection Pattern, point C in Fig. 4-22 (d), $\Omega/\Omega_{cr} = 1.150$, $M/M_{cr} = 1.030$
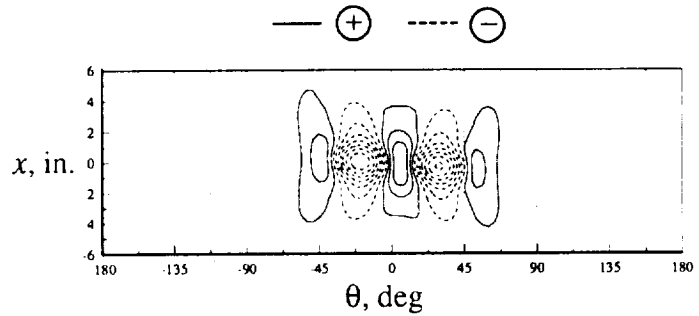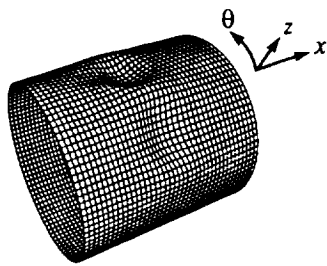
(b) Deflection Pattern, point E in Fig. 4-22 (d), $\Omega/\Omega_{cr} = 1.259$, $M/M_{cr} = 1.025$
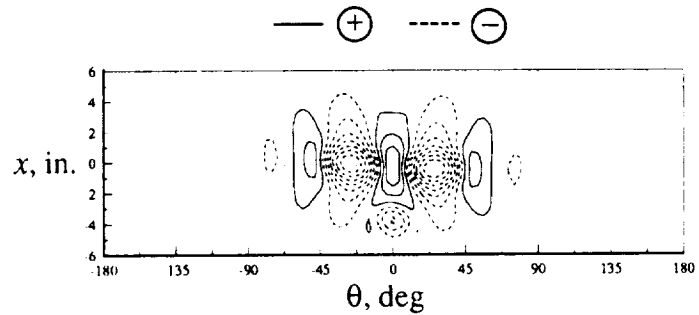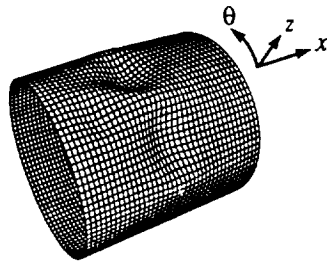
(c) Deflection Pattern, point G in Fig. 4-22 (d), $\Omega/\Omega_{cr} = 1.454$, $M/M_{cr} = 1.096$
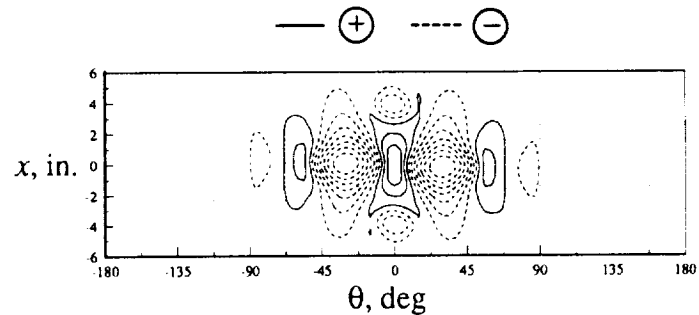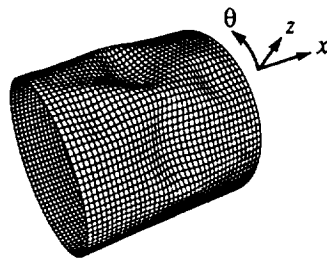
(d) Deflection Pattern, point I in Fig. 4-22 (d), $\Omega/\Omega_{cr} = 2.389$, $M/M_{cr} = 1.543$

Fig. 4-35 Predicted Postbuckling Deflection Patterns, CYL-3A, $[\mp45/0_2]_S$, $L/R = 2$
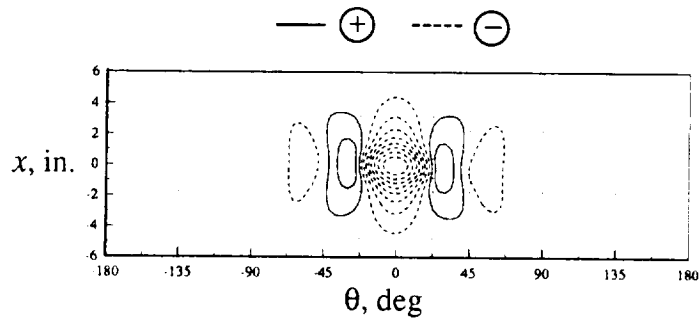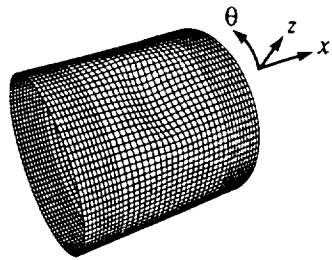
(a) Deflection Pattern, point C in Fig. 4-22 (f), $\Omega/\Omega_{cr} = 0.651$, $M/M_{cr} = 0.543$
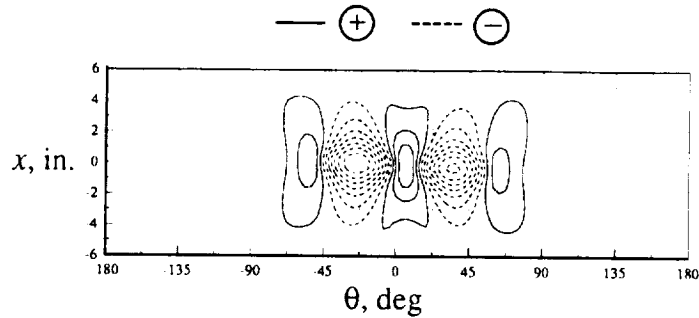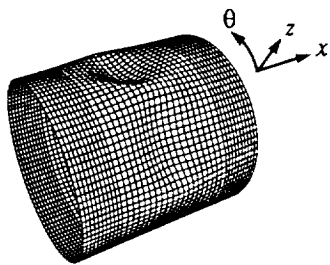
(b) Deflection Pattern, point E in Fig. 4-22 (f), $\Omega/\Omega_{cr} = 0.754$, $M/M_{cr} = 0.564$
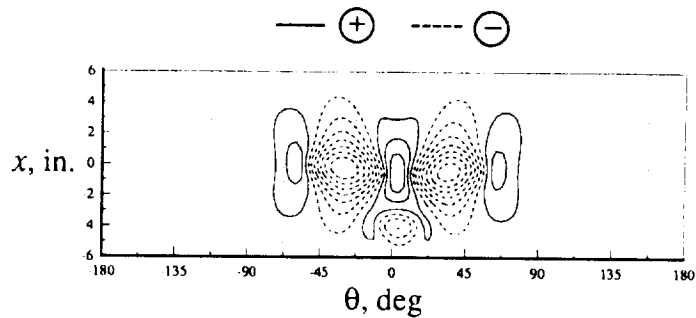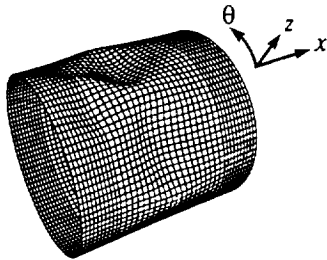
(c) Deflection Pattern, point G in Fig. 4-22 (f), $\Omega/\Omega_{cr} = 0.938$, $M/M_{cr} = 0.627$
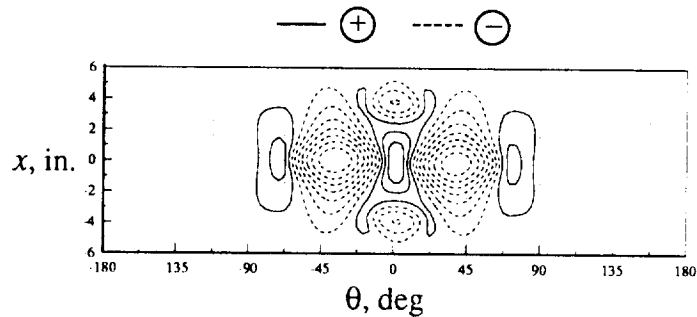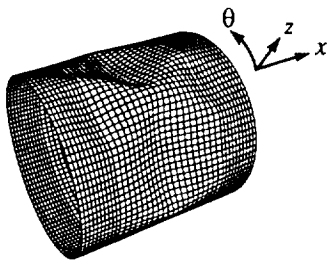
(d) Deflection Pattern, point I in Fig. 4-22 (f), $\Omega/\Omega_{cr} = 1.800$, $M/M_{cr} = 1.054$

Fig. 4-36 Predicted Postbuckling Deflection Patterns, CYL-4B, $[\mp 45/90_2]_S$, $L/R = 2$

(a) Predicted axial strain profile, θ = 0°

(b) Predicted circumferential strain profile, x/L = 0

(c) Measured axial strain profile, θ = 0°

(d) Measured circumferential strain profile, x/L = 0
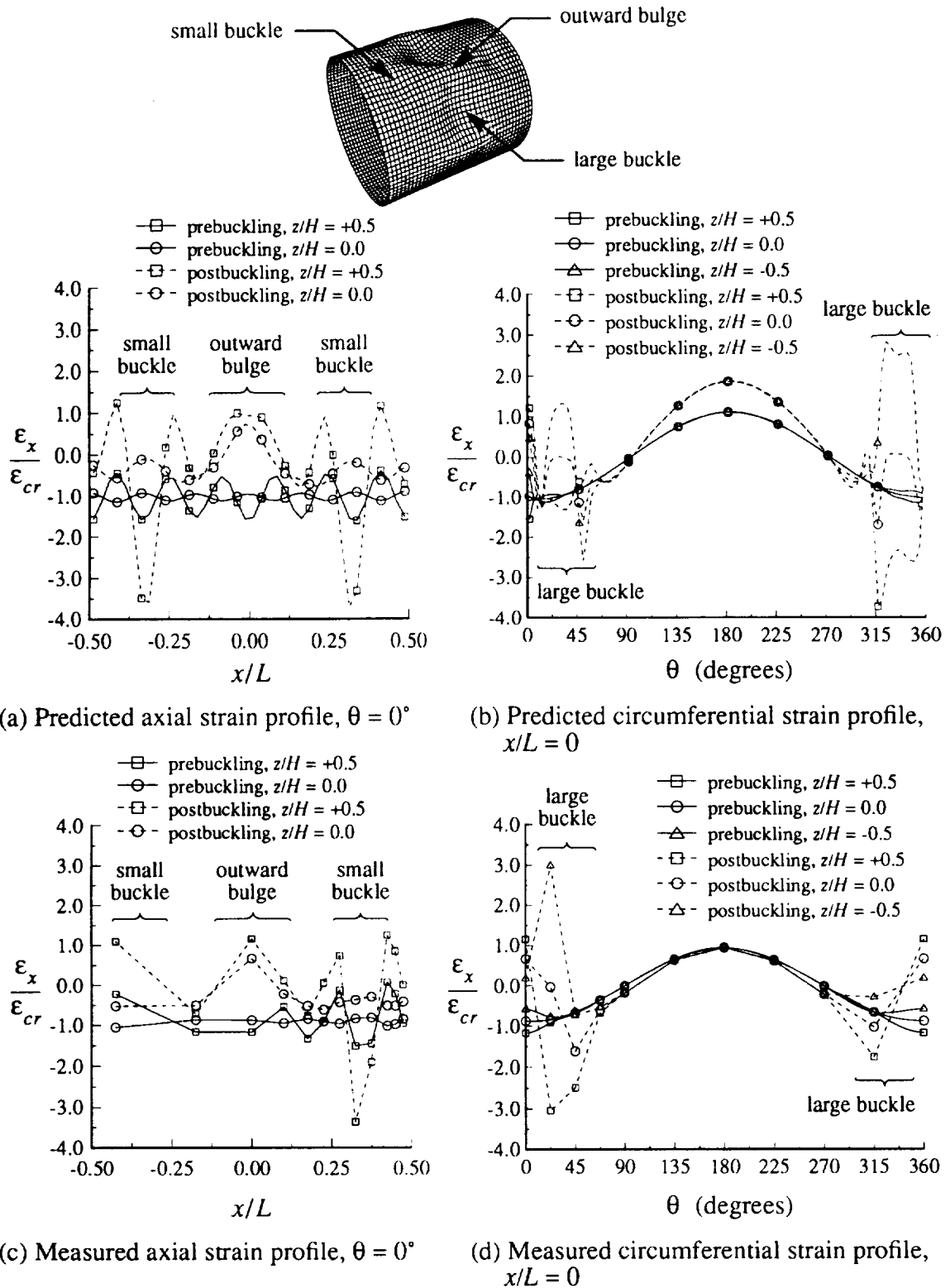
Fig. 4-37 Postbuckling Strain Profile Comparison, CYL-3A, [∓45/0₂]ₛ, L/R = 2

110
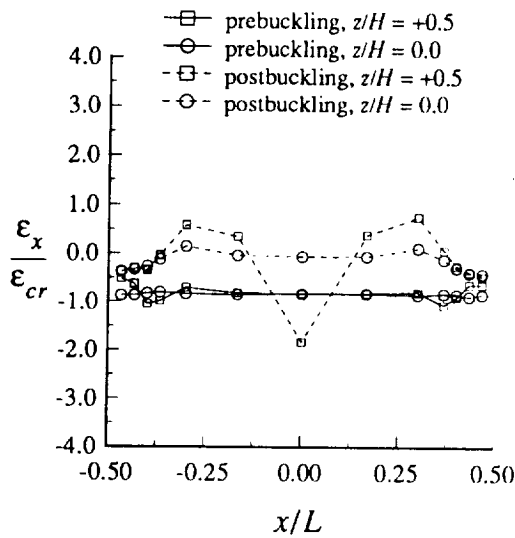
(a) Axial strain profile, $\theta = 0°$
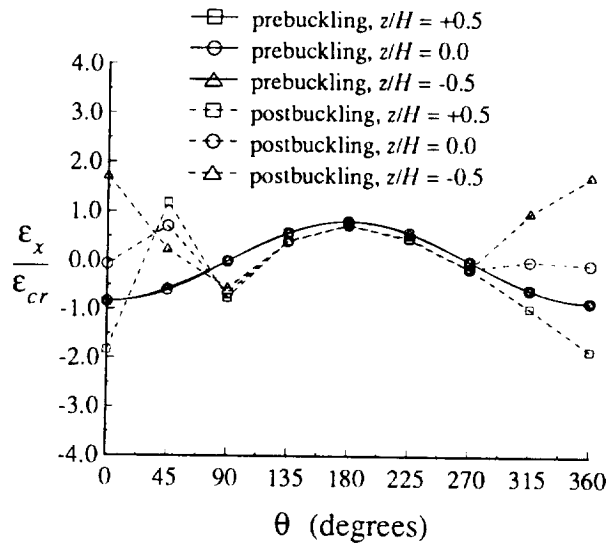
(b) Circumferential strain profile, $x/L = 0$

Fig. 4-38 Measured Postbuckling Strain Profiles, CYL-1A, $[\mp 45/0/90]_S$, $L/R = 2$
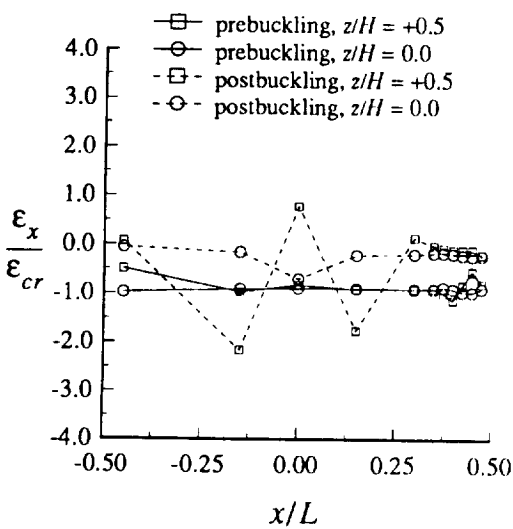
(a) Axial strain profile, $\theta = 0°$
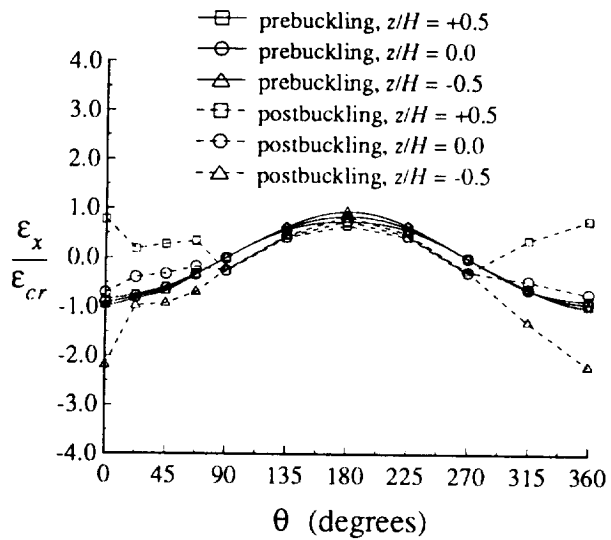
(b) Circumferential strain profile, $x/L = 0$

Fig. 4-39 Measured Postbuckling Strain Profiles, CYL-1B, $[\mp 45/0/90]_S$, $L/R = 2$

Fig. 4-37 (a) exhibits the characteristic prebuckling bending boundary layer along the entire length of the cylinder. The postbuckling strains show a combination of the short prebuckling boundary layer wavelength near the ends of the cylinder and a longer wavelength near the mid-length of the cylinder. These wavelengths correspond to the small inward buckles and the outward bulge shown in the figure. Inward buckles are identified by the comparatively large values of compressive strains on the outer cylinder surface, z/H = +0.5. Similarly, outward bulges are identified by large values of tensile strains. Although the number of strain gage locations are somewhat limited (see Fig. 4-27 (b)), it is clear from Fig. 4-37 (c) that the measured axial strain profile indicates the same features as the predicted strain profile. Fig. 4-37 further demonstrates that the maximum inplane postbuckling strain values occur near the center of the buckles and are up to three times greater than the prebuckling strain values for this specimen.

(a) Axial strain profile, $\theta = 0°$ (b) Circumferential strain profile, $x/L = 0$
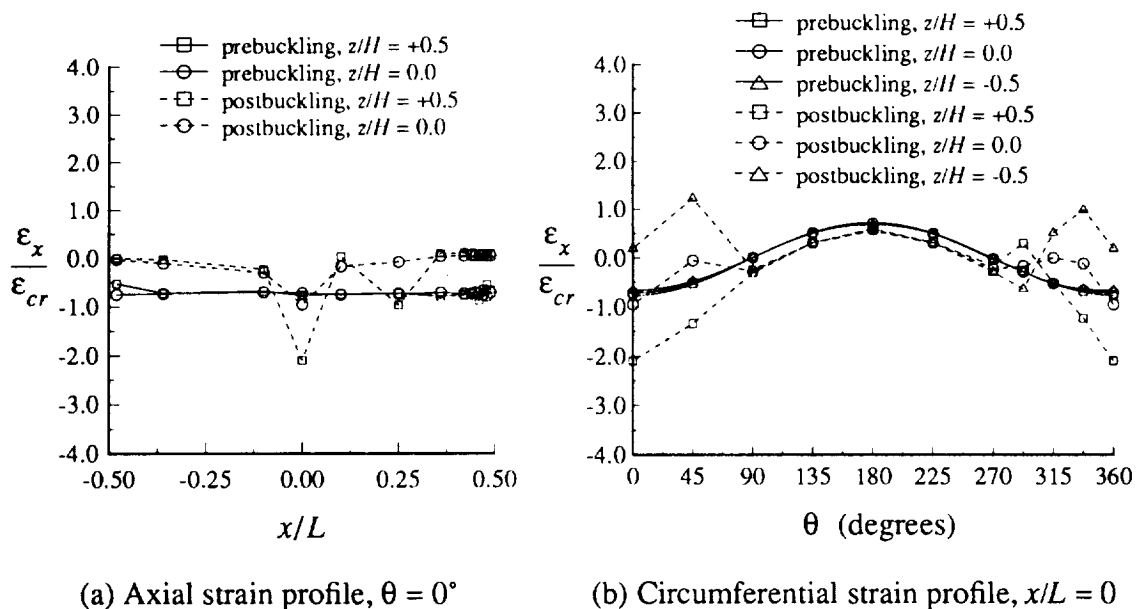
Fig. 4-40 Measured Postbuckling Strain Profiles, CYL-2, $[\mp45/0/90]_S$, $L/R = 5$

The circumferential strain profiles, Fig. 4-37 (b) and (d), exhibit a smoothly varying sinusoidal prebuckling strain distribution, as expected. The perturbations in the postbuckling strain distribution indicate the location of the large buckles on the compression side of the cylinder. The sinusoidal variation of the strains on the tension side of the cylinder, observed in prebuckling, is not appreciably affected by the presence of the buckles.

Although the details of the postbuckling strain profiles for the other specimens vary considerably, similar features are evident. The measured strains confirm that the postbuckling deflection patterns were confined to the compression side of the cylinders in each case. The circumferential distribution of the axial strains on the tension side of the cylinders remained relatively undisturbed after buckling. Locations of the inward buckles, observed in the postbuckling deflection patterns shown in Figs. 4-27 through Fig. 4-32, can be identified by the large compressive strain values at the outer cylinder surface, $z/H = +0.5$. The magnitude of the postbuckling surface strains reached a value of up to three times that of the corresponding maximum prebuckling strain.

(a) Axial strain profile, $\theta = 0°$ (b) Circumferential strain profile, $x/L = 0$
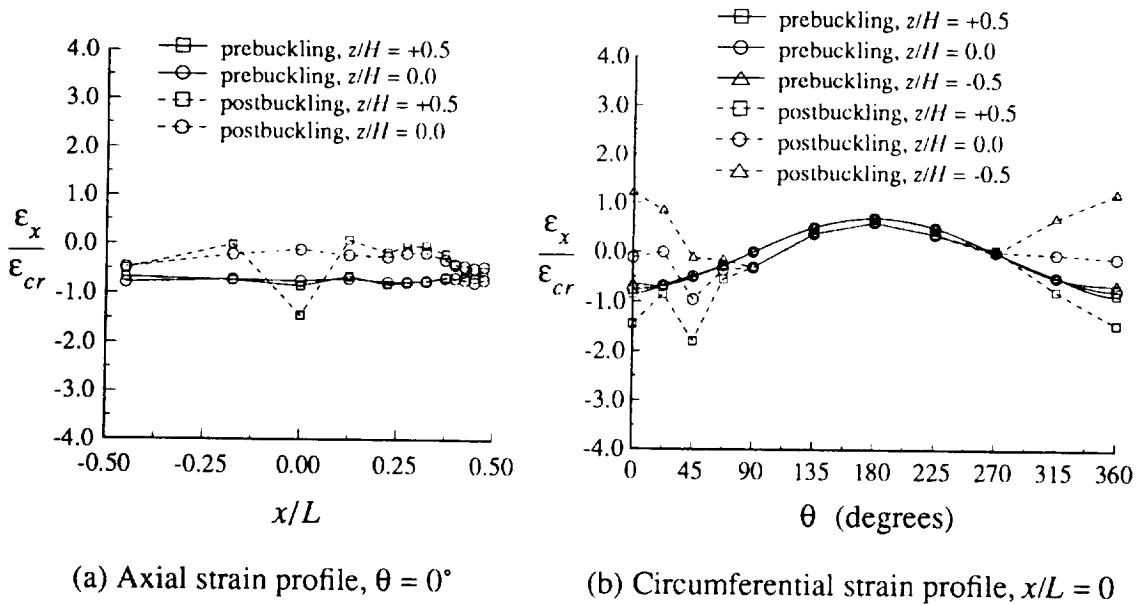
Fig. 4-41 Measured Postbuckling Strain Profiles, CYL-4A, $[\mp 45/90_2]_S$, $L/R = 2$

4.4.3 Postbuckling Material Failure

Observations indicated that material failure was initiated at, or near, the nodal lines of the postbuckling deflection patterns. The locations of visible material damage are indicated on the traces of the postbuckling deflection patterns shown in Figs. 4-27 through Fig. 4-32. Visible material damage at the nodal lines of the postbuckled shapes, rather than at the center of the buckles where the surface strains were maximum, suggests that ultimate failure was induced by an interlaminar shear failure mode. This observation is consistent

with previous investigations of the postbuckling failure characteristics of flat graphite-epoxy plates [92, 93].

Visible material damage was confined to the nodal regions in the $[\mp45/0/90]_S$ and the $[\mp45/0_2]_S$ specimens. Final failure of the $[\mp45/0_2]_S$ specimen was initiated at the nodal lines of the secondary buckles. Material damage in the $[\mp45/90_2]_S$ specimens propagated approximately 270° around the circumference of the specimens, near the mid-length.

(a) Axial strain profile, $\theta = 0°$

(b) Circumferential strain profile, $x/L = 0$
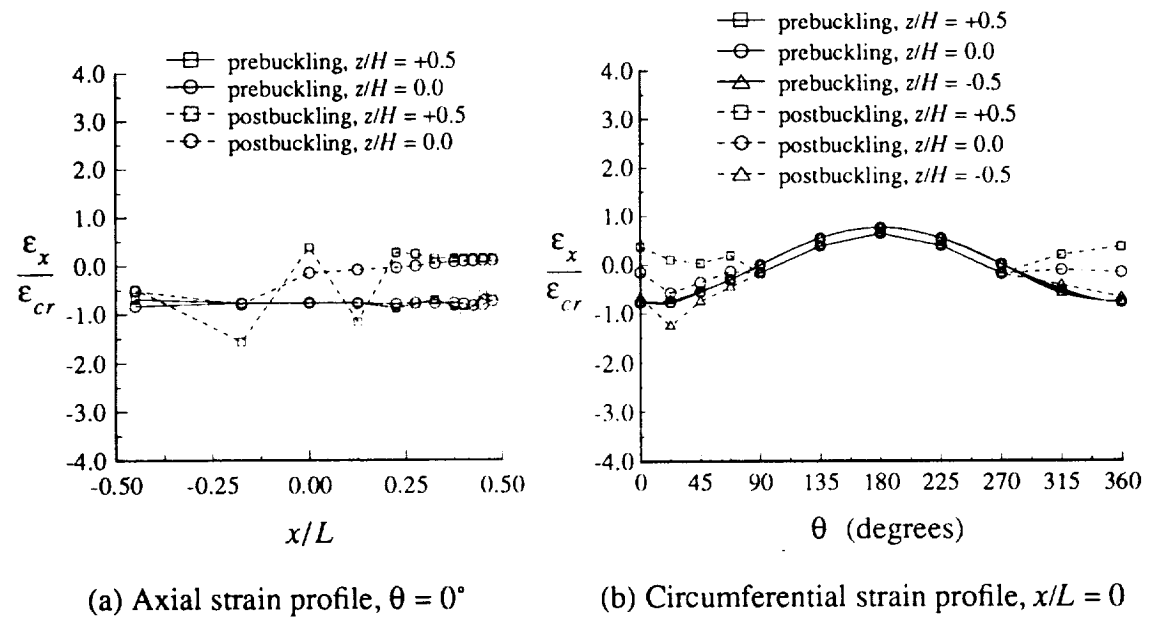
Fig. 4-42 Measured Postbuckling Strain Profiles, CYL-4B, $[\mp45/90_2]_S$, $L/R = 2$

5. Discrepancies

Chapter 4 demonstrated that in most cases the nonlinear character of the measured pre-buckling strain responses in the boundary layer region could be predicted accurately, assuming perfectly clamped boundary conditions. In the case of the $[\mp45/0_2]_S$ specimen, significant discrepancies were observed between the measured and predicted strain amplitudes in the boundary layer region, particularly at higher values of end-rotation. Sections 2.1.3 and 2.1.4 showed that the prebuckling strain responses were sensitive to non-ideal boundary conditions and geometric imperfections. It will be shown that non-ideal boundary conditions may have influenced the prebuckling responses of the $[\mp45/0_2]_S$ specimen.

The classical buckling parameters were previously seen to provide a reasonable first-order approximation to the predicted buckling values. To further explore potential sources of discrepancies between predicted and measured responses, the sensitivity of the classical buckling parameters to the thickness and stiffness properties of the three laminates is investigated.

Another potential source of discrepancies were the ply seams that were introduced during the manufacturing process. To assess the effect of this type of manufacturing defect on the cylinder responses, a preliminary finite element analysis of two typical observed seam types was conducted.

5.1 Non-Ideal Boundary Conditions

Elastic Supports

It was shown in section 2.1.3 that the strain and displacement responses in the boundary layer region were sensitive to the flexibility of the support conditions. Relaxing the radial and the rotational stiffnesses can substantially alter the peak amplitudes and the overall

115

character of the responses. Given the low-stiffness potting compound used in the experiments, it is apparent that some relaxation of the clamped radial and rotational restraints was allowed to take place.

A wide range of elastic stiffness parameters was studied with the nonlinear Donnell analysis in an effort to explain the discrepancies between the measured and predicted responses for the $[\mp45/0_2]_S$ specimen CYL-3A. The axial surface strain at the end of the compression side of the cylinder was taken as a measure of the sensitivity to the boundary conditions. The strain responses were computed at the end-rotation value $\Omega/\Omega_{cr}^{exp} = 0.90$. The results of this parameter study are summarized in Fig. 5-1. The figure shows the effect of an 'elastic' radial support ($K_Q = 1\times10^3$ psi) and a relatively 'rigid' radial support ($K_Q = 1\times10^6$ psi). The flat segments on the curves define the range of values of K_M that correspond to either the 'simple' support or the 'clamped' support conditions. The values of K_M that define the range of 'elastic' support conditions falls in between the indicated simple support and the clamped support regions. The difference between the two curves indicates that the radial stiffness of the supports should be considered in addition to the usual simple support and clamped support conditions. Relative to the strain response with the 'rigid' radial support, 'elastic' radial supports can cause strains at the end of the cylinder to be alleviated by up to 60% for the 'simple' support condition and up to 20% for the clamped 'support' condition.
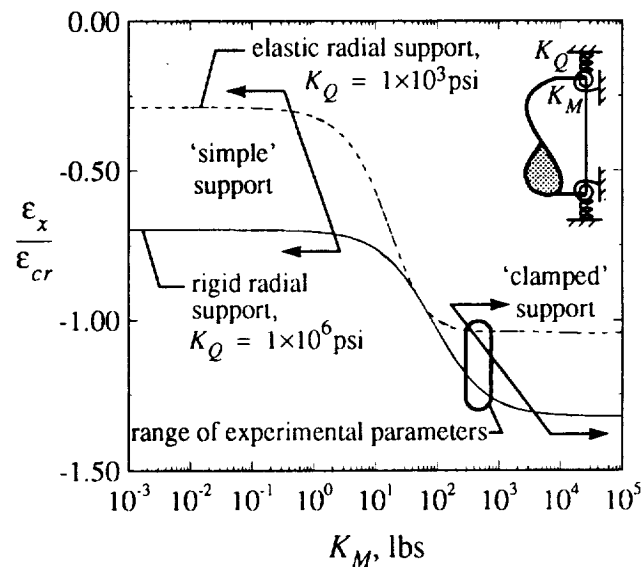
Fig. 5-1 Effect of Elastic Support Parameters

The axial surface strain responses corresponding to K_M = 1 lb, 100 lbs, and 500 lbs are compared to the measured values in Fig. 5-2 (a) and (b) for the elastic and rigid radial supports, respectively. The strains are compared for $\theta = 0°$ and $z/H = +0.5$ for the end-rotation $\Omega/\Omega_{cr}^{exp} = 0.90$. Although optimum correlation is not observed this figure, it is demonstrated that the predicted peak strain responses can reach the values of the measured strains, thus indicating the correct trends.

(a) Rigid Radial Support,
$K_Q = 1 \times 10^6$ psi

(b) Elastic Radial Support,
$K_Q = 1 \times 10^3$ psi
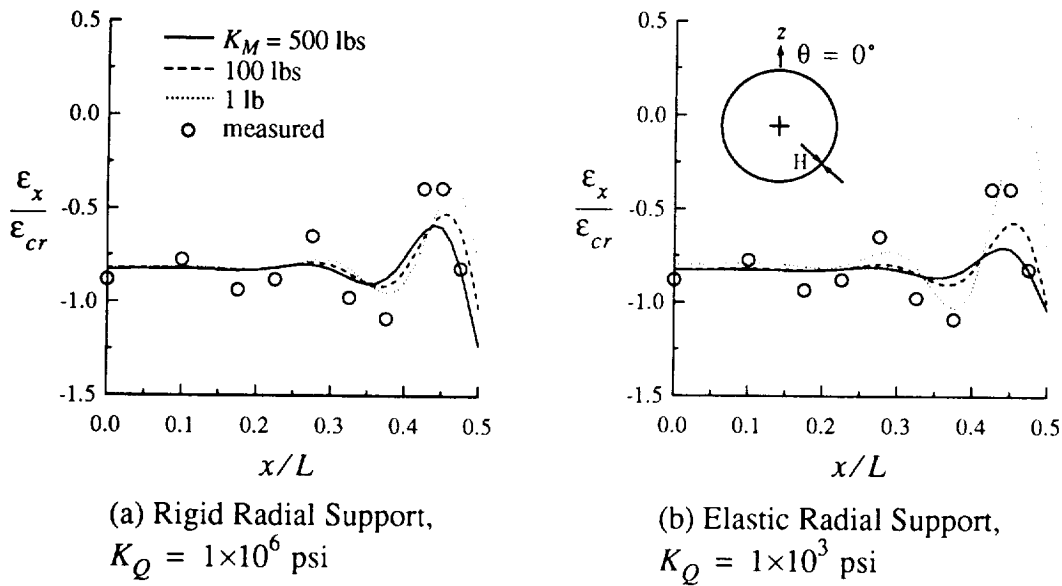
Fig. 5-2 Effect of Elastic Support Conditions

As a matter of interest, it is mentioned here that other investigators have studied the effect of the flexibility of the support conditions on the buckling responses of cylindrical shells. For example, Abramovich et al. [94] used a vibration-correlation technique to define the experimental boundary conditions for the axial compression of metallic stringer-stiffened shells.

Radial End-Deformations

Section 2.1.3 demonstrated that radial end-deformations of 10% to 20% of the cylinder wall thickness substantially affected the peak strain amplitudes in the boundary layer region. During the specimen preparation process it was found in some cases that radial end-deformations resulted from the process of potting the cylinder ends into the loading

rings (see section "Radial Deformations due to Potting Procedure" in Appendix D). The maximum value of radial pinching was 23% of the wall thickness and the maximum value of expansion was 12% of the wall thickness. Although the radial end-deformation data is somewhat limited, it is apparent that radial end-deformations may have been a factor in influencing the measured responses.

Axial Pre-Straining

Compressive axial pre-straining of the test specimens is another possible source of discrepancies in the strain data. Pre-straining of test specimens is difficult to quantify and was assumed to be negligible in the analyses. In the experiments, minor pre-straining was induced while bolting the specimens into the test fixture. The pre-straining was induced by forcing the end surface of the test specimen together with the back plate of the test fixture. Furthermore, deviations from flatness in the ends of the specimen and loading rings and the back plate of the fixture tended to induce local deformations in the specimen.

To determine the severity of the pre-straining effect, the $[\mp45/0/90]_S$ specimen with L/R = 5 was instrumented before being bolted into the test fixture. Also, the face of one of the fixture back plates was measured for flatness. The back plate was found to be flat to within 0.001 to 0.002 inches. Surface shape profiles of the potted ends of the cylinders were measured along a number radii. A typical end-shape profile is shown in Fig. 5-3 (a). The deviation from flatness of the potted cylinder end is plotted as a function of radial position in this figure. The local deviations due to the inner loading ring, low melting-point alloy, tabbed cylinder, and outer loading ring are clearly visible in the end-shape profile. Typically, the difference between the maximum and minimum values was approximately 0.002 to 0.004 inches.

The axial pre-strains were measured both near the end and at the center of specimen after increasing the torque in the mounting bolts. The magnitude of the pre-strains at the mid-length of the cylinder were found to be small in comparison to the strains near the ends, suggesting that the pre-straining was confined to a region near the ends of the specimen. The average end-shape of the midsurface of the specimens, Δ_{ave}, and the axial midsurface pre-strains near the end of the cylinder, ϵ_x^P, are plotted as a function of the circumferential location in Fig. 5-3 (b). The measurement locations are indicated in Fig. 5-3 (a). It is seen from this figure that the strain profile correlates well with the average end-shape, Δ_{ave}. The magnitude of the maximum compressive pre-straining near the end of the cylinder was

118

(a) Specimen End-Shape

(b) Axial Pre-Strains and Average End-Shape as a function of Circumferential Location
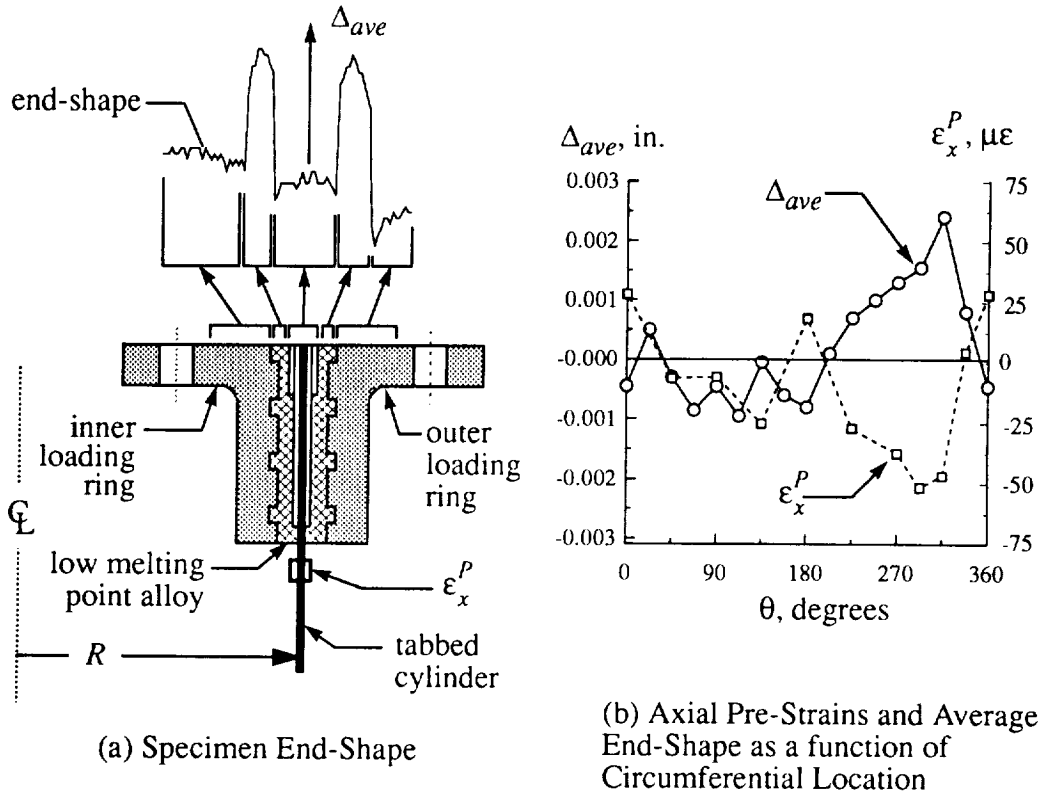
Fig. 5-3 Axial Pre-Loading due to Specimen End-Shape

approximately 75 $\mu\varepsilon$. This maximum pre-strain value represents approximately 1% of the measured buckling strain for the $[\mp45/90_2]_S$ specimens, 2% for the $[\mp45/0/90]_S$ specimens, and 5% for the $[\mp45/0_2]_S$ specimen. Correlation may be slightly improved if pre-straining is accounted for in the analyses, particularly when specimen buckling strains are relatively low, as in the case of the $[\mp45/0_2]_S$ specimen.

Combined Effect of Non-Ideal Boundary Conditions and Initial Imperfections

The investigation of non-ideal boundary conditions demonstrated that the effects of the radial and rotational stiffnesses of the elastic supports, radial end-deformations, and axial pre-straining can be important considerations. It was shown earlier that the strain responses were exacerbated by including the effects of an initial axisymmetric imperfection.

The individual non-ideal parameters were combined to determine whether the measured strain responses for the $[\mp45/0_2]_S$ specimen may have been affected by conditions other than the measured shape imperfection. Numerous combinations of the elastic support stiffness parameters, K_Q and K_M, radial end-deformations, w_R, and a compressive axial pre-strain, ϵ_x^P, were investigated. The measured imperfection shape was simulated by including a mild axisymmetric imperfection of the form given by Eq. (2.35). The non-ideal parameters were varied using the insight gained from the individual parameter studies discussed previously. The result of this exercise is shown in Fig. 5-4 for the end-rotation value $\Omega/\Omega_{cr}^{exp} = 0.90$. The predicted strains for the non-ideal cylinder are compared to the strains predicted for the perfectly clamped cylinder and the measured strains. The strain profiles in the figure are for $\theta = 0°$ and $z/H = +0.5$. It is seen that the correlation between the axial strains on the compression side of the non-ideal cylinder and the measured values can be dramatically improved relative to the perfectly clamped cylinder. Evaluating the buckling capacity using the nonlinear Donnell prebuckling analysis indicates that the non-ideal conditions reduce the buckling capacity of the cylinder by approximately 8% relative to the perfect cylinder.

Similar studies were conducted with the other test specimens. Correlation between the measured and predicted strains showed some improvement for all specimens when considering non-ideal conditions. The non-ideal parameters are summarized in Table 5-1 for all

$$\bar{w}(x, \theta) = -0.005 H \cos\frac{11\pi x}{12}$$

CYL-3A, $[\mp45/0_2]_S$,

$\Omega/\Omega_{cr}^{exp} = 0.90$,

$L/R = 2$,

$R/H = 157.5$,

$z/H = +0.5$

$\theta = 0°$

Non-ideal parameters:

$K_Q = 3{,}000$ psi,

$K_M = 700$ lbs,

$w_R/H = -0.15$,

$\epsilon_x^P = 75 \ \mu\epsilon$
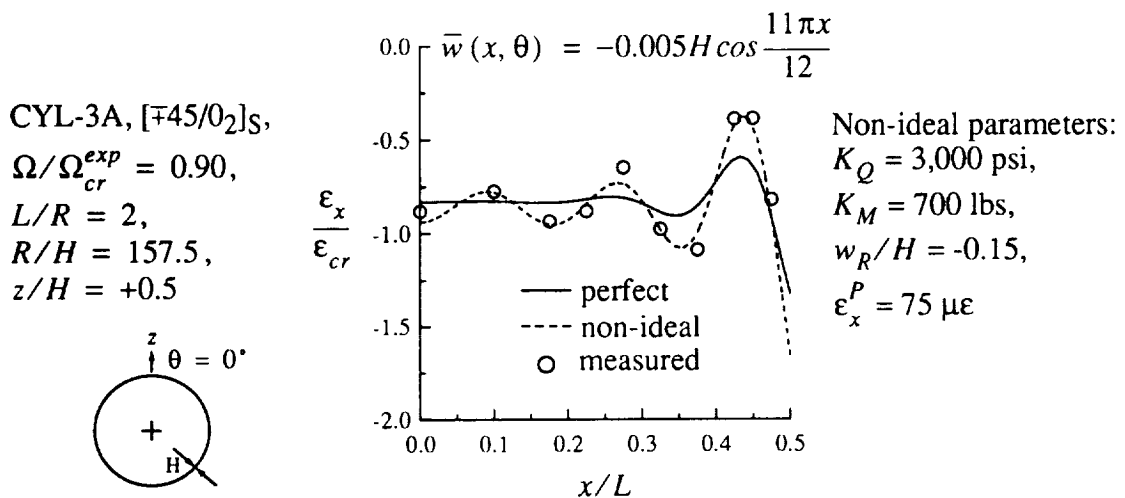
Fig. 5-4 Correlation with Non-ideal Boundary Conditions and Initial Imperfections

specimens. The range of values of K_M and K_Q presented in this table are indicated in Fig. 5-1, which shows that the effective rotational and radial stiffnesses of the supports were somewhat less than those of an ideally clamped support.

Table 5-1 Summary of Non-Ideal Parameters

Specimen Identification Code	Wall Construction	K_Q, psi	K_M, lbs	w_R/H	ϵ_x^P, μs	ξ[a]	m[b]
CYL-1A	[∓45/0/90]$_S$	3,000	300	-0.15	0	-0.001	15
CYL-1B		3,000	300	-0.15	0	-0.001	15
CYL-2		3,000	300	-0.15	0	-0.010	37
CYL-3A	[∓45/0$_2$]$_S$	3,000	700	-0.15	75	-0.005	11
CYL-4A	[∓45/90$_2$]$_S$	8,000	500	-0.05	0	+0.010	17
CYL-4B		8,000	800	-0.05	0	+0.010	17

a. Amplitude parameter for axisymmetric imperfection, $\xi = \bar{w}/H$.

b. Half-wavelength parameter for axisymmetric imperfection, see Eq. (1.2).

5.2 Property Variations

In the analyses, it was assumed that the thickness and stiffness properties the laminates were distributed uniformly throughout each specimen. In practice, some spatial variation of the properties was evident as a result of the manufacturing processes involved in fabricating the specimens (see section "Graphite-Epoxy Cylinder Fabrication" in Appendix D). Local variations in the specimen thickness and stiffness properties can perturb the pre-buckling strain responses and reduce the buckling capacity of the specimens in some instances. To investigate this potential source of discrepancies between the measured and predicted buckling values, a study was conducted to determine the sensitivity of the buckling parameters with regard to various lamina properties.

Variations in Ply Thickness and Material Properties

The sensitivity to variations in the ply thickness, h, and the material properties, E_1, E_2, G_{12}, and v_{12} was evaluated using the classical buckling estimates, Eqs. (2.40) through (2.42). The individual properties were varied about the average property values by $\pm 20\%$

and the resulting buckling parameters were computed for the $[\mp45/0/90]_S$, $[\mp45/0_2]_S$, and $[\mp45/90_2]_S$ laminates. The average properties values were $h = 0.0046$ in., $E_1 = 23.38$ Msi, $E_2 = 1.75$ Msi, $G_{12} = 1.03$ Msi, and $\nu_{12} = 0.285$.

The percent variation of the buckling parameters Ω_{cr}, ε_{cr}, and M_{cr} are plotted in Figs. 5-5 through 5-7 as a function of the percent variation of the ply thickness, the stiffness properties, and Poisson's ratio. Part (a) of each figure corresponds to the variation of Ω_{cr} or ε_{cr}, and part (b) corresponds to the variation of M_{cr}. In studying these figures, it is evident from Fig. 5-5 (a) that the values of Ω_{cr} and ε_{cr} are most sensitive to h. Figs. 5-5 (b) and 5-6 (b) indicate that the values of M_{cr} are most sensitive to h and E_1. Some sensitivity to laminate orthotropy is observed in Figs. 5-6 and 5-7.

(a) Ω_{cr}, ε_{cr} vs. h

(b) M_{cr} vs. h
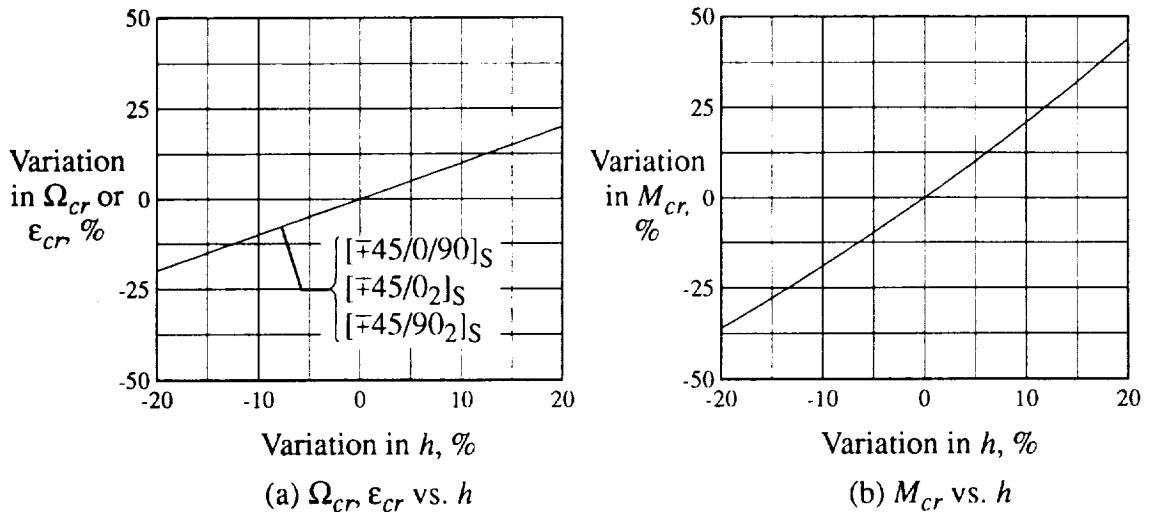
Fig. 5-5 Sensitivity to Ply Thickness

As a matter of interest, the buckling parameters Ω_{cr}, ε_{cr}, and M_{cr} were computed from the classical buckling estimates, Eqs. (2.40) through (2.42), assuming nominal cylinder dimensions and material properties, i.e. $R = 6$ inches and the nominal material properties as given in Table E-2. The resulting values were then compared to the classical buckling estimates computed with the properties corresponding to the test specimens (see Table 4-1). The difference between the buckling parameters assuming nominal properties and the buckling parameters assuming the specimen properties is found to be similar to the 16% to 24% change in E_1 due to the change in fiber volume fraction, V_f, found to occur in the test specimens (see Table E-4).
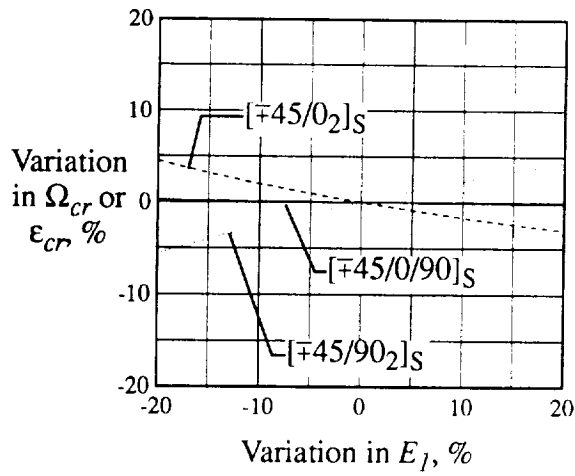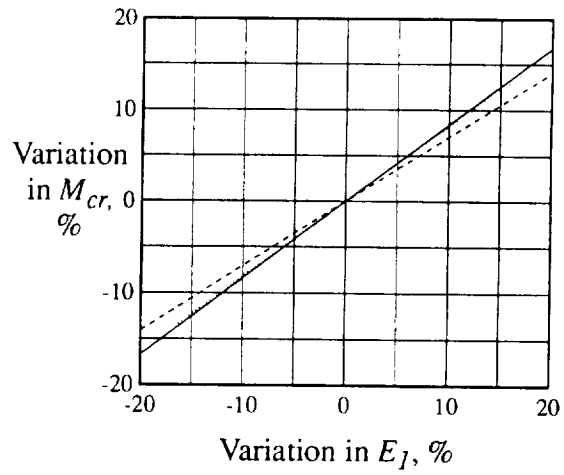
(a) $\Omega_{cr}, \varepsilon_{cr}$ vs. E_1

(b) M_{cr} vs. E_1
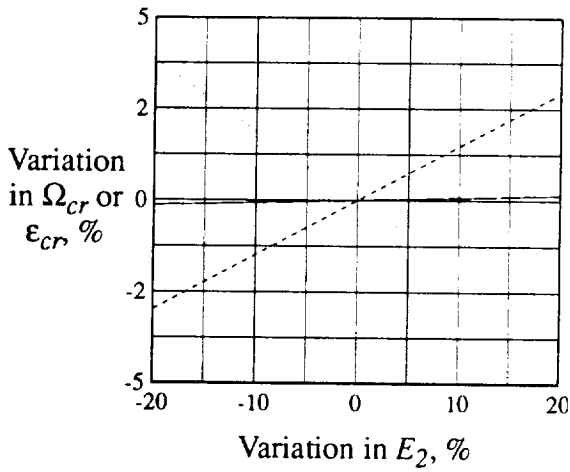
(c) $\Omega_{cr}, \varepsilon_{cr}$ vs. E_2
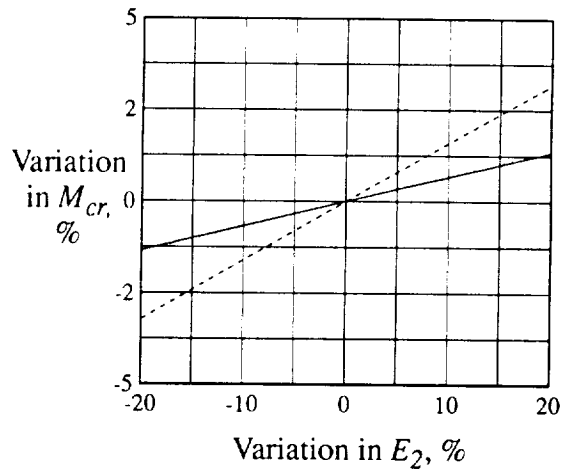
(d) M_{cr} vs. E_2
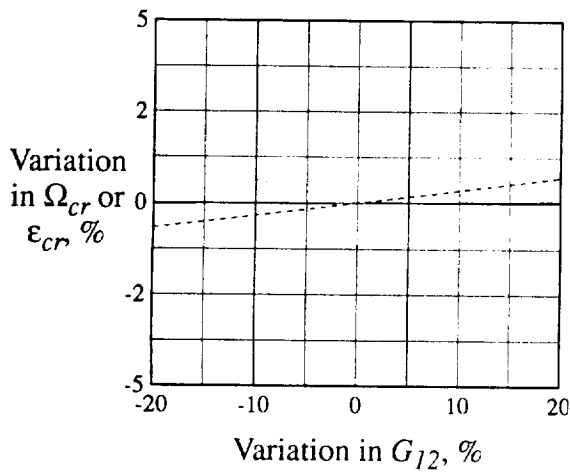
(e) $\Omega_{cr}, \varepsilon_{cr}$ vs. G_{12}
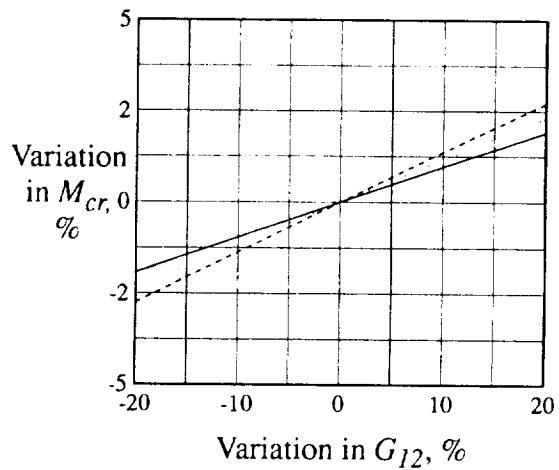
(f) M_{cr} vs. G_{12}

Fig. 5-6 Sensitivity to Stiffness Properties

123

(a) $\Omega_{cr}, \varepsilon_{cr}$ vs. v_{12} (b) M_{cr} vs. v_{12}
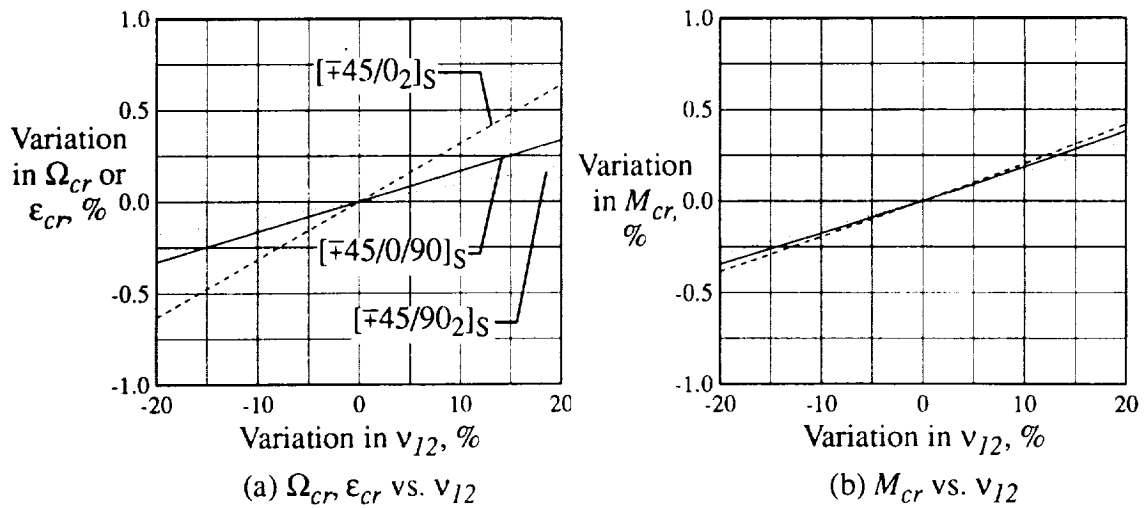
Fig. 5-7 Sensitivity to Poisson's Ratio

Post-failure thickness surveys of two circumferential locations on the undamaged tensile sides of the specimens with $L/R = 2$ were conducted. The results of the thickness survey are summarized in Table 5-2. The mean wall thickness, and the minimum and maximum thickness values are reported in the table. The minimum and maximum values are given as

Table 5-2 Thickness Survey[a]

Specimen Identification Code	Wall Construction	Mean[b] Thickness, in.	Minimum Thickness, %	Maximum Thickness, %
CYL-1A		0.0368	-4.4	+10.1
CYL-1B	$[\mp45/0/90]_S$	0.0384	-5.2	+14.1
CYL-2		n/a[c]		
CYL-3A	$[\mp45/0_2]_S$	0.0389	-4.9	+7.2
CYL-4A		0.0389	-6.4	+6.9
CYL-4B	$[\mp45/90_2]_S$	0.0390	-6.4	+8.2

a. Axial scans were conducted at $\theta = 157.5°$ and $202.5°$.

b. Computed from 188 measurements points.

c. Thickness data not available.

the percent difference relative to the mean thickness. The minimum thickness values are 4% to 6% less than the mean thickness and the maximum thickness values are 7% to 14%

greater than the mean thickness. Comparing the minimum thickness values in Table 5-2 to those in Fig. 5-5 suggests that locations of minimum thickness on the compression side of the specimens may have led to slight reductions in the buckling values.

5.3 Ply Seams

Thickness and stiffness discontinuities were sometimes the result of the ply seams that were introduced during the fabrication process (see section "Graphite-Epoxy Cylinder Fabrication" in Appendix D). To investigate the sensitivity to this type of manufacturing defect, two small strips were cut from a $[\mp45/0_2]_S$ cylinder. The edges of the strips were polished and photographed under a microscope. Photomicrographs of internal overlap and gap seams are shown in Figs. 5-8 (a) and (b), respectively. The two outer dark layers on the top and the bottom of the laminate indicate the locations of the $\mp45°$ plies and the four light layers indicate the $0°$ plies. The overlap seam occurs in $+45°$ ply that is adjacent to a $0°$ ply. The gap seam is the result of a gap in a $+45°$ ply adjacent to a $0°$ ply. The characteristic dimensions of the seams illustrated in Fig. 5-8 are on the order of the laminate wall thickness.

A preliminary analysis was conducted to assess the effect of the seams. Both overlap and gap seams were modeled as stiffness discontinuities using the STAGS finite element program. Overlap and gap seams were modeled with the stiffness properties of an appropriate 9-ply laminate and 7-ply laminate, respectively. A number of axial, helical, and circumferential seams were analyzed. The axial seams were located at $\theta = 0°$ and the helical and circumferential seams were oriented to perturb the boundary layer regions on the compression side near the ends of the cylinders.

The effect of the seams was assessed by conducting a nonlinear prebuckling analysis and then a linear bifurcation analysis. Both perfect and imperfect cylinder geometries were considered. The net effect of the seams was to locally perturb the prebuckling displacements. The seams had only a minor effect on the buckling end-rotation of the cylinders, typically on the order of 1%. It was therefore concluded that these particular types of gap and overlap seams had a negligible effect on the buckling response of the specimens. However, the effect of ply seams may be significant for other loading conditions, such as internal pressure.
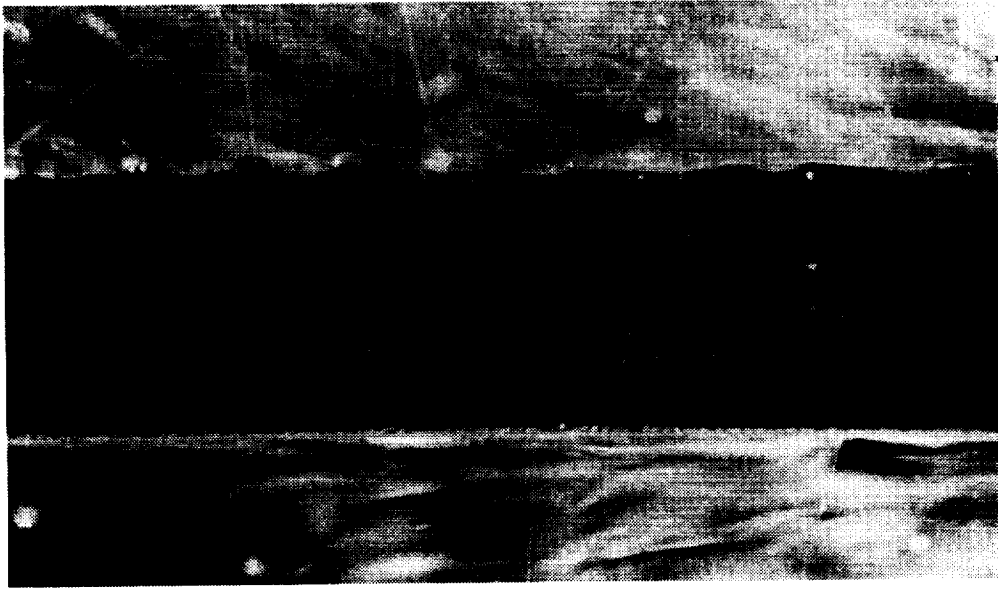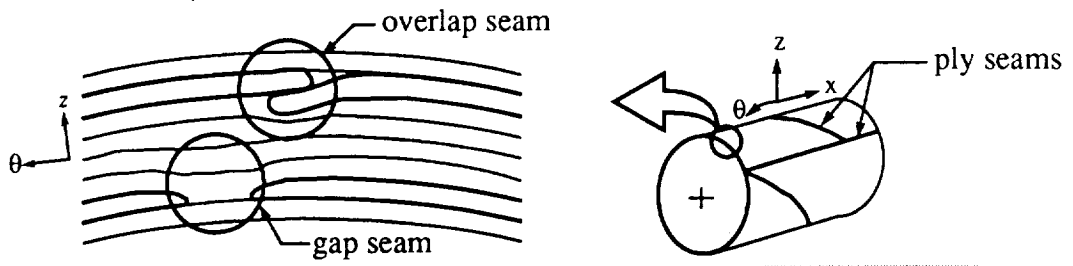
(a) Overlap seam
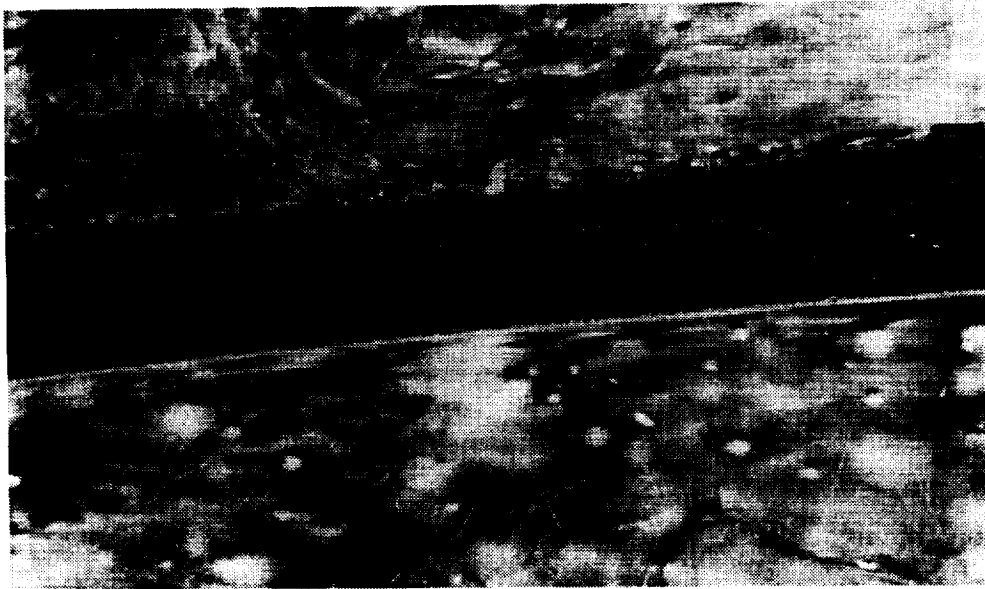
(b) Gap seam

Fig. 5-8 Photomicrographs Showing Ply Seams

126

6. Conclusions and Recommendations

The goal of the present work was to accurately predict the behavior of thin-walled composite cylinders subjected to bending. Typical applications include transport aircraft fuselage structures, launch vehicles, transportation and storage containers, etc. To achieve the stated goal, an in-depth numerical and experimental investigation of the bending behavior of six eight-ply graphite-epoxy cylinders was conducted. The cylinders had a nominal radius of six inches, a length-to-radius ratio of 2 and 5, and a radius-to-thickness ratio of approximately 160. A $[\mp45/0/90]_S$ quasi-isotropic layup and two orthotropic layups, $[\mp45/0_2]_S$ and $[\mp45/90_2]_S$, were studied.

A geometrically nonlinear special-purpose analysis, based on Donnell's nonlinear shell equations, was developed to study the prebuckling responses due to bending, and gain insight into the effects of non-ideal boundary conditions and initial geometric imperfections. A geometrically nonlinear finite element analysis was utilized to compare with the prebuckling solutions of the special-purpose analysis and to study the buckling and postbuckling responses of both geometrically perfect and imperfect cylinders. An analytical approximation of the measured shape imperfections was employed to represent the imperfect cylinder geometries. Extensive experimental data were acquired electronically from quasi-static tests of six specimens using a test fixture specifically designed for the present investigation. The experimental data were compared to predictions for both perfect and imperfect cylinder geometries. Prebuckling results were presented in the form of displacement and strain profiles. Buckling end-rotations, moments, and strains were reported, and predicted mode shapes were presented. Observed and predicted moment vs. end-rotation relations, deflection patterns, and strain profiles were illustrated for the postbuckling responses.

127

6.1 Conclusions

The conclusions drawn from this investigation are presented according to the three major response categories of prebuckling, buckling, and postbuckling. Comments are also made regarding observed material failure.

6.1.1 Prebuckling

The analyses and measured data clearly indicate that a geometrically nonlinear analysis is required to accurately predict the bending boundary layer that develops from the ends of the cylinder. The boundary layer is confined to a region near the end of the cylinder on the tension side, but develops along the length of the cylinder on the compression side as the end-rotation is increased. It is further concluded that the overall displacement and strain responses and the character of the boundary layer regions are sensitive to the orthotropy of the laminates, the radius and thickness of the cylinders, the value of applied end-rotation, and the initial geometric imperfections. For example, regarding the sensitivity to orthotropy, compared to a quasi-isotropic $[\mp 45/0/90]_S$ cylinder with a radius equal to 6 inches, the attenuation length of the boundary effects is 23% longer for a $[\mp 45/0_2]_S$ cylinder, and 16% shorter for a $[\mp 45/90_2]_S$ cylinder.

It is concluded from discrepancies observed between the measured and predicted strains for some specimens that non-ideal boundary conditions can have a measurable effect on the prebuckling responses in the boundary layer region. In particular, radial stiffness of the supports should be considered, in addition to the rotational stiffness of the supports. In comparison to 'rigid' radial supports, 'elastic' radial supports can alleviate strains at the end of a cylinder by up to 60% for 'simple' support conditions and up to 20% for clamped 'support' conditions. Additionally, geometric imperfections with amplitudes of only 1% of the cylinder wall thickness can exacerbate the peak amplitudes of the prebuckling responses when the imperfection contains the axial half-wave length corresponding to the characteristic half-wave length of the boundary layer responses. The peak amplitudes are also exacerbated by radial deformations applied to the cylinder ends.

6.1.2 Buckling

With regard to buckling, it can be concluded from the classical buckling analysis, the special use of the prebuckling analysis, and the finite element buckling predictions that the orthotropy of the laminates greatly influences the buckling end-rotation and strain values,

and to a lesser extent, the buckling moment values. Further, accurate buckling predictions can be obtained from a bifurcation analysis conducted relative to a nonlinear prebuckling state in consideration of analytical representations of measured initial geometric shape imperfections. The measured buckling end-rotations are 6% to 20% less than the predicted buckling values. For cylinders with $L/R = 2$, the average measured buckling moment values for the orthotropic $[\mp45/90_2]_S$ and $[\mp45/0_2]_S$ cylinders are approximately 10% and 20%, respectively, less than those for the quasi-isotropic $[\mp45/0/90]_S$ cylinders. The measured buckling moment for the quasi-isotropic $[\mp45/0/90]_S$ cylinder with $L/R = 5$ is approximately 10% less than the average buckling moment for the $[\mp45/0/90]_S$ cylinders with $L/R = 2$. The predicted buckling moment values compare similarly. Regarding the measured buckling strain and end-rotation values for cylinders with $L/R = 2$, the average values for the orthotropic $[\mp45/0_2]_S$ cylinder are approximately one half of the average measured buckling values for the $[\mp45/0/90]_S$ cylinders, and the average buckling values for the orthotropic $[\mp45/90_2]_S$ cylinders are approximately twice the corresponding buckling values. Finally, the measured buckling strain value for the $[\mp45/0/90]_S$ cylinder with $L/R = 5$ is slightly less than the average buckling strain value for the $[\mp45/0/90]_S$ cylinders with $L/R = 2$. The corresponding buckling end-rotation is slightly greater than two times the average end-rotation value for the $[\mp45/0/90]_S$ cylinders with $L/R = 2$. The predicted buckling strain and end-rotation values compare similarly.

With regard to anisotropy, it is concluded that skewing of the predicted buckling shapes is induced by the presence of the bending stiffness terms, D_{16} and D_{26}. The buckling shapes corresponding to the $[\mp45/90_2]_S$ cylinders exhibit significant skewing compared to the shapes for the $[\mp45/0/90]_S$ and $[\mp45/0_2]_S$ cylinders. Also, as was observed with the $[\mp45/0_2]_S$ cylinder with $L/R = 2$, outward radial prebuckling deflections on the compression side of the cylinder, controlled to some extent by the orthotropy of the laminate, may tend to improve the stability of the prebuckling behavior.

The buckling resistance of the cylinders is most sensitive to variations in the ply thickness, h, somewhat sensitive to variations in the longitudinal Young's modulus, E_1, and relatively insensitive to variations in E_2, G_{12}, and v_{12}. Also, observed gap and overlap ply seams appear to have negligible influence on the predicted buckling end-rotation of the cylinders.

6.1.3 Postbuckling

Finite element analyses of the specimens required considerable computational effort to obtain the postbuckling responses and were typically marked by numerical difficulties. Successful analyses provide valuable insight into the postbuckling behavior. The postbuckling responses indicate an equilibrium path with numerous scallop-shaped branches that are comprised of both stable and unstable segments. Each branch corresponds to a unique postbuckling deflection pattern. The experimentally observed postbuckling deflection patterns and strain profiles show strikingly similar features to the predictions for all three laminates.

The predicted postbuckling moment vs. end-rotation relations provide a lower bound estimate for the buckling moment for cylinders with known shape imperfections. Lower bound estimates are shown to depend on the cylinder layup and length. For the cylinders with $L/R = 2$, the lower bound estimates for the buckling moments were approximately 45%, 50%, and 60% less than the predicted buckling moment values corresponding to the geometrically perfect $[\mp 45/0_2]_S$, $[\mp 45/0/90]_S$, and $[\mp 45/90_2]_S$ cylinders, respectively. The corresponding estimate was 60% less than the predicted buckling moment for the geometrically perfect $[\mp 45/0/90]_S$ cylinder with $L/R = 5$. Comparing the lower bound estimates for the cylinders with $L/R = 2$ suggests that the $[\mp 45/0_2]_S$ cylinder has the greatest absolute lower bound moment capacity, followed by the $[\mp 45/0/90]_S$ and the $[\mp 45/90_2]_S$ cylinders.

6.1.4 Material Failure

Material failure is not an issue in the prebuckling of the thin-walled cylinders considered in this investigation. The large deflections observed during the buckling process induced only minor visible material damage in some cylinders. Further visible material damage is initiated in the vicinity of the nodal lines of the postbuckling deflection patterns during continued loading in the postbuckling range. Ultimate failure is initiated at these same locations. From the observed failure locations, it is concluded that ultimate failure can be attributed to an interlaminar shear failure mode. The extent of observed material damage indicates that hoop-stiff cylinders are less effective in containing material damage than quasi-isotropic and axially-stiff cylinders.

6.2 Recommendations for Further Research

A number of issues regarding the theoretical and experimental aspects of the present study are felt to be important but were not considered in this investigation. Some of these are:

1. The special use of the Donnell theory prebuckling analysis indicated that non-ideal boundary conditions can reduce the buckling resistance of the cylinders. Further investigations should be conducted to determine how non-ideal conditions can influence the buckling values and modes.

2. The classical buckling parameters were shown to be relatively sensitive to variations in the cylinder wall thickness. It remains to be shown whether models that include local cylinder wall thickness variations can lead to improved correlation between predicted and measured buckling values.

3. Transverse shear deformations may be an important consideration with the short wavelength responses observed in the prebuckling boundary layer region. This effect should be investigated.

4. The postbuckling interlaminar shear failure mode should be investigated numerically as new versions of the STAGS postprocessing program become available.

5. As the next step toward the understanding of composite structures, such as an aircraft fuselage or a launch vehicle, it is recommended to study the important loading condition of combined bending and internal pressure. The present analytical tools and experimental apparatus are ideally suited for such an investigation.

6. A further extension of the present work would be to investigate the bending responses of cylinders with other layups and geometries. Also, cylinders with stiffeners, cutouts, and impact damage could be investigated.

References

1. Tennyson, R.C., Chan, K., Muggeridge, D.B., "The Effect of Axisymmetric Shape Imperfections on the Buckling of Laminated Anisotropic Circular Cylinders," *C.A.S.I. Transactions*, Vol. 4, No. 2, September 1971, pp. 131-139.

2. Tennyson, R. C., "Buckling of Laminated Composite Cylinders: A Review," *Composites*, January, Vol. 1, 1975, pp. 17-24.

3. Simitses, G. J., "Buckling and Postbuckling of Imperfect Cylindrical Shells: A Review," *Applied Mechanics Review*, Vol. 39, No. 10, October, 1986.

4. Adams, S. F., Maiti, M., Mark, R. E., "Three-Dimensional Elasticity Solution of a Composite Beam," *Journal of Composite Materials*, Vol. 1, 1967, pp. 122-135.

5. dos Reis, H. L. M., Goldman, R. B., "Thin-Walled Laminated Composite Cylindrical Tubes: Part II - Bending Analysis," *Journal of Composites Technology & Research*, Vol. 9, No. 2, Summer, 1987, pp. 53-57.

6. Nicol, D. A. C., "Bending and Flexure of Reinforced Tube," *J. Inst. Maths Applics*, Vol. 21, 1978, pp. 117-126.

7. Pagano, N. J., "Pure Bending of Helical Wound Composite Cylinders," *Analysis of the Test Methods for High Modulus Fibers and Composites*, ASTM Special Technical Publication 521, 1973, pp. 255-263.

8. Reissner, E., Tsai, W. T., "Pure Bending, Stretching, and Twisting of Anisotropic Cylindrical Shells," *Journal of Applied Mechanics*, Vol. 94, March, 1972, pp. 148-154.

9. Reissner, E., Tsai, W. T., "On Pure Bending and Stretching of Orthotropic Laminated Cylindrical Shells," *Journal of Applied Mechanics*, Vol. 41, March, 1974, pp. 168-172.

References

10. Fuchs, H. P., Hyer, M. W., "The Bending Response of Thin-Walled Laminated Composite Cylinders," *Composite Structures*, Vol. 22, 1992, pp. 87-107.

11. Fuchs, H. P., Hyer, M. W., "The Nonlinear Bending Response of Thin-Walled Laminated Composite Cylinders," AIAA Paper No. 92-2230CP, *Proceedings of the 33rd Structures, Structural Dynamics, and Materials Conference*, Dallas, TX, April 13-15, 1992, pp. 70-78.

12. Flügge, W., "Die Stabilität der Kreiszylinderschale," *Ingenieur-Archiv*, III. Band, 5 Heft, 1932, pp. 486-491, 501-506 (also *Stresses in Shells*, 2nd ed., Springer-Verlag, New York, NY, 1973, pp. 478-490.)

13. Seide, P., Weingarten, V. I., "On the Buckling of Circular Cylindrical Shells Under Pure Bending," *Journal of Applied Mechanics*, Vol. 28, March, 1961, pp. 112-116.

14. Bijlaard, P. P., Gallagher, R. H., "Elastic Instability of a Cylindrical Shell Under Arbitrary Circumferential Variation of Axial Stress," *Journal of the Aerospace Sciences*, Vol. 27, No. 11, November, 1960, pp. 854-859.

15. Libai, A., Durban, D., "Buckling of Cylindrical Shells Subjected to Nonuniform Axial Loads," *Journal of Applied Mechanics*, Vol. 44, No. 4, December, 1977, pp. 714-719.

16. Peterson, J. P., Seide, P., Weingarten, V. I., "Buckling of Thin-Walled Circular Cylinders," NASA SP-8007, NASA Space Vehicle Design Criteria, September 1965, rev. August, 1968.

17. Block, D. L., "Buckling of Eccentrically Stiffened Orthotropic Cylinders Under Pure Bending," NASA TN D-3351, 1966.

18. Holston, A., Jr., "Buckling of Inhomogeneous Anisotropic Cylindrical Shells by Bending," *AIAA Journal*, Vol. 6, No. 10, October, 1968, pp. 1837-1841.

19. Karyadi, E., "Buckling of Circular Cylindrical Shells Subjected to Combined Loads (Axial Compression, Normal Pressure, Bending and Transverse Shear Loading)," Delft University of Technology, Memorandum M-663, Delft, The Netherlands, September, 1992.

20. Knops, H. A. J., "Buckling of Anisotropic Cylindrical Shells Subjected to Combined Axial Compression, Normal Pressure, Bending and Shear Loading," Delft University of Technology, Report LR-611, Delft, The Netherlands, December, 1989.

References

21. Lou, K. A., Yaniv, G., "Buckling of Circular Cylindrical Composite Shells under Axial Compression and Bending Loads," *Journal of Composite Materials*, Vol. 25, No. 2, February, 1991, pp. 162-187.

22. Mah, G. B., Almroth, B. O., Pittner, E.V., "Buckling of Orthotropic Cylinders," *AIAA Journal*, Vol. 6, No. 4, April, 1968, pp. 598-602.

23. Ugural, A. G., Cheng, S.,"Buckling of Composite Cylindrical Shells under Pure Bending," *AIAA Journal*, Vol. 6, No. 2, February, 1968, pp. 349-354.

24. Villhart, V., Bang, C., Palazotto, A. N., "Instability of Short Stiffened and Composite Cylindrical Shells Under Bending with Prebuckling Displacements," *Computers & Structures*, Vol. 16, No. 6, 1983, pp. 773-775.

25. Peterson, J. P., Anderson, J. K., "Structural Behavior and Buckling Strength of Honeycomb Sandwich Cylinders Subjected to Bending," NASA TN D-2926, August, 1965.

26. Gellatly, R. A., Gallagher, R. H., "Sandwich Cylinder Instability under Nonuniform Axial Stress," *AIAA Journal*, Vol. 2, No. 2, February, 1964, pp. 398-400.

27. Reese, C. D., Bert, C. W., "Buckling of Orthotropic Sandwich Cylinders Under Axial Compression and Bending," *Journal of Aircraft*, Vol. 11, No. 4, April, 1974, pp. 207-212.

28. Wang, C. T., Vaccaro, R. J., Desanto, D. F., "Buckling of Sandwich Cylinders under Combined Compression, Torsion, and Bending Loads," *Journal of Applied Mechanics*, Vol. 22, No. 3, September, 1966, pp. 324-328.

29. Brazier, L. G., "The Flexure of Thin Cylindrical Shells and Other 'Thin' Sections," *Late of the Royal Aircraft Establishment*, Reports and Memoranda No. 1081 (M.49.), May, 1926 (also "On The Flexure of Thin Cylindrical Shells and Other 'Thin' Sections," *Proceedings of the Royal Society of London*, Series A, Vol. 116, 1927, pp. 104-114.)

30. Chwalla, E., "Reine Biegung Schlanker, Dünnwandiger Rohre mit Gerader Achse," *Zeitschrift für Angewandte Mathematik und Mechanik*, Vol. 13, 1933, pp. 48-53.

31. Na, T. Y., Turski, C. E., "Solution of the Non-Linear Differential Equations for Finite Bending of a Thin-Walled Tube by Parameter Differentiation," *Aeronautical Quarterly*, Vol. 25, Part 1, February, 1974, pp. 14-18.

References

32. Reissner, E., "On Finite Bending of Pressurized Tubes," *Journal of Applied Mechanics*, Vol. 26, September, 1959, pp. 386-392.

33. Reissner, E., "On Finite Pure Bending of Cylindrical Tubes," *Österreichesches Ingenieur-Archiv*, Vol. 15, 1961, pp. 165-172.

34. Reissner, E., Weinitschke, H. J., "Finite Pure Bending of Circular Cylindrical Tubes," *Quarterly of Applied Mathematics*, Vol. XX, No. 4, January, 1963.

35. Thurston, G. A., "Newton's Method Applied to Problems in Nonlinear Mechanics," *Journal of Applied Mechanics*, Vol. 32, No. 2, June, 1965.

36. Thurston, G. A., "Critical Bending Moment of Circular Cylindrical Tubes," *Journal of Applied Mechanics*, Vol. 44, Series E, No. 1, March, 1977, pp. 173-174.

37. Weinitschke, H. J., "Die Stabilität Elliptischer Zylinderschalen Bei Reiner Biegung," *Zeitschrift für Angewandte Mathematik und Mechanik*, Vol. 50, 1970, pp. 411-422.

38. Wood, J. D., "The Flexure of a Uniformly Pressurized Circular, Cylindrical Shell," *Journal of Applied Mechanics*, Vol. 80, December, 1958, pp. 453-458.

39. Kedward, K. T., "Nonlinear Collapse of Thin-Walled Composite Cylinders Under Flexural Loading," *Proceedings of the 2nd International Conference on Composite Materials (ICCM2)*, Toronto, 1978, pp. 353-365.

40. Stockwell, A. E., Cooper, P. A., "Collapse of Composite Tubes Under End Moments," *Proceedings of the 33rd Structures, Structural Dynamics, and Materials (SDM) Conference*, Dallas, TX, April 13-15, 1992.

41. Axelrad, E. L., "Pinpointing the Upper Critical Bending Load of a Pipe by Calculating Geometric Nonlinearity," Akademii Nauk SSSR, *Izvestiya Mekhanika*, Vol. 4, 1965, pp. 133-139.

42. Calladine, C. R., *Theory of Shell Structures*, Cambridge University Press, Cambridge, U. K., 1983, pp. 614-621.

43. Almroth, B. O., Starnes, J. H., Jr., "The Computer in Shell Stability Analysis," *Journal of the Engineering Mechanics Division*, ASCE, Vol. 101, No. EM6, Proc. Paper 11811, December, 1975, pp. 873-888.

References

44. Axelrad, E. L., Emmerling, F. A., "Elastic Tubes," Applied Mechanics Reviews, Vol. 37, No.7, July, 1984, pp. 891-897.

45. Axelrad, E. L., Emmerling, F. A., "Collapse Load Of Elastic Tubes Under Bending," *Israel Journal of Technology*, Vol. 22, 1984/85, pp. 89-94.

46. Emmerling, F. A., "Nichtlineare Biegung und Beulen von Zylindern und Krummen Rohren Bei Normaldruck," *Ingenieur-Archiv* 52, Springer-Verlag, 1982, pp. 1-16.

47. Fabian, O., "Collapse of Cylindrical, Elastic Tubes Under Combined Bending, Pressure, and Axial Loads," *International Journal of Solids and Structures*, Vol. 13, pp. 1257-1270, 1977.

48. Knight, N. F., Macy, S. C., McCleary, S. L., "Assessment of Structural Analysis Technology for Elastic Shell Collapse Problems," in Computational Structural Mechanics and Multidisciplinary Optimization, R. V. Grandhi, W. J. Stroud, and V. B. Venkayya (editors), ASME AD, Vol. 16, 1989, pp. 1-17.

49. McAleese, J. D., "Collapse of Long Stiffened Circular Cylinders Under Combined Axial Bending and Pressure Loading," Ph.D. Dissertation, Case Western Reserve University, January, 1984.

50. Stephens, W., Starnes, J. H., Jr., Almroth, B. O., "Collapse of Long Cylindrical Shells under Combined Bending and Pressure Loads," *AIAA Journal*, Vol. 13, No. 1, January, 1975, pp. 20-25.

51. Elmabruk, M. A., "Initial Postbuckling Behavior of Thin Cylindrical Shells Under Pure Bending, and Effect of Initial Antisymmetric Imperfection On The Buckling Moment," Ph.D. Dissertation, University of Southern California, January, 1983.

52. Berdnikov, Y. N., Nozdrin, A. S., "Stability of Cylindrical Shell in Elastoplastic Region with Pure Bending (Yield Theory)," Soviet Aeronautics, Vol. 17, No. 4, 1974, pp. 17-24.

53. Darevskii, V. M., "Stability of a Console Cylindrical Shell Under Bending by a Transverse Force With Twisting and Internal Pressure," *ARS Journal*, Vol. 31, No. 1, January, 1961.

References

54. Donnell, L. H., "A New Theory for the Buckling of Thin Cylinders Under Axial Compression and Bending," *Transactions Am. Soc. Mech. Engr.*, Vol. 56, 1934, pp. 795-806.

55. Grinenko, N. I., Khishchenko, Yu.M., Chernoglazov, G. S., "Experimental Study of Stability of Reinforced Cylindrical Shells Under Pure Bending," *Prikladnaya Mekhanika*, Vol. 12, No. 5, May, 1976, pp. 50-55.

56. Lundquist, E., "Strength Tests of Thin-Walled Duralumin Cylinders in Pure Bending," NACA Technical Note 479, December, 1933.

57. Seide, P., Weingarten, V. I., Morgan, E. J., "Final Report on the Development of Design Criteria for Elastic Stability of Thin Shell Structures," Space Technology Labs. STL/TR-60-0000-19425, Inc., Los Angeles, CA, December 31, 1960.

58. Spence, J., Toh, S. L., "Collapse of Thin Orthotropic Elliptical Cylindrical Shells Under Combined Bending and Pressure Loads," *Journal of Applied Mechanics*, March, 1979.

59. Stuart, F. R., Goto, J. T., Sechler, E. E., "The Buckling of Thin-Walled Circular Cylinders Under Axial Compression and Bending," NASA CR-1160, September, 1968.

60. Suer, H., Harris, L., Skene, W., Benjamin, R., "The Bending Stability of Thin-Walled Unstiffened Circular Cylinders Including the Effects of Internal Pressure," *Journal of the Aeronautical Sciences*, Vol. 25, No. 5, May, 1958, pp. 281-287.

61. Turkin, K. D., "Stability of Reinforced Circular Cylindrical Shell Subjected to Compression and Pure Bending," *Raschet Prostranstvennykh Konstruktsiy*, No. 4, 1958, pp. 477-498 (also NASA TT-F-8298).

62. Card, M. F. "Bending Tests of Large-Diameter Stiffened Cylinders Susceptible to General Instability," NASA TN D-2200, April, 1964.

63. Davis, R., Carder, F., "Buckling Tests of a 10-Foot Diameter Stiffened Cylinder with Rectangular Cutouts," NASA TM 88996, 1987.

64. Dow, M. B., Peterson, J. P., "Bending and Compression Tests of Pressurized Ring-Stiffened Cylinders," NASA TN D-360, April, 1960.

References

65. Guggenheim Aeronautical Laboratory, California Institute of Technology, "Some Investigations of the General Instability of Stiffened Metal Cylinders V - Stiffened Metal Cylinders Subjected to Pure Bending," NACA Technical Note 909, August, 1943.

66. Hedgepeth, J. M., Hall, D. B., "Stability of Stiffened Cylinders," *AIAA Journal*, Vol. 3, No. 12, December, 1965, pp. 2275-2286.

67. Hoff, N. J., Boley, B. A., "Stresses in and General Instability of Monocoque Cylinders with Cutouts I - Experimental Investigation of Cylinders with a Symmetric Cutout Subjected to Pure Bending," NACA Technical Note 1013, June, 1946.

68. Hoff, N. J., Boley, B. A., "Stresses in and General Instability of Monocoque Cylinders with Cutouts IV - Pure Bending Tests of Cylinders with Side Cutout," NACA Technical Note 1264, February, 1948.

69. Hoff, N. J., Fuchs, S. J., Cirillo, A. J., "The Inward Bulge Type Buckling of Monocoque Cylinders II - Experimental Investigation of the Buckling in Combined Bending and Compression," NACA Technical Note 939, October, 1944.

70. Hoff, N. J., Boley, B. A., Nardo, S. V., "The Inward Bulge Type Buckling of Monocoque Cylinders IV - Experimental Investigation of Cylinders Subjected to Pure Bending," NACA Technical Note 1499, September, 1948.

71. Lakshmikantham, C., Gerard, G., Milligan, R. W., "Bending General Instability of Shallow-Stiffened Cylinders," *International Journal of Mech. Sci.*, Vol. 11, 1969, pp. 41-51.

72. Mossman, R., Robinson, R., "Bending Tests of Metal Monocoque Fuselage Construction," NACA Technical Note 357, November, 1930.

73. Peterson, J. P., "Bending Tests of Ring-Stiffened Circular Cylinders," NACA Technical Note 3735, July, 1956.

74. Peterson, J. P., Anderson, J. K., "Bending Tests of Large-Diameter Ring Stiffened Corrugated Cylinders," NASA TN D-3336, March, 1966.

References

75. Bert, C. W., Veragen, P. M., "Experiments on Nonlinear Transverse-Curvature Behavior of Composite-Material Blades and Shells," *Composites '86: Recent Advances in Japan and the United States* (Proc. 3rd Japan-U.S. Conference, Tokyo); Japan Soc. for Composite Matls., 1986, pp. 197-195.

76. Brown, T. S., Rezin, D. B., "Hybrid Composite Driveshaft Design Considerations," *Modern Developments in Composite Materials and Structures*, Winter Annual Meeting of the ASME, New York, NY, December 2-7, 1979.

77. Holston, A. Jr., Feldman, A., Stang, D. A., "Stability of Filament Wound Cylinders Under Combined Loading," Air Force Flight Dynamics Laboratory, Wright-Patterson Air Force Base, OH, AFFDL-TR-67-55, May 1967.

78. Hose, D. R., Kitching, R., "Glass Reinforced Composites of Mixed Wall Construction," *International Journal for Pressure Vessels & Piping*, Vol. 27, 1987, pp. 305-323.

79. Hütter, U., "Optimization of Shell Structures Under Bending and Torsion Loads," *Proceedings of the 5'th Symposium on Structural Mechanics*, ONR Structural Mechanics Series, Mechanics of Composite Materials, 1967, pp. 527-549.

80. Mamalis, A. G., Manolakos, D. E., Viegelhahn, G. L., Baldoukas, A. K., "Bending of Fibre-Reinforced Composite Thin-Walled Tubes," *Composites*, Vol. 21, 1990, pp. 431-438.

81. Zien, H. M., "Bending of Laminated Anisotropic Composite Cylinders," *Journal of Composite Materials*, Vol. 7, 1973, pp. 394-398.

82. Davis, R., "Buckling Test of a 3-Meter-Diameter Corrugated Graphite-Epoxy Ring-Stiffened Cylinder," NASA Technical Paper 2032, July, 1982.

83. Almroth, B. O., Brogan, F. A., Stanley, G. M., "Structural Analysis of General Shells, Vol. 2: User Instructions for STAGSC-1," NASA CR-165670, March, 1978.

84. MACSYMA™ User's Guide, Symbolics, Inc. Document No. SMI0500040.0, January, 1988.

85. IMSL MATH/LIBRARY User's Manual, IMSL Inc., Houston, TX, 1987, pp. 660-671.

86. Lentini, M., Pereyra, V., "An Adaptive Finite Difference Solver For Nonlinear Two-Point Boundary Problems With Mild Boundary Layers," *SIAM Journal of Numerical Analysis*, Vol. 14, 1977, pp. 91-111.

References

87. Pereyra, V., "PASVA3: An Adaptive Finite Difference Fortran Program For First Order Nonlinear, Ordinary Boundary Problems," *Lecture Notes in Computer Science*, edited by G. Goos and J. Hartmanis, Springer Verlag, 1979, pp. 67-88.

88. Rankin, C., Brogan, F., "The Computational Structural Mechanics Testbed Structural Element Processor ES5: STAGS Shell Element," NASA CR-4358, May, 1991.

89. Khot, N. S., Venkayya, V. B., "Effect of Fiber Orientation on Initial Postbuckling Behavior and Imperfection Sensitivity of Composite Cylindrical Shells," Air Force Flight Dynamics Laboratory, Wright-Patterson Air Force Base, OH, AFFDL-TR-70-125, December, 1970.

90. Arbocz, J., "The Effect of Initial Imperfections on Shell Stability - an Updated Review," Delft University of Technology, Report LR-695, Delft, The Netherlands, September, 1992.

91. von Kármán, T., Tsien, H.-S., "The Buckling of Thin Cylindrical Shells under Axial Compression," *Journal of the Aeronautical Sciences*, Vol. 8, No. 8, June, 1941, pp. 303-312.

92. Jeffrey, G. L., "Postbuckling of Laminated Anisotropic Panels," NASA Technical Memorandum 100509, October, 1987.

93. Starnes, J. H., Jr., Rouse, M., "Postbuckling and Failure Characteristics of Selected Flat Rectangular Graphite-Epoxy Plates Loaded in Compression," AIAA Paper No. 81-0543, *Proceedings of the 22nd Structures, Structural Dynamics, and Materials Conference*, Atlanta, GA, April 6-8, 1981.

94. Abramovich, H., Weller, T., Singer, J., "Effect of Sequence of Combined Loading on Buckling of Stiffened Shells," *Experimental Mechanics*, March, 1988, pp. 1-13.

Appendix A: Comments on Donnell Shell Theory

There have been a number of comparisons between various geometrically linear shell theories in the literature for a wide range of geometries of isotropic cylinders (see for example [A1] and [A2]). The theories by Donnell [A3], Sanders [A4], and Flügge [A5] are widely used and represent increasing levels of sophistication. Flügge's theory is generally considered to be the most accurate. In the comparisons, it is concluded for isotropic shells that nearly all theories give essentially the same results for axisymmetric loadings, while some discrepancies may occur between Donnell theory and higher-order theories for edge loadings which contain one to four circumferential harmonics, such as in the case of pure bending. However, for the case of a single circumferential harmonic, bending gradients in the circumferential direction are generally mild so that the response is adequately described by membrane terms. Also, agreement between the various shell theories tends to improve with increasing 'thinness', or large R/H values, of the shell wall. Similar shell theory comparisons have yet to be made with composite cylinders. No comments are made in the above mentioned references with regard to the influence of the L/R ratio for cylinders with harmonic edge loading.

Reference [A6] compares the buckling loads for orthotropic cylinders subjected to axial compression in consideration of the geometrically nonlinear Donnell and Sanders[*] kinematics. It concludes that correlation between both theories depends primarily on cylinder the L/R ratio and fiber orientation. Generally, Donnell theory overestimates the buckling loads compared to Sanders, but is good agreement for 'short' cylinders.

Reference [A7] compares bending buckling moments and compression buckling loads using geometrically linear Donnell and Love kinematics for the case of composite cylin-

---

[*] Rotations about the normal are neglected in [A6], so that the resulting kinematics are the nonlinear equivalent of the Love kinematics described in [A7].

141

ders. It is shown for axial compression buckling that correlation between the two theories depends primarily on the L/R ratio. The effect of L/R tends to diminish with increasing R/H. These observations support those made in [A6]. For bending buckling, it is found that both the Donnell and Love buckling equations give practically identical results for a wide range of R/H and L/R.

Overall, it is felt that the range of geometries investigated in this study fall in the 'short' and 'thin' category. It has yet to be shown that practical differences exist between Donnell and Flügge predictions for the prebuckling responses of either isotropic or composite cylinders.

References

A1. Akeju, T. A. I., "Reduced Thin Shell Equations for Circular Cylinders," *ASCE*, Journal of Engineering Mechanics Division, Vol. 107, No. EM1, February 1981, pp. 249-255.

A2. Houghton, D. S., Johns, D. J., "A Comparison of the Characteristic Equations in the Theory of Circular Cylindrical Shells," *The Aeronautical Quarterly*, Vol. 12, August 1961, pp. 228-236.

A3. Donnell, L. H., "A New Theory for the Buckling of Thin Cylinders Under Axial Compression and Bending," *Transactions Am. Soc. Mech. Engr.*, Vol. 56, 1934, pp. 795-806.

A4. Sanders, J. L., "An Improved First-Approximation Theory For Thin Shells," NASA Technical Report R-24, 1959.

A5. Flügge, W., *Stresses in Shells*, 2nd ed., Springer Verlag, Berlin, 1973, pp. 206-212.

A6. Simitses, G. J., Shaw, D., Sheinman, I., "The Accuracy of Donnell's Equations for Axially Loaded, Imperfect Orthotropic Cylinders," *Computers & Structures*, Vol. 20, No. 6, 1985, pp. 939-945.

A7. Lou, K. A., Yaniv, G., "Buckling of Circular Cylindrical Composite Shells under Axial Compression and Bending Loads," *Journal of Composite Materials*, Vol. 25, No. 2, February, 1991, pp. 162-187.

Appendix B: Constitutive Relations

The geometry of a laminate is defined in Fig. B-1. Each ply of the laminate is assumed to be subjected to plane stress so that the stresses in the k'th ply of the laminate can be described by Hooke's law as

$$\left\{ \begin{array}{c} \sigma_x \\ \sigma_\theta \\ \tau_{x\theta} \end{array} \right\}^{(k)} = \left[\begin{array}{ccc} \overline{Q}_{11} & \overline{Q}_{12} & \overline{Q}_{16} \\ \overline{Q}_{12} & \overline{Q}_{22} & \overline{Q}_{26} \\ \overline{Q}_{16} & \overline{Q}_{26} & \overline{Q}_{66} \end{array} \right]^{(k)} \left\{ \begin{array}{c} \varepsilon_x - \varepsilon_x^P \\ \varepsilon_\theta - \varepsilon_\theta^P \\ \gamma_{x\theta} - \gamma_{x\theta}^P \end{array} \right\}. \tag{B.1}$$

The superscript 'P' in Eq. (B.1) refers to an initial pre-strain that may be present in the laminate before mechanical loading takes place. The $\overline{Q}_{ij}$'s are the transformed reduced ply stiffnesses of the k'th ply [B1, p. 51]. The initial pre-strained state may be due to a variety of conditions such as initial geometric imperfections, thermal effects, mechanical preloading, etc.

1-2-3 = fiber oriented coordinate system

x-θ-z = laminate coordinate system

(a) Ply Orientation   (b) Laminate Geometry
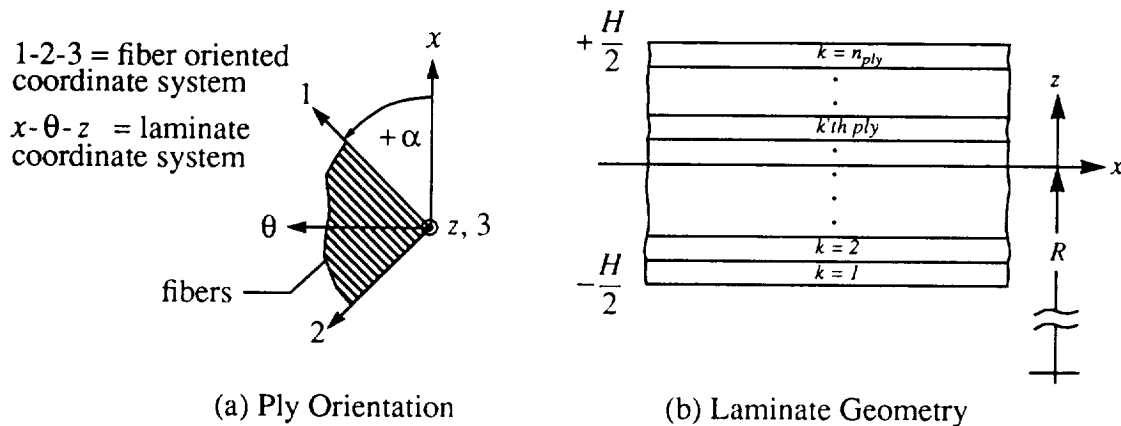
Fig. B-1 Laminate Geometry

Appendix B

Integrating the inplane stresses in Eq. (B.1) with respect to the thickness coordinate, z, leads to the standard definitions of the force and moment resultants

$$\{N_x, N_\theta, N_{x\theta}\} = \int_{-H/2}^{+H/2} \{\sigma_x, \sigma_\theta, \tau_{x\theta}\}^{(k)} dz$$

$$\{M_x, M_\theta, M_{x\theta}\} = \int_{-H/2}^{+H/2} \{\sigma_x, \sigma_\theta, \tau_{x\theta}\}^{(k)} z\,dz.$$

(B.2)

The resultants are illustrated in Fig. B-2. Carrying out the integration in the above equation results in the classical laminate constitutive relation

$$
\begin{Bmatrix} N_x \\ N_\theta \\ N_{x\theta} \\ M_x \\ M_\theta \\ M_{x\theta} \end{Bmatrix} =
\begin{bmatrix}
A_{11} & A_{12} & A_{16} & B_{11} & B_{12} & B_{16} \\
A_{12} & A_{22} & A_{26} & B_{12} & B_{22} & B_{26} \\
A_{16} & A_{26} & A_{66} & B_{16} & B_{26} & B_{66} \\
B_{11} & B_{12} & B_{16} & D_{11} & D_{12} & D_{16} \\
B_{12} & B_{22} & B_{26} & D_{12} & D_{22} & D_{26} \\
B_{16} & B_{26} & B_{66} & D_{16} & D_{26} & D_{66}
\end{bmatrix}
\begin{Bmatrix} \varepsilon_x^o \\ \varepsilon_\theta^o \\ \gamma_{x\theta}^o \\ \kappa_x^o \\ \kappa_\theta^o \\ \kappa_{x\theta}^o \end{Bmatrix} -
\begin{Bmatrix} N_x^P \\ N_\theta^P \\ N_{x\theta}^P \\ M_x^P \\ M_\theta^P \\ M_{x\theta}^P \end{Bmatrix},
$$

(B.3)

where A_{ij}, B_{ij}, and D_{ij} ($i, j = 1, 2$, and 6) are the elements of the laminate extensional, coupling, and bending stiffness matrices, respectively, and the quantities denoted by the superscript 'P' are the pre-straining force and moment resultants. The elements of the stiffness matrices are computed from the relations

$$A_{ij} = \sum_{k=1}^{n_{ply}} \overline{Q}_{ij}^{(k)} (z_k - z_{k-1})$$

$$B_{ij} = \frac{1}{2} \sum_{k=1}^{n_{ply}} \overline{Q}_{ij}^{(k)} (z_k^2 - z_{k-1}^2)$$

(B.4)

$$D_{ij} = \frac{1}{3} \sum_{k=1}^{n_{ply}} \overline{Q}_{ij}^{(k)} (z_k^3 - z_{k-1}^3).$$

Specializing Eq. (B.3) to the case of balanced and symmetric laminates, such as the laminates to be considered in this investigation, results in the simplifications $A_{16} = A_{26} = 0$ and $B_{ij} = 0$. Eq. (B.3) decouples due to this simplification and the resultants become

$$
\left\{
\begin{array}{c}
N_x \\
N_\theta \\
N_{x\theta}
\end{array}
\right\}
=
\begin{bmatrix}
A_{11} & A_{12} & 0 \\
A_{12} & A_{22} & 0 \\
0 & 0 & A_{66}
\end{bmatrix}
\left\{
\begin{array}{c}
\varepsilon_x^o \\
\varepsilon_\theta^o \\
\gamma_{x\theta}^o
\end{array}
\right\}
-
\left\{
\begin{array}{c}
N_x^P \\
N_\theta^P \\
N_{x\theta}^P
\end{array}
\right\}
$$

(B.5)

$$
\left\{
\begin{array}{c}
M_x \\
M_\theta \\
M_{x\theta}
\end{array}
\right\}
=
\begin{bmatrix}
D_{11} & D_{12} & D_{16} \\
D_{12} & D_{22} & D_{26} \\
D_{16} & D_{26} & D_{66}
\end{bmatrix}
\left\{
\begin{array}{c}
\kappa_x^o \\
\kappa_\theta^o \\
\kappa_{x\theta}^o
\end{array}
\right\}
-
\left\{
\begin{array}{c}
M_x^P \\
M_\theta^P \\
M_{x\theta}^P
\end{array}
\right\}.
$$

For the case of pre-straining due to geometric imperfections, thermal effects, or mechanical preloading, the pre-straining force and moment resultants in Eq. (B.5) are defined as

$$
\left\{
\begin{array}{c}
N_x^P \\
N_\theta^P \\
N_{x\theta}^P
\end{array}
\right\}
=
\begin{bmatrix}
A_{11} & A_{12} & 0 \\
A_{12} & A_{22} & 0 \\
0 & 0 & A_{66}
\end{bmatrix}
\left\{
\begin{array}{c}
\bar{\varepsilon}_x^o \\
\bar{\varepsilon}_\theta^o \\
\bar{\gamma}_{x\theta}^o
\end{array}
\right\}
+
\left\{
\begin{array}{c}
N_x^T \\
N_\theta^T \\
N_{x\theta}^T
\end{array}
\right\}
$$

(B.6)

$$
\left\{
\begin{array}{c}
M_x^P \\
M_\theta^P \\
M_{x\theta}^P
\end{array}
\right\}
=
\begin{bmatrix}
D_{11} & D_{12} & D_{16} \\
D_{12} & D_{22} & D_{26} \\
D_{16} & D_{26} & D_{66}
\end{bmatrix}
\left\{
\begin{array}{c}
\bar{\kappa}_x^o \\
\bar{\kappa}_\theta^o \\
\bar{\kappa}_{x\theta}^o
\end{array}
\right\}
+
\left\{
\begin{array}{c}
M_x^T \\
M_\theta^T \\
M_{x\theta}^T
\end{array}
\right\}.
$$

The overbar in Eq. (B.6) indicates known functions representing the pre-straining and the superscript 'T' indicates known thermal force and moment resultants. The thermal resultants are defined in [B1, pp. 196-197]. The pre-straining terms are discussed in the following for the case of initial geometric imperfections.

(a) Force Resultants   (b) Moment Resultants
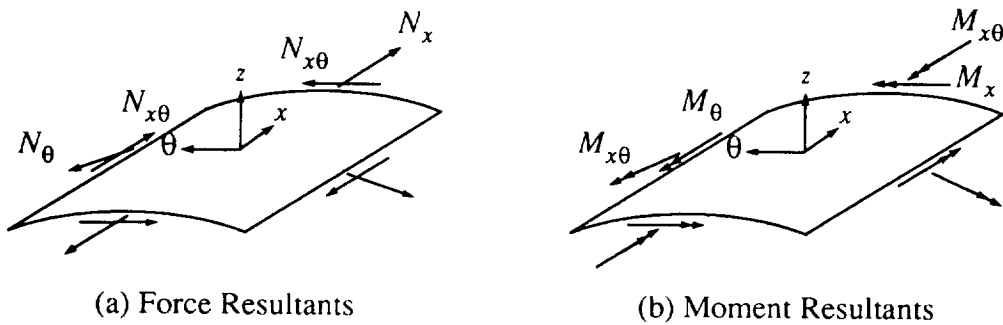
Fig. B-2 Force and Moment Resultants

145

Appendix B

Initial Geometric Imperfections

Geometric shape imperfections can significantly influence the cylinder responses and are therefore considered in the present analysis. It is assumed that the geometric imperfection is in the form of an initial radial displacement imperfection that can be represented by the series

$$\frac{\overline{w}(x, \theta)}{H} = \sum_{k=0}^{k_{max}} \sum_{l=0}^{N} \left[\cos\frac{k\pi x}{L} (A_{kl}\cos l\theta + B_{kl}\sin l\theta) \right.$$

$$\left. + \sin\frac{k\pi x}{L} (C_{kl}\cos l\theta + D_{kl}\sin l\theta) \right],$$

(B.7)

where the axial half-wave number of the imperfection is given by the integer k and circumferential full-wave number is given by the integer l. The quantity k_{max} is the maximum number of axial imperfection terms to be studied. The range of l is limited by the number of harmonic terms included in the prebuckling analysis, N. The A_{kl}, B_{kl}, C_{kl}, and D_{kl} are Fourier coefficients.

The associated pre-loading midsurface strain and curvature terms are obtained by substituting the assumed form of the radial imperfection, Eq. (B.7), into the strain-displacement equations. Keeping only the first order imperfection quantities results in the expressions

$$\overline{\varepsilon}_x^o = 0 \qquad\qquad \overline{\kappa}_x^o = -\frac{\partial^2 \overline{w}(x, \theta)}{\partial x^2}$$

$$\overline{\varepsilon}_\theta^o = \frac{\overline{w}(x, \theta)}{R} \qquad\qquad \overline{\kappa}_\theta^o = -\frac{\partial^2 \overline{w}(x, \theta)}{R^2 \partial\theta^2}$$

(B.8)

$$\overline{\gamma}_{x\theta}^o = 0 \qquad\qquad \overline{\kappa}_{x\theta}^o = -2\frac{\partial^2 \overline{w}(x, \theta)}{R\partial x\partial\theta}.$$

The pre-straining force and moment resultants are computed from Eqs. (B.6) and (B.8).

References

B1. Jones, R. M., *Mechanics of Composite Materials*, Hemisphere Publishing Corporation, New York, 1975.

Appendix C: Derivation of Governing Equations

Two-Dimensional Partial Differential Equations

The equilibrium equations can be reduced to a set of eight coupled first-order partial differential equations for the practical case of laminates with balanced symmetric stacking sequences. This form is achieved by eliminating the variables N_θ, M_θ, and $M_{x\theta}$ from the equations by writing these in terms of the eight primary response variables. The collection of these eight response variables is denoted as $\vec{Y}(x, \theta)$.

Some useful simplifications are made when substituting the expressions

$$\varepsilon_x^\circ = \frac{\partial u^\circ}{\partial x} + \frac{1}{2}(\beta_x^\circ)^2 = \frac{N_x + N_x^P}{A_{11}} - \frac{A_{12}}{A_{11}}\varepsilon_\theta^\circ$$

$$\kappa_x^\circ = \frac{\partial \beta_x^\circ}{\partial x} = \frac{M_x + M_x^P}{D_{11}} - \frac{D_{12}}{D_{11}}\kappa_\theta^\circ - \frac{D_{16}}{D_{11}}\kappa_{x\theta}^\circ,$$

(C.1)

obtained from the definitions of N_x and M_x, into the definitions of N_θ, M_θ, and $M_{x\theta}$. This substitution results in the following expressions for the variables to be eliminated

$$N_\theta = \frac{A_{12}}{A_{11}}N_x + A^*\varepsilon_\theta^\circ + \left[\frac{A_{12}}{A_{11}}N_x^P - N_\theta^P\right]$$

$$M_\theta = \frac{D_{12}}{D_{11}}M_x + D_1^*\kappa_\theta^\circ + D_2^*\kappa_{x\theta}^\circ + \left[\frac{D_{12}}{D_{11}}M_x^P - M_\theta^P\right]$$

(C.2)

$$M_{x\theta} = \frac{D_{16}}{D_{11}}M_x + D_2^*\kappa_\theta^\circ + D_3^*\kappa_{x\theta}^\circ + \left[\frac{D_{16}}{D_{11}}M_x^P - M_{x\theta}^P\right].$$

Appendix C

The eight first-order governing equations are derived assuming that all terms in Eq. (C.2) can be described in terms of the eight response variables. The steps involved in obtaining each of the eight governing equations are:

1. The first equation is obtained by solving directly for $\dfrac{\partial u^\circ}{\partial x}$ from the first of equations Eq. (C.1), and substituting in the definition of ε_θ° .

2. The second equation is obtained similarly by solving for $\dfrac{\partial v^\circ}{\partial x}$ in the definition of $N_{x\theta}$, substituting for $\gamma_{x\theta}^\circ$.

3. The third equation is the definition of β_x° .

4. The fourth equation is directly obtained from the definition of κ_x° , substituting for κ_θ° and $\kappa_{x\theta}^\circ$.

5. The fifth equation is obtained directly from the first equilibrium equation, $\partial N_x/\partial x = -\partial N_{x\theta}/R\partial\theta$.

6. The sixth equation is obtained from the second equilibrium equation, $\partial N_{x\theta}/\partial x = -\partial N_\theta/R\partial\theta$, along with first of equations Eq. (C.2) and the definition of ε_θ° .

7. The seventh equation is obtained from the third equilibrium equation along with the first and second of equations Eq. (C.2).

8. The final equation is derived from the definition of Q_x, along with the third of equations Eq. (C.2).

One-Dimensional Ordinary Differential Equations

The derivation of the one-dimensional equations is considerably involved due to the complexity of the two-dimensional partial differential equations derived above and would have been extremely difficult without the aid of a symbolic manipulator. The derivation of the first-order partial differential equations and the generation of the equations involves the following general steps for the analyses with $N = 3$ and $N = 5$:

1. Substitution of solution form, $\vec{\Upsilon}(x, \theta)$, into the two-dimensional partial differential equations, carrying out the expansion of nonlinear terms.

2. Trigonometric simplification of nonlinear terms. This process involved expanding products of trigonometric terms and lead to higher-order harmonics that must be neglected in the analysis (see section "Truncation of Higher-Order Terms" below).

3. Equate leading coefficients of trigonometric terms on each side of the equation of expanded equations.

148

4. Separate each expanded equation into $2N + 1$ equations, where each equation corresponds to the leading coefficients of the elements of the vector $\vec{\Psi}(\theta)$.

The FORTRAN statements for all of the resulting $8 \times (2N + 1)$ one-dimensional equations were generated directly by the symbolic manipulator.

Truncation of Higher-Order Terms

The expansion of nonlinear terms, such as the term $(\beta_x^o)^2$, involves products of trigonometric terms. Consider a typical nonlinear term such as $sin^2 N\theta$. This term may be simplified to the quantity $1/2 - 1/2\,cos2N\theta$ using trigonometric identities. It is observed from this trigonometric simplification that the higher-order harmonic $2N$ appears. In general, raising trigonometric terms to a power 'r' results in harmonics of the order $r \cdot N$. Terms involving harmonics greater than order N must be neglected in the analysis in order to have an equal number of equations and unknowns. This is justified since the coefficients of higher-order harmonics are negligibly small until the vicinity of the collapse rotation is reached, after which a large number of harmonics is most likely required.

Appendix D: Specimen Fabrication and Preparation

Six 12-inch-diameter test specimens were made from Hercules AS4/3502 graphite-epoxy unidirectional prepreg tape. Special tabs were made from fiberglass cloth tape and attached to the specimens in a secondary layup process. A typical test specimen is shown in Fig. D-1. The steps involved in fabricating and preparing the specimens for testing are described in the following.

D.1 Graphite-Epoxy Cylinder Fabrication

Mandrel Preparation

A 48-in.-long, 12-in.-diameter aluminum mandrel was designed and constructed specifically for the fabrication of the bending test specimens. Before fabrication could take place, it was necessary to prepare the mandrel. The mandrel was cleaned with solvent to remove all resin deposits from any previous cylinder curing cycle. Next, the mandrel was sprayed with Frekote 33 release agent and left standing for one hour. This step was then repeated for a second time before proceeding with the tape layup process, which is described next.

Tape Layup

The prepreg material was cut into suitably sized segments before starting the layup procedure. Each ply was formed by joining a number of 12-inch-wide prepreg tape strips side-by-side with tape. The joined strips were placed at the desired ply orientation and cut to form one large rectangular-shaped ply, measuring approximately 38 inches in width and 48 inches in length. This method of constructing the desired ply orientations is illustrated in Fig. D-2 (a) through (c). Under certain circumstances, it is possible to form a seam due

to gaps or overlaps in the adjacent prepreg strips. The gaps and overlaps formed either axial, circumferential, or helical seams, depending on the ply orientation.

Each ply was wrapped around the mandrel with the aid of a belt winder. The beltwinder is a device consisting of a motor driven canvas belt and a number of rollers that support the belt and the mandrel, as illustrated in Fig. D-3. Each ply was slowly fed onto the mandrel via the canvas belt as shown in the figure. An axial seam was introduced in each ply in the form of an overlap of up to approximately 1/8 inch as a result of this wrapping technique. Seams of adjacent plies were staggered to minimize the effects of any local stiffness discontinuities that may have occurred.
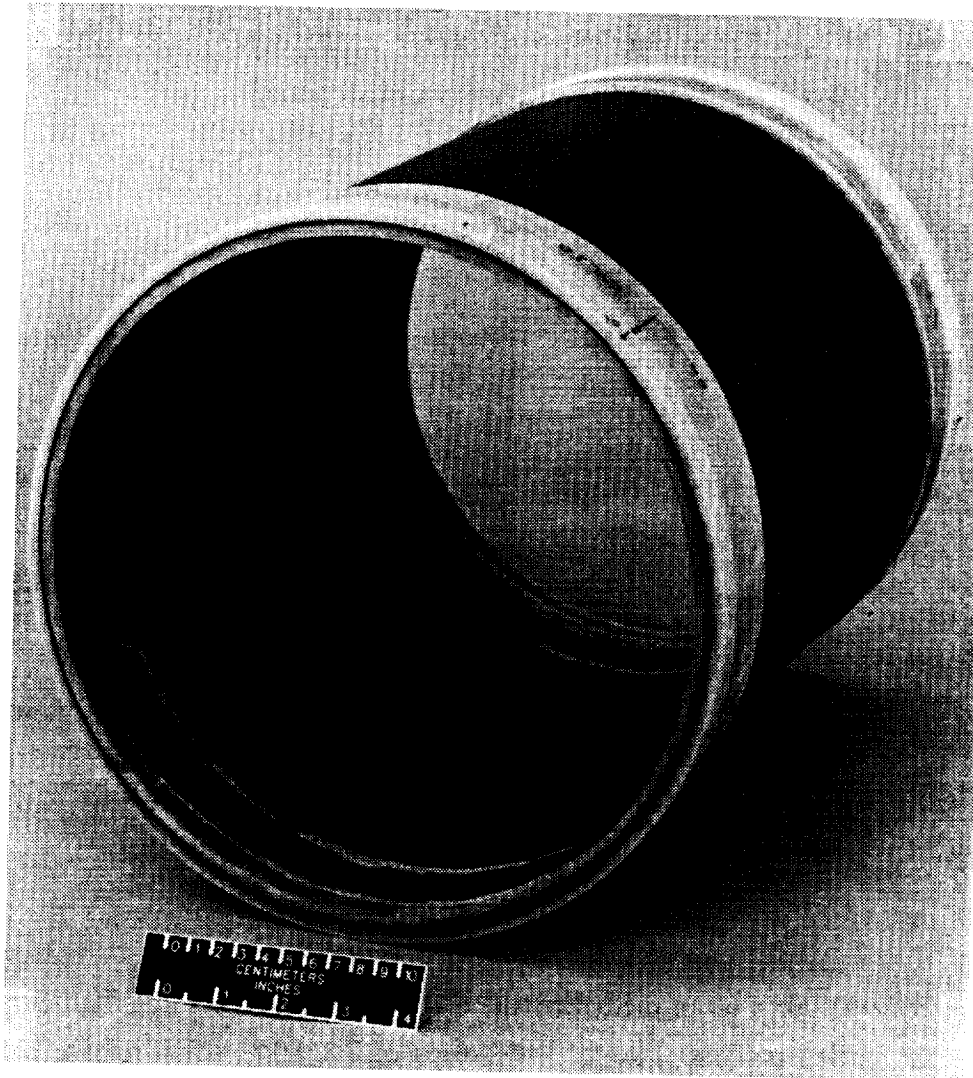
Fig. D-1 Typical Test Specimen

151

(a) 0° ply   (b) 90° ply   (c) -45° ply

Fig. D-2 Prepreg Ply Construction

Top View

Side View

Fig. D-3 Tape Layup Procedure

Curing

The mandrel was taken off of the beltwinder and placed on to a holding fixture in preparation for the curing process. Two-in.-wide strips of TX 1040 teflon release cloth and Mochberg bleeder paper were cut to length, allowing for a two inch overhang on each end

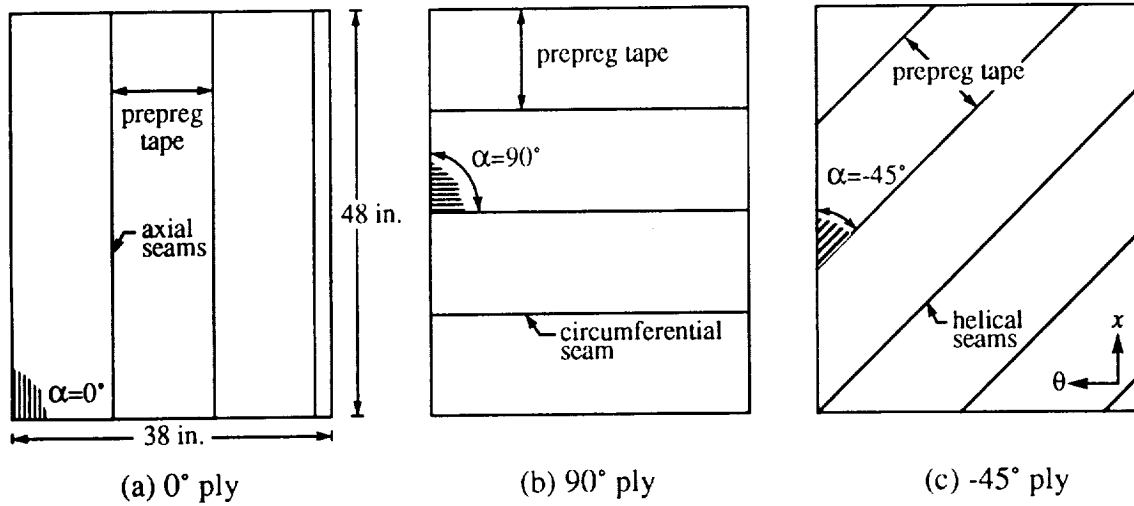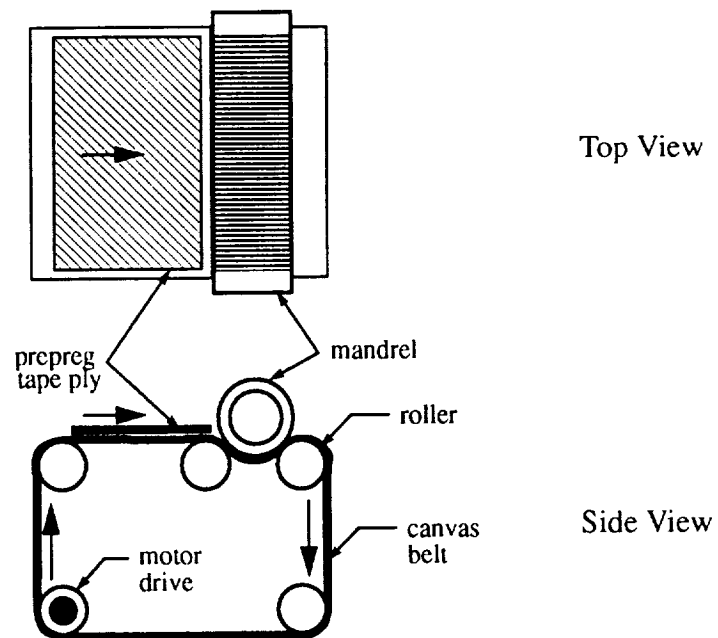of the cylinder. The release cloth strips were attached to the cylinder using teflon tape, overlapping the adjacent strip by approximately one inch. The bleeder paper was attached in a similar fashion. GS-43 sealant was then applied to the ends of the mandrel to form an air-tight seal with the vacuum bag. The vacuum hoses were then connected to vacuum ports on the mandrel once the mandrel was placed into the autoclave. The cylinder was then cured at the manufacturer's recommended temperature and pressure cycles while drawing a vacuum. Once curing was complete, the completed cylinder was removed from the mandrel.

Nondestructive Evaluation

Each cylinder was visually inspected after the fabrication process was completed. Ply seams and surface wrinkles were evident in some of the cylinders after the curing cycle was completed. The surface wrinkles were attributed to the wrinkles in the canvas belt of the beltwinder. Axial, helical, and circumferential ply seam orientations, introduced by the manufacturing process described in the preceding, were clearly visible in some specimens. Fig. D-4 illustrates a specimen where all three seam orientations are visible.

Next, each cylinder was inspected ultrasonically to check for the presence of internal voids, porosity, delaminations, and other anomalies. An automated C-scan procedure, shown schematically in Fig. D-5, was used to accomplish this task. The cylinder to be inspected was placed on a turntable in a water-filled C-scan tank. The ultrasonic scans were conducted such that the inner and outer probes indexed axially (vertically in the figure) after each 360° revolution of the turntable. Due to the length of the cylinders, two scans were required.

Both the visual inspection and the C-scan of cylinder CYL-3 indicated the presence of a 1.5 inch by 2.5 inch internal defect. The defect turned out to be a piece of backing tape left over from the cylinder layup procedure. This manufacturing defect lead to the fabrication of only one $L/R = 2$ bending test specimen instead of two.

D.2 Fiberglass Tabbing Procedure

The test specimens were cut to length on the aluminum mandrel using a diamond tipped cutting wheel before laying-up the fiberglass tabs on the cylinder ends. The tabs were
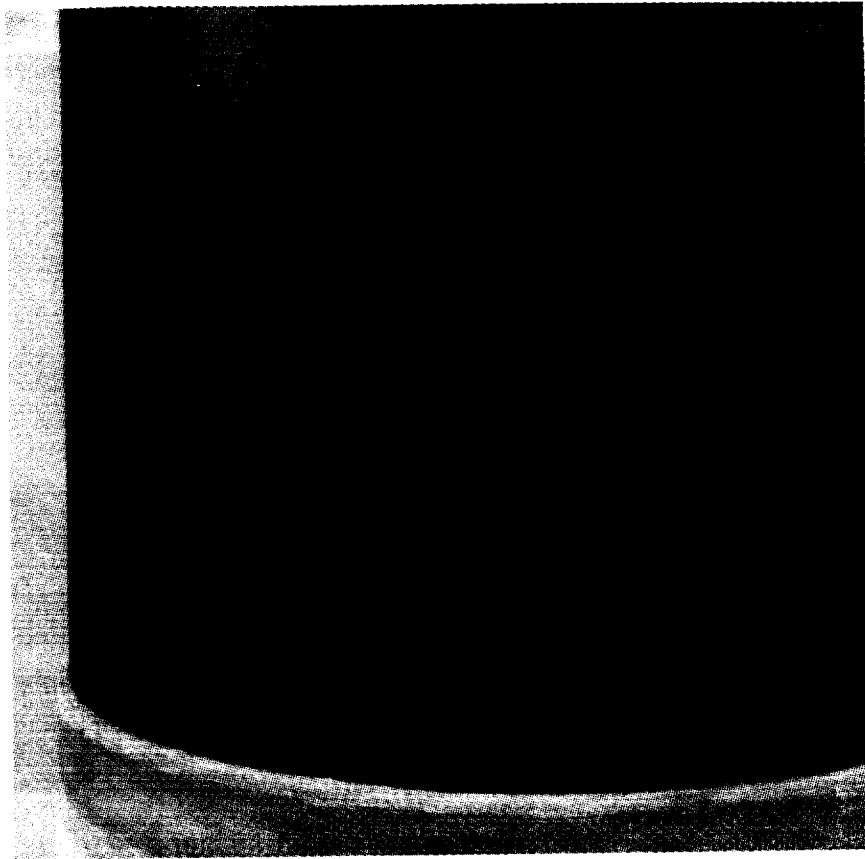
Fig. D-4 Axial, Helical, and Circumferential Ply Seams

stepped in thickness, as shown in Fig. D-6, for the purpose of introducing the bending loads into the specimen. The following materials were required for laying up the tabs:

- 1 in. masking tape
- 2 in. masking tape
- 1 in. teflon tape
- 1 in.-wide by 0.013 in.-thick fiber-glass cloth tape
- 3 in.-wide by 0.013 in.-thick fiber-glass cloth tape
- Kraft paper
- Polyethylene sheet

- 1 in. paint brush
- 3 in. squeegee
- Bondo™
- G.L.R. 125 resin
- G.L.H. 226 hardener
- 12 in.-diameter split aluminum disk (internal)
- 12 in.-diameter split aluminum ring (external)

154
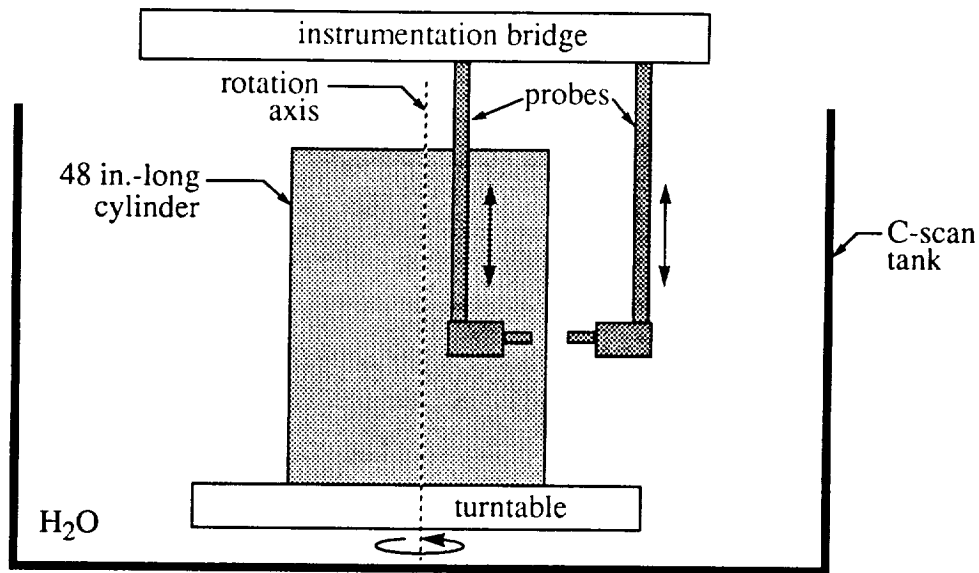
Fig. D-5 C-Scan Setup

Preparation of Cylinder Ends

To achieve a good bond between the fiberglass tabs and the graphite-epoxy cylinder, it was necessary to prepare the internal and external surfaces of the cylinder's ends. Approximately four inches of each end of the cylinder was wiped off with a paper wiper moistened with M.E.K. The inside and outside mid section of each cylinder was then masked off with brown paper and masking tape leaving 2.75 inches exposed at each end. The exposed end sections were then sandblasted using 120 grit aluminum oxide at 40 psi. The ends were again wiped with M.E.K. Next, the ends were re-masked using 1 in. teflon tape adjacent to sandblasted regions. Two in. masking tape was placed over teflon tape with a 5/8 inch overlap.

A split external aluminum ring and split internal disk were coated with release agent. The internal disk was fitted into the cylinder 2.75 in. from the end and tacked into place with a fillet of Bondo™. A plywood disk was fitted into the opposite end of cylinder for support and to maintain circular shape. The outer split ring was then attached to the cylinder in a similar fashion. Twelve pieces of 0.013 in.-thick and 40 in.-long segments were cut from a roll of 3 in.-wide fiberglass cloth tape along with six pieces of 0.013 in.-thick and 40 in.-long segments from a roll of 1 in.-wide fiberglass cloth tape for the inside tab layup of one end of the cylinder. A 480 in. length of the 3 in. tape and a 240 in. length of the 1 in. tape were cut for use for the outside tab layup.
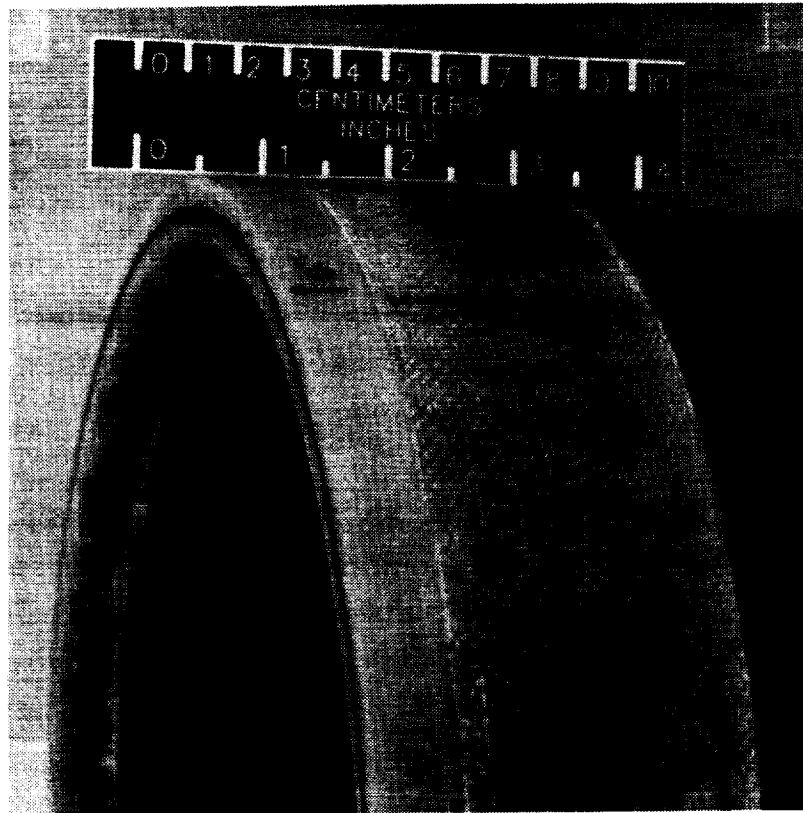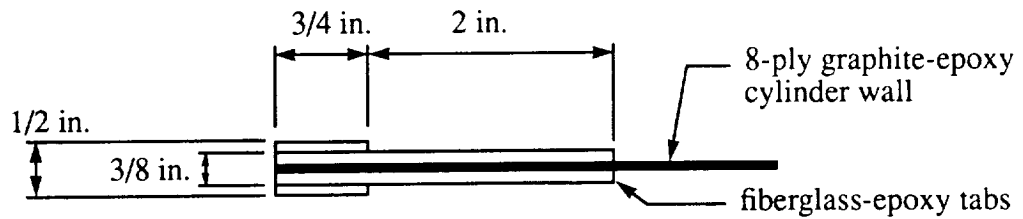
Fig. D-6 Detail View of Fiberglass Tab

Tabbing

The inside 2.75 in. length of one end of the cylinder was coated with G.L.R. 125 resin and G.L.H. 226 hardener. A length of 3 in. cloth tape was spread out on a plastic sheet and saturated with the resin/hardener mixture. The tape was then rolled up in preparation for laying up the inner tab. The saturated 3 in. cloth tape was then carefully unrolled around the inside cylinder wall as shown in Fig. D-7 (a), making sure that it was butted up against the inner aluminum disk. Care was taken to work out any air bubbles. This procedure was repeated for the remaining eleven strips of 3 in. fiberglass cloth. The outside cloth tape was prepared and applied up in a similar fashion, working with approximately 3 foot-lengths at

a time. Again, care was taken to ensure that the tape was butted up against the outer aluminum split ring evenly and that the air bubbles were worked out. The strips of 1 in.-wide tape were saturated with the resin/hardener mixture and applied 2 in. from inside disk. This was repeated until all 1 in.-wide cloth strips were applied. The entire setup, shown in Fig. D-7 (b), was left standing overnight to cure at room temperature. The external split ring and internal split disk were then removed and set up for tabbing the opposite end of the cylinder. This entire procedure was then repeated for other end of cylinder. Both ends of each cylinder were ground flat and parallel as a final step.

D.3 Specimen Potting

Potting Procedure

Each end of the test specimen was potted in the annular space between an inner and an outer aluminum loading ring using a low-temperature melting point alloy. Both Belmont alloy 2505 and Cerrobend® alloy were used as a potting compound, depending on the availability at the time of potting. There was no preference for either alloy since the material specifications were identical. The melting point of these alloys is 158 °F.

The inner and outer loading rings were bolted concentrically to a flat aluminum plate with a central access hole in preparation for the potting process. The test specimen was then centered in the annular region between the rings and held in place using four radial set screws. This assembly was placed on top of a hot plate and uniformly heated to a temperature of approximately 175 °F. The alloy was heated to 200-220 °F in a vacuum oven and carefully poured into the inner and outer annular regions between the rings and the cylinder wall. Both the inner and outer annular region were slightly over-filled. The set screws were backed out after the alloy started to solidify and the entire assembly was allowed to cool at room temperature. A potted end is shown during the cooling phase in the photo of Fig. D-8. This procedure was repeated for the opposite end, making sure that the bolt holes on all of the loading rings were aligned properly.

Radial Deformations due to Potting Procedure

Small radial deformations of the cylinder ends were observed after potting some of the specimens. This effect was attributed to the thermal contraction of the aluminum loading rings that occurred during the cool-down phase of the potting procedure. In an effort to
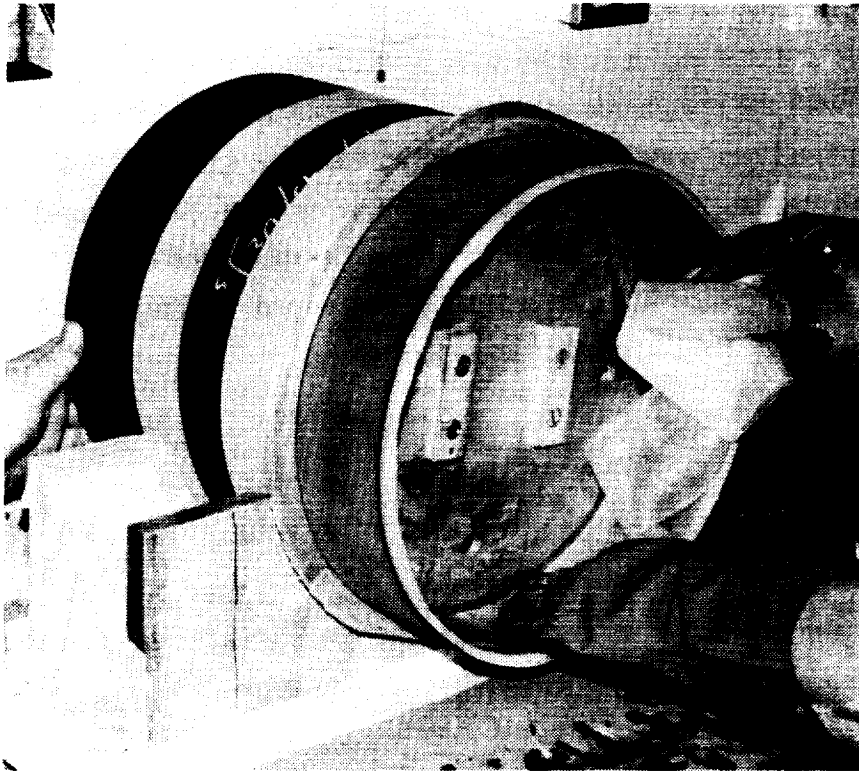
(a) Layup of
fiberglass tab

(b) Completed
fiberglass tab

Fig. D-7 Fabrication of Fiberglass Tabs

158
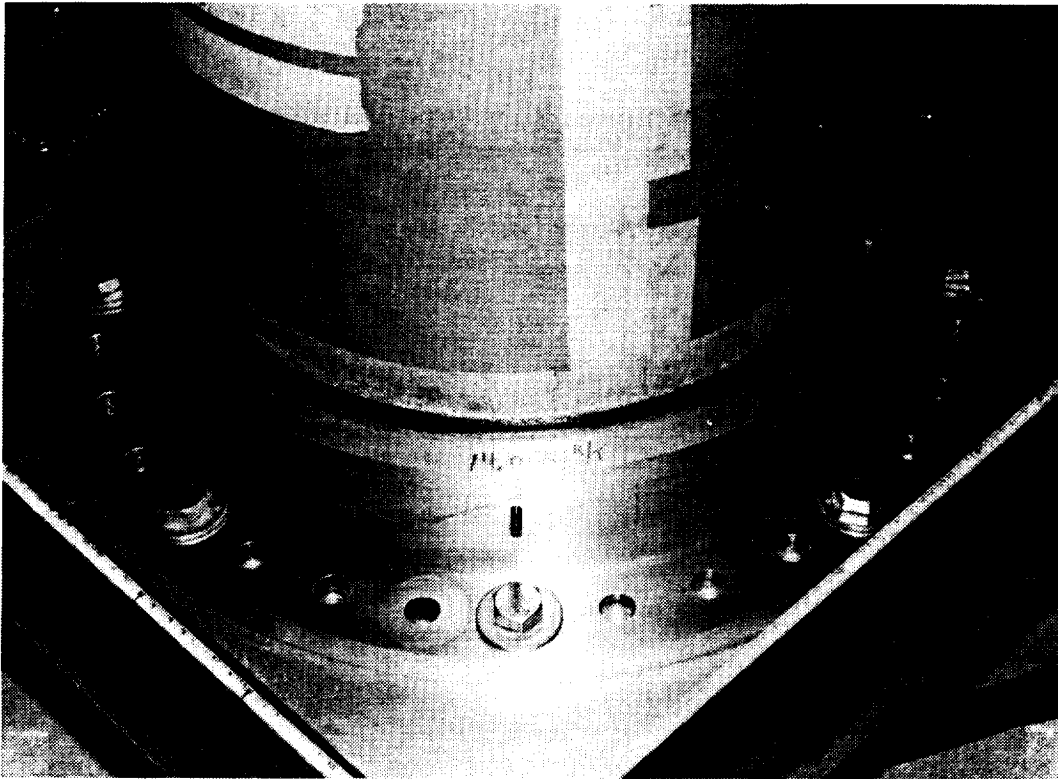
Fig. D-8 Potted Specimen End

quantify the effect of the thermal deformations, up to four diameter measurements were made at each end of some specimens before the potting procedure and again after the potting procedure was completed. The diameters were measured 1/8 inch from the surface of the low-temperature melting point alloy at specified θ-locations. The measurement results are given in terms of the change in radius, w_R, and are summarized in Table D-1. The value of w_R was computed from the relation $w_R = (d_i - d_f)/2$, where d_i is the initial cylinder diameter and d_f is the final diameter. This radial deformation is depicted in Fig. 2-3 (c).

Table D-1 indicates that both radial pinching and expansion can occur as a result of the potting process. The most severe pinching was observed to occur in specimen CYL-2 as -0.0085 in., or 23% of the wall thickness. The most severe expansion was observed to occur in specimen CYL-1B as $+0.0045$ in., or 12% of the wall thickness. The quasi-isotropic $[\mp 45/0/90]_S$ specimens and the axially stiff $[\mp 45/0_2]_S$ specimen tended to exhibit the greatest amount of pinching. The hoop-stiff $[\mp 45/90_2]_S$ specimens, in contrast, tended to

159

exhibit only a slight radial expansion (approximately +0.0015 in. or 4% of the wall thickness).

Table D-1 Measured Radial End-Deformations

θ-location	$\dfrac{x}{L}$	w_R, in.					
		CYL-1A	CYL-1B	CYL-2	CYL-3A	CYL-4A	CYL-4B
0° - 180°	+0.49	a		+0.002	-0.005	+0.002	+0.001
45° - 225°				+0.0018		+0.002	+0.0015
90° - 270°				-0.0015	+0.0015	+0.001	+0.001
135° - 315°				+0.0025		+0.002	+0.001
0° - 180°	-0.49		-0.006	-0.001	-0.001	+0.001	+0.0015
45° - 225°				-0.0085		+0.001	+0.002
90° - 270°			+0.0045	-0.006	0.000	+0.002	+0.001
135° - 315°				+0.0005		+0.002	+0.001

a. No measurement available

Appendix E: Properties

Pertinent information regarding the cylinder wall thickness measurement data, mechanical properties, and stiffness properties is presented here for each test specimen.

Wall Thickness Measurement

The average wall thickness of each cylinder was computed from measurements at 48 selected locations using a 6-in.-deep micrometer. The measurement locations are shown in Fig. E-1 and the data are summarized in Table E-1. The wall thickness was found to be greater in the vicinity of visible ply seam overlaps than in the regions away from the seams. The thickness measurements in Table E-1 represent the average cylinder wall thickness, H, the average ply thickness, h, the minimum and maximum wall thicknesses, H_{min} and H_{max}, respectively, and the standard deviation of the measurement data. The data do not include the visible ply seams.

Table E-1 Specimen Wall Thickness Measurements

Specimen I.D. Code	Wall Construction	H, in.	h, in.	H_{min}, in.	H_{max}, in.	Standard Deviation, in.
CYL-1A	[∓45/0/90]$_S$	0.0374	0.0047	0.0350	0.0390	0.0007
CYL-1B		0.0375	0.0047	0.0360	0.0390	0.0007
CYL-2		0.0368	0.0046	0.0355	0.0400	0.0009
CYL-3A	[∓45/0$_2$]$_S$	0.0381	0.0048	0.0355	0.0400	0.0010
CYL-4A	[∓45/90$_2$]$_S$	0.0369	0.0046	0.0350	0.0390	0.0009
CYL-4B		0.0358	0.0045	0.0330	0.0385	0.0012
Average values		0.0371	0.0046			

(a) 4 Axial Positions   (b) 12 Circumferential Positions
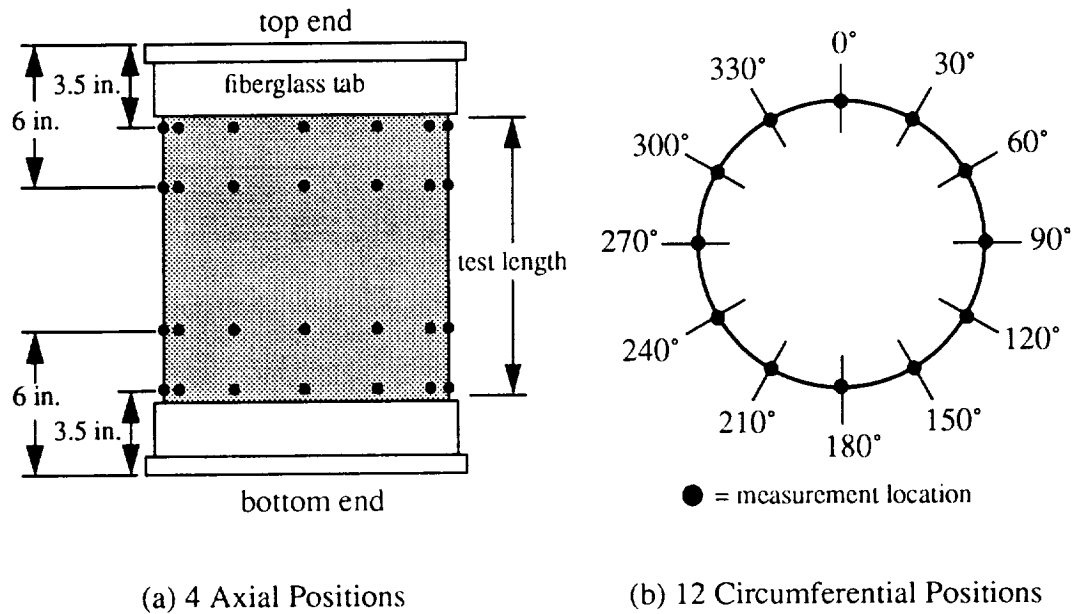
Fig. E-1 Thickness Measurement Locations

Mechanical Properties

The nominal mechanical properties for AS4/3502 graphite-epoxy were obtained from reference [E1, p. 116] and are summarized in Table E-2. The nominal ply thickness in [E1] was assumed to be 0.0055 inches. Comparing the average measured value of h = 0.0046 inches (see Table E-1) to the nominal ply thickness of 0.0055 inches indicates that the measured ply thicknesses were approximately 16% thinner than the nominal ply thickness.

Table E-2 Nominal Mechanical Properties for AS4/3502 Graphite-Epoxy

E_1, Msi	E_2, Msi	G_{12}, Msi	v_{12}
19.625[a]	1.455[a]	0.82	0.295[a]

a. Value represents average of tension and compression modulus.

The measured ply thicknesses suggest that the actual fiber volume fractions, V_f, were greater than assumed value of 0.62 [E2]. It was concluded that the assumed nominal material properties were affected by the increased fiber volume fraction to some extent. The source of the reduced thicknesses was attributed to excessive resin flow during the curing

of the cylinders. The effect of the reduced ply thickness is depicted schematically in Fig. E-2. In this figure, the initial ply thickness is $t^o_{ply} = t_f + t^o_m$, where t_f is the net thickness of the fibers and t^o_m is the initial net thickness of the matrix. After curing, it is assumed that

$$t^o_{ply} = t_f + t^o_m$$

$$t_{ply} = t_f + t_m = t_f + (t^o_m - \Delta t)$$

(a) Assumed Nominal Ply Thickness   (b) Actual Ply Thickness
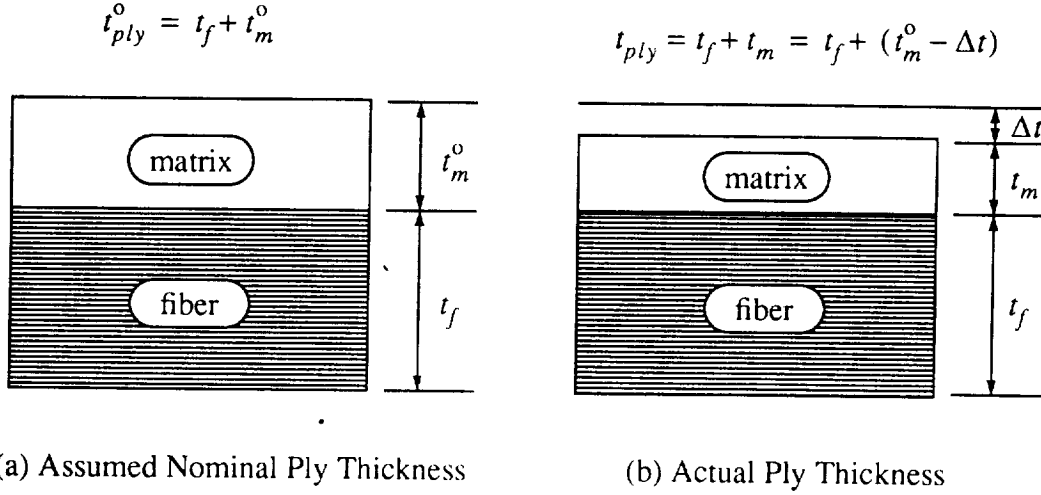
Fig. E-2 Effect of Reduced Ply Thickness on Fiber Volume Fraction

the final ply thickness is given by $t_{ply} = t_f + (t^o_m - \Delta t)$, where Δt is the net reduction in thickness. The new matrix volume fraction, V_m, is computed as

$$V_m = \frac{t_m}{t_{ply}}.$$ (E.1)

The corresponding adjusted fiber volume fraction, V_f, is larger than the assumed fiber volume fraction and is given by

$$V_f = 1 - V_m = 1 - \frac{t_m}{t_{ply}}.$$ (E.2)

Adjusted mechanical properties were computed for each specimen based on the computed laminate volume fractions, Eqs. (E.1) and (E.2), the nominal mechanical properties given in Table E-2, and the rule of mixtures procedures described in reference [E3][*]. The resulting thickness-adjusted mechanical properties and average values are summarized in Table E-3.

---

[*] The matrix Poisson's ratio was assumed to be 0.35.

The relative change in the nominal mechanical properties due to the thickness-adjusted value of V_f is reported in Table E-4. The values in this table are given as the percent change relative to the nominal properties. For an average ply thickness reduction of approximately 16%, the average increase in V_f, E_1, and E_2 is approximately 19%. The shear modulus, G_{12}, increases by approximately 26% and Poisson's ratio, v_{12}, decreases by approximately 3%.

Table E-3 Thickness Adjusted Mechanical Properties

Specimen I.D. Code	E_1, Msi	E_2, Msi	G_{12}, Msi	v_{12}
CYL-1A	23.24	1.74	1.02	0.285
CYL-1B	23.18	1.73	1.02	0.285
CYL-2	23.24	1.74	1.02	0.285
CYL-3A	22.83	1.70	0.99	0.286
CYL-4A	23.55	1.77	1.04	0.284
CYL-4B	24.26	1.84	1.09	0.282
Average[a]	23.38	1.75	1.03	0.285

a. average ply thickness is 0.0046 in.

Table E-4 Change in Mechanical Properties Due to Adjusted Volume Fraction

Specimen I.D. Code	Ply Thickness	V_f	E_1	E_2	G_{12}	v_{12}
CYL-1A	-15.0	+17.6	+18.4	+19.5	+24.7	-3.3
CYL-1B	-14.8	+17.3	+18.1	+19.1	+24.2	-3.2
CYL-2	-15.0	+17.6	+18.4	+19.5	+24.7	-3.3
CYL-3A	-13.4	+15.5	+16.3	+16.9	+21.3	-2.9
CYL-4A	-16.1	+19.3	+20.0	+21.5	+27.2	-3.6
CYL-4B	-18.6	+22.9	+23.6	+26.3	+33.3	-4.3
Average	-15.5	+18.4	+19.1	+20.5	+25.9	-3.4

Appendix E

The laminate extensional and bending stiffness properties are summarized in Tables E-5 and E-6, respectively. The stiffness properties were computed from the data given in Tables E-1 and E-3. The effective inplane laminate properties are summarized in Table E-7.

Table E-5 Laminate Extensional Stiffnesses

Specimen I.D. Code	Wall Construction	A_{11}, lbs/in.	A_{12}, lbs/in.	A_{22}, lbs/in.	A_{66}, lbs/in.
CYL-1A		376,227	112,417	376,227	131,905
CYL-1B	$[\mp45/0/90]_S$	376,169	112,292	376,169	131,938
CYL-2		376,227	112,417	376,227	131,905
CYL-3A	$[\mp45/0_2]_S$	578,575	112,647	173,624	131,726
CYL-4A	$[\mp45/90_2]_S$	180,217	115,466	596,421	136,426
CYL-4B		174,825	112,012	578,579	132,345

Table E-6 Laminate Bending Stiffnesses

Specimen I.D. Code	Wall Construction	D_{11}, in.-lbs	D_{12}, in.-lbs	D_{22}, in.-lbs	D_{16}, in.-lbs	D_{26}, in.-lbs	D_{66}, in.-lbs
CYL-1A		40.1	21.3	31.2	-6.6	-6.6	23.6
CYL-1B	$[\mp45/0/90]_S$	40.3	21.4	31.4	-6.7	-6.7	23.7
CYL-2		40.1	21.3	31.2	-6.6	-6.6	23.6
CYL-3A	$[\mp45/0_2]_S$	43.1	22.2	30.8	-6.9	-6.9	24.5
CYL-4A	$[\mp45/90_2]_S$	30.0	21.3	41.8	-6.6	-6.6	23.7
CYL-4B		27.4	19.4	38.1	-6.1	-6.1	21.6

165

Table E-7 Effective Inplane Laminate Properties

Specimen I.D. Code	Wall Construction	E_x, Msi[a]	E_θ, Msi[b]	$G_{x\theta}$, Msi[c]	$v_{x\theta}$[d]
CYL-1A		9.164	9.164	3.528	0.299
CYL-1B	$[\mp 45/0/90]_S$	9.139	9.139	3.518	0.299
CYL-2		9.164	9.164	3.528	0.299
CYL-3A	$[\mp 45/0_2]_S$	13.274	3.985	3.460	0.648
CYL-4A		4.132	13.720	3.579	0.194
CYL-4B	$[\mp 45/90_2]_S$	4.278	14.158	3.697	0.193

a. $E_x = (A_{11}A_{22} - A_{12}^2) / (HA_{22})$

b. $E_\theta = (A_{11}A_{22} - A_{12}^2) / (HA_{11})$

c. $G_{x\theta} = A_{66}/H$

d. $v_{x\theta} = A_{12}/A_{22}$

References

E1. Sensmeier, M. D., Griffin, O. H., Jr., Johnson, E. R., "Static and Dynamic Large Deflection Response of Graphite-Epoxy Beams," NASA CR-4118, 1988.

E2. Anonymous, Product Data for Hercules Carbon Prepreg Tape AS4/3502, Number 855-2, Hercules Incorporated, Wilmington, DE 19894.

E3. Tsai, S. W., *Theory of Composites Design*, Think Composites, Dayton OH, 1992, pp. 7.1-7.8.

Appendix F: Surface Shape Measurement

The external surface of each specimen was accurately measured using a Brown & Sharpe validator coordinate measurement system, resulting in a three-dimensional surface representation of each cylinder. Surface coordinates were measured every 1/8 inch axially and every 2° circumferentially, yielding approximately 17,000 measurement points for the $L/R = 2$ specimens and over 43,000 measurement points for the $L/R = 5$ specimen. These data were then reduced to compute a Fourier series representation of the surface shape and an average midsurface radius for each specimen. The Fourier analysis software used for these calculations, Tudshell, is described in reference [F1]. The measured shape imperfections were best described by a half-wave cosine representation of the form

$$\frac{\bar{w}(x, \theta)}{H} = \sum_{k=0}^{k_{max}} \sum_{l=0}^{l_{max}} \cos\frac{k\pi\bar{x}}{L} \left[A_{kl}\cos l\theta + B_{kl}\sin l\theta \right] , \tag{F.1}$$

where A_{kl} and B_{kl} are the Fourier coefficients and $\bar{x}$ is aligned with the cylinder x-axis but is measured relative to the end of the cylinder. The number of half-waves in the axial direction is k and the number of full waves in the circumferential direction is l. The range of k was limited to $0 < k < 18$ for the $L/R = 2$ specimens and $0 < k < 39$ for the $L/R = 5$ specimen. The range of l was limited to $0 < l < 50$ for all specimens. The radial shape imperfection was modeled as an initial strain imperfection. An external user-written subroutine was used to compute the radial shape imperfection for each specimen in the STAGS finite element analysis. Details of the implementation of the geometric imperfections can be found in [F2].

A schematic of the measurement setup is shown in Fig. F-1. The contact probe scans the specimen surface in three-dimensional cartesian space by indexing in the circumferential direction and performing scans along the axial direction. All measurements were referred

to a fixed point on the potted specimen which was positioned on the measurement table. The results of the surface measurements are shown graphically in the form of three-dimensional surface plots in Figs. F-2 thru F-7.
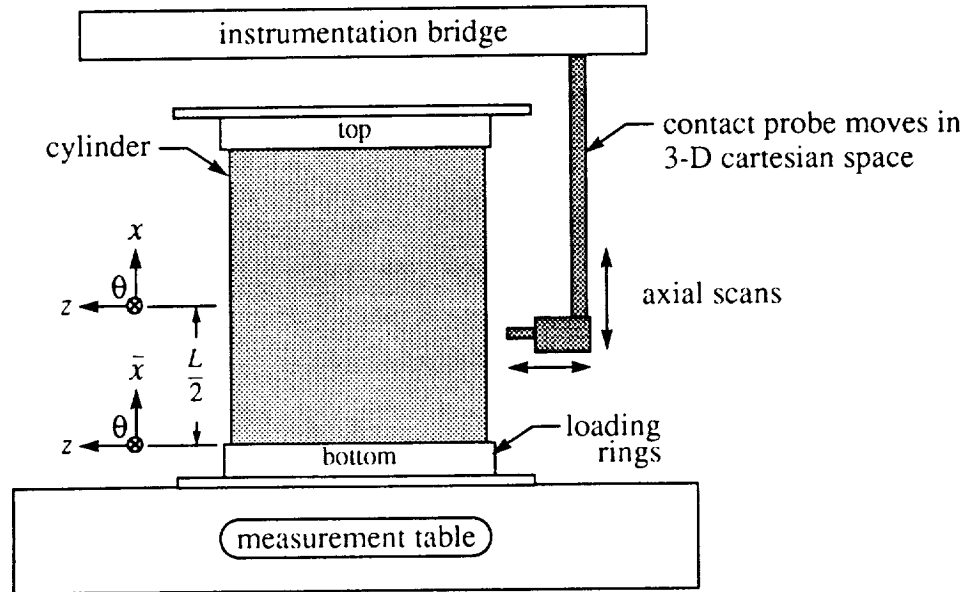
Fig. F-1 Surface Shape Measurement Setup

The surface plots show that the imperfection shapes are characterized by low frequency oscillations in the circumferential direction and comparatively little variation in the axial direction. The peak imperfection amplitudes for each specimen, w_{min} and w_{max}, are summarized in Table F-1.

Table F-1 Peak Imperfection Amplitudes

Specimen Identification Code	Wall Construction	$\dfrac{w_{min}}{H}$	$\dfrac{w_{max}}{H}$	$\dfrac{w_{max} - w_{min}}{H}$
CYL-1A		-0.239	0.346	0.585
CYL-1B	$[\mp45/0/90]_S$	-0.432	0.565	0.997
CYL-2		-0.541	0.866	1.407
CYL-3A	$[\mp45/0_2]_S$	-0.203	0.333	0.536
CYL-4A		-0.325	0.398	0.723
CYL-4B	$[\mp45/90_2]_S$	-0.382	0.354	0.736

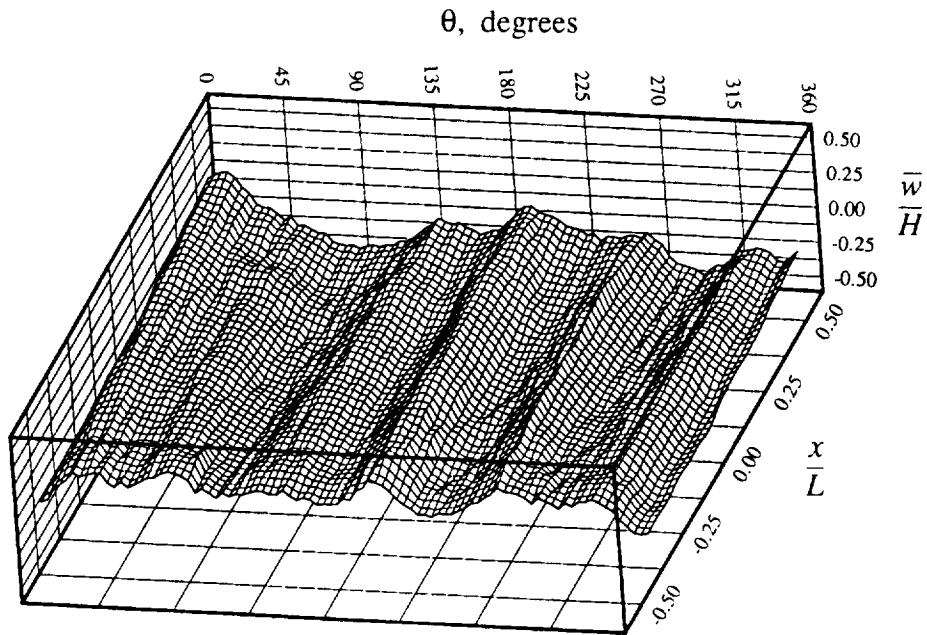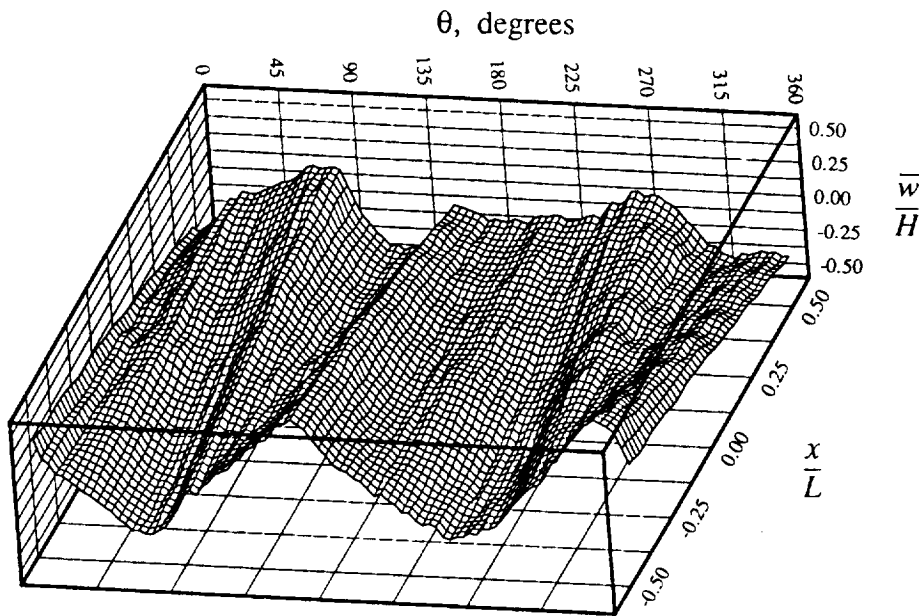**Fig. F-2 Measured Surface Shape, CYL-1A, [∓45/0/90]$_S$, $L/R = 2$**

Fig. F-3 Measured Surface Shape, CYL-1B, [∓45/0/90]$_S$, $L/R = 2$

θ, degrees
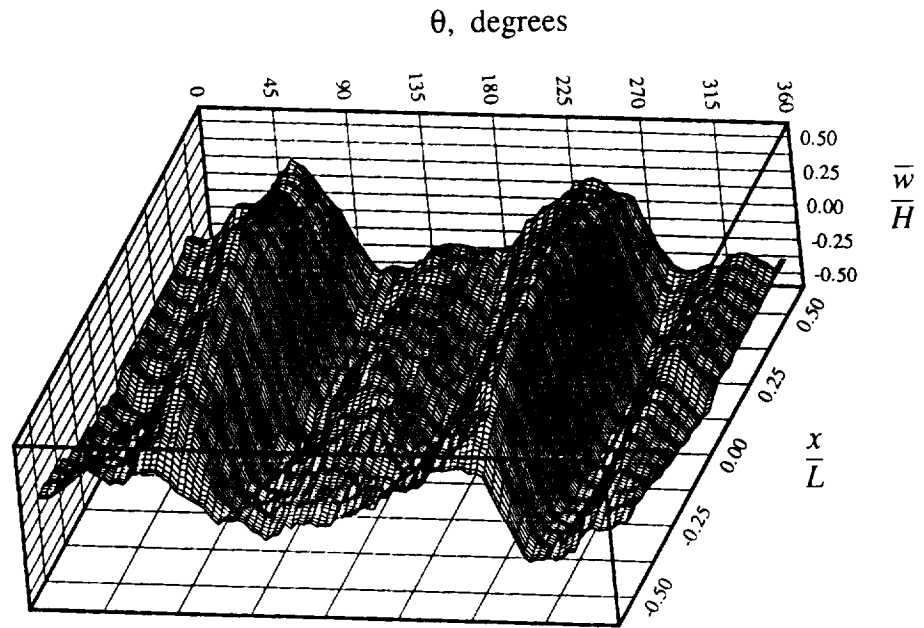

Fig. F-4 Measured Surface Shape, CYL-2, [∓45/0/90]$_S$, L/R = 5

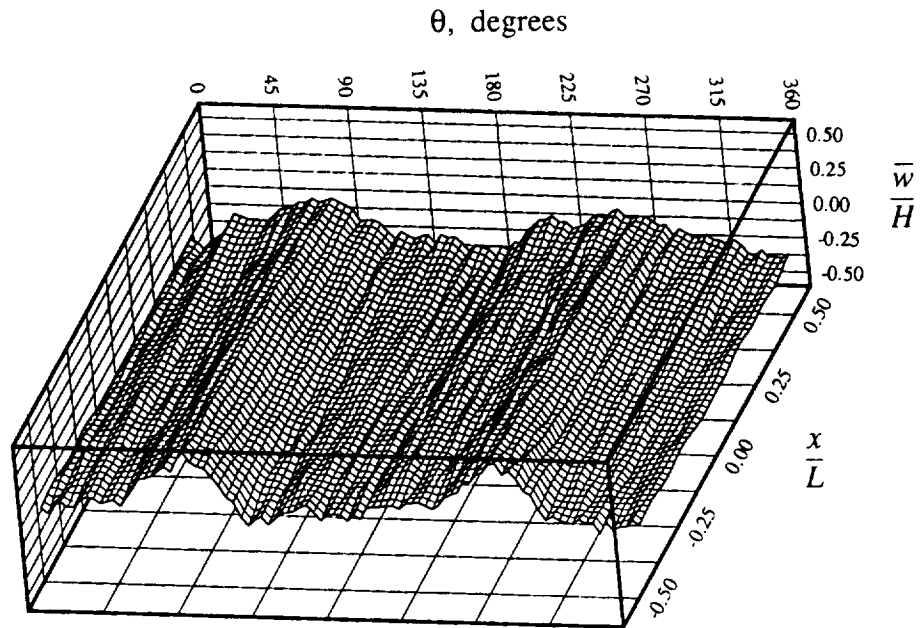θ, degrees

Fig. F-5 Measured Surface Shape, CYL-3A, [∓45/0$_2$]$_S$, L/R = 2

θ, degrees
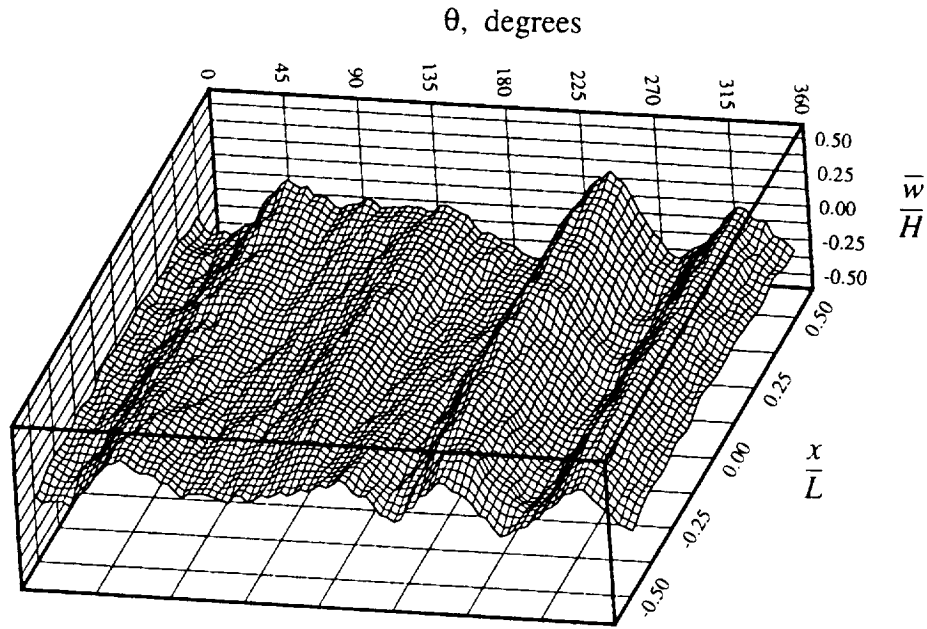
Fig. F-6 Measured Surface Shape, CYL-4A, [∓45/90₂]ₛ, _L/R_ = 2

θ, degrees
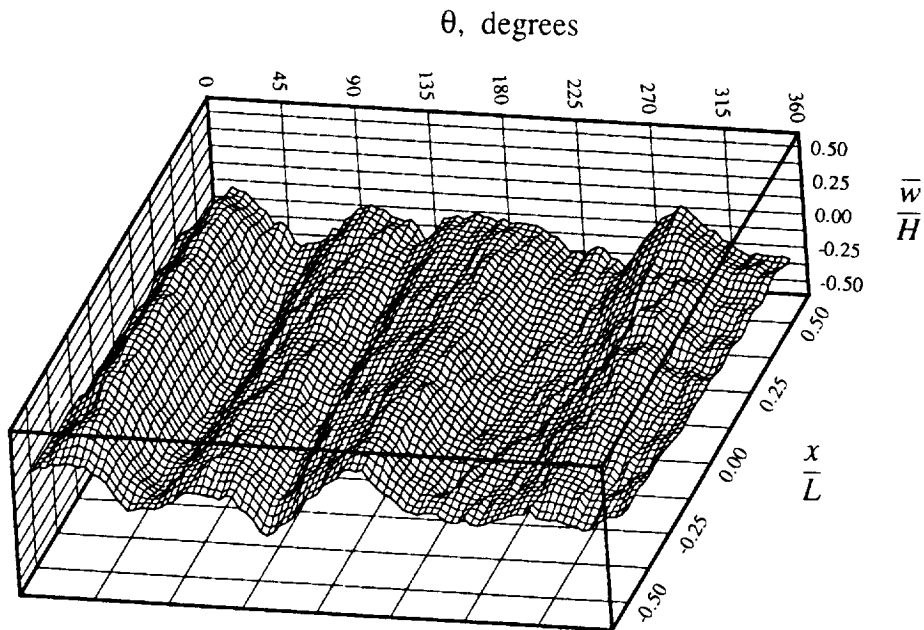
Fig. F-7 Measured Surface Shape, CYL-4B, [∓45/90₂]ₛ, _L/R_ = 2

Appendix F

References

F1. Cartalas, C., van der Hoeven, H. J. C., Klompé, "Guide to the Datareduction of Imperfection Surveys on Circular Shells," Delft University of Technology, Memorandum M-622, Delft, The Netherlands, 1989.

F2. Rankin, C., Brogan, F., "Improved Plasticity and Imperfections in the STAGSC-1 Computer Code, Phase 2: Implementation," Lockheed Palo Alto Research laboratory, Palo Alto, CA, LMSC-F386402, July, 1990.

BIBLIOGRAPHIC DATA SHEET	1. Report No. CCMS-93-19, VPI-E-93-11	2.	3. Recipient's Accession No.

4. Title and Subtitle Numerical and Experimental Investigation of the Bending Response of Thin-Walled Composite Cylinders	5. Report Date September 1993
	6.

7. Author(s) J. P. Fuchs, M. W. Hyer, and J. H. Starnes, Jr.	8. Performing Organization Rept. No. VPI-E-93-11, CCMS-93-19

9. Performing Organization Name and Address Virginia Polytechnic Institute and State University Department of Engineering Science and Mechanics Blacksburg, VA 24061-0219	10. Project/Task/Work Unit No.
	11. Contract/Grant No. NAG-1-343

12. Sponsoring Organization Name and Address Aircraft Structures Branch National Aeronautics and Space Administration Langley Research Center Hampton, VA 23681-0001	13. Type of Report & Period Covered Interim Report 95 8/88-9/93
	14.

15. Supplementary Notes   This report constitutes the Ph.D. thesis in Engineering Mechanics of the first author. The second author is on the faculty of Virginia Polytechnic Institute and State University, while the third author is the Head of the Aircraft Structures Branch of the NASA Langley Research Center.

16. Abstract

A numerical and experimental investigation of the bending behavior of six eight-ply graphite-epoxy circular cylinders is presented. Bending is induced by applying a known end-rotation to each end of the cylinder, analogous to a beam in bending. The cylinders have a nominal radius of 6 inches, a length-to-radius ratio of 2 and 5, and a radius-to-thickness ratio of approximately 160. A $[\mp45/0/90]_s$ quasi-isotropic layup and two orthotropic layups, $[\mp45/0_2]_s$ and $[\mp45/90_2]_s$, are studied. A geometrically nonlinear special-purpose analysis, based on Donnell's nonlinear shell equations, is developed to study the prebuckling responses and gain insight into the effects of non-ideal boundary conditions and initial geometric imperfections. A geometrically nonlinear finite element analysis is utilized to compare with the prebuckling solutions of the special-purpose analysis and to study the buckling and postbuckling responses of both geometrically perfect and imperfect cylinders. The imperfect cylinder geometries are represented by an analytical approximation of the measured shape imperfections. Extensive experimental data are obtained from quasi-static tests of the cylinders using a test fixture specifically designed for the present investigation. A description of the test fixture is included. The experimental data are compared to predictions for both perfect and imperfect cylinder geometries. Prebuckling results are presented in the form of displacement and strain profiles. Buckling end-rotations, moments, and strains are reported, and predicted mode shapes are presented. Observed and predicted moment vs. end-rotation relations, deflection patterns, and strain profiles are illustrated for the post-buckling responses. It is found that a geometrically nonlinear boundary layer behavior characterizes the prebuckling responses. The boundary layer behavior is sensitive to laminate orthotropy, cylinder geometry, initial geometric imperfections, applied end-rotation, and non-ideal boundary conditions. Buckling end-rotations, strains, and moments are influenced by laminate orthotropy and initial geometric imperfections. Measured buckling results correlate well with predictions for the geometrically imperfect specimens. The postbuckling analyses predict equilibrium paths with a number of scallop-shaped branches that correspond to unique deflection patterns. The observed postbuckling deflection patterns and measured strain profiles show striking similarities to the predictions in some cases. Ultimate failure of the cylinders is attributed to an interlaminar shear failure mode along the nodal lines of the postbuckling deflection patterns.

17. Key Words and Document Analysis.   17a. Descriptors Composite materials, thin-walled cylinders, bending, nonlinear analysis, initial geometric imperfections, prebuckling, buckling, postbuckling, material failure
17b. Identifiers/Open-Ended Terms
17c. COSATI Field/Group

18. Availability Statement	19. Security Class (This Report) UNCLASSIFIED	21. No. of Pages 190
	20. Security Class (This Page) UNCLASSIFIED	22. Price